DISS. ETH Nr. 13058

TAILORED ORGANIC THIN FILMS
ON GOLD AND TITANIUM

PEPTIDE-GRAFTING, PROTEIN RESISTANCE AND PHYSICAL
CHARACTERIZATION

A dissertation submitted to the

SWISS FEDERAL INSTITUTE OF TECHNOLOGY ZÜRICH

for the degree of Doctor of Technical Science

presented by

SHOU-JUN XIAO

M. Sc. Chemistry, Fudan University

born on Dec. 07, 1963

China

accepted on the recommendation of

PROF. DR. N.D. SPENCER, examiner

DR. M. TEXTOR, co-examiner

DR. H. SIGRIST, co-examiner

ZÜRICH 1999

Acknowledgments

Abstract

In order to improve the biocompatibility of titanium implants widely used in biomedical applications, the cell-adhesive, RGD-containing peptides were immobilized on titanium surfaces through a three-step reaction procedure. The first step is silanization of titanium surfaces with (3-aminopropyl)triethoxysilane, resulting in a multilayer film of poly(3-aminopropyl)siloxane. The second reaction step, a key step of this modification procedure, is grafting functional crosslinking groups (maleimide, iodoacetate, succinimidyl ester, and arylazide) through the surface reaction of primary amines with succinimidyl esters. The final step is the covalent attachment of RGD-containing peptides through a thioether, an amide linkage, or a photochemical reaction. Two model, cell-adhesive peptides, H-Gly-Arg-Gly-Asp-Ser-Pro-Cys-OH (GRGDSPC) and H-Arg-Gly-Asp-Cys-OH (RGDC) were immobilized through covalent addition of the cysteine thiol (-SH) group to the maleimidyl group. An approximate coverage of 0.2~0.4 peptides per nm^2 was calculated through independent quantitative analyses. The RGD-modified samples were then tested with the osteoblastic cell line MC3T3-E1 and rat bone marrow cells *in vitro*. Preliminary cell culture results show positive effects for osteoblastic cell line MC3T3-E1 but negative effects for rat bone marrow cells in cell adhesion, differentiation, and integration. X-ray photoelectron spectroscopy (XPS), infrared reflection absorption spectroscopy (IRAS), time-of-flight secondary ion mass spectroscopy (ToF-SIMS), ellipsometry, and radiolabeling techniques were applied to characterize the surfaces. The controversy as regards the interpretation of the IRAS spectra, especially for the maleimidylhexanoyl pendant surface, motivates us to investigate the detail of the surface reactions of primary amines with amino-reactive heterobifunctional crosslinkers.

Two model aminothiols, cystamine and 4-aminothiophenol, were self-assembled on gold surfaces as the starting films for model investigations. Different types of thiol-, amino-, and photo-reactive crosslinkers were then attached to the two amino-terminated SAMs. Based on IRAS and XPS measurements, two types of reaction schemes have been observed: (1) modification through single group binding, (2) occurrence of side reactions and production of multiple-group-modified surfaces. A typical example for the latter case is the reaction of N-succinimidyl-6-maleimidyl hexanoate (EMCS) with terminal NH_2 groups, producing a mixture of both maleimidyl and succinimidyl ester groups on the surface. The conclusion is confirmed by the study of SAMs of pure N, N'-bis(maleimidylhexanoyl)cystamine (BMHC), synthesized separately. The functionalized surfaces with crosslinking groups can be used for further specific or non-specific attachment of biomolecules.

Finally, two types of poly(ethylene glycol) (PEG) were grafted to amino-terminated surfaces, methoxy-PEG in a "standing-up" configuration and bridging-PEG in a "lying-down" configuration. Their surface structures and reaction yields were studied with IRAS and XPS. The protein resistance of PEG-coatings was evaluated with the optical waveguide lightmode spectroscopy (OWLS). Only the bridging PEG exhibited protein resistance.

Zusammenfassung

Um die Biokompatibilität von Titanoberflächen für Implantate und biomedizinische Anwendungen zu verbessern, wurden zelladhäsive Oligopeptide, die eine RGD-Sequenz enthalten, mittels einer Dreistufen-Reaktion kovalent an die Titanoberfläche angebunden. Der erste Schritt beinhaltet die Silanisierung von Titanoberflächen mit (3-Aminopropyl)triethoxysilan, welche zu einem Mehrschichten-Film bestehend aus Poly(aminopropyl)siloxan führt. Der zweite Reaktionschritt, der entscheidende Schritt der gesamten Reaktionssequenz, ist das Anknüpfen von funktionellen Vernetzungsgruppen (Maleimid, Iodacetat, Succinimidyl-Ester, und Arylazid) durch die Oberflaechenreaktion von primären Amiden mit Succinimidyl-Estern. Im letzten Schritt wird das RGD-enthaltende Peptid über die Thiolfunktion addiert (Amid-Bindung oder über eine photochemische Reaktion). Zwei zelladhäsive Modell-Peptide H-Gly-Arg-Gly-Asp-Ser-Pro-Cys-OH (GRGDSPC) und H-Arg-Gly-Asp-Cys-OH (RGDC) wurden durch kovalente Addition der Cystein-Thiol-Gruppe an die Maleimidyl-Gruppe immobilisiert. Ein ungefährer Bedeckungsgrad von 0.2-0.4 Peptid/nm² wurde mit unabhänigigen quantitativen Methoden berechnet. Die RGD-modifizierten Proben wurden in der Osteoblastzelllinie MC3T3-E1 und Rattenknochenmarkzellen *in vitro* getestet. Die ersten Zellkulturresultate zeigen bezüglich Zelladhäsion, Differenzierung und Integration positive Effekte für Osteoblasten und negative Effekte für die Knochenmarkzellen. Um die Oberflächen zu charakterisieren, wurden X-Ray Photoelectron Spectroscopty (XPS), Infrared Reflection Absoeption Spectroscopy (IRAS), Time-of-Flight Secondary Ion Mass Spectroscopy (ToF-SIMS), Ellipsometrie und Radiolabeling Techniken eingesetzt. Die kontroverse Interpretation von IRAS-Spektren, speziell für Maleimidylhexanoyl, motivierte uns, die Details der Oberflaechenreaktionen von primären Aminen mit aminoreaktiven heterobifunktionellen Vernetzungsmolekülen zu untersuchen.

Im Hinblick auf ein verbessertes Verständnis der Reaktionsmechanismen an der Oberfläche wurden zwei Modell-Aminothiole, Cystamin und 4-Aminothiophenol, auf Goldoberflächen adsorbiert (selbstorganisierende Monoschichten, SAM). Verschiedene Typen von Thiol-, Amino- und Photo-reaktiven Vernetzungsmolekülen wurden an die aminoterminierten SAMs angebunden. Basierend auf XPS und IRAS Messungen wurden zwei verschiedene Reaktionsschemata beobachten: (1) Modifikation durch Ein-Gruppen-Bindung, (2) auftreten von Nebenreaktionen und Produktion von Mehrfach-Gruppen-modifizierten Oberflächen. Ein typisches Beispiel für den zweiten Fall ist die Reaktion von N-Succinimidyl-6-maleimido-caproat (EMCS) mit NH2-Endgruppen, was zu einer Mischung von Maleimidyl- und Succinimidylestergruppen auf der Oberfläche führt. Diese Schlussfolgerung wird durch die Untersuchung von SAMs bestätigt, für welche speziell

synthetisiertes, reines N,N'-Bis(maleimidylhexanoyl)cystamin (BMHC) verwendet wurde. Die funktionalisierten Oberflächen mit vernetzenden Gruppen können für spezifische oder unspezifische Bindung von Biomolekülen an die Oberfläche benutzt werden.

Zum Schluss wurden zwei Typen von Polyethylenglykolen auf aminoterminierten Oberflächen aufgebracht: Methoxy-PEG in "standing-up"-Konfiguration und bridging-PEG in "lying-down" Konfiguration. Ihre Oberflächenstruktur und Reaktionskinetik wurden mit IRAS und XPS studiert. Die Resistenz gegen Proteinadsorption wurde mit Optical Waveguide Lightmode Spectroscopy (OWLS) ermittelt. Nur das bridging-PEG zeigte Resistenz gegen Proteinadsorption.

Table of contents

Abbreviations

One- and three letter code for amino acids used in this thesis.

Name	Three letter code	One letter code
Arginine	Arg	R
Aspartic acid	Asp	D
Cysteine	Cys	C
Glycine	Gly	G
Proline	Pro	P
Serine	Ser	S

Chemicals

4-ATP	4-Aminothiophenol
α-MEM	α-Minimum essential medium
ANS	N-5-Azido-2-nitrobenzoyloxysuccinimide
APS	Poly(3-aminopropyl)siloxane
APTES	3-Aminopropyltriethoxysilane
BMHC	N,N'-Bis(maleimidylhexanoyl)cystamine
DMF	N,N'-Dimethyl formamide
DMSO	Dimethyl sulfoxide
DNA	Deoxyribo nucleic acid
DSS	Di-(N-succinimidyl) suberate
DTSP	Dithiobis(N-succinimidyl propionate)
ECM	Extra cellular matrix
EDTA	Ethylene diamine tetraacetic acid
EMCS	N-Succinimidyl-6-maleimidylhexanoate
FA	Formaldehyde
FCS	Fetal calf serum
GRGDSPC	H-Gly-Arg-Gly-Asp-Ser-Pro-Cys-OH
HEPES	2-[4-(2-Hydroxyethyl)-1-piperazynil] ethanesulfonic acid
MHA	N-(Maleimidylhexanoyl)aniline
OTS	Octadecyltrichlorosilane
PBS	Phosphate buffered saline
PEG	Poly(ethylene glycol)
PG	Phenylglyoxal

RBM	Rat bone marrow cells
RGD	H-Arg-Gly-Asp-OH
RGDC	H-Arg-Gly-Asp-Cys-OH
SBB	N-Succinimidyl-4-benzoylbenzoate
SC	Di-(N-succinimidyl) carbonate
SIA	N-Succinimidyl iodoacetate
SMB	N-Succinimidyl-4-maleimidylbutanoate
SMBZ	N-Succinimidyl-3-maleimidylbenzoate
SMCC	N-Succinimidyl trans-4-(maleimidylmethyl)cyclohexane-1-carboxylate
SMO	N-Succinimidyl-8-maleimidyloctanoate
SMP	N-Succinimidyl-3-maleimidylpropionate
SMPB	N-Succinimidyl-4-(4-maleimidylphenyl)-butyrate
SMU	N-Succinimidyl-6-maleimidylundecanoate
TRAP	Tartrate resistant acidic phosphatase

Modified titanium surfaces

Ti	Water-vapor-plasma-pretreated titanium surface
A	**Ti** + APTES or Poly(3-aminopropyl)siloxane modified **Ti**
M	Maleimide-modified **A**
P	Peptide- or L-cysteine-modified **M**

TiAM3	A + SMP
TiAM4	A + SMB
TiAM6	A + EMCS
TiAM8	A + SMO
TiAM11	A + SMU
TiAMC	A + SMCC

CM6	L-cysteine + TiAM6
CM3	L-cysteine + TiAM3
CMC	L-cysteine + TiAMC
GM6	GRGDSPC + TiAM6
GM3	GRGDSPC + TiAM3
GMC	GRGRSPC + TiAMC
RM6	RGDC + TiAM6

RM3   RGDC + TiAM3
RMC   RGDC + TiAMC

^{14}CA   [^{14}C]-formaldehyde + **A**
^{35}SM6   [^{35}S]-L-cysteine + TiAM6
^{14}CGM6   [^{14}C]-Phenylglyoxal + GM6

Modified gold surfaces

Au   Gold
AuC   Au + cystamine
AuB   Au + 4-aminothiophenol (4-ATP)
AuCM3   AuC + SMP
AuCM4   AuC + SMB
AuCM6   AuC + EMCS
AuCM8   AuC + SMO
AuCM11   AuC + SMU
AuCMC   AuC + SMCC
AuCMB   AuC + SMBZ
AuCMP   AuC + SMPB
AuCIA   AuC + SIA
AuCAZ   AuC + ANS
AuCBB   AuC + SBB
AuCSC   AuC + SC
AuCTP   AuC + DTSP
AuCS8   AuC + DSS
AuBM3   AuB + SMP
AuBM4   AuB + SMB
AuBM6   AuB + EMCS
AuBM8   AuB + SMO
AuBM11   AuB + SMU
AuBMC   AuB + SMCC
AuBMB   AuB + SMBZ
AuBMP   AuB + SMPB
AuBIA   AuB + SIA
AuBSC   AuB + SC

AuBTP	AuB + DTSP
AuBS8	AuB + DSS
M3	Maleimidyl propionoyl group
M4	Maleimidyl butanoyl group
M6	Multiple groups of hexanoyl maleimide & succinimidyl ester
M8	Multiple groups of octanoyl maleimide & succinimidyl ester
M11	Multiple groups of undecanoyl maleimide & succinimidyl ester
MB	Maleimidyl benzoyl group
MP	Maleimidylphenyl butanoyl group

Instruments

AFM	Atomic force microscopy
amu	Atomic mass unit
E_B	Binding energy
E_F	Fermi energy
E_K	Kinetic energy
FTIR	Fourier transform infrared spectroscopy
IRAS	Infrared reflection absorption spectroscopy
NEXAFS	Near-edge X-ray absorption fine structure spectroscopy
NMR	Nuclear magnetic resonance spectroscopy
OWLS	Optical waveguide lightmode spectroscopy
SEM	Scanning electron microscopy
ToF-SIMS	Time-of-flight secondary ion mass spectroscopy
XPS	X-ray photoelectron spectroscopy

Miscellaneous

amor	amorphous
asym	asymmetric
crys	crystalline
ECM	Extra cellular matrix
mal	maleimidyl group
SAM	Self-assembled monolayer
suc	succinimidyl group
sym	symmetric

1. Outline

1.1 Introduction

Biomaterials are nonviable materials used in medical devices, intended to interact with biological systems. Suture threads, contact lenses, artificial hip joints, dental implants, and heart valves are some common examples of the application of biomaterials. When these materials evoke a biological response that is compatible with the intended functionality over the intended period of treatment, they have come to be termed *biocompatible*.

Biomaterials are used and developed to direct, supplement or replace organs or living tissues and, as such, they have to fulfill the mechanical and biological functions required. They also have to be sterilizable and be suited to processing. But, above all, these materials must be compatible with the living environment. The interaction of biomaterials with the living environment can be classified as either *biotolerant, bioinert* or *bioactive*, conveying respectively the sense of negative (but tolerable) local host response, absence of local host response, and positive (desired) local host response.

Many classes of materials contribute to the field of biomaterials. For example, metallic elements (titanium, gold), alloys (stainless steel, titanium, cobalt-chromium alloys) and ceramics (porcelain, alumina, hydroxyapatite) can be used for structural purposes in orthopedic, dental applications, or for cardiovascular devices; natural or synthetic polymers such as polysaccharides, collagen, polyurethane, silicones, polyacrylates, etc., can be used in suture materials (biodegradable or not), artificial organs, contact lenses, intraocular lenses, tissue regeneration, encapsulating membranes for drug delivery, adhesives for orthopedic and dental applications, dialysis membranes, blood bags, etc.

Among these materials, titanium and its alloys have received a broad interest because of their important market share and wide applications in medical systems. Titanium and its alloys have excellent properties for implant materials, particularly in bone applications. They are biocompatible with the human body. They are easy to be sterilized, positioned, and fixed. After implantation, they are resistant to general corrosion, pitting attack, and crevice corrosion in physiological fluids. Thus, they have a long life span as an implant up to about 20 years. Titanium and its alloys have been successfully used in diverse

applications such as hip joints, osteosynthesis devices, pacemakers, knee and shoulder prostheses, heart valves, screws, and nails. They are on the verge of becoming the metals of choice for implant and surgical applications.

Table 1-1   Nature and properties of physical adsorption and chemical binding.

	Physical adsorption	**Chemical binding**
Principles	- Van der Waals forces - hydrophobic forces - electrostatic interactions	- covalent bond - complexation - coordination
Advantages	- easy to prepare under mild experimental conditions - adsorption reversible - biological activity retained	- controlled coverage - stable in physiological conditions and for multiple use
Disadvantages	- not stable under all physiological conditions - one time use - poor reproducibility	- reaction conditions stringent - some biological activity may be lost

A current trend to enhance biocompatibility consists of chemical modification of the biomaterial surface by the grafting of biologically active molecules such as peptides, proteins, and antibodies. This procedure offers the advantage of improving surface properties with respect to biocompatibility without adverse effect on the bulk properties of the system. Immobilization of such molecules can be achieved by a variety of different techniques that exploit either physical adsorption (through Van der Waals, hydrophobic, or electrostatic forces) or chemical binding. Both approaches have advantages and disadvantages. Physical adsorption processes are generally experimentally simple and often allow retention of the biomolecular activity. However, the adsorption is often reversible, with target molecules being removed by certain buffers or detergents or replaced by other molecules in solution. In contrast, chemical immobilization involves the covalent bonding (or complexation) of the target molecule to the solid phase. This method is experimentally more difficult and often exposes the molecule to a harsher environment. However, the resultant irreversible binding which can be produced with high levels of surface coverage makes this approach more popular, although in some cases chemical binding can alter the conformational structure and active center of the molecule, causing a

reduction in activity. Some aspects of the physical adsorption and chemical binding are summarized in Table 1-1.

1.2 Aim of the work

The aim of the work is to design a surface modification method for covalent attachment of Arg-Gly-Asp (RGD)-containing peptides on Ti surfaces. It is expected that the novel surfaces will improve the biocompatibility and functionality of titanium used in application where a fast and complete integration into the host tissue is required. This method can also be applied to covalently bind other interesting molecules, such as proteins, peptides, DNA/RNA strands, and poly(ethylene glycol) (PEG) on solid substrate surfaces with potential applications in biomaterials and biosensors. The key step of the method investigated in this thesis is the reaction between amine-grafted solid substrate surfaces and succinimidyl esters. Although this reaction has been thoroughly studied in bulk solutions (especially in aqueous buffer for protein cross-linking and conjugation), the same type of reaction is just beginning to be applied to self-assembled films.[1-3] The physico-chemical characterization of the resulting surface is, as we know, still rudimentary, and the details of the surface reaction are not yet well understood. For this reason, we have chosen self-assembled aminothiols on Au surfaces, which are more reproducible for surface characterization than aminosilanes, as model surfaces, in order to study the details of the reaction.

The work can be divided into 3 parts:
1. Covalent attachment of RGD-containing peptides on titanium (oxide) surfaces and *in vitro* cell culture tests
2. Investigation of the surface reactions of succinimidyl esters with aminothiol SAMs on Au surfaces
3. Immobilization of PEG on amino-terminated surfaces: a study of the protein resistance

1.2.1 Covalent attachment of RGD-containing peptides on Ti surfaces

Titanium is the primary material to be modified in this work. It is generally accepted that the inert passivation layer, ~5 nm amorphous TiO_2, contributes to its excellent biocompatibility. Although titanium is a successful biocompatible (bioinert) material, there is still considerable interest, from the standpoint of both surgeon and patient, in increasing both speed (healing time) and degree (long-term success) of close bone aposition. One

way is to produce a bioactive surface instead of the bioinert surface, guiding the specific cell adhesion, cell proliferation and differentiation. Two model peptides, H-Arg-Gly-Asp-Cys-OH (RGDC) and H-Gly-Arg-Gly-Asp-Ser-Pro-Cys-OH (GRGDSPC) were grafted on titanium surfaces through a three-step reaction procedure. First, the titanium surface was silanized with an aminosilane. Secondly, a maleimidyl group was introduced through the reaction of the free primary amino group with the succinimidyl ester group. Finally, the RGD-containing peptide with terminal cysteine was covalently bound to the maleimidyl group. For each step, the surface sensitive characterization methods (XPS, IRAS, and radiolabeling techniques) were used to qualitatively and quantitatively analyze the surface.
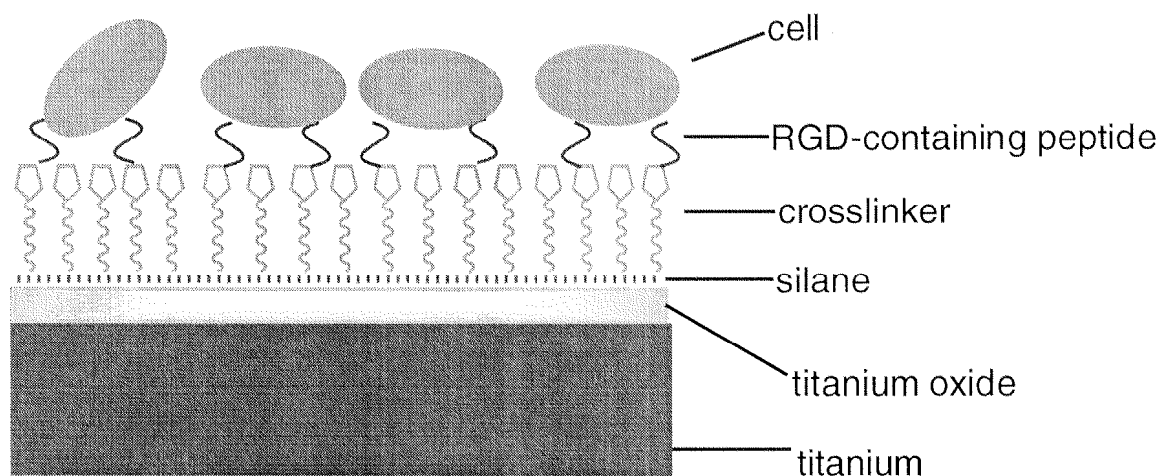
Figure 1-1   Schematic drawing of the functionalized surface. The titanium sample with a passivation TiO_2 layer was first activated with an aminosilane, secondly connected to a crosslinker, thirdly to a RGD-containing peptide, and finally used for cell culture tests.

The novel Ti surfaces modified with RGD-containing peptides were tested *in vitro*. The osteoblastic cell line MC3T3-E1 and the adult primary bone marrow cells were used in the test. The MC3T3 cell line is taken since it is one of the most commonly used cell lines in studies related to load-bearing implants and bone diseases. Bone marrow cells are used for the present study since most bone replacement materials are implanted in an adult bone and therefore are in direct contact with bone marrow.

1.2.2 Surface reactions of succinimidyl esters with aminothiol SAMs on Au surfaces

Self-assembled monolayers (SAMs) on gold have potential applications in biosensors, biomaterials, and microfabrication. One important direction is immobilization of bioactive

molecules. Generally, two methods are available: One is the direct anchoring of the target molecule synthesized with thiols exposed on the molecular surface, and the other is the use of stepwise grafting reactions. In this thesis, a new strategy in the latter category is introduced. We studied the surface reactions of two aminothiol SAMs, cystamine and 4-aminothiophenol (4-ATP), with a series of bifunctional crosslinkers bearing succinimidyl esters. A variety of crosslinking groups of amino-, thiol-, and photo-reactive reagents can be grafted on amino-terminated surfaces. These functional surfaces can be used further for grafting biomolecules. The main characterization tools used were infrared reflection absorption spectroscopy (IRAS) and x-ray photoelectron spectroscopy (XPS).

1.2.3 Immobilization of poly(ethylene glycol) on NH_2-terminated surfaces

Poly(ethylene glycol) (PEG) is a water-soluble, very flexible, and highly mobile polymer. Protein adsorption has been shown to be strongly reduced upon coating of surfaces with PEG derivatives. "Steric repulsion" or "steric forces" are thought to be responsible for the repulsive forces acting on the proteins when they approach a surface with terminally attached PEG chains.[4,5] In addition, PEG/water interfaces are thought to have low interfacial free energies, and thus low driving forces for protein adsorption.[6] PEG coatings may be used in biomaterials, chromatography, biosensors, electrophoresis, and other applications.

Based on the reaction of succinimidyl esters with terminal NH_2 groups, we can introduce different kinds of PEG polymers on Au, Ti, and optical waveguide chips (with oxide surfaces such as TiO_2). The PEG chains can have different configurations, such as "standing up" or "lying down" structures on the surface. Their protein resistance behavior was studied with the optical waveguide lightmode spectroscopy (OWLS).

1.3 Outline of the work

The work done in this thesis is outlined in the form of a flow chart. The following explanations are given for the flow chart:

1st reaction step: Formation of self-assembled films with terminal amino groups
It is well known that there are two common kinds of chemical reagents for SAM formation, organosilane and organosulfur. The derivatives of organosilanes are used to modify the solid oxide surfaces with hydroxyl groups, and those of organosulfurs to

modify noble metals such as Au, Ag, and Pt.[127,128] We used 3-aminopropyltriethoxysilane for modifying Ti metal and TiO$_2$. Ti metal samples were used later on for *in vitro* cell culture tests, while TiO$_2$ samples were tested in both cell culture and OWLS measurements. It should be noted that titanium (metal) samples always carry a passive, natural oxide film and the chemical modifications therefore are reactions with titanium oxide (TiO$_2$) both on titanium metal and on synthetic TiO$_2$ films. Two simple aminothiols, cystamine and 4-aminothiophenol, were used to modify Au surfaces.

2nd reaction step: Introduction of functional crosslinking groups to the surface through the surface reaction of succinimidyl esters with terminal amino groups

The reaction of succinimidyl esters with terminal NH$_2$ groups immobilized on solid surfaces is a main topic studied in this thesis. Through this reaction, the thiol-reactive crosslinking groups such as maleimide and iodoacetamide, the amino-reactive groups such as succinimidyl ester, and the photocrosslinking groups such as arylazide and benzophenone can be grafted on solid surfaces. With these functional groups, further immobilization of variable biomolecules becomes feasible.

3rd reaction step: Immobilization of biomolecules

As model peptides, two RGD-containing peptides, RGDC and GRGDSPC, were grafted on maleimide-modified Ti surfaces. It is obvious that many kinds of biomolecules can be fixed through these modified surfaces with such effective crosslinking groups. Different applications need different functional crosslinkers: e.g. proteins or peptides with exposed thiol groups can be fixed through maleimides or α-iodoacetamides, those with exposed amino groups can be attached through succinimidyl esters, and protein or peptide patterns can be formed through photocrosslinkers. This method has potential applications in biomaterials, biosensors, bioreactors, etc.

Flow chart showing the principal research areas described in this thesis
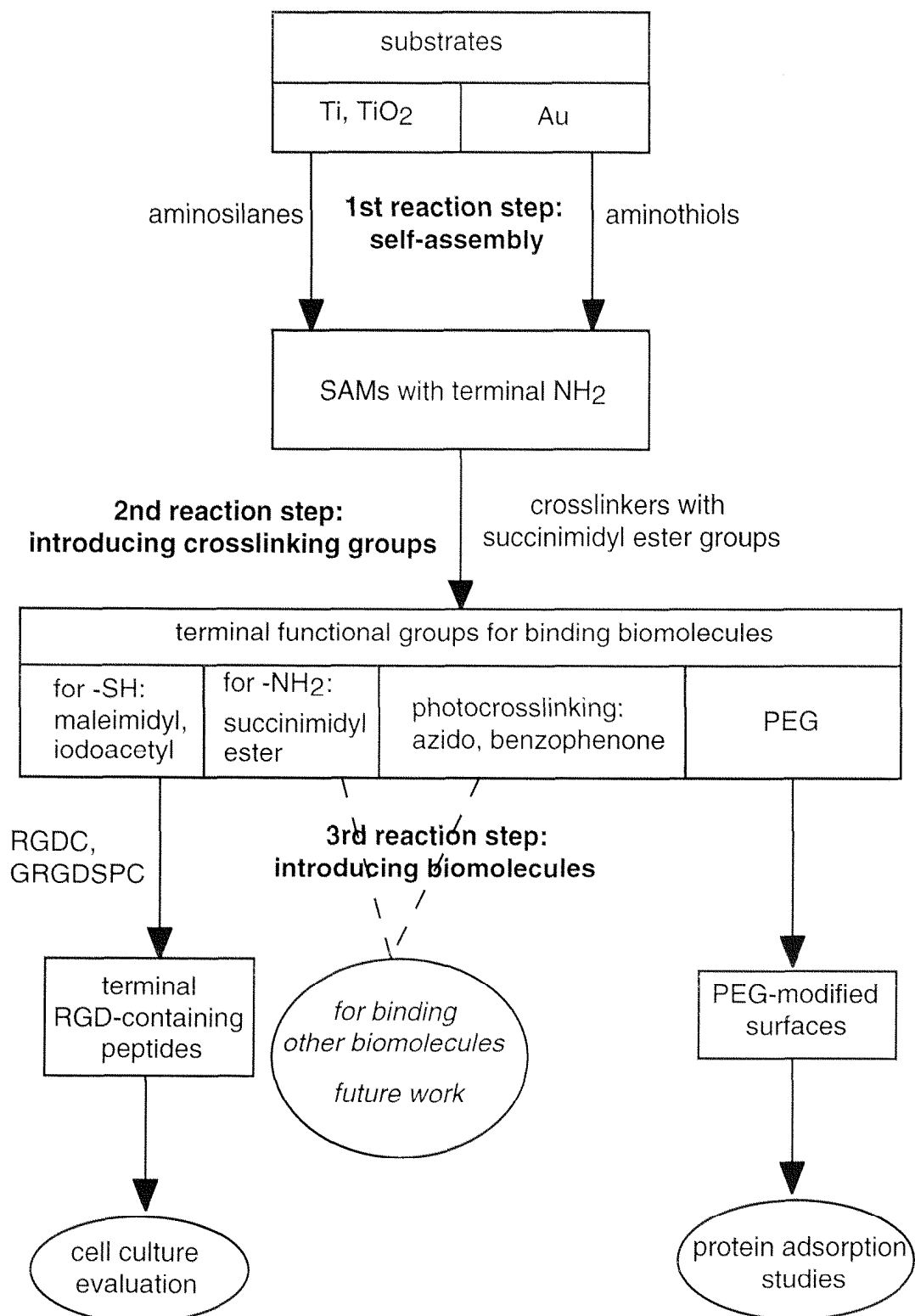
2. Background

2.1 Titanium as a biomaterial

Titanium was discovered in 1790 and is the earth's ninth most abundant element. The Kroll process (developed in 1936) allowed titanium to be produced in commercial quantities. The Kroll process involves the chlorination of the raw ore to produce titanium tetrachloride ($TiCl_4$). This chloride compound is then reduced with solid magnesium metal in an inert atmosphere to produce $MgCl_2$ and a porous ingot of titanium (known as a sponge). Iron chloride and residual magnesium chloride are then leached out to purify the ingot, which is then densified. The titanium used in the manufacture of modular implant components has a nominal purity of 99.0%.

Titanium is an allotropic element. At room temperature, the hexagonal close packed (hcp) structure, known as the α phase, is thermodynamically stable. When heated to temperatures in excess of 883°C (1621°F), it transforms into the body centered cubic (bcc) β phase.

Titanium has advantageous bulk properties, such as low modulus of elasticity, light weight, poor heat conduction, and high strength to weight ratio. Its biocompatibility derives from its surface characteristics. A thin oxide surface layer (called passivation layer), ~5 nm thick, stoichiometrically resembling TiO_2, is formed spontaneously in air (Freshly exposed metallic surfaces will adsorb and react with oxygen present in the atmosphere almost instantaneously). It is extremely adherent and electrochemically inert and therefore titanium and many of its alloys show very high corrosion resistance. The passivation oxide layer of metals forms to varying degrees, depending on the magnitude of the free energy of formation of the metallic oxide and the availability of oxygen or other species at the surface. This oxide layer can serve to greatly reduce the transport of corrosive species to the underlying metal's surface. The following reaction equations represent the formation of the passivation oxide layer.

$$Ti + O_2 \Leftrightarrow TiO_2 \qquad\qquad\qquad \Delta G_{298} = -890 \text{ kJ mol}^{-1}$$

$$Ti + 2H_2O \Leftrightarrow \{Ti(OH)_3\}_s + \tfrac{3}{2} H_2 \qquad\qquad \Delta G_{298} = -340 \text{ kJ mol}^{-1}$$

$$Ti + 2H_2O \Leftrightarrow \{TiO_2\}_s + 2H_2 \qquad\qquad \Delta G_{298} = -414 \text{ kJ mol}^{-1}$$
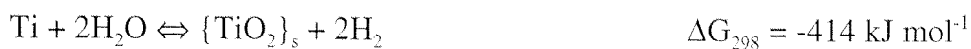
The excellent soft- and hard-tissue response to titanium implants can partly be explained by the physical chemical characteristics of the passivated Ti-tissue interface.

- The passivation oxide layer is thermodynamically stable under physiological conditions.

- The repassivation/passivation is very fast once the tenacious passive layer is breached. This rapid process provides a unique advantage for the biomedical application.

- The solubility of TiO_2 (the surface species) in water or physiological solutions is so low (in the range of 10^{-6} M) that the dissolved species in the body has essentially no harmful effect for up to 20 years.

- The isoelectric point of the passivation surface is in the range of pH 5 ~ 7, and therefore in the physiological solution (pH = 7.4) the weakly negatively charged surface has a gentle interaction with the adsorbed proteins.
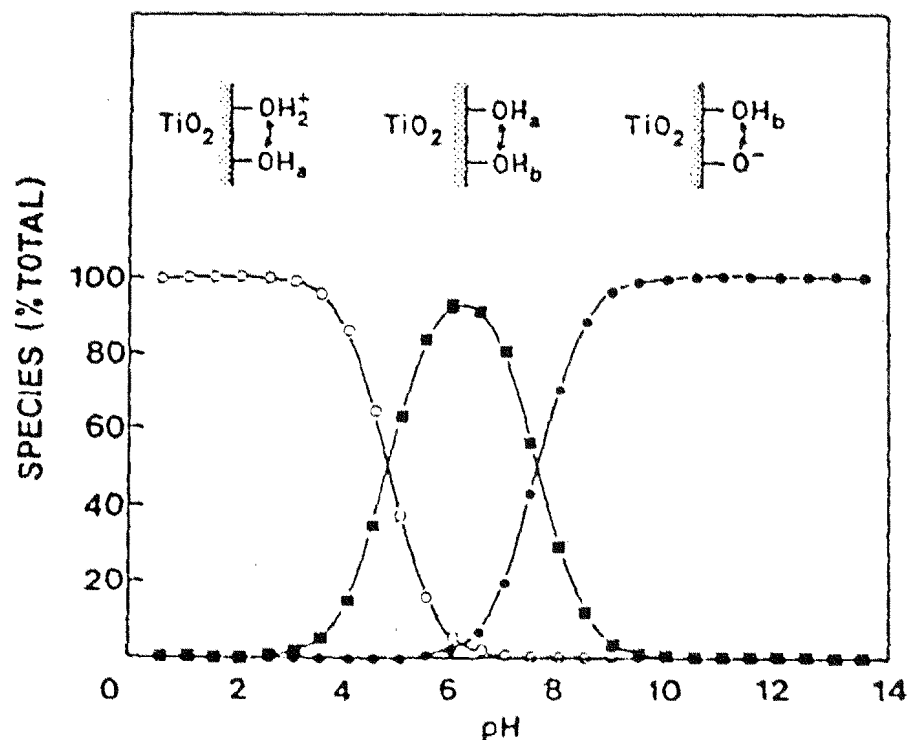
Figure 2-1   *Diagram indicating the TiO_2 surface charge as a function of pH.[7] The oxide is amphoteric and —OH_a denotes acidic hydroxyl groups and —OH_b basic hydroxyl groups. m, positive surface charge; l negative surface charge; n, neutral surface charge.*

However, in the presence of mechanical abrasion, even the most tenacious passive film can be broken. Once this occurs, the surrounding chemistry (i.e., the availability of free oxygen, water, or other oxygen-containing species) and the nature of the metal-oxide bond

will determine the rate at which the protective layer is repaired. If an insufficient amount of oxygen is available, the layer may remain damaged and corrosion is likely to occur.

Table 2-1   The physico-chemical modifications for Ti and Ti-alloys.[8]

Surface modification	Coating materials	Method	Reference
Coating	Al_2O_3	CVD(a)	9
		Dual ion beam deposition	10
	Carbides	CVD(a)	9
	CPC(b), HA(c)	Electrophoretic deposition	11-13
		Hot isostatic pressing	14
		Ion assisted sputtering	
		Plasma spraying	
		Sputtering	
	Diamond	CVD(a)	15
	Silicides	CVD(a)	9
	TiN	CVD(a)	16
		Ion implantation	17
		Ion nitriding	18
		Reactive sputtering	19
	TiO_2	Dual ion beam deposition	10
		Plasma spraying	20
Oxide-layer treatment		Aging	21
		Anodic oxidation	21
		Electropolishing	22
		Nitric acid passivation	22
		RF (radio frequency) plasma	23
		Thermal oxidation	21
Diverse others	HA-Glass-Ti-composite(c)	Firing and etching	24
	PMMA-Dacron®(d)	Embedded in PMMA, then coated with Dacron®	25
	Polymer	Silanization	26

(a) CVD = Chemical vapor deposition. (b) CPC = Calcium phosphate ceramics. (c) HA = Hydroxyapatite. (d) PMMA = Poly(methylmethacrylate).

As mentioned above, Ti is an unsurpassed material for many orthopedic and dental implants, mainly due to its bulk properties and osseointegrative characteristics. That is why a lot of investigations deal with the modification of the surface properties to enhance biocompatibility in a bioactive or bioinert direction. The currently applied physical and chemical modifications of Ti and Ti-alloys are essentially i) coating, and ii) direct treatment of the oxide layer including a multitude of mechanical, physical, and chemical treatment (Table 2-2).

However, up to now, there is no report about the biochemical modification of titanium surfaces. The reasons could be:

1. The concept of bio-guided surfaces has only developed in recent years.
2. Although the technique of SAMs has been studied for years, application in biomaterials is just beginning to be studied.
3. Until now, there have been some practical problems for biomaterials applications. For example, sterilization in industry (autoclave, γ-sterilization) will destroy the immobilized biomolecules; the multi-step modification procedure and the expensive biomolecules will largely increase the product price, etc.

2.2 Self-assembled organic mono- and multilayers

Self-assembled monolayers (SAMs) are ordered molecular assemblies formed by the adsorption of an active surfactant on a solid surface (Figure 2-2). This simple process makes SAMs inherently manufacturable and thus technologically attractive for building supramolecules and for surface engineering. The order in these two-dimensional systems is produced by a spontaneous assembly process at the interface, as the system approaches equilibrium.

Adsorbed molecules
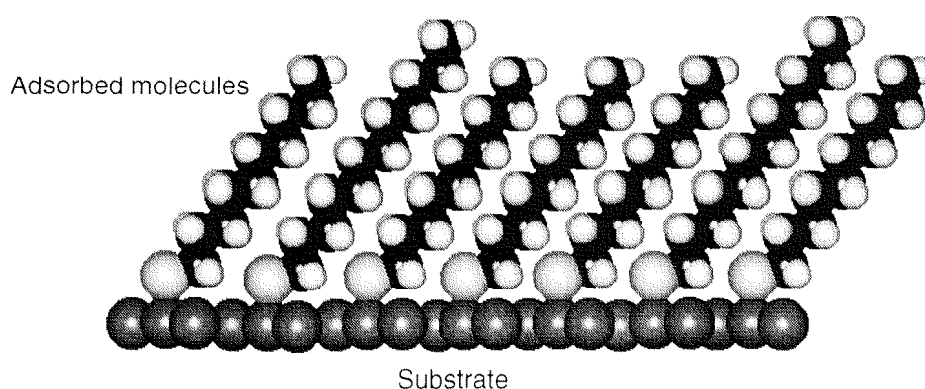
Substrate

Figure 2-2   *Schematic drawing of self-assembled monolayers (SAMs) on solid substrates.*

SAMs provide the needed design flexibility, both at the individual molecular and at the material levels, and offer a vehicle for investigation of specific interactions at interfaces. These studies may eventually produce the capabilities needed for assemblies of three-dimensional structures. Due to their dense and stable structure, SAMs have potential applications in biomaterials, corrosion prevention, wear protection, microfabrication, and more. In addition, the biomimetic and biocompatible nature of SAMs makes their application in chemical and biochemical sensing promising.

2.2.1 Organosilane self-assembled films

Self-assembled films of alkylchlorosilanes, alkylalkoxysilanes, and alkylaminosilanes require hydroxylated surfaces as substrates for their formation. The driving force for this self-assembly is the in situ formation of polysiloxane. These films can be prepared on a wide variety of the solid substrates, such as silica,[27] glass,[28,29] mica,[30] teflon,[31] and titania.[26,32]

2.2.1.1 Parameters influencing the film quality

Water content

High-quality siloxane films are not simple to produce, mainly because of the need to carefully control the amount of water in solution or the hydroxyl groups on the substrates. Excess water always results in facile polymerization in solution and polysiloxane deposition of the surface. Recently, McGovern et al. have shown that extraction of surface moisture, followed by octadecyltrichlorosilane (OTS) hydrolysis and subsequent surface adsorption may be the mechanism of SAM formation.[28] They suggested a moisture quantity of 0.15 mg/100 ml of solvent as the optimum condition for the formation of closely packed monolayers. X-ray photoelectron spectroscopy (XPS) studies confirm the complete surface reaction of the -Si(OEt)$_3$ groups, upon the formation of a complete SAM. Tripp and Hair used infrared spectroscopy to provide direct evidence for the full hydrolysis of methylchlorosilanes to methylsilanols, at the solid-gas interface, by surface water on a hydrated silica.[33]

Temperature

Temperature has been found to play an important role in silane film formation. The issue is the competition between the reaction of hydrolyzed (or partially hydrolyzed) silyl groups with other such groups in solution to form a polymer, and the reaction of such groups with surface Si-OH moieties to form a SAM. As temperature decreases, the preference for surface reaction increases. Moreover, as temperature decreases, the reaction kinetics

decreases as well, resulting in the diminution of the thermal disorder of the forming ultrathin film, the formation of an ordered assembly, and the gain of Van der Waals interaction energy.

Reproducibility

The reproducibility of silane film formation is still a problem, since the quality of the film formed is very sensitive to reaction conditions. For example, Sukenik et al. reported that 2-15 min is enough for the formation of a monolayer,[26] while Wasserman et al.[34] suggested over 24 h. Vandenberg et al. suggested that 3-aminotriethoxysilane forms a heterogeneous island structure,[27] while others concluded that these films are homogeneous. Banga et al. studied the adsorption of OTS onto glass and silicon oxide surfaces,[35] and Israelachvili and co-workers investigated the adsorption of OTS on mica.[36] They discovered that OTS forms monolayers on mica by nucleating isolated domains, whose fractal dimensions increase with increased surface coverage. Grunze et al. studied OTS SAMs on silicon and emphasized that in order to obtain reproducible, good quality films, samples must be prepared under class 100 clean room conditions.[37] They found that OTS SAMs formed on silicon, first by the growth of large islands and then by filling in with smaller islands until the film is complete.

2.2.1.2 Surface reactions

Surface reactions can be carried out on ω-substituted alkyl silanes. SAMs have been reported, starting from alkyltrichlorosilanes with terminal functional groups of olefins, esters, halogen,[38] cyanide, thiocyanide, and others.[39] With these functional groups, the in-situ transformations can be performed from olefin to alcohol, dibromide, or acid; ester to acid, or alcohol; halogen to azide and amine. Sukenik et al.[39] converted the bromo-terminated SAMs to the thiocyanato-terminated monolayers by simply treating them with a 0.1 M KSCN solution in DMF for 20 h. Similarly, NaN_3, Na_2S, and Na_2S_2 gave complete conversions of the bromo-terminated monolayers, as was evident from X-ray photoelectron spectroscopy (XPS). Reduction of the thiocyanato, cyanide, and azide surfaces by $LiAlH_4$ gave the mercapto- and amino-terminated monolayers in complete conversions. They reported that reaction rates obey the following order of leaving groups I > Br > Cl, and XCH_2CO > $PhCH_2X$ > CH_2CH_2X. Competition reactions using thiolates and amines as nucleophiles show a clear thiolate preference. Reactions with small peptide fragments with cysteine moieties as the nucleophiles resulted in grafting of the monolayer surface with these peptides. This may be important for the development of biosensors.

ω-Amino silanes are the most common reagents for immobilization of biomolecules such as proteins, peptides, and nucleosides. The NH_2 can be further modified with versatile linking moieties. For example, glutaraldehyde[40] yields an aldehyde that can form an imine linkage with primary amines on the protein. Another method[40] employs succinic anhydride, followed by a carbodiimide, to form a carboxyl group; this can then be coupled by an amide linkage with primary amines on the protein. A further method[41] employs p-nitrobenzoyl chloride, followed by reduction with sodium dithionite and treatment with HCl to form a diazonium salt. This salt can combine with the aromatic rings of tyrosine and histidine in the protein as well as with primary amines in an acrylamine linkage. A fourth method[40] uses a mixture of carbodiimide and enzyme, which couples the enzyme by a carboxyl group to the surface. The method described here uses bifunctional crosslinkers bearing succinimidyl esters, which introduce many functional crosslinking groups for grafting biomolecules on solid surfaces.

2.2.2 Organosulfur self-assembled films

Sulfur compounds have a strong affinity to transition metal surfaces.[42,43] This is probably because of the possibility of forming multiple bonds with surface metal clusters.[44] The number of reported surface active organosulfur compounds that form monolayers on gold has increased in recent years. These include, among others, di-n-alkyl sulfide, di-n-alkyl disulfides, thiophenols, cysteines, etc. However, the most thoroughly studied, and probably best understood type of self-assembled monolayer (SAM) is that of alkanethiolates on Au(111) surfaces.

It is generally accepted that gold does not have a stable surface oxide; therefore, its surface can be cleaned simply by removing the physically adsorbed contaminants with organic solvents. However, recently King showed that oxidation of gold by UV and ozone at 25 ^{0}C gives a ~17 Å thick Au_2O_3 layer,[45] which is stable to extended exposure to ultrahigh vacuum (UHV) and water and ethanol rinses. Our XPS measurements also showed the existence of trace oxygen.

2.2.2.1 Adsorption mechanism

Kinetic studies of alkanethiol adsorption onto Au(111) surfaces have shown that for relatively dilute solutions (10^{-3} M), two distinct adsorption kinetics can be observed: a very fast step, which takes a few minutes to form a lower density phase (the so-called striped phase),[46] and a slow step, which lasts several hours, at the end of which the thickness and

contact angles reach their final values. The initial step, well described by diffusion-controlled Langmuir adsorption, has been found to strongly depend on thiol concentration. At 1 mM solution the first step is finished after ~1 min, while it requires over 100 min at 1 µM concentration.[47] The second step can be described as a surface crystallization process, where alkyl chains are transformed from a disordered state into an ordered state, thus forming a two-dimensional crystal with a defined unit cell. Therefore, the kinetics of the first step is governed by the surface-head group reaction, and the activation energy may depend on the electron density of the adsorbing sulfur. On the other hand, the kinetics of the second step is related to chain disorder (e.g., gauche defects), the different components of chain-chain interaction (Van der Waals, dipole-dipole, etc.), and the surface mobility of chains. It has also been found that the kinetics is faster for longer alkyl chains, probably due to the increased Van der Waals interactions.

Chemisorption of alkanethiols as well as of di-n-alkyl disulfides on clean gold gives indistinguishable monolayers,[48] probably forming the Au(I) thiolate (RS-) species. A simple oxidative addition of the S-S bond to the gold surface is possibly the mechanism in the formation of SAMs from disulfides. The rates of formation of SAMs from dialkyl disulfides or alkanethiols were indistinguishable, but the rate of replacement of molecules from SAMs by thiols was much faster than by disulfides.

2.2.2.2 Stability of SAMs

The restricted stability of alkanethiolate SAMs has been reported by many papers, although until recently there has been no conclusive evidence. Hickman et al. reported some loss in the electroactivity of ferrocenyl alkanethiolate SAMs upon soaking in hexane,[49] while Collard and Fox did not observe such a loss when the same SAM was immersed in ethanol.[50] Exposure of other electroactive SAMs to nonaqueous electrolytes also gave clues of instability.[51] Recently alkanethiolates bearing radiolabeled (^{35}S) head groups have been incorporated into SAMs on a variety of substrates.[52] This work addresses issues that are central to our understanding of thiolate SAMs. The thermal stability of alkanethiolate SAMs has been addressed in a number of papers. Nuzzo et al. have reported loss of sulfur from hexadecanethiolate over the range of 170-230 °C.[53] Lavrich et. al. reported the existence of two desorption peaks (physical and chemical desorption) for some short chain sulfur compounds. By using radiolabeled hexadecanethiolate monolayers, a complete loss of surface sulfur at 210 °C was observed, with some loss occurring at 100 °C.[52]

2.2.2.3 Orientation studies

FTIR studies reveal that the alkyl chains in SAMs of thiolates on Au(111) usually are tilted ~26-28 degree from the surface normal, and display ~52-55 degree rotation about the molecular axis.[54] This tilt is a result of the chains reestablishing Van der Waals contact in an assembly with ~5 Å S–S distance, larger than the distance of ~4.6 Å, usually quoted for perpendicular alkyl chains in a close packed layer. On the other hand, thiolate monolayers on Ag(111) are more densely packed due to the shorter S–S distance. It is well accepted today that in carefully prepared SAMs of alkanethiolates on a clean Ag(111) surface the alkyl chains are practically perpendicular to the surface.

Near-edge X-ray absorption fine structure spectroscopy (NEXAFS) studies of alkane thiol SAMs on Au exhibited that the carbon chain axes of hexadecanethiol, octadecanethiol, and docosanethiol incline at an angle of about 30^0–35^0 from the surface normal, while those alkane thiols with short carbon chains such as dodecanethiol have a larger angle of about 40^0–50^0.[158,159,160]

2.3 Crosslinking and conjugation reactions

2.3.1 Introduction

The concept of cross-linking and conjugation originally stems from protein and peptide chemistry. Chemical cross-linking involves joining of two molecular components by a covalent bond achieved through the use of cross-linking reagents. The components may be proteins, drugs, nucleic acids, or solid substrates. The chemical cross-linkers are bifunctional reagents containing two reactive functional groups derived from classical chemical modification agents. The reagents are capable of reacting with the side chains of the amino acids of proteins. They may be classified into homobifunctional, heterobifunctional, and zero-length crosslinkers. The zero-length crosslinkers are essentially group-activating reagents which cause the formation of a covalent bond between the components without incorporation of any extrinsic atoms. The homobifunctional reagents consist of two identical functional groups and the heterobifunctional reagents contain two different types of reactive functional moieties.

Model reactions for the three kinds of crosslinkers are shown in Figure 2-3.

a)   Carbodiimides are examples of zero-length crosslinkers
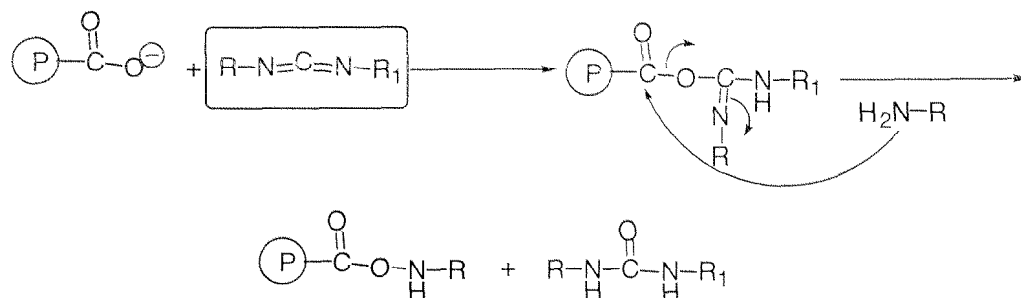
b)   Reagents with bifunctional succinimidyl esters are examples of homobifunctional
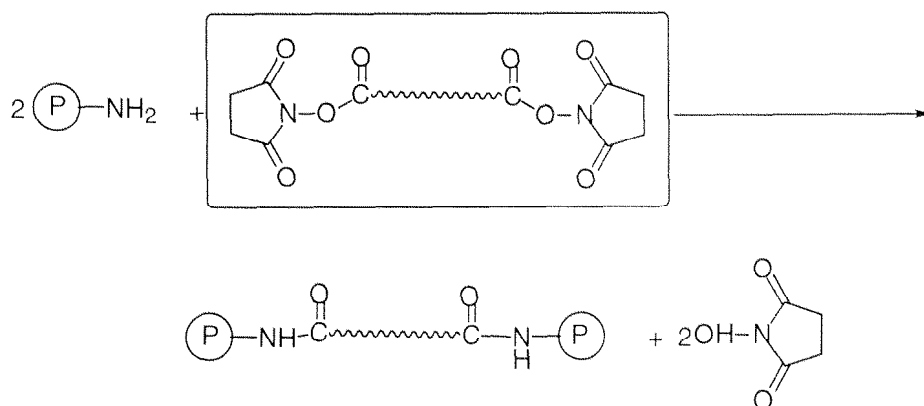
crosslinkers

c)   Reagents with succinimidyl ester- and maleimidyl groups are examples of

heterobifunctional crosslinkers
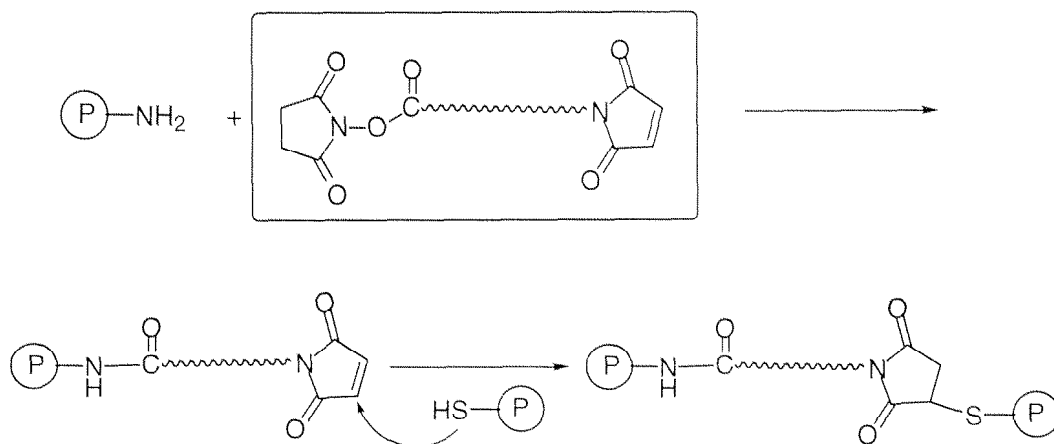
Figure 2-3   *Schematic   representations   of   zero-length,   homobifunctional,   and*
heterobifunctional crosslinkers.

Crosslinking and conjugation have been used in many scientific and technological fields such as protein chemistry, gene engineering, immunology, and medicine. The crosslinkers have been applied to stabilize tertiary structures of proteins,[55] to study protein-protein interactions of subunits in oligomeric proteins, and in complex structures such as ribosomes, to determine distances between reactive groups within or between protein subunits, to attach ligands to solid supports,[56] and to identify membrane receptors.

Although crosslinking and conjugation are often used interchangeably, there is a fine distinction in connotation between these two terms according to Wang.[57] *Crosslinking usually refers to the joining of two molecular species that have some sort of affinity between them, that is, they either exist as an aggregate or can associate under certain conditions.* Thus, the chemical bonding between a ligand and its receptor is usually referred to as cross-linking. Similarly, crosslinking is used for the covalent bonding between subunits of enzymes. *Conjugation, on the other hand, denotes the coupling of two unrelated species.* In our case, the peptides or proteins are immobilized on the solid supported substrates (e.g. Ti, TiO_2, Au, Ag), referring to as conjugation.

2.3.2 Reactive groups of proteins

Chemical crosslinking and conjugation of proteins and peptides depend on the reactivities of the constituents of proteins as well as the specificities of crosslinkers used. In order to preserve the biological activity of the individual protein, the reaction site on the protein must be those amino acids that are not involved in its biological functions. The biological activity loss of proteins can be caused by disturbances of their secondary and tertiary structures, their surface charges, their hydrophobic and hydrophilic properties, and their native conformations. Thus, only those amino acid residues that are not situated at the active centers or settings critical to the integrity of the tertiary structures of proteins may be targets for chemical modification. Such amino acids must be located on the surface of the protein and are easily accessible by crosslinkers. It follows, therefore, that the identity of the reactive functional groups on the exterior of a protein is the most important factor that controls its reactivity towards crosslinking reagents. By knowing which functional groups are located at the protein - solvent interface, the protein may be modified without sacrificing its biological activity.

Compositions of proteins and peptides

All proteins are composed of amino acids. There are twenty common amino acids with side chains of different sizes, shapes, charges, polarities, and chemical reactivity. These

physico-chemical properties determine the precise structure and function of each individual protein. Glycine, alanine, valine, leucine, isoleucine, methionine, and proline have nonpolar aliphatic side chains while phenylalanine and tryptophan have nonpolar aromatic side groups. These hydrophobic amino acids are generally located in the interior of proteins forming the so called hydrophobic core of many molecules. Other amino acids, arginine, aspartic acid, glutamic acid, cysteine, histidine, lysine, and tyrosine have ionizable side chains. Together with asparagine, glutamine, serine, and threonine which contain non-ionic polar groups, they are usually located on the protein surface where they can interact strongly with the aqueous environment.
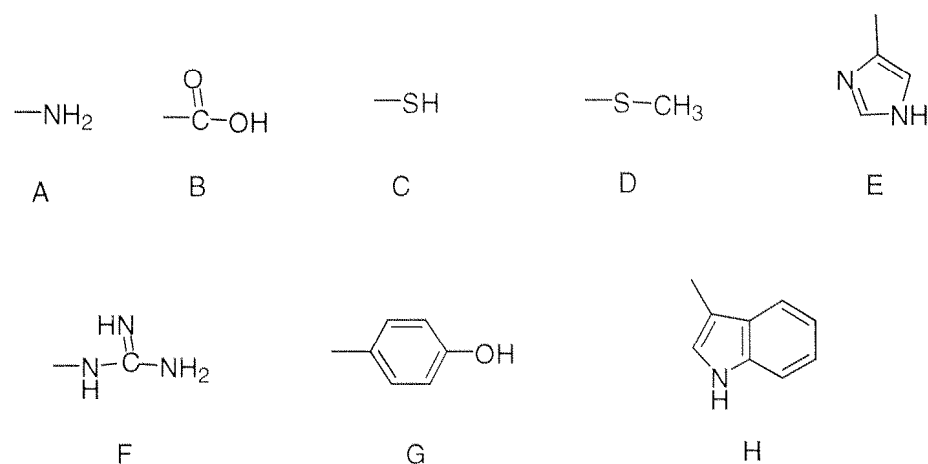
Figure 2-4   *Reactive groups of amino acid side chains. Functional groups A to F are the six most reactive entities. G and H are less reactive. (A) Amino groups of N-terminal amino acids and ε-amino groups of lysines; (B) carboxyl groups of aspartic, glutamic acids and C-terminal amino acids; (C) thiol group of cysteine; (D) thioether of methionine; (E) imidazolyl group of histidine; (F) guanidinyl group of arginine; (G) phenolic group of tyrosine; and (H) indolyl group of tryptophan.*

Reactive amino acid side chains

The chemical reactivities of peptides and proteins depend on the side chains of their amino acid compositions as well as the free amino and carboxyl groups of the N- and C-terminal residues, respectively. Studies of chemical modification have revealed that only a few of the amino acid side chains are really reactive. Of the twenty amino acids, the alkyl side chains of the hydrophobic residues are chemically inert except the photochemical insertion. Only eight of the hydrophilic side chains are chemically active. These are the guanidinyl group of arginine, the γ- and β-carboxyl groups of glutamic and aspartic acids, respectively, the thiol group of cysteine, the imidazolyl group of histidine, the ε-amino group of lysine, the thiolether moiety of methionine, the indolyl group of tryptophan and the phenolic hydroxyl group of tyrosine (Figure 2-4).

Table 2-2 summarizes the various chemical modification reactions of these active side chains. The most important reactions are alkylation and acylation. In alkylation, an alkyl group is transferred to the nucleophilic atom, whereas in acylation, an acyl group is bonded.

Table 2-2   Chemical modification of amino acid side chains.

Amino Acid	Side Chain	Alkylation or Arylation	Acylation	Oxidation
cysteine	$-CH_2SH$	+	+	+
lysine	$-NH_2$	+	+	-
methionine	$-S-CH_3$	+	-	+
histidine	imidazolyl	+	+	+
tyrosine	$-Ph-OH$	+	+	+
tryptophan	indolyl	+	-	+
aspartic and glutamic acids	$-COOH$	-	+	-
arginine	$-NHC(=NH)NH_2$	-	-	-

2.3.3 Nucleophilic substitution and addition reactions

Most of the protein modification reactions are nucleophilic substitution and addition reactions. For example, the reaction of succinimidyl esters with amino groups is an S_N2 substitution, while that of maleimidyl groups with thiols is a nucleophilic addition. The reaction rate of S_N2 substitution, a bimolecular nucleophilic substitution reaction, depends on the chemical reactivity of the involved species and the steric effects. The chemical reactivity involves the ability of the leaving-group to leave and the nucleophilicity of the attacking group. The easier it is for the leaving group to come off, the faster the reaction will be. Similarly, the greater the nucleophilicity, the more expeditiously the product will be formed. In term of protein modification, the relative chemical reactivity is basically a function of nucleophilicity of the amino acid side chains. On the other hand, the steric effects play a more important role on the surface reactions. Generally, in the bulk chemistry the less the bulky groups around the reactive target-atom, the easier the reaction will be. However on the surface, besides the native properties of molecules, the neighboring molecules also affect the steric hindrance. The denser the packed molecules,

the more difficult the reaction will be. Therefore, a densely packed monolayer is not an ideal candidate for S_N2 surface reactions. Nucleophilic additions are accepted as stepwise reactions. They are classified to base- and acid-catalyzed additions. In order to avoid the side-reactions, the specific reaction of maleimidyl groups with thiols is often carried out under weakly acidic conditions.

2.3.4 Effects of pH

Because protonation decreases the nucleophilicity of a species, the pH of the medium affects the rate of many nucleophilic reactions. The relationship between protonation and the pH depends on the pK_a of the nucleophile. Table 2-3 lists the pK_as of the reactive groups in free amino groups and in model peptides. Because the pK_a is a function of temperature, ionic strength, and microenvironment of the ionizable group, the table reflects only the approximate values of these groups in proteins. Using these values, the ratio of protonated to deprotonated species at a certain pH can be calculated by the Henderson-Hesselbalch equation:

$$pH = pK_a + \log\{[A^-]/[AH]\}$$

Table 2-3   *pK_a of some reactive groups in amino acids and model peptides.*[57]

Functional group	Amino acid residue	pKa in free amino acid	pKa in model peptides
α—COOH	C-terminal	1.8 - 2.6	3.1 – 3.7
β—COOH	aspartic acid	3.9	4.4 – 4.6
γ—COOH	glutamic acid	4.3	4.4 – 4.6
α—NH_3^+	N-terminal	8.8 – 10.8	7.6 – 8.0
—SH	cysteine	8.3	8.5 – 8.8
ϵ— NH_3^+	lysine	10.8	10.0 – 10.2
-NHC(=NH_2^+)NH_2	arginine	12.5	>12

Thus, at a fixed pH, the most reactive group is usually the one with the lowest pK_a. Because of their differences in the pK_a values, the degree of protonation of these amino acid side-chain groups at a certain pH provides a basis for differential modification. For

example, at neutrality, the amino groups are protonated rendering them unreactive. For a selective reaction with the carboxyl group, the condition of an acidic pH should be selected. At higher pHs, other nucleophiles, particularly the thiol group, will react. As a consequence, it should be obvious that changing the pH also provides a means to control the course of a chemical reaction.

2.4 The cell-adhesive peptide Arg-Gly-Asp (RGD)

In the early 80s, M.D. Pierschbacher discovered that the cell attachment activity could be mimicked by short, immobilized, synthetic peptides containing a short three amino acid sequence, arginine-glycine-aspartic acid (RGD).[58]
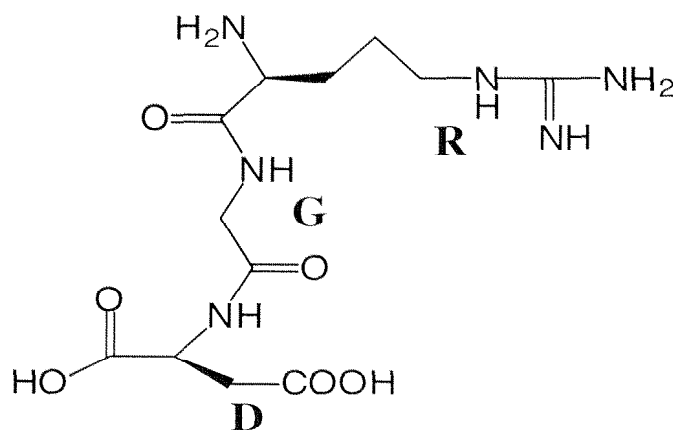
Figure 2-5   Chemical structure of RGD.

The recognition site for many of the integrins that bind to extracellular matrix and platelet adhesion proteins is the tripeptide RGD.[59] The role of the RGD sequence as the recognition site was demonstrated by making progressively smaller fragments of fibronectin and by assaying for the cell attachment-promoting activity in the fragments and in synthetic peptides reproducing the amino acid sequences of such fragments. When coated onto a surface, the fragments and synthetic peptides containing the RGD sequence promote cell attachment, whereas in solution they inhibit the attachment of cells to a surface coated with fibronectin or the peptides themselves. Changes in the peptides as small as the exchange of alanine for the glycine or glutamic acid for the aspartic acid, which constitute the addition of a single methyl or methylene group to the RGD tripeptide, or the replacement of the arginine with a lysine residue, eliminate these activities of the peptides.[60] Conformation of the amino acids is also important; a peptide in which the

aspartic acid is in the D-form is inactive. The RGD sequence is also the cell recognition site of a surprising number of other extracellular matrix (ECM) and platelet adhesion proteins. In addition to fibronectin, these include vitronectin, collagens, fibrinogen, von Willebrand factor, osteopontin, bone sialoprotein I, thrombospondin, tenascin, laminin, and entactin.
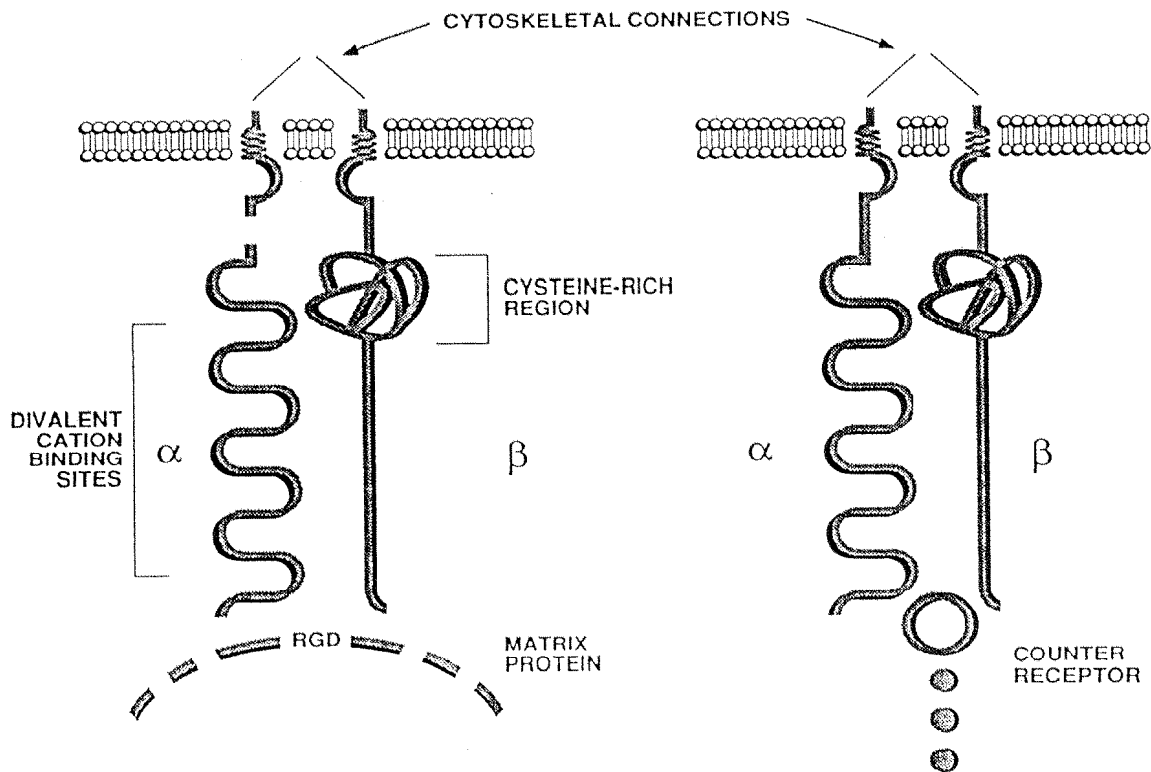
Figure 2-6   *Schematic drawing of the general structure of integrin.[61] Two types of integrins are shown, one with an α subunit which is proteolytically processed into two disulfide-linked fragments at a cleavage site (shown as a gap in the structure on the left). Other integrins have α subunits that are not processed.*

Integrins are a family of membrane glycoproteins consisting of two subunits, α and β. The structural models for the various integrins are depicted in Figure 2-6. The α subunits are homologous to one another but not to the β subunits, which form their own homologous group. Both integrin subunits have a large extracellular domain, a transmembrane segment, and a cytoplasmic tail. The α and β subunits are noncovalently bound to one another, and this association is promoted by divalent cations.

In Figure 2-7 are listed the commonly accepted ligands for many integrins. It is clear that the specificity of ligands is quite complex, for one integrin can bind more than one ECM protein, and in addition, a single ECM protein can bind to more than one integrin. In the latter case, when the binding is RGD dependent, more than one integrin is using the same general binding region on a single ECM protein, the RGD sequence.
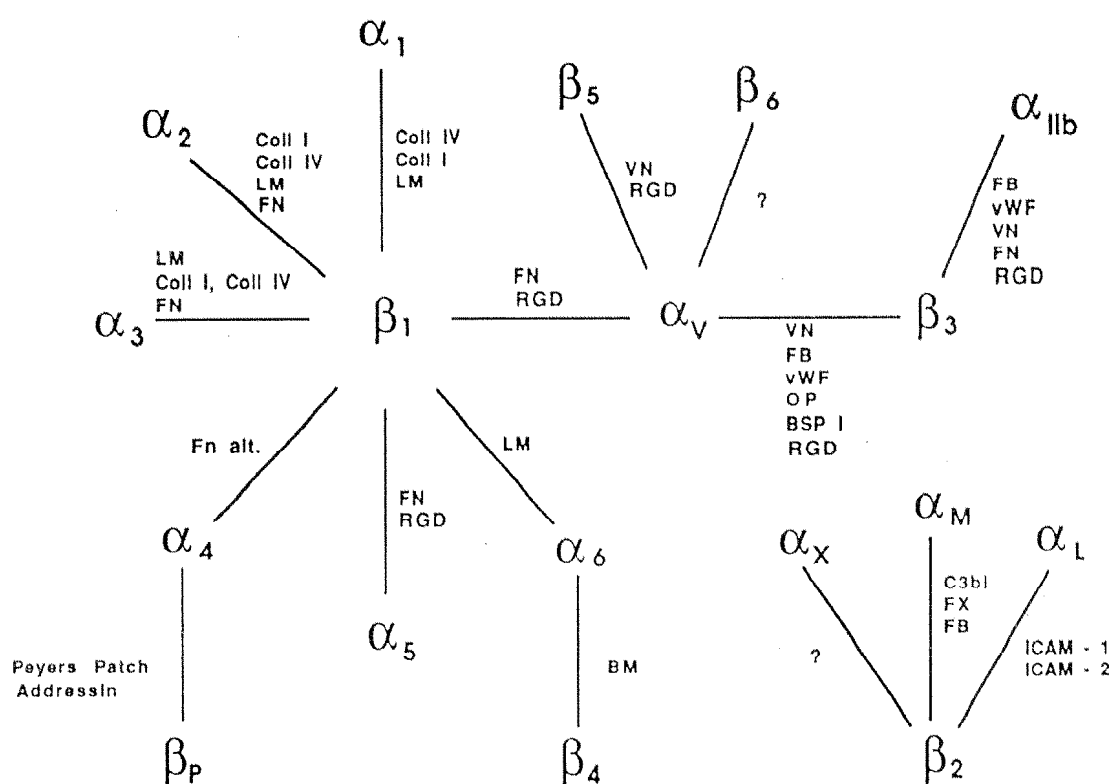
Figure 2-7   *Integrin family.[62] The known subunits, the subunit combinations that form the known integrins, and the known ligands for these integrins are shown. Also shown is the RGD specificity of those integrins that bind to this sequence. FN, fibronectin; Fn alt., fibronectin alternatively spliced domain; LM, laminin; VN, vitronectin; Coll, collagen; vWF, von Willebrand factor; FB, fibrinogen; OP, osteopontin; BSP 1, bone sialoprotein 1; ICAM-1, ICAM-2, intercellular adhesion molecules; FX, factor X; BM, basement membrane; C3bi, complement component C3bi.*

Cell adhesion plays an important role in a variety of basic biological processes, including guiding cells into their appropriate locations in the body, providing cell anchorage, and controlling cell proliferation, differentiation, and apoptosis. Adhesion peptides have found important uses as probes for these phenomena. In addition, there are also practical applications for these peptides.

Adhesive peptides can be used in two different ways: When attached to a surface, they promote cell attachment, whereas when presented in solution, they prevent attachment that would otherwise occur. Both modes of using the peptide have found applications: Surface-coated RGD peptides are being investigated for improvement of tissue compatibility of various implanted devices. For example, Massia and Hubbell[63-65] covalently immobilized RGD peptides on glycophase glass and evaluated its effect on human endothelial cell culture. They observed the promotion of cell adhesion and growth on these peptide-modified surfaces. Glass et al. attached RGD on a polymer matrix, hyaluronic acid, and

characterized their biological activity.[66] Dee studied the enhancement of osteoblast mineralization on RGD-modified substrates.[67] To minimize protein adsorption while providing a site for cell attachment, several groups have successfully modified PEG polymers (or PEG oligomers) with RGD-containing peptides.[68,69] In contrast, the soluble peptides targeted for individual integrins show promise as potential drugs for the treatment of a number of diseases.[70]

Other applications being explored include the targeting of the specific integrin ($\alpha_v\beta_3$) in osteoporosis. Osteoclasts attach to bone through this integrin (and possibly some other α_v integrins), and inhibiting their attachment with peptides prevents bone degradation *in vitro*[71] and *in vivo*.[72] Protein engineering with RGD can have applications in protein targeting and gene therapy with viruses. Advances in the application of RGD and related sequences to various purposes will depend on detailed understanding of integrin-ligand recognition. Much progress has been made recently in this field. Adhesion peptides, RGD in particular, have provided a great deal of information about cell adhesion mechanisms and are serving as a basis for the development of a new group of pharmaceuticals.

3. Characterization techniques

3.1 X-ray photoelectron spectroscopy (XPS)

3.1.1 Principles

XPS is an abbreviation for X-ray Photoelectron Spectroscopy. Another name is ESCA which is an acronym for Electron Spectroscopy for Chemical Analysis.

In XPS or ESCA, a beam of (monochromatic) X-rays is first produced by electron bombardment of an anode material (Al, Mg, Si). When the X-rays interact with the sample under investigation, they can ionize electrons that are in core levels (such as 1s, 2s, etc.). If the binding energy of the electron in the core hole was E_B, then the kinetic energy of the electron ejected from the surface can be given in the energy diagram (Figure 3-1).
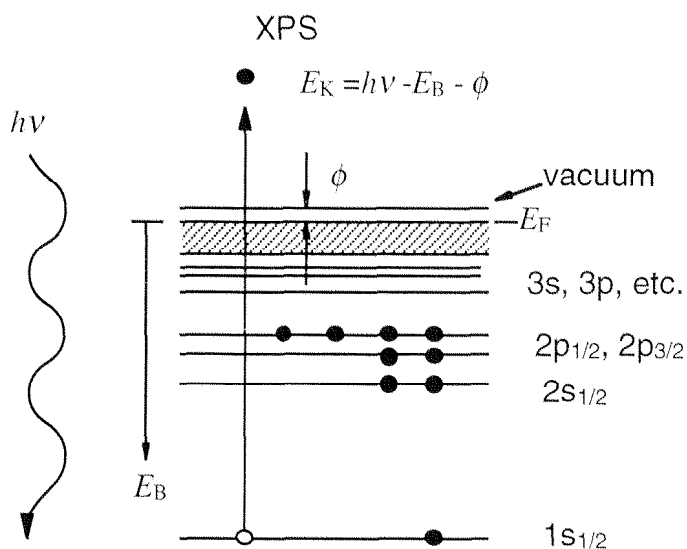
Figure 3-1   *Schematic diagram of the X-ray photoelectron emission process.*

$$E_K = h\nu - E_B - \phi$$

where E_K is the measured electron kinetic energy, hv the energy of the exciting radiation, E_B the binding energy of the electron in the solid, and ϕ the spectrometer work function. Since hv is a well-defined quantity, the electron binding energies can be calculated by measuring the kinetic energies of the electrons that are ejected from the sample, using the above equation. The electron energies are measured using an electrostatic energy analyzer such as a "hemispherical analyzer". The analyzer measures the kinetic energy distribution of the emitted electrons.

3.1.2 Instruments

A schematic drawing of the main components of the SAGE 100 XPS instrument is shown in Figure 3.2. The main components of the system include: the vacuum system, the x-ray sources, the sample stage, and the analyzer. The energy discrimination of the electrons is obtained by sweeping the potential(s) in the lens or by using a grid system in front of the analyzer. The sensitivity of the instrument is dependent on the X-ray source used, the analyzed area, geometrical factors and the efficiencies of the lens, the analyzer and the detector. The energy resolution is due to the inherent width of the X-ray radiation and the resolving power of the spectrometer.
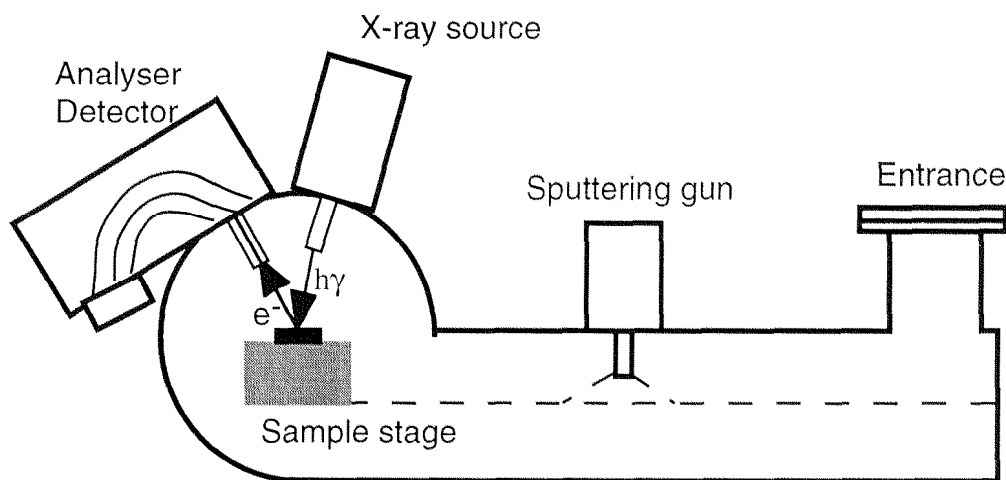
Figure 3-2   Schematic drawing of Sage 100 XPS instrument.

3.1.3 XPS qualitative and quantitative analyses

XPS can provide the following information:

1. Elemental identification. Because the number of protons increases as we progress through the periodic table, the electron binding energies for a fixed core level (such as the 1s level) will increase monotonically; thus, measuring the electron kinetic energy is equivalent to determining which elements are present on the surface.

2. Oxidation states for any given elements. There will be small shifts in the binding energies due to changes in oxidation states; higher oxidation states generally have higher binding energies, and emit electrons with lower kinetic energies.

3. Quantitative analyses through curve fitting and calculation of atomic concentrations because the photoelectron intensity is directly related to the atomic concentrations of the photoemitting atoms.

4. Depth profiling when combined with ion etching (sputtering) techniques.

5. Images or maps showing the distribution of the elements or their chemical states over the surface. Modern instruments can have a spatial resolution down to a few microns.

XPS survey and detailed spectra
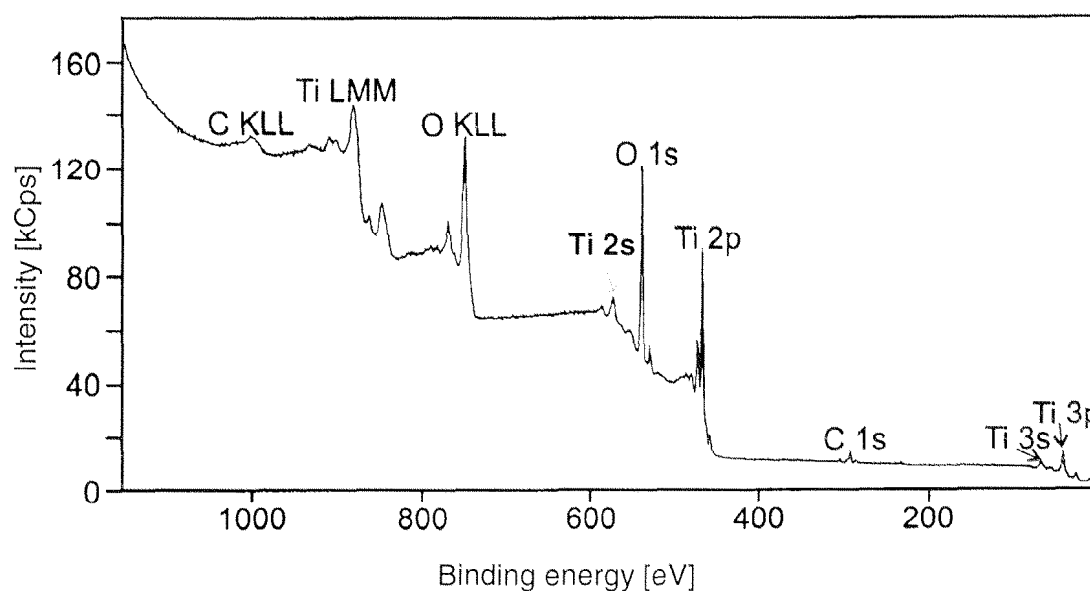
Figure 3-3   XPS survey spectrum of a sputtered Ti coating. It shows that three elements: Ti, O, and C are present on the top surface. The XPS peaks of Ti 2p and O 1s and the Auger peaks of Ti LMM and O KLL are strong. The trace contaminated hydrocarbon C 1s and its Auger peak C KLL are weak.

Figure 3.3 depicts a wide-scan spectrum of a sputtered Ti coating obtained using Mg Kα radiation and an analyzer operating in the constant pass energy mode (50 eV). A series of peaks are observed on a background which generally increases to low kinetic energy (high binding energy) but which also shows step-like increases on the low kinetic energy side of each significant peak due to energy-loss effects.

From the survey spectrum, we know that there are three elements present at the surface: Ti, O, and C. The conclusion is based not only on the observation of the main XPS peaks: Ti 2p, O 1s, and C 1s, but also on the weak peaks: Ti 3p, Ti 2s, Ti 3s and the Auger peaks: Ti LMM, O KLL, and C KLL. To get the exact chemical shift and do the quantitative analysis, the detailed narrow scan spectra are needed.

Curve fitting

In many cases the information provided by photoelectron spectroscopy is contained in a spectrum that consists of a number of overlapping peaks, often of different peak shapes and intensities. The core region is characterized by a series of chemically shifted peaks, satellites, energy loss features and Auger peaks. In the valence region the spectra will reflect all the complex features of the ground state valence band, together with complications due to the need to include the excited state (i.e. joint density of states) at low photon energies. In both cases, the spectra often cannot be unambiguously analyzed and there is no standard way to proceed with the analysis. In our case, we mainly consider the core region. In the core region the spectra frequently consist of overlapping chemically shifted peaks. The peak positions can sometimes be determined in a qualitative manner by derivative spectra. Once approximate peak positions have been found the data can be fitted by curve fitting methods. In the Sage 100 software, Gaussian and Lorentzian functions are used.

XPS quantification

In a homogenous surface, the peak intensity detected for element A (I_A) can be expressed as follows:

$$I_A = N_A \cdot \sigma_A^e(h\nu) \cdot L_A(\gamma) \cdot \lambda_M(E_{kin}) \cdot B$$

where

I_A : XPS measured intensity of atom A, [cps·eV]

N_A : atomic density of atom A, [atoms/volume]

$\sigma_A^e(h\nu)$: cross section for atom A, electron e and photon energy $h\nu$

$L_A(\gamma)$: angular asymmetry factor

γ : angle between the x-ray beam and the e-beam to the spectrometer

$\lambda_M(E_{kin})$: mean free path length at E_{kin} and in the matrix M, [Å]

E_{kin} : kinetic energy, [eV]

B : instrumental constant including:

         - the transmission function, $T = f(E_A)$

         - detector efficiency

         - flux of the X-ray characteristic line

         - etc.

From the above equation, we can easily get the atomic concentration of X_A:

$$X_A = \frac{I_A / I_A^\infty}{\sum_{i=A,B} I_i / I_i^\infty}$$

where I_A^∞ is the intensity from pure A and may be considered to be a sensitivity factor, the sum is over all of the constituents of the solid.

3.1.4 Experimental conditions

Table 3-1   *Typical experimental conditions for XPS instrument SAGE 100.*

Parameter	Value
Measured area	9x9 mm^2
Emission angle (between the sample surface plane and the detector)	90^0
X-ray source	Mg (300 W, 12 kV) Al (390 W, 13 kV)
Survey spectra Pass energy Step Measure period	 50 eV 1 eV 0.1 s
Detailed spectra Pass energy Step Measure period	 14 eV 0.1 eV 0.1 s
Vacuum during measurements	2.5x10^{-8} mbar

XPS spectra were recorded using a Specs SAGE 100 system with unmonochromatized Mg Kα radiation at 300 W. Measurements were carried out using a take-off angle of 90^0 with respect to the sample surface. The analyzed area was typically 9x9 mm^2. Survey scans over a binding energy range of 0-1150 eV were taken for each sample with a constant detector pass energy range of 50 eV, followed by a high-resolution XPS measurement (pass energy 14 eV) for quantitative determination of binding energy and

atomic concentration. Background subtraction, peak integration and fitting were carried out using SpecsLab software. Electron binding energies measured from Ti-based surfaces were calibrated to the hydrocarbon C 1s at 284.6 eV on pure titanium surfaces and those measured from Au-based surfaces to Au $4f_{7/2}$ at 84.0 eV. To convert peak areas to surface concentration, sensitivity factors published by Evans et al. were used.[73]

3.2 Time-of-flight secondary ion mass spectroscopy (ToF-SIMS)

The technique of Secondary Ion Mass Spectrometry (SIMS) is the most sensitive of all the commonly-employed surface analytical techniques — this is because of the inherent sensitivity associated with mass spectrometric-based techniques.

Dynamic SIMS uses high primary current densities which allows for high secondary ion intensities, but on the other hand leads to loss of surface materials by sputtering (several monolayers) and surface induced modifications. This technique is therefore appropriate to the analysis of concentration depth profiles. On the other hand, *Static SIMS* uses low primary currents so as to limit sample contamination and degradation and therefore allows the analysis of the outermost surface of both inorganic and organic materials. *Images* of the lateral distribution of mass-separated secondary ions can be recorded by rastering a focused primary ion beam over a particular area of the surface.

3.2.1 Basic principles

When fast ions hit a solid surface they penetrate into the surface region to an appreciable depth. As they penetrate into the solid the primary ions transfer their kinetic energy to the atoms of the solid in successive individual collisions. Through subsequent collisions, part of this energy can find its way back to the surface, where it may cause surface particles to be emitted (Figure 3-4). The atomic and molecular surface constitutes emitted as a result of primary ion bombardment are observed as neutral particles or as positive or negative secondary ions. These particles originate almost entirely from the uppermost layer of atoms or molecules, and therefore they yield direct information about its chemical composition. In the production of secondary ions from organic molecules, proton transfer and cation addition both play dominant roles. A characteristic feature of an organic

molecule M is the appearance of the quasi-molecular ions $(M+H)^+$, $(M+cation)^+$, and $(M-H)^-$ (Figure 3-4).

In secondary ion analysis with a time-of-flight spectrometer, the surface is bombarded by a pulsed primary ion beam. Between two successive pulses, the extracted secondary ions are post-accelerated and separated in a flight tube according to their mass. It is essential that the ions to be analyzed enter the flight path simultaneously or at least within the shortest possible time interval. To achieve this the area of the surface to be analyzed is bombarded with pulses of primary ions whose duration is kept as short as possible (≤ 1 ns). The mass resolution $\Delta m/m$ of a ToF-SIMS spectrometer can be as high as 10,000, depending on the mass, which is of significant importance for mass spectral interpretation. Moreover, ToF-SIMS analyzers can in theory provide information for a virtually unlimited mass range (in practice limited by experimental factors and fragment stability to approximate 10,000 amu) which is particularly advantageous for the study of organic compounds such as polymers, peptides or proteins.

$(M + H)^+$ $(M - H)^-$

$(M + Me)^+$
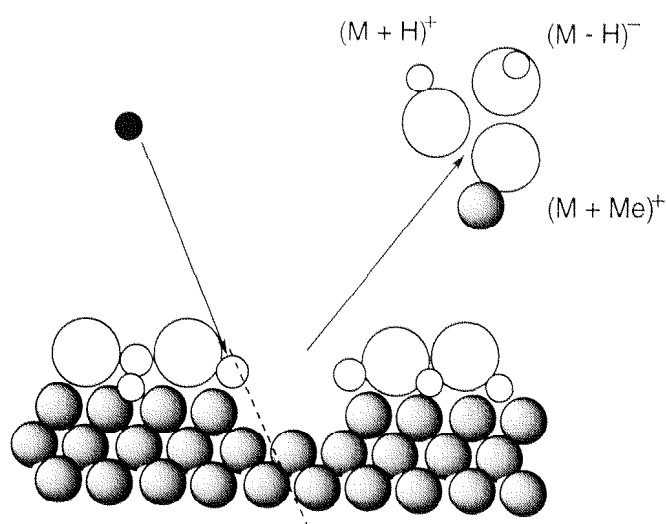
Figure 3-4   *Formation of secondary ions.*[155] *When a metal surface Me (Ag, Au, Pt ...; hatched circles) covered by a monolayer of molecules M (white circles) is bombarded with a primary ion (black circle), secondary ions are emitted, typically including the quasi-molecular ions (M + H)⁺, (M - H)⁻, and (M + Me)⁺. The neutral particles, fragment ions, and metal ions also emitted are not shown here.*

3.2.2 Used spectrometer

Figure 3-5 shows schematically the construction of a modern energy-focusing time-of-flight secondary ion mass spectrometer. The instrument consists of three main components: the primary ion source, the accelerating and flight path system, and the detector. The primary ion source produces mass-separated pulses of primary ions with a

frequency of several kHz; this is achieved by pulsed 90^0 bending and subsequent compression of a continuous ion beam, which is generated, for example, by an electron impact ion source. This pulsed beam can then be focused by means of an ion-optic lens system to a diameter of less than 5 µm if required. If a liquid-metal ion source is used instead, the pulsed ion beam can be reduced to a diameter of less than 0.1 µm.

The beam path contains several ion-optic elements: a beam extractor, an ion lens which focuses the ion beam onto the detector, and a reflectron with a retarding electric field, which has an energy-focusing function on the secondary ions and thus largely eliminates the adverse effect of their initial energy spread on the mass resolution. The detection system consists of a detector (combining a photoconverter electrode, channel plate, scintillator, and photomultiplier) and a counter giving high time resolution.
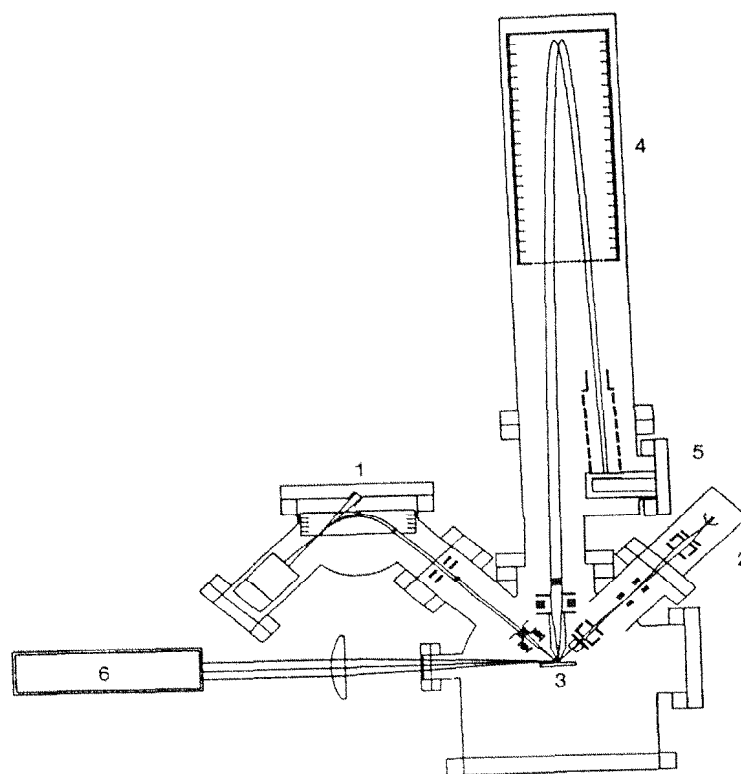
Figure 3-5   *Construction of a modern high-resolution time-of-flight secondary ion mass spectrometer. The system includes two primary ion sources giving different beam diameters, a pulsed, mass-separating electron impact ion source (1) and a pulsed, fine-focusing liquid metal ion source (2), as well as the target (3), a reflectron for energy focusing of the mass-separated secondary ions (4), a detector (5), and a laser for post-ionization of emitted neutral particles (6).*

The performance of a time-of-flight secondary ion mass spectrometer is determined by the characteristics of the primary ion source, the flight path, and the detection system. The quality of the primary ion source is determined by the mass separation, the duration of the primary ion pulse, and the focusing of the beam. That of the secondary ion optical system and of the overall flight path is determined by the transmission efficiency and the energy focusing. Lastly, the quality of the detection system depends on its response probability, time resolution, dead time, and maximum data handling rate.

3.2.3 ToF-SIMS experimental conditions

ToF-SIMS measurements were performed on a commercial model, PHI 7200 (Physical Electronics). The experimental conditions were listed in Table 3-2.

Table 3-2   *Experimental parameters for ToF-SIMS measurements (positive).*

Parameter	Value
Ion gun	Cs^+
Mode	pos. & neg.
Mass range [amu]	0-1000
Back pressure (mbar)	$< 10^{-9}$
Ion source	8 kV Cs^+
Raster size (μm^2)	100x100
Post acc. voltage (kV)	11
Spat. resolution	128x128
Ion dose (ions/cm^2)	$10^{11} \sim 10^{12}$
Time per step (ns)	0.625

Three to five areas were usually analyzed per sample. Most of the mass spectra obtained from the same sample type were nearly identical and only one spectrum is discussed.

Calibration of the mass spectra in the positive mass range was based on hydrogen and saturated molecular hydrocarbon fragments (amu) CH_3^+ (15.025), $C_2H_5^+$ (29.04), $C_3H_7^+$ (43.05), $C_4H_9^+$ (57.07). In the negative mass range, the calibration was based on CH^- (13.01), C_2H^- (25.01), C_3H^- (37.01), and C_4H^- (49.01).

3.3 Infrared reflection absorption spectroscopy (IRAS)

The application of spectroscopic techniques to the study of surfaces generally requires a very high absolute sensitivity. It must be possible to detect at least one-tenth of a monolayer (corresponding to about 10^{14} atoms or molecules) and to draw meaningful information from the spectra. IR spectroscopy was in fact the first spectroscopic method to be used in the study of adsorbed species. In 1954 Eischens, Pliskin and Francis measured vibrational spectra of CO adsorbed on silica-supported Ni, Pd, Pt and Cu catalysts by transmission through a thin wafer of the materials.[74] The high dispersion of the metal in such a sample results a high effective surface area, and thus there are sufficient absorbing species to give high-quality spectra from submonolayer coverages of the adsorbate. It was not until the late 1960s that infrared reflection absorption spectroscopy (IRAS) was developed by Pritchard and coworkers for studying adsorbates on compact polycrystalline surfaces and single-crystal samples.[75,76] This development was prompted by the work of Greenler, who derived the optimal conditions for the success of this experiment.[77] He showed in model calculations that for metal surfaces only the component of the E vector normal to the surface is likely to be effective in exciting dipole-active vibrations and then only at high angles of incidence.
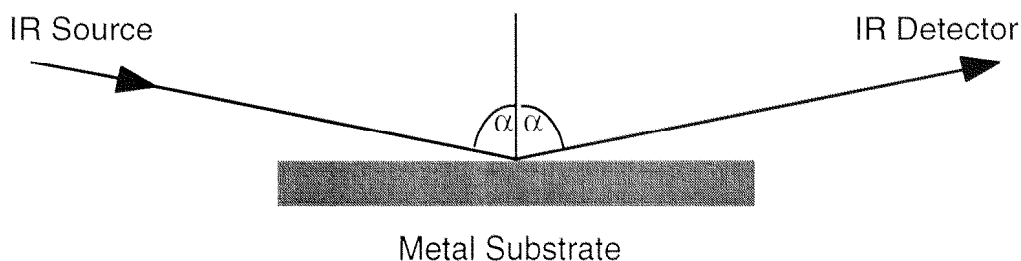
Figure 3-6   Schematic representation of IRAS experimental set-up. The incidence angle α is about 80°.

3.3.1 Theoretical considerations

In general, the intensity of a given mode is proportional to the square of the scalar product of the E field and the transition moment with respect to the normal coordinate,

$$I \propto (\mu \times E)^2 \propto \cos^2\theta$$

where θ is the angle between the vector of the electric field E of the incident light and the direction of the transition moment μ of the IR-active group, I is the intensity of the

absorption. Absorption is hence maximal for μ and **E** being parallel, and zero if they are perpendicular with respect to each other. Therefore, FT-IRAS does not only yield information on the chemical structure of a molecule, but also on its orientation with respect to an external reference system. In the case of the grazing incidence FT-IRAS measurement configuration, the existing light interacts with a thin organic film adsorbed on a metallic support. Consequently, only the electric field normal to the support interacts with the IR transition dipole moments of the adsorbed molecules.
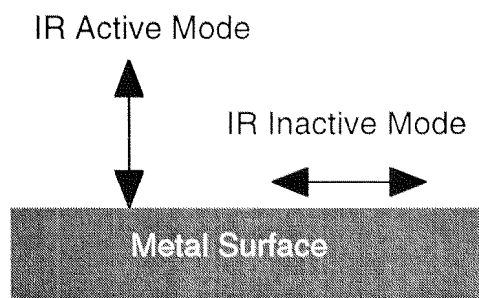
Figure 3-7   *The so-called "surface selection rule" for the IRAS. The transition dipole moment perpendicular to the surface is IR-active, while that parallel to the surface is IR inactive.*

There are several methods that have been developed to estimate the molecular orientation based on the above principle. One popular method has been developed by D.L. Allara, et al.[54,78] He calculated the FT-IRAS spectra using optical constants from bulk transmission spectra, and hence obtained the molecular orientation of the adsorbed layers. This is the most suitable method for C-H stretching modes. The following assumptions were made to calculate the molecular orientation:

1. The structure of the adsorbed layer is homogeneous and isotropic, thus structurally identical with the bulk material. In this case accurate calculation of the IRAS spectrum of the adsorbed layer from the bulk transmission spectrum is possible (for an ideally flat substrate with known optical functions and for a known thickness of the adsorbed layer).

2. The adsorbed layer is anisotropic, but otherwise identical with the bulk structure. The calculated spectrum (I_{calc}) of the isotropic adsorption layer must be scaled accordingly (yielding I_{obs}):

$$I_{obs} = 3\cos^2\theta \times I_{calc}$$

with θ being the angle between the transition moment μ and the surface normal.

In contrast, when the adsorbed layer undergoes significant changes relative to the bulk material with regard to force constants, normal modes, and charge distributions, spectra of adsorbed layers significantly differ from bulk spectra (band positions, intensities, and shapes). In such cases, it is impossible to make simple interpretations from comparisons of bulk and adsorbates.

The second method was suggested by M.K. Debe.[79,80] He measured a series of IRAS spectra from films of bulk thickness (>1000 Å) down to near monolayer thickness. The individual band absorbances are then normalized to constant equivalent thickness, obtained from the spectrum's average band absorbance, and plotted as a function of this "thickness". From the fractional change in the so normalized band intensities between the random bulk and the oriented monolayer states and a reliable knowledge of the transition moment directions of the vibrational modes producing those bands, the orientation of the transition moment directions relative to the surface normal E field can be deduced. The following formula is used to calculate the orientation of the adsorbates:

$$\delta_i \equiv \frac{I_i^t - I_i^b}{I_i^b} = 3\cos^2\theta - 1$$

where δ is the percentage change in the thickness-normalized band absorbances, I_i^t the projected intensity of band i in the thin film, I_i^b the intensity of band i in the bulk, θ the angle between the direction of the transition moment and the surface normal. The method can be applied to different kinds of films including spin-coated organic films. However it needs a large amount of works to record serial spectra of thin films with different thickness. It is not very suitable for investigating SAMs.

The third method, discussed in the following chapters, was suggested by K. Iida, et. al.[81] and was used by us to calculate the maleimide orientation in Section 5.6.3.

3.3.2 Vibrational mode assignments

Normal vibration modes of benzene

In order to illustrate the notation used later for the explanation of IR spectra of aromatic compounds such as 4-aminothiophenol (4-ATP), the normal vibration modes of benzene and their correspondent IR-active band frequencies are shown in Figure 3-8.[82] The point group of benzene is V_h; the para-di-substituted benzene such as 4-aminothiophenol is in point group C_{2v}.
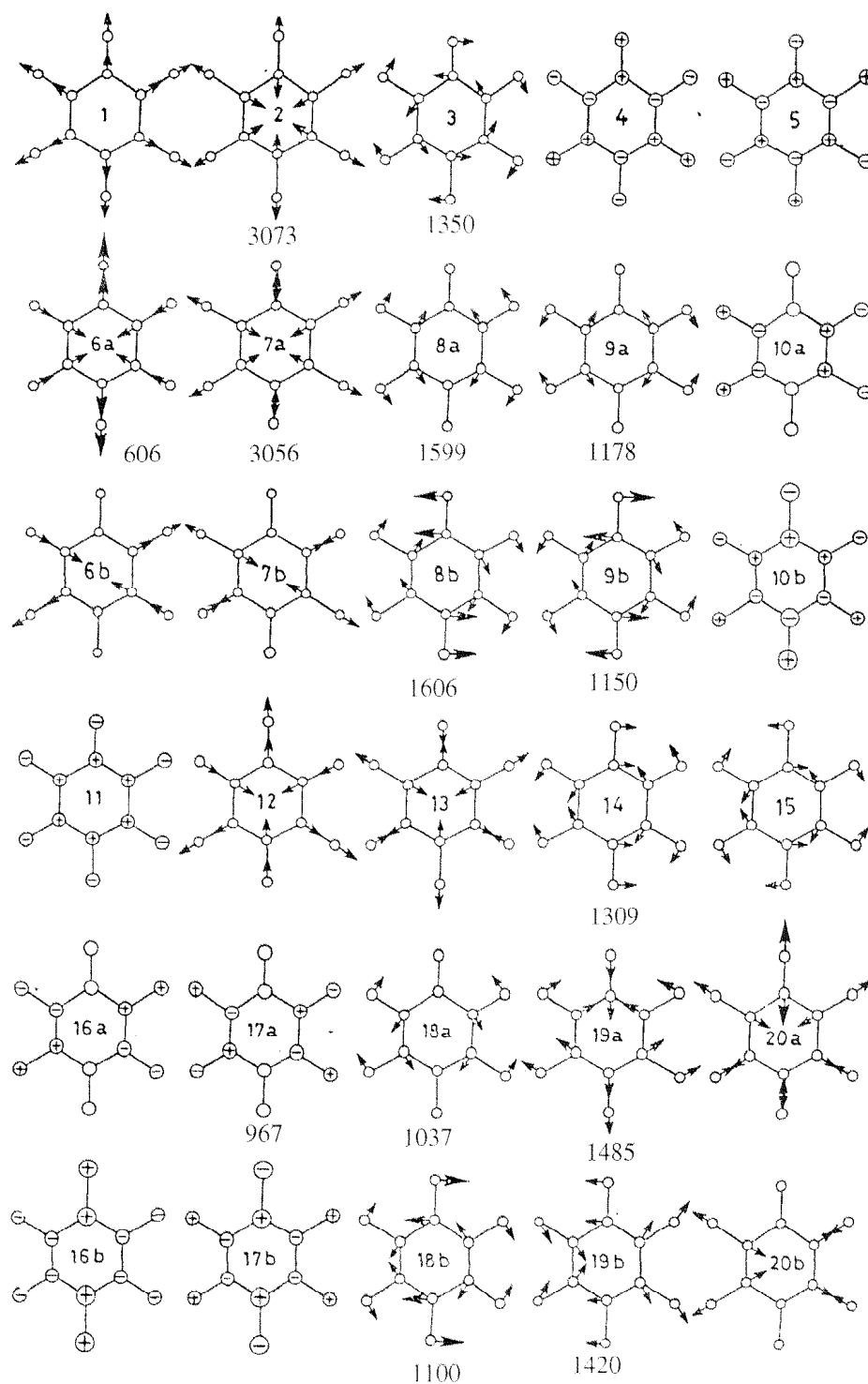
Figure 3-8   *Normal vibration modes of benzene: Their corresponding IR-active bands*
(in cm⁻¹) are shown under the modes.

Amide bands

Amide bond formation is the key step for grafting crosslinkers on terminal NH_2 surfaces. It is also the basic bond in peptides and proteins. The amide bands are introduced below:

1. Amide I band: The band observed in the region 1700-1650 cm^{-1} is termed as the Amide I band. This vibration is essentially a C=O stretching frequency.

2. Amide II band: The in-plane N-H bending frequency and the resonance stiffened C-N bond stretching frequency fall close together and therefore interact. The C-N-H vibration where the nitrogen and the hydrogen move in opposite directions relative to the carbon involves both N-H bending and C-N stretching and absorbs strongly near 1550 cm^{-1}. This mode of vibration of the amide group is termed as the Amide II.

3. Amide III band: The amide III band, besides the stretching of the C-N and C-C bond, involves considerable in-plane bending vibration of the N-H bond. In N-substituted secondary amides this mode of vibration absorbs near 1250 cm^{-1} region.

Amide I, II, and III are the most interesting bands with strong intensities, while other peaks are weak and less discussed in the literature.

Amide I ($\sim$1650 cm^{-1})   Amide II ($\sim$1550 cm^{-1})   Amide III ($\sim$1250 cm^{-1})
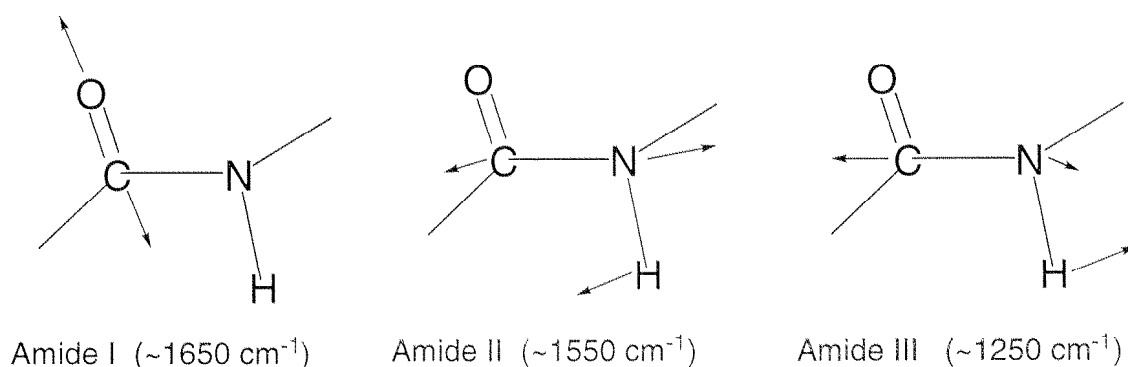
Figure 3-9   Vibration modes of amide I, amide II, and amide III.

3.3.3 Experimental set-up and substrate related peaks in IRAS spectra

The IRAS measurements were performed on a Bruker IFS 66V spectrometer operating under vacuum of ca. 0.5 mbar. A mercury-cadmium-telluride (MCT) detector under liquid nitrogen was used to collect spectra with a resolution of 2 cm^{-1}. The angle of incidence was 80^{0} from the surface normal. Pure Ti and Au mirrors were used as the references. For both sample and reference, 500 scans were collected.

Since IRAS spectra depend on both the reference and the sample surfaces, there are some irregular peaks ('ghost' peaks) resulting from contaminations on the reference or sample surface. It is very important to choose the 'standard' reference. Fresh Au or long-time stored Au surfaces as the references show differences in the IRAS spectra for the same sample. For example, if a long-time stored Au is used as the reference, the C-H stretching bands are often negative. If a fresh Au surface is used as the reference, the C-H stretching

bands are positive, but a strong negative peak at 1398 cm^{-1} always appears, probably related to different adsorbed species. Table 3-3 lists the 'ghost' peaks typically observed on Au surfaces.

Table 3-3   FT-IRAS peaks related to the Au reference substrate.

Frequency (cm^{-1})	Origin of the peak
3748	?
ca. 3700 and 3600	densely distributed sharp bands from water vapor in air
ca. 3625	free O-H
2972-2843	hydrocarbon contaminants adsorbed on the Au reference or the Au sample
ca. 2360 and 2335	CO_2 in air
1880	?
1780 1730 1701	possible carbonyl contaminant adsorption
1650	?
1600	water vapor in air
1575	?
1398 (-)	possibly adsorbed gas on the Au reference (for the fresh Au)
ca. 1380	?
1350-700	some unexpected peaks for some reference substrates
under 700	detector limitation

On titanium surfaces, the main 'ghost' peaks are at wavenumbers of 2972-2843, 2509, 2431, 2074, 2022, 1886, 1795, 1263, and 1114 cm^{-1}.

3.4 Contact angle measurements

Contact angle measurements are often used to assess changes in the wetting characteristics of a surface and hence indicate a change in surface energy. The technique is based on the three-phase boundary equilibrium described by Young's equation, (Fig 3-10)
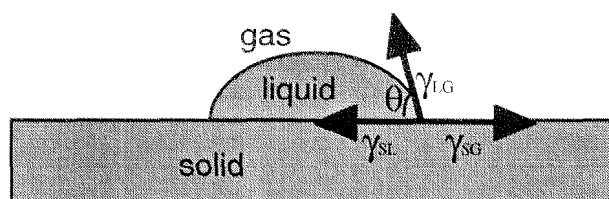
Figure 3-10   Schematic representation of the Young's equation.

$$\gamma_{LG}\cos\theta = \gamma_{SG} - \gamma_{SL}$$

where γ_{ij} is the interfacial tension between the phases i and j, with subscripts L, G, S corresponding to liquid, gas, and solid phase respectively and θ refers to the equilibrium contact angle.

The Young's equation applies for a perfectly homogeneous atomically flat and rigid surface and therefore supposes many simplifications. In the case of real surfaces, the contact angle value is affected by surface roughness, heterogeneity, vapor spreading pressure, and chemical contamination of the wetting liquid. Although the technique to measure contact angles is easy, data interpretation is not straightforward and the nature of different contributions to the surface is a matter of discussion.

Generally, we can define the complete wetting, wetting, partial wetting, and nonwetting according to Figure 3-11.
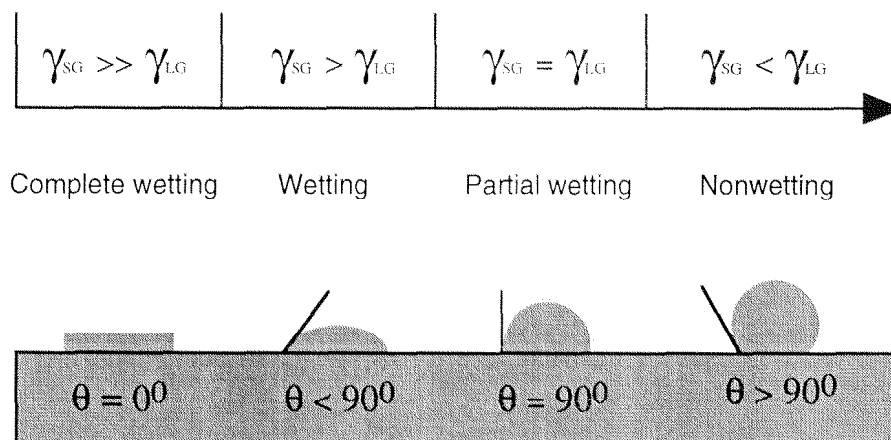
Figure 3-11   Schematic representation of wettability.

The advancing contact angle measurement has been carried out on a Ramé-Hart NRL model goniometer at room temperature and ambient humidity. For the measurements, 3 µl

of water were put on the surface, followed by adding another 3 μl to the first drop, and measuring the contact angle within 1 min.

3.5 Ellipsometry

Ellipsometry provides another nondestructive method for measuring both thickness and refractive index of transparent films. The principle is based on evaluating the change in the state of polarization of light reflected from a substrate. The state of polarization is determined by the relative amplitude of the parallel and perpendicular components of radiation and the phase difference between the two components.

The ellipsometry is used by us for determination of thickness of ultrathin organic films on the Ti or Au substrate. To measure the film thickness, the optical constants of the film-substrate system must be known. This is one of the problems dealing with ellipsometry because there are limited optical constants determined and published for only a few systems. Fortunately, the SAMs-Au system has been thoroughly studied and the optical constants ($n_{Au} = 0.15$, $k_{Au} = 3.6$, and $n_{SAM} = 1.45$) are used by us to calculate the film thickness when the laser wavelength is 632.8 nm. The film thickness on Ti and Au was measured on a PLASMOS SD 2300 ellipsometer, equipped with a He-Ne laser ($\lambda = 632.8$ nm), at an angle of incidence of 70^0.

3.6 Radiolabeling techniques

Radiolabeling technique is widely used in biochemical studies of protein, DNA/RNA, and cell structure and function. At least one atom in a radiolabeled molecule is present in a radioactive form, called a *radioisotope*. The presence of a radioisotope does not change the chemical properties of a molecule. The most commonly used radioisotopes are ^{14}C, ^{35}S, ^{32}P, ^{125}I, and ^3H. For quantitative analysis, the *specific radioactivity*, which is the amount of radioactivity per unit of material, must be known. The specific radioactivity of a labeled compound depends on the ratio of unstable radioactive atoms to stable nonradioactive atoms. It also depends on the probability of decay of the radioisotope. The amount of radioactivity in a labeled material can be measured with a *scintillation counter*. In a scintillation counter, a radiolabeled sample is mixed with a liquid containing a fluorescent compound that emits a flash of light when it adsorbs the energy of the β particles or γ rays

released during decay of the radioisotope; a phototube in the instrument detects and counts these light flashes.

The radioactivity of our samples was measured by scintillation counting in 5 ml scintillation fluid (1080 ml toluene, 920 ml Triton X-100, 5.4 g 2,5-diphenyloxazole, 0.2 g 1,4-bis-2-(5-phenyloxazolyl) benzene, and 40 ml acetic acid) on a Tri-Carb 2300TR liquid scintillation counter (Packard Instrument Co., USA).

3.7 Other techniques

Atomic force microscopy
Atomic force microscopy is a novel technique developed by Binnig et al.[83] The principle of this technique is based on the existence of a distance dependent force between a surface and a tip or sensor, typically of <100 nm radius. By scanning a tip over a surface, the surface topography or the lateral force distribution can be obtained. The force can be calculated from the deflection of a static cantilever, and typically is in the order of 1 nN. An AFM instrument Nanoscope E (Digital Instruments, Santa Barbara, USA) was used by us to measure the surface topography and roughness of coated Ti and Au in air.

Near-edge X-ray absorption fine structure spectroscopy (NEXAFS)
For photon energies far above the photoelectric threshold, i.e. at core level absorption edges, the photoelectric yield is closely related to the absorption coefficient. The so-called NEXAFS technique is based on this physical process and has found many applications. It can be used to investigate the electronic structure of ultrathin films and to determine the orientation of segments of adsorbed molecules. In order to investigate the molecular structure of functional groups on the surfaces AuCM6 and TiAM6 (see Abbreviations), the NEXAFS measurements were kindly performed by Drs. G. Hähner and D. Brovelli at the National Synchrotron Light Source (NSLS), Brookhaven National Laboratory (New York).

3.8 Survey of characterization techniques

Table 3-4   *Summary of the different surface sensitive techniques and their characteristic properties.*

Technique & usable environment	Information depth & lateral resolution	Selected advantages	Selected disadvantages
XPS (Vacuum)	Atomic composition and oxidation state 0.5-10 nm (depth) 100 μm - mm (lateral)	Surface selective Chemical oxidation state Easy quantification Easy sample preparation Depth profiling with variable angle	Possible sample damage Sample charging, particularly for monochromatized X-ray source
IRAS (Liquid, air, and vacuum)	Molecular structure and orientation ~0.05-1 μm (depth) ~10 μm (lateral)	Excellent chemical information Nondestructive Can be quantitative	Poor depth resolution
ToF-SIMS (Vacuum)	Molecular structure and composition ~ 1 nm (depth) > 50 nm (lateral)	Excellent mass resolution Imaging capability Chemical structure information High sensitivity	Quantification difficult Peak interpretation often complicated and time-consuming
NEXAFS (Vacuum)	Molecular structure and orientation ~10 nm (depth) ~ mm (lateral)	Surface selective Chemical bonds Molecular orientation	Tunable X-ray source necessary (synchrotron)
AFM (Liquid, air, and vacuum)	Topography Lateral imaging Atomic scale	Extremely surface selective Atomic resolution imaging of surface topography	Quantitative interpretations difficult Artifacts
Contact Angle Goniometer (Air)	Surface wettability or surface energy	Easy handling	Less 'fingerprint' information
Ellipsometry (Liquid and air)	Surface film thickness Refractive index	Non destructive High precision film thickness	Other experiments needed to complement results
Radiolabeling	Special group concentration	Quantitative surface concentration measurement	Harmful to environment

4. Covalent attachment of cell-adhesive, (Arg-Gly-Asp)-containing peptides to titanium surfaces

4.1 Introduction

Much attention has recently been directed toward the development of bioactive and biocompatible material surfaces for a variety of technological applications, among them biosensors,[84] bioreactors,[85] chromatographic supports[86] and functionalized building blocks for biomaterials. A major challenge in the development of functional surfaces is to design strategies, employing either existing synthetic technologies or novel fabrication methods, to assemble various complex molecular species on material surfaces, such as organized thin organic films functionalized with peptides, proteins, or DNA/RNA strands. To select appropriate synthetic routes, the following restrictions have to be considered: (1) the attachment site and chemistry must not interfere with the functional structure or the active site of the biomolecule, (2) the attached biomolecule must not be denatured or inactivated at the surface during or following attachment, and (3) the attached biomolecule should be stably bound at the surface through linkages that are not susceptible to disruption by hydrolysis or other interactions with species in the environment.

Titanium is a successful biocompatible material that is extensively used today for manufacturing bone-anchoring systems, such as dental implants or hip-joint fixation and replacement, as well as for pacemakers, heart-valves, and ear-drum drainage tubes. It has advantageous bulk and surface properties: in particular, a low modulus of elasticity, a high strength-to-weight ratio, excellent resistance to corrosion and an inert, biocompatible surface oxide film.[87] The surface chemistry and structure is one of the prime factors governing bone integration[86] and there is–from the standpoint of both surgeon and patient–considerable interest in increasing both speed of formation (healing time) and degree (long-term success) of close bone aposition for cement-free implantation. To further improve the biocompatibility of titanium, many physical and chemical surface modification methods such as electrochemical oxidation, plasma-coating with titanium or hydroxyapatite, and ion implantation are in use.[8] Reports concerning biochemical modification to change a bioinert surface to a bioactive surface, however, are rare. One example is a paper by Sukenik et al. [26] describing the modification of the titanium surface with terminal groups such as CH_3, OH, and Br through silanization and their biological effect in neural cell culture tests.

The amino acid sequence RGD (Arg-Gly-Asp), is present in many extracellular matrix (ECM) proteins and has been found to play an important role for cellular growth, differentiation, proliferation, and regulation of overall cell function.[59] Immobilized, synthetic, RGD-containing peptides on solid supports such as polymers[66] and silicon oxide surfaces[63] have been reported to mediate specific surface-cell interactions and to promote cell organization. Studies of cell migration suggest the importance of the surface density of RGD sequences for efficient cell-matrix interaction.[88]

The most commonly used immobilization methods on inorganic oxide surfaces involve reactively deposited silane films with terminal functional groups that can be further modified with different linking moieties. For aminosilanes, a variety of routes for further modification have been applied, e.g. (1) reaction with glutaraldehyde,[89,90] yielding an aldehyde that can form an imine linkage with primary amines on the peptides, or (2) reaction with a mixture of peptides and carbodiimide, yielding an amide linkage with carboxyl groups on the peptides.[67,91] The two methods utilize the primary amino groups and carboxyl groups that occur with high frequency in peptides and proteins, but specific attachment at a defined site is very difficult with these functionalities. It is apparent that these approaches must produce highly heterogeneous surfaces.

The most recently examined method employs heterobifunctional crosslinkers with both thiol- and amino-reactive moieties, which have been widely used in protein conjugation and cross-linking.[57] Bathia et al.[3,92] linked the maleimidyl group onto thiol-terminal silanized silica surfaces, followed by immobilization of anti-IgG antibody through the reaction of the primary amine moieties with the succinimidyl ester. Hong et al [1,2] achieved the attachment of cytochrome by reaction of a succinimidyl ester with amine-terminated, silanized glass surfaces, followed by covalent binding of a single unique cysteine thiol on the cytochrome through maleimide. Using similar chemistry, Heyse et al.[93] attached thiol-bearing phospholipids onto optical waveguide surfaces (SiO_2-TiO_2 waveguide layer); Chrisey et al.[94,95] immobilized DNA on silica surfaces; and Matsuzawa et al.[96] attached a synthetic peptide on glass for neuron culture tests. This functionalization technique satisfies to some extent the aforementioned requirements: production of a single functional site and mild reaction conditions. A particular advantage is the much higher surface coverage of biomolecules with this method compared to other coupling approaches. Although the surfaces were characterized by radiolabeling, UV-VIS spectroscopy, and subjected to biological activity assays, our knowledge regarding the physico-chemical properties of these surfaces is still rudimentary.

We will describe the binding of RGDC and GRGDSPC onto maleimide-functionalized titanium surfaces and the use of a variety of surface functionalization and characterization

techniques in the following text. The aim of the work is to covalently bind cell-adhesive RGD-containing peptides onto Ti surfaces and to evaluate the biocompatibility of these novel surfaces. Both surface sensitive techniques (XPS, IRAS, ToF-SIMS, ellipsometry, contact angle goniometer) and radiolabeling methods were used to qualitatively and quantitatively characterize the surfaces after each reaction step. Good agreement is achieved between XPS and radiolabeling techniques as regards the quantitative estimation of surface coverages. The results of cell culture tests and the biocompatibility performance of these novel surfaces are discussed briefly at the end.

4.2 Materials and methods

4.2.1 Materials

Table 4-1   Supporting substrates and Ti or TiO_2-coatings.

Substrate & source	Dimension (mm)	Surface coating	Application	Coating source
Commercial float glass	250x12x2	100 nm Ti 20 nm TiO_2	General use for surface analysis (XPS, ToF-SIMS)	Leybold Z600 (PSI, Villigen)
Round glass cover slips (Huber & Co. AG)	∅: 15; thickness: 0.16	100 nm Ti 20 nm TiO_2 both sides	Surface analysis and specially for cell culture	Leybold Z600 (PSI, Villigen)
Round silicon wafer (Balzers)	∅: 100	100 nm Ti	For IRAS measurement	Leybold Z600 (PSI, Villigen)

The titanium metal and oxide coatings were kindly provided by Dr. P. Böni and Mr. M. Horisberger of the Paul Scherrer Institute (PSI). The sources and coating methods for the supporting substrates and titanium-containing films are listed in Table 4-1.

The 100-nm-thick Ti coatings were produced on both sides of round glass cover slips (diameter 15 mm, thickness 0.16 mm) (Huber & Co. AG, Reinach/Switzerland) in a Leybold Z600 DC-magnetron sputtering facility.[97] Under the same conditions, Ti films on larger silicon wafers were also prepared for IRAS measurements.

Pure water was obtained from an EASYpure™ device, Barnstead/USA. (3-Aminopropyl)triethoxysilane (APTES) was bought from Fluka, Buchs/Switzerland, distilled, stored, and used under N_2. The heterocrosslinkers, N-succinimidyl-3-maleimidylpropionate (SMP), N-succinimidyl-4-maleimidylbutyrate (SMB), N-succinimidyl-6-maleimidylhexanoate (EMCS), N-succinimidyl-8-maleimidyloctanoate (SMO), and N-succinimidyl-11-maleimidylundecanoate (SMU) were purchased from Fluka; N-succinimidyl trans-4-(maleimidylmethyl)cyclohexane-1-carboxylate (SMCC) was purchased from Molecular Probe, Netherlands. The radiolabeling reagents, [^{14}C]-formaldehyde ([^{14}C]-FA) with specific radioactivity 54.0 mCi/mmol, [^{35}S]-L-cysteine ([^{35}S]-Cys) with 20-150 mCi/mmol, and [^{14}C]-phenylglyoxal ([^{14}C]-PG) with 27.0 mCi/mmol, were purchased from Amersham, Buckinghamshire/UK, stored, and used as indicated. RGDC (65.2%) and GRGDSPC (65%) were purchased from Bachem AG, Bubendorf/Switzerland, and all other chemicals were obtained from Fluka.
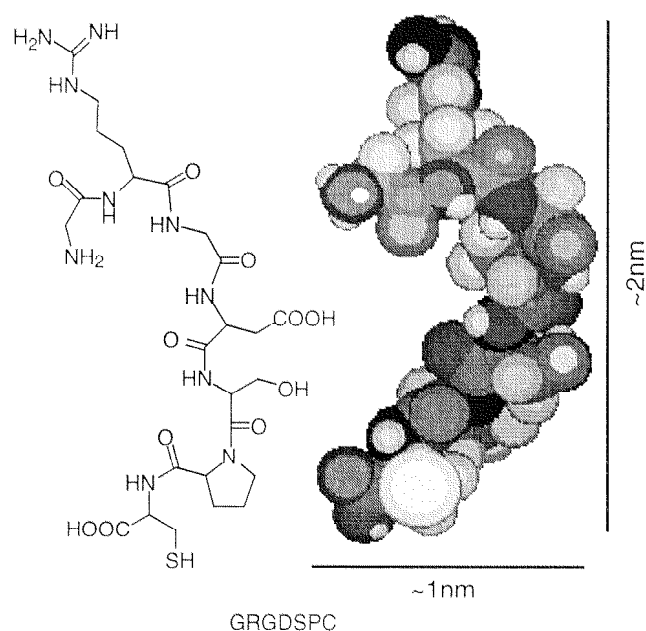
Figure 4-1   Molecular structures of the peptide GRGDSPC. The space-filling model of GRGDSPC with the minimum energy conformation calculated from MM2 is shown on the right.

The molecular structures of crosslinkers used in this thesis are shown in Appendix. The molecular structure of GRGDSPC is illustrated in Figure 4-1.

4.2.2 Surface modification route

The surface modification route is shown in Figure 4-2. Water-vapor-plasma-pretreated titanium surfaces were first activated by APTES, followed by reaction of terminal amines with

succinimidyl esters of the crosslinkers, and finally by the covalent binding of the thiol-bearing, RGD-containing peptides through maleimidyl groups.

The different surfaces are defined as follows: **Ti**: water-vapor-plasma-pretreated titanium surface; **A**: poly(3-aminopropyl)siloxane-modified surface; ^{14}**CA**: [^{14}C]-formaldehyde+A; **M**: maleimide-modified surface; **TiAM6**: A+EMCS; **M6**: multiple groups of hexanoyl maleimide and succinimidyl ester; ^{35}**SM6**: [^{35}S]-L-cysteine+TiAM6; **TiAM3**: A+SMP; **M3**: N-maleimidyl-3-propanoyl group; **TiAMC**: A+SMCC; **MC**: trans-4-(maleimidylmethyl)cyclohexane-1-carbonyl group; **P**: peptide- or L-cysteine-modified surface; **CM6**: L-cysteine+TiAM6; **CM3**: L-cysteine+TiAM3; **CMC**: L-cysteine+TiAMC; **GM6**: GRGDSPC+TiAM6; **RM6**: RGDC+TiAM6; **GM3**: GRGDSPC+TiAM3; **RM3**: RGDC+TiAM3; **GMC**: GRGRSPC+TiAMC; **RMC**: RGDC+TiAMC; ^{14}**CGM6**: [^{14}C]-phenylglyoxal+GM6; **TiAM4**: A+SMB; **TiAM8**: A+SMO; **TiAM11**: A+SMU.

Surface Ti   Surface A   Surface M   Surface P
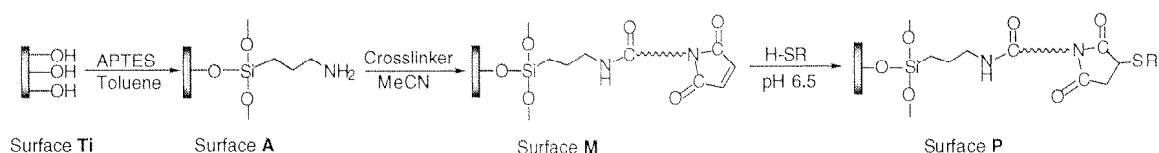
Figure 4-2   *Schematic representation of the modification route. Surface Ti: water-vapor-plasma-pretreated titanium; Surface A: poly(3-aminopropyl)siloxane pendant surface; Surface M: maleimide-modified surfaces with different alkyl chains; Surface P: peptide- or L-cysteine-modified surfaces; H-SR: L-cysteine, RGDC, GRGDSPC.*

Although the second step surface reactions with many other crosslinkers such as N-succinimidyl iodoacetate (SIA), N-succinimidyl-3-maleimidylbenzoate (SMBZ), N-succinimidyl-4-(4-maleimidylphenyl)-butyrate (SMPB), N-5-azido-2-nitrobenzoyloxy-succinimide (ANS), and N-succinimidyl 4-benzoylbenzoate (SBB) were carried out by us, the characteristics of these surfaces with IRAS and XPS are similar to those surfaces produced by reaction of these crosslinkers with cystamine SAMs on gold surfaces in next chapter and thus are omitted in this chapter.

4.2.3 Chemical functionalization

4.2.3.1 Pretreatment

The purpose of pretreatment is to achieve cleanliness and to increase the hydroxyl group concentration on the surface. The hydroxyl group concentration on the substrate surface is one

parameter affecting the quality of siloxane films. We evaluated four pretreatment methods with XPS on the titanium-containing surface. The four pretreatment methods are as follows:

1. HCl/H_2SO_4 procedure: The titanium-containing substrates were incubated in a solution of 1:1 (v/v) methanol/HCl(37%) at room temperature for 30 min, followed by rinsing five times with water. The substrates were then treated in concentrated sulphuric acid at room temperature for 15 min, and again washed extensively with water. After treatment in boiling water for 10 min, they were washed 5 times with water, rinsed with acetone, and dried under vacuum for 12 h. The pretreatment resulted in a slight decrease of titanium coating thickness. XPS measurements, however, showed no glass to be exposed on the surface.

2. Water plasma procedure: The samples and 5 g ice were placed in a Plasma Cleaner/Sterilizer PDC-32G (Harrick, New York) chamber. The plasma was triggered and applied for 2 min under a pressure 0.4 mbar.

3. Hydroperoxide procedure: The samples were placed in 1.5 M H_2O_2 aqueous solution at room temperature for 10 min, then washed with pure water 10 times and dried under vacuum overnight.

4. HNO_3 procedure: The samples were placed in 30% HNO_3 for 10 min, then washed with water thoroughly and dried under vacuum overnight.

4.2.3.2 Preparation of silanized samples.

Prior to silanization, the titanium-coated glass cover slips were first pretreated by water-vapor-plasma cleaning (0.4 mbar, 2 min), then dried in vacuum for 1 h. Three hundred samples of **Ti** were incubated using a self-fabricated glass holder in 200 ml of dry toluene containing 2 ml APTES (43 mM) at 80 ^{0}C for 48 h. After reaction, the substrates were ultrasonically washed with chloroform five times, acetone twice, methanol five times, and extensively rinsed with water, then dried in vacuum and cured at 100 ^{0}C under N_2 for 1 h. The treated samples (**A**) were stored under argon for further reactions as detailed below.

Five samples of type **A** were acetylated by overnight treatment at room temperature with a mixture of toluene (1 ml), acetic acid anhydride (100 µl) and dry pyridine (100 µl). After 12 h, the samples were rinsed with toluene, CH_2Cl_2 and ethanol.

4.2.3.3 Preparation of maleimide- (M) and peptide- (or L-cysteine-) modified (P) samples.

Twenty silanized titanium samples (A) were placed in a self-fabricated polypropylene vessel with 2 ml acetonitrile (CH_3CN) containing 5.0 mM crosslinkers. After incubation at 20 ^0C for 30 min, with 30 s sonication every 10 min, the excess crosslinker solution was removed, and the samples were washed extensively with acetonitrile, acetone, and hexane. After drying with N_2, the samples were subject to the next chemical step. Twenty maleimide-grafted substrates were incubated at 20 ^0C for 1 h in 2 ml water containing 2.0 mM peptide or L-cysteine, with 30 s sonication every 10 min. The pH of the peptide or L-cysteine solution was adjusted to 6.5 with 0.1 M NaOH before injection. The peptide-grafted substrates were washed thoroughly with water, dried with N_2, and stored in argon.

4.2.4 Surface analysis methods

The experimental conditions for XPS, IRAS, contact angle goniometer, and ellipsometry measurements have been described in the previous chapter. Some additional details are listed below:

Ellipsometry

The optical constants of surface Ti were determined in at least four different areas on each individual substrate. The thickness of the modified organic films was calculated using the software for a single organic thin film and a refractive index of 1.45.

Contact angle measurements

Advancing contact angles were measured on a Ramé-Hart NRL model goniometer at room temperature and ambient humidity. The contact angles are 30, 44, 60, and 45^0 for surfaces Ti, A, TiAM6, and GM6 respectively. The experimental error of this method is estimated to be ±3^0.

Radiolabeling procedure

[^{14}C]-Formaldehyde labeling of surface A was performed in a self-fabricated metal sample holder with 4 wells (diameter = 7 mm). Acetonitrile (50 μl) containing 10.0 mM $NaBH_3CN$ and 2.0 mM [^{14}C]-formaldehyde was injected into each well. After incubation for 4 h at 20 ^0C, the excess radioactive solution was removed and the exposed surface washed with CH_3CN 10 times and water 10 times. The demounted samples were extensively washed again with water, and then dried with N_2. The same procedure was also applied to the control surfaces of Ti and

acetylated-**A**. The radioactivity of each sample was measured by scintillation counting in 5 ml scintillation fluid (1080 ml toluene, 920 ml Triton X-100, 5.4 g 2,5-diphenyloxazole, 0.2 g 1,4-bis-2-(5-phenyloxazolyl) benzene, and 40 ml acetic acid) on a Tri-Carb 2300TR liquid scintillation counter (Packard Instrument Co., USA).

Maleimide-functionalized substrates (**M**), kept between two metal plates, were covered with 50 µl 0.11 µCi/µl [^{35}S]-cysteine aqueous solution in each well. The pH of the solution was adjusted to 6.5 by 0.1 mM NaOH before use. After incubation for 1 h at 20 ^{0}C, the excess radioactive solution was rinsed off 10 times with water. The substrates were then removed from the metal plates, washed again with excess water, dried with N_2, and the radioactivity determined. Control experiments for the covalent binding of cysteine to maleimide functionalized substrates were carried out as above by applying the same [^{35}S]-cysteine solution to surface **A** and unlabeled-L–cysteine-reacted surface **M**.

Radiolabeling of RGD-grafted surfaces was carried out by injecting 50 µl sodium phosphate (25 mM) buffer (pH 7.4) containing 5 mM [^{14}C]-PG to each well as described above, incubating for 24 h at 20 ^{0}C, then washing thoroughly with water, drying with N_2, and counting as detailed above.

The degradation experiments were carried out with the radiolabeled surfaces, ^{14}CA, ^{35}SM6, and ^{14}CGM6 by measuring their specific radioactivity loss as a function of storage time in 5 ml water at room temperature.

4.3 Results and discussion
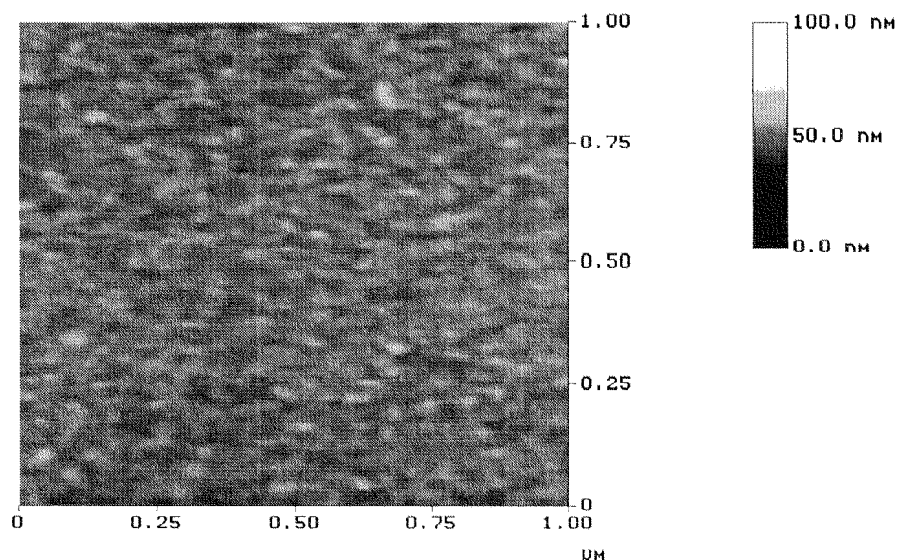
4.3.1 Substrates and pretreatments

Figure 4-3   AFM topography of sputtered Ti coatings on round glass cover slips.

Atomic force microscopy was used to evaluate the surface roughness of the sputtered Ti coatings. Figure 4-3 shows the surface structure of Ti coatings. The size of Ti particles is ~20 nm and the arithmetic mean of the roughness height, Ra, is ~1.7 nm.

The purpose of pretreatment is to clean the surface and to increase the hydroxyl groups on the surface. The atomic concentrations calculated from XPS in Table 4-2 clearly show the decreasing hydrocarbon contamination after pretreatments. However, it is difficult to evaluate the surface density of hydroxyl groups due to different oxygen species (OH, H_2O, and organic O) appearing in the range of 531 - 533 eV. The different pretreatments do not result in big differences for further silanization. So, for convenience, we use the water vapor plasma as the standard protocol.

The detailed XPS spectra of pretreated titanium surfaces are shown in Figure 4-4. Three elements are detected: titanium, oxygen, and contaminated carbon. The main carbon species is hydrocarbon 71% (C 1s at 284.6 eV), and the rest species may be the oxygen-bonded carbon, C 1s 286.0 eV (20%) attributable to $\underline{C}$-O and C 1s 288.3 eV (9%) attributable to $\underline{C}$=O. The main oxygen species is titanium dioxide (O 1s 530.0 eV, 84.2%) and the rest portion (O 1s 532.0 eV, 15.8%) can be assigned to hydroxyl groups, adsorbed water, and contaminated organic oxygen. The main titanium species detected on the outermost layer is titanium dioxide

(Ti $2p_{3/2}$ at 458.5 eV and Ti $2p_{1/2}$ at 464.3 eV), and a small portion of titanium metal (Ti $2p_{3/2}$ at 453.3 eV) is also observed because the XPS information depth is deeper than the thickness of the native TiO_2 layer (~5 nm). In fact, the Ti 2p peak can be deconvoluted to Ti^{4+}, Ti^{3+}, Ti^{2+}, and Ti^0.[98]

Table 4-2   *Atomic concentrations of coated TiO_2 and Ti films before and after pretreatments (average values from 3 samples).*

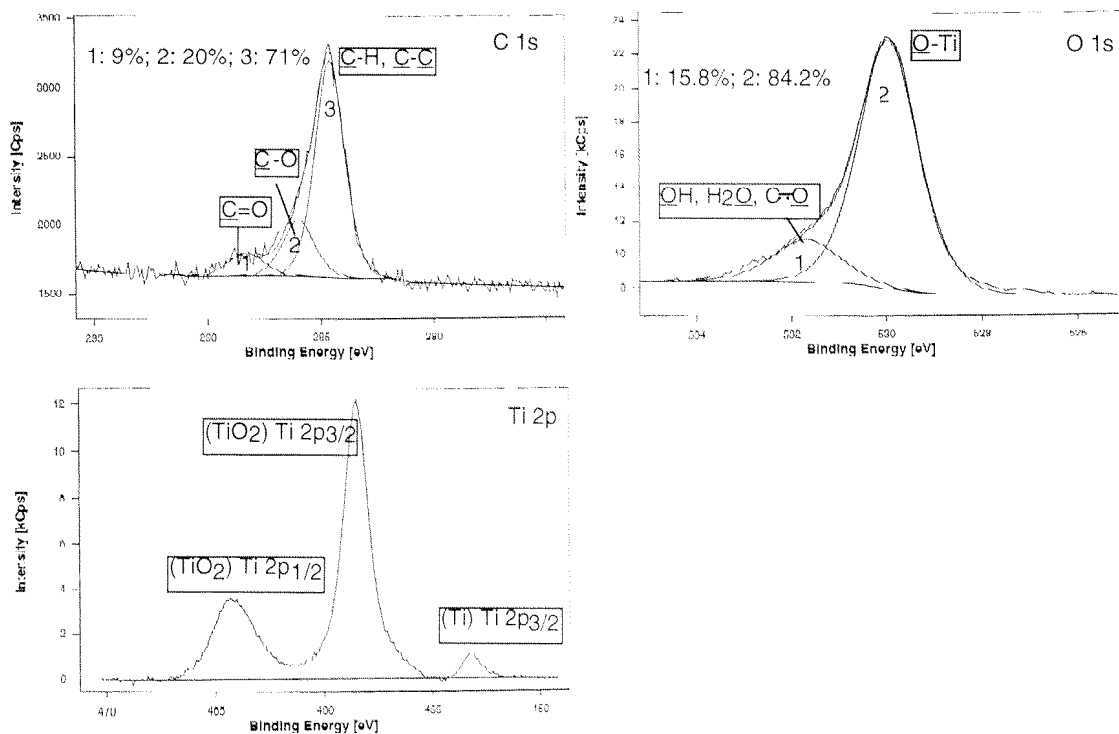| TiO₂ surface	C	Ti	O	N
in air	16	24	60	
HCl/H₂SO₄	12	24	64	
H₂O₂	11	25	64	
HNO₃	11	24	64	1
plasma	12	25	63	
Ti surface	**C**	**Ti**	**O**	**N**
in air	31	21	48	
HCl/H₂SO₄	18	23	59	
H₂O₂	20	22	58	
HNO₃	16	23	60	1
plasma	18	24	58	

Figure 4-4   *The detailed XPS spectra of C 1s, O 1s and Ti 2p of pretreated titanium samples.*

4.3.2 Silanization procedure

Silanization is the crucial step as regards subsequent reproducibility of the chemical functionalization. Although silanization has been extensively studied, the resulting structure, coverage, orientation, and organization of the layers have not yet been satisfactorily determined and are still the subject of controversy.[99] It is generally accepted that silanization on inorganic surfaces occurs by reaction of silanol groups with hydroxyl groups present on oxide surfaces. Due to the ability of the silane to polymerize at the surface, the siloxane film can be produced as a monolayer or multilayer, depending on substrates, silane properties, and reaction conditions. In general, long-alkyl-chain silanes tend to form monolayers, while short bifunctional silanes, such as aminosilanes, tend to form multilayers.

Pretreatment of the titanium surface is an essential prerequisite for reproducible silanization. Untreated titanium films (as sputtered) gave unsatisfactory results. Optimum surface cleanliness and reactivity were achieved through water vapor plasma treatment, although other pretreatments such as H_2O_2, HNO_3, and H_2SO_4/HCl also gave satisfactory results.

APTES was chosen to silanize the titanium surface. From our experience, the reaction media (aqueous or organic), temperature, concentration, ratio of reactants, incubation time, washing steps, etc. influence the amount of APS on titanium surfaces, to different degrees. Silanization in aqueous media resulted in a low surface concentration of amines (atomic ratio N/Si < 0.5 from XPS), which was not beneficial for further modification. However, silanization in toluene produced an APS film with a consistently high concentration of amines (N/Si=0.7, see Table 4-4).

To get the same thickness of APS thin films in different batches is not easy. At the beginning, we intended to follow an exact protocol to control the film thickness. However the data measured from XPS and ellipsometry turned out to be scattered. The extended silanization (toluene, 80 ^{0}C, and 48 h) produced a thick APS film, which, when treated by a three-step washing procedure: apolar organic solvent, polar organic solvent, and water resulted in a thin, smooth film. Apolar organic solvents remove the physically adsorbed silane and toluene; polar organic solvents make the surface hydrophilic; water can hydrolyze the loosely bound APS films and remove them.[100] We found that the APS film thickness can be well controlled within a narrow range mainly by controlling the immersion time in water. XPS can be used to follow the changes because the ratio O_{532}/O_{530} is sensitive to the change of film thickness. Figure 4-5 shows the relationship between the film thickness and the atomic ratio O_{532}/O_{530}. The measured points with standard errors are from the ellipsometer. The solid line is estimated from the following formula:[161]

$$d = \lambda_A \cdot \cos\theta \cdot In\left[\frac{I_A}{I_{TiO_2}} \cdot \frac{N_{TiO_2}^{\infty} \cdot \lambda_{TiO_2}^{\infty}}{N_A^{\infty} \cdot \lambda_A^{\infty}} + 1\right]$$

where d is the thickness of the APS film, λ_A is the attenuation length of APS at the thickness d, θ is the angle between the detector and the sample surface normal ($\theta=0$ for Sage 100), I_A and I_{TiO_2} are the measured intensities of O 1s from APS and TiO_2 at the thickness d respectively, N_x^{∞} is the molecular density of the pure compound x (molecule/volume), and λ_x^{∞} is the attenuation length of the pure compound x. For TiO_2, these data can be obtained from the literature: $\lambda_{TiO_2}^{\infty}=15.3$ Å at 795 eV, $N_{TiO_2}^{\infty}=2.9\times10^{22}$ molecules/cm^3. We do not know the attenuation lengths of APS films. However, it is generally accepted that the ultrathin organic films have the similar values. Both Swalen[156] and Bain[157] gave $\lambda = \sim40$ Å and $\lambda^{\infty} = \sim32$ Å at 1168 eV after a series of measurements on Langmuir-Blodgett films and on alkane thiol SAMs. They suggested that λ does not vary greatly with the thickness of the organic overlayer and the kinetic energy of photoelectrons within a narrow energy range (707-1169 eV). We assume that APS films have the same attenuation lengths and similar properties as those ultrathin organic films. In addition, we assume APS has the same mass density as APTES 0.95 g/cm^3; then the molecular density of APS is 4.8×10^{21} molecule/cm^3. Therefore we can calculate the APS film thickness from the atomic ratio O_{532}/O_{530}. The estimated data are shown in Figure 4-5 (solid line). They are larger than the correspondent measured values.

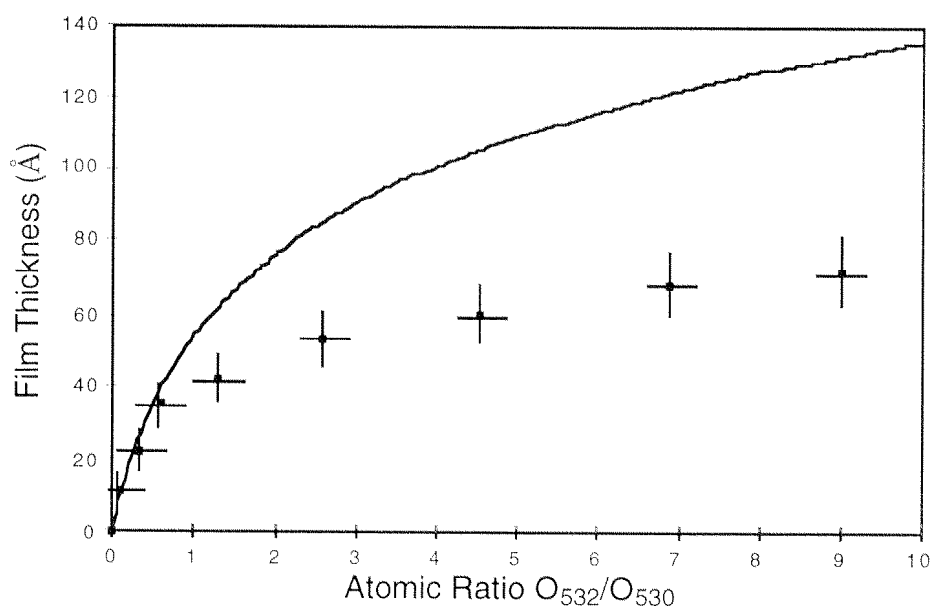

Figure 4-5   *The relationship between the atomic ratio O_{532}/O_{530} and the film thickness for APS films on titanium surfaces. The points with standard errors are from ellipsometer, and the solid line is calculated from the formula.*

The optimum APS film thickness, in our case is between 1 and 3 nm with enough free amino groups for reaction with succinimidyl esters and minimal interference for IRAS measurements.

To exclude batch-to-batch variations and to get reproducible data for the further modification, a large number of samples (300 pieces) were produced in one batch with the same reaction conditions, washing steps and curing. Curing has been widely used to stabilize the siloxane films, because it drives the surface derivatization reaction further to completion. As a result, the cured films are more resistant to hydrolysis. However, a long time (12 h) curing at 100 ^{0}C in air resulted in a pronounced reduction of the surface amine concentration, as a result of oxidation of primary amines to imines and nitriles.[101] This significantly reduced the reaction yield of the subsequent reaction step with succinimidyl ester. Curing for 1 h at 100 ^{0}C under N_2 gas was employed in the present study.

The surface coverage of amino groups on samples of this batch was determined as 6.0 NH_2 groups/nm^2 via reaction of the amine with [^{14}C]-formaldehyde. The surface coverage of hydroxyl groups on TiO_2 surface was estimated to be 6 OH groups/nm^2.[102] One aminosilane molecule reacts with 2 or 3 OH groups on the TiO_2 surface. Considering the N/Si ratio of 0.7 (Table 4-4), 9 silicon atoms per nm^2 would be present for every 4-6 APS layers on surface **A**. However, this does not mean that there are less than 25% primary amines exposed to the surface, since the surface roughness enhances the total proportion of exposed amines.

4.3.3 Monitoring reaction steps by XPS

XPS was used to monitor each reaction step as it can provide information on chemical structure, atomic concentration, and surface contamination. Figure 4-6 illustrates the changes of the atomic concentrations on the above surfaces. Figure 4-7 shows the evolution of the XPS signals of C 1s, N 1s, Ti 2p, and O 1s from **Ti** to **A**, **TiAM6**, and **GM6**. Table 4-3 lists the experimental XPS binding energies of the deconvoluted detailed spectra and the proposed assignments to chemical bonds/oxidation states based on chemical shifts. Surfaces modified with other crosslinkers and peptides gave results consistent with the proposed interpretation and are not presented here.

Water-vapor-plasma-pretreated titanium surface
Spectra of surface **Ti** show three elements: Ti, O, and C. Ti $2p_{3/2}$ at 458.5 eV and Ti $2p_{1/2}$ at 464.3 eV are assigned to TiO_2, Ti $2p_{3/2}$ at 453.3 eV is due to Ti metal because the XPS

information depth is greater than the thickness of the native TiO_2 layer (~5 nm).[98] O 1s at 530.0 eV is typical for TiO_2, while C 1s at 284.6 eV is due to the environmental hydrocarbon contamination.
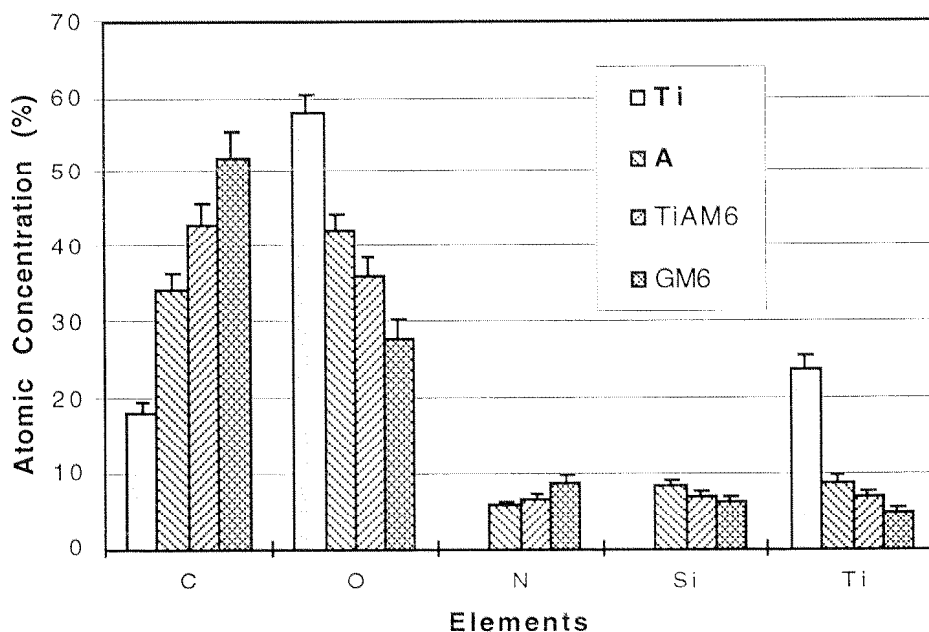

Figure 4-6   *Atomic concentrations of C, O, N, Si, and Ti calculated from XPS intensities on surfaces Ti, A, TiAM6, and GM6. Abbreviations; see Section 4.2.2.*

Silanized surface

The silanization reaction from surface **Ti** to **A** can be followed by XPS via the appearance of N (N 1s at around 400 eV) and Si (Si 2p at 102.0 and 153.0 eV), as well as the new high binding energy peak of O 1s at 532.3 eV due to Si-O. The broad N 1s peak can be deconvoluted into two peaks 399.6 eV (75%) due to free amines and 401.7 eV (25%) assigned to protonated amines.[103]

Maleimide-modified surface

The C 1s spectra of surface TiAM6 can be deconvoluted into four peaks with those at binding energies 289.0 eV and 288.2 eV being assigned to the newly introduced imide and amide functionalities, respectively. The N 1s emission has a new predominant contribution between 400 and 401 eV, again indicative of amide and imide functional groups reported to have binding energies of 400.1 and 400.7 eV respectively.[104] The disappearance of the Ti $2p_{3/2}$ (metal) peak at 453.3 eV demonstrates that the total thickness of the oxide plus organic surface layer now exceeds the information depth of XPS (ca. 8 nm).

TiAM3 and TiAMC show similar XPS chemical shifts and the spectra are not shown here. The C 1s intensities above 288.0 eV are somewhat lower compared to TiAM6 and exhibit

shoulders rather than obvious peaks (not shown here). This implies that the largest surface coverage occurs in the case of TiAM6, which is consistent with results discussed below.

Peptide-modified surface

On the peptide-modified surface, GM6, no significant chemical shifts from TiAM6 were observed. The concentration of the newly introduced thiolether group is too low to be detected with confidence. The guanidinyl C 1s (289.0 eV) and amide C 1s (288.2 eV) overlap the imide and amide C 1s. Carboxyl, hydroxyl, and amide O 1s peaks at around 532 eV overlap Si-O and carbonyl O 1s. The guanidinyl (C=NH) N 1s at around 402 eV overlaps the protonated amines. However, the significant increase of the relative peak areas of N 1s, of O 1s above 532.0 eV, and of C 1s above 288.0 eV, as well as the decrease of the Ti 2p and Si 2p, are consistent with the presence of peptides.

Table 4-3   *XPS binding energies C 1s, N 1s, Ti 2p, and O 1s for the surfaces Ti, A, TiAM6, GM6 and the proposed assignments to surface functionalities.*

Surface	C 1s region E_B(eV), %, assignments	N 1s region E_B(eV),%,	Ti 2p region[2] E_B(eV), %, assignments	O 1s region E_B(eV), %,
Ti	284.6 (100) hydrocarbon[1]		453.3 (5) $2p_{3/2}$ Ti metal 458.5 (63) $2p_{3/2}$ TiO$_2$ 464.3 (32) $2p_{1/2}$ TiO$_2$	530.0 (84) TiO$_2$ 531.7 (16) OH
A	285.0 (72) C-C 286.4 (22) C-N 288.3 (6) C=O[1]	399.6 (75) NH$_2$ 401.7 (25) NH$_3^+$	453.3 (1) $2p_{3/2}$ Ti metal 458.5 (66) $2p_{3/2}$ TiO$_2$ 464.3 (33) $2p_{1/2}$ TiO$_2$	530.0 (58) TiO$_2$ 532.4 (42) SiO
TiAM6	285.1 (56) C-C 286.3 (26) C-N 288.2 (6) amide-C 289 (12) imide-C	399.6 (21) NH$_2$ 400.1 (25) amide-N 400.7 (30) imide-N 401.7 (24) NH$_3^+$	458.5 (67) $2p_{3/2}$ TiO$_2$ 464.3 (33) $2p_{1/2}$ TiO$_2$	530.0 (48) TiO$_2$ 532.4 (52) SiO, C=O
GM6	285.1 (51) C-C 286.3 (29) C-N, C-O 288.2 (9) amide-C 289.0 (11) imide-, carboxyl-, guanidinyl-C	399.6 (14) NH$_2$ 400.1 (39) amide-N 400.7 (26) imide-N 401.7 (21) NH$_3^+$, guanidinyl-N	458.5 (67) $2p_{3/2}$ TiO$_2$ 464.3 (33) $2p_{1/2}$ TiO$_2$	530.0 (45) TiO$_2$ 532.4 (55) SiO, C=O, COOH, C-OH

[1]Trace contamination. [2]The detailed deconvolution of Ti 2p to different titanium oxidation states; see ref [98].
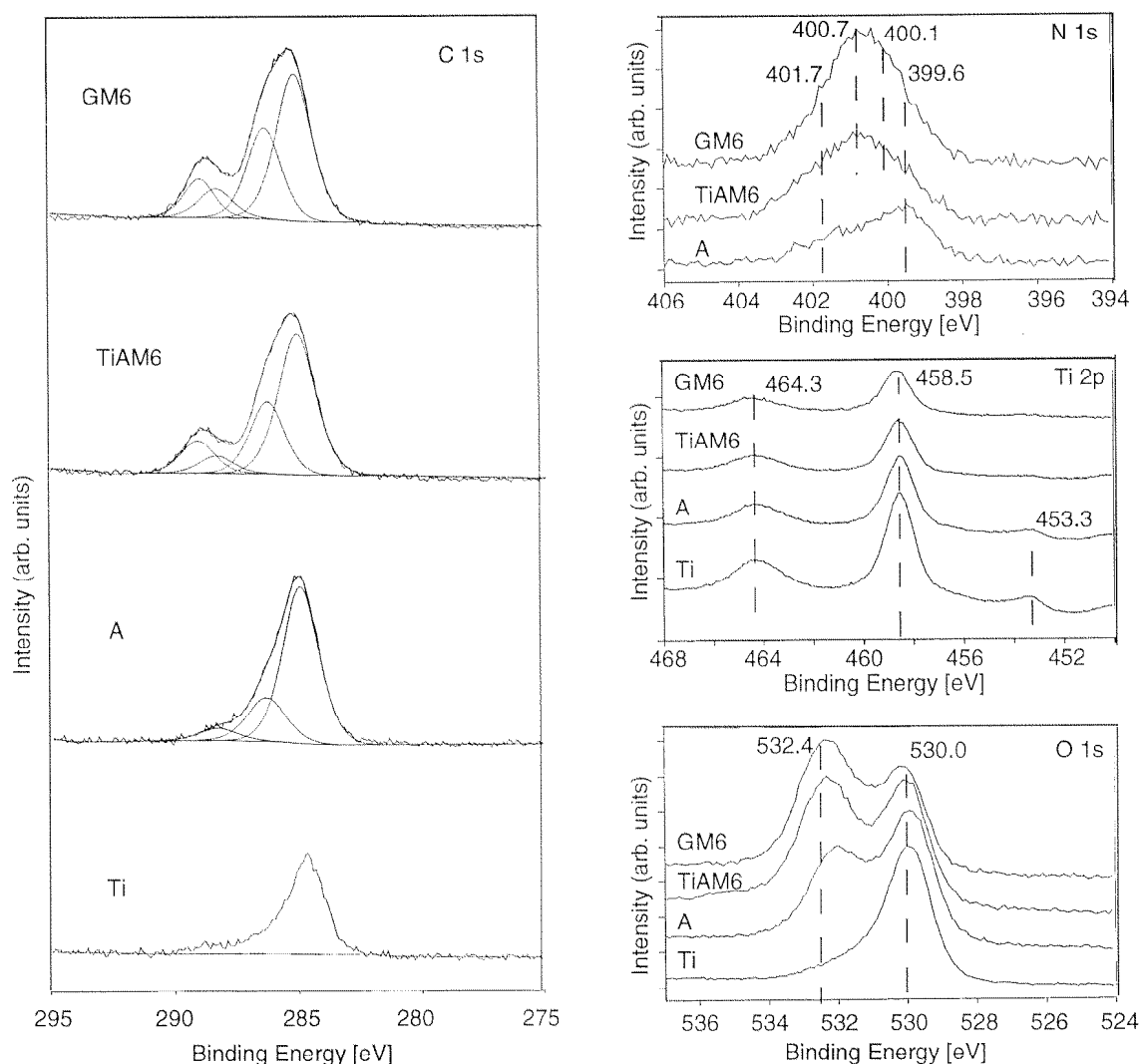
Figure 4-7   *Results of the XPS surface analysis: evolution of C 1s, N 1s, Ti 2p, and O 1s*
                   *spectra from **Ti** to **A**, TiAM6, and GM6. Abbreviations; see Section 4.2.2.*

4.3.4 Estimation of reaction yields

Atomic concentrations calculated from XPS intensities depend on the measured volume and the chemical components within this volume. Quantitative statements as regards reaction yields for the subsequent modification reactions are difficult because of the inevitable carbon contamination and oxygen content on the starting surface **Ti**, and the changes of the chemical components and the film thickness on different surfaces. Although the average atomic concentrations reflect the sequential reactions well, the above mentioned factors, as well as the usual quantitative error can result in a considerable deviation in the case of the low-concentration elements such as N and Si. Fortunately, silicon, which is not present on the starting surface, **Ti**, can be used as an internal reference. The absolute silicon surface content

from **A** through **P** remains constant. Since the whole organic surface layer thickness is below the information depth of XPS, the atomic ratio of N to Si is a more representative parameter than the atomic concentration to follow quantitative surface changes. The reaction yields can be deduced from the following simple formula:

Reaction yield (**A**→**M**) = (imide-N content on **M**) / (N content on **A**)

$$R_{A \to M} = \frac{n_{N(M)} - n_{N(A)}}{n_{N(A)}} = \frac{(N/Si)_M - (N/Si)_A}{(N/Si)_A} \tag{1}$$

Reaction yield (**M**→**P**) = [(peptide-N content on **P**)/m] / (imide-N content on **M**)

$$R_{M \to P} = \frac{\left(n_{N(P)} - n_{N(M)}\right)/m}{n_{N(M)} - n_{N(A)}} = \frac{\left[(N/Si)_P - (N/Si)_M\right]/m}{(N/Si)_M - (N/Si)_A} \tag{2}$$

where $R_{X \to Y}$ is the reaction yield from **X** to **Y**, $n_{N(i)}$ is the absolute nitrogen content of surface i, and $(N/Si)_i$ is the atomic ratio of N to Si on surface i. The divisor m takes account of the m nitrogen atom(s) in one peptide molecule (1 for cysteine, 7 for RGDC, and 10 for GRGDSPC).

The calculated reaction yields are summarized in Table 4-4. EMCS in the reaction **A** → TiAM6 shows the highest reaction yield among the 3 crosslinkers, suggesting the importance of steric hindrance. SMP has a short chain of 3 methylene groups between succinimidyl ester and maleimide, SMCC a bulky cyclohexane, while EMCS has a longer chain of 6 methylene groups. The former two have more rigid structures than the latter. One possible explanation is that EMCS, due to its molecular flexibility, has a higher probability of reaching partially occupied, reactive sites on the surface. Another factor could be the molecular organization on the surface: Because of the shorter spacer and molecular configuration, M3 and MC groups are bound close to the binding sites, leading to increased disorder on a macroscale, and occupying more space. Particularly in the valley areas, the steric hindrance from the occupied maleimidyl group could largely inhibit the accessibility of the surface. However, for the M6 group, the relatively longer spacer with its potential for greater interchain Van der Waals interactions may result in some long-range ordering.

For thioether formation, the molecular size seems to be the key factor affecting the reaction yields. This might be the reason for the high yield (up to 80%) for cysteine and the generally low yields (about 18%) for RGDC and GRGDSPC.

Table 4-4   *XPS atomic ratios N/Si for APS, maleimide, and peptide (or L-cysteine) modified surfaces and the reaction yields estimated using the formula (1) and (2) (see text in Section 4.3.4). Abbreviations; see Section 4.2.2.*

Surface	N/Si ($\pm$S.D.)	Reaction (X$\rightarrow$Y)	$R_{X \rightarrow Y}$ % ($\pm$calculated error)
A	0.70$\pm$0.02		
TiAM6	0.95$\pm$0.02	A $\rightarrow$ TiAM6	36$\pm$5
TiAM3	0.90$\pm$0.02	A $\rightarrow$ TiAM3	29$\pm$5
TiAMC	0.87$\pm$0.02	A $\rightarrow$ TiAMC	24$\pm$5
CM6	1.15$\pm$0.04	TiAM6 $\rightarrow$ CM6	80$\pm$20
CM3	1.05$\pm$0.04	TiAM3 $\rightarrow$ CM3	75$\pm$25
CMC	1.00$\pm$0.04	TiAMC $\rightarrow$ CMC	76$\pm$32
RM6	1.26$\pm$0.03	TiAM6 $\rightarrow$ RM6	15$\pm$3
RM3	1.15$\pm$0.04	TiAM3 $\rightarrow$ RM3	18$\pm$4
RMC	1.05$\pm$0.03	TiAMC $\rightarrow$ RMC	15$\pm$4
GM6	1.40$\pm$0.04	TiAM6 $\rightarrow$ GM6	18$\pm$3
GM3	1.26$\pm$0.03	TiAM3 $\rightarrow$ GM3	18$\pm$3
GMC	1.20$\pm$0.03	TiAMC $\rightarrow$ GMC	19$\pm$4

4.3.5 Surface coverage

Quantitative surface coverages were determined using radiolabeling techniques. $[^{14}C]$-Formaldehyde, $[^{35}S]$-cysteine, and $[^{14}C]$-phenylglyoxal were employed to measure the surface coverage of primary amine in **A**, maleimide in **M**, and peptide in **P**, respectively.

The surface coverages of maleimide and peptide were additionally estimated based on the radiolabeling-derived amine surface concentration on **A** and the XPS-derived reaction yields shown in Table 4-4. These data are in quite good agreement with the directly measured values (see Table 4-5).

4.3.5.1 $[^{14}C]$-Formaldehyde radiolabeling on silanized surfaces.

$[^{14}C]$-Formaldehyde with $NaBH_3CN$ has been used as a standard procedure to label the free amino groups of proteins.[105] The primary amine reacts first with formaldehyde to form a Schiff base, which is then reduced by $NaBH_3CN$ to the secondary amine. Although the

secondary amine can again react and form the tertiary amine, the stoichiometry of $[NH_2]/[H_2CO]$ can be fairly well controlled to 1 under appropriate reaction conditions. We carried out the reaction in CH_3CN solution at 20 ^0C for 4 h. It is assumed that the small formaldehyde molecule can diffuse into the open-structure APS film and react with all the primary amine groups. With these assumptions, the surface concentration (1.0 $nmol/cm^2$) and coverage (6.0 $group/nm^2$) of primary amines can be simply calculated from the specific radioactivity and the radiolabeled area. To exclude contributions from physically adsorbed ^{14}C labeled formaldehyde, the surfaces of Ti and acetylated A were used as controls (Figure 4-8). Only negligible amounts of about 1 nCi/cm^2 (0.02 $nmol/cm^2$) were detected in these cases.
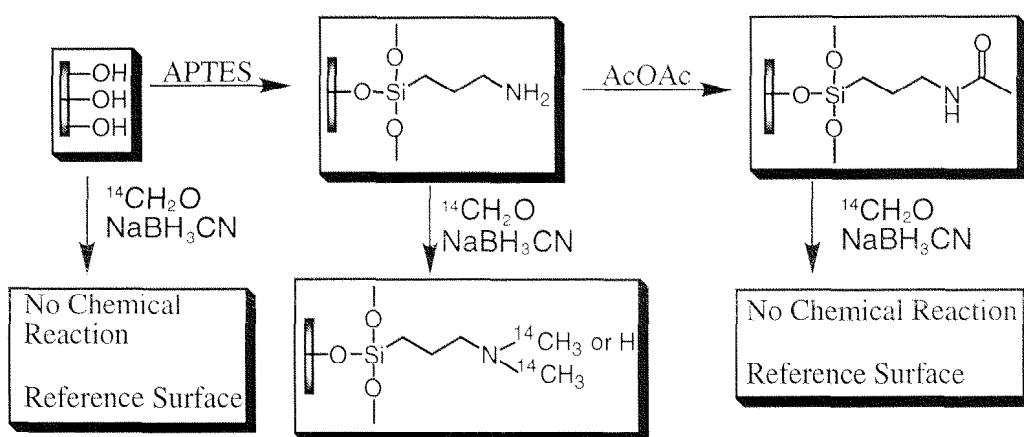

Figure 4-8   The radiolabeling reaction of $[^{14}C]$-formaldehyde with amino groups on the aminosilanized titanium surface: The products are ^{14}C labeled secondary and/or tertiary amines; the control surfaces of Ti and acetylated A have no chemical reactions with formaldehyde and therefore there are only negligible radioactivity counts.

4.3.5.2 $[^{35}S]$-Cysteine radiolabeling on maleimide-modified surfaces

$[^{35}S]$-Cysteine was chosen to label the maleimidyl groups because of two reasons: (1) to mimic the reaction of terminal cysteine on peptides with maleimidyl groups; (2) to evaluate the surface coverage and reactivity of maleimide since maleimidyl groups may hydrolyze to maleamic acid. A still open question is whether cysteine reacted completely with maleimide or not. The estimated reaction yields from XPS were used to calculate the maleimide coverage. The estimated surface coverages of maleimide are only semiquantitative, however, since the specific radioactivity is specified by the supplier as 20 to 150 mCi/mmol. Surface A and the unlabeled-cysteine-reacted surface M were used as the control surfaces (Figure 4-9). Only negligible amounts of around 1 nCi/cm^2 on control surfaces were detected and thus supported the covalent nature of the bond.
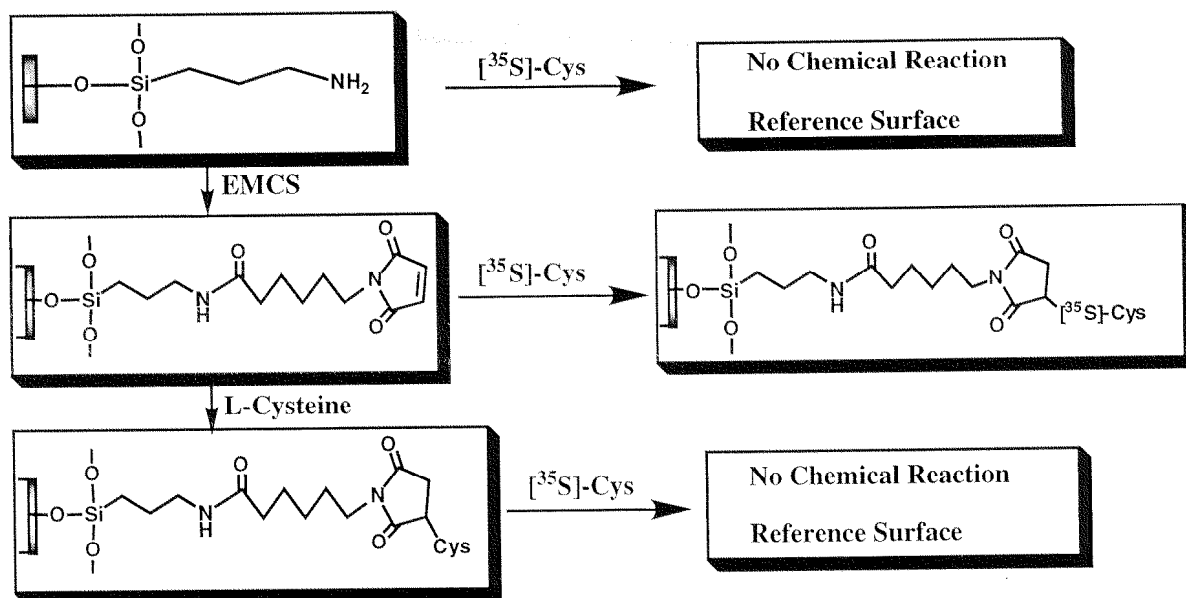
Figure 4-9   The radiolabeling reaction of [^{35}S]-cysteine with terminal maleimide. The control surfaces are **A** and unlabeled-cysteine-reacted **M**.

4.3.5.3 [^{14}C]-Phenylglyoxal radiolabeling on peptide-modified surfaces
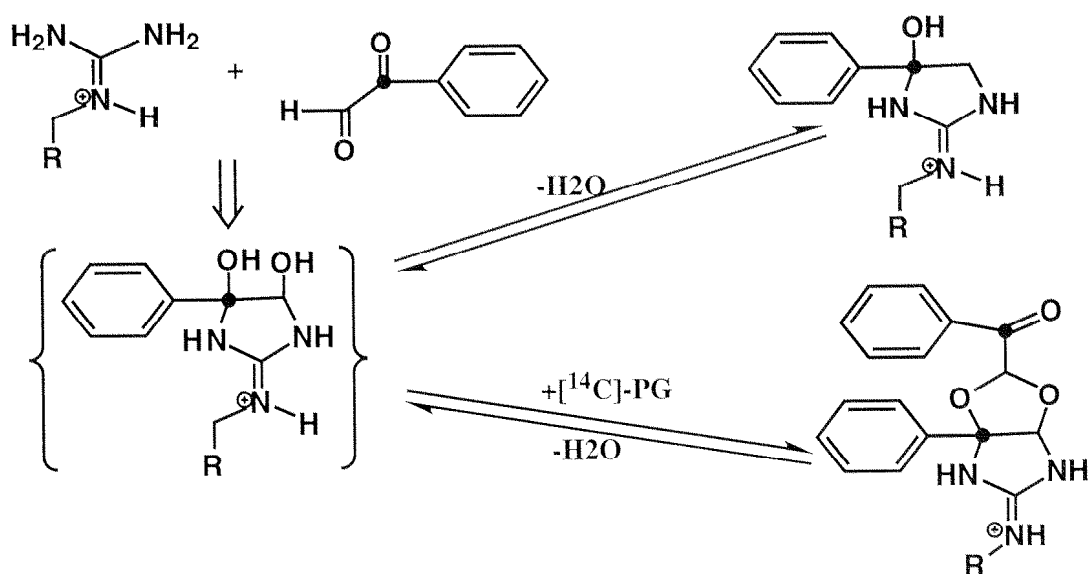
Figure 4-10   The radiolabeling reaction of [^{14}C]-phenylglyoxal with the guanidinyl group: Two adducts can be formed with a stoichiometric ratio (phenylglyoxal/guanidine) of 1 or 2.

A standard target reaction of the guanidinyl moiety of arginine residues is with 1,2-dicarbonyl reagents.[106] Under mild alkaline conditions, these compounds condense with the guanidinyl group in an initial reaction very similar to the Schiff base formation, which is followed by

further rearrangement to form different products. Arginine-containing peptides or proteins can form adducts with phenylglyoxal in a stoichiometric ratio (phenyglyoxal/arginine) of 1 or 2 (Figure 4-10) depending on the peptides or proteins involved, and the reaction conditions. Following a published procedure,[107] we carried out the reaction in 25 mM sodium phosphate buffer (pH 7.4) at 20 $^{\circ}$C for 24 h. A stoichiometry of 2 phenylglyoxal to 1 arginine is assumed here to calculate the peptide surface coverages. Both the direct radiolabeling measurements and the indirect calculation from the estimated reaction yields indicate surface coverages in the same range of 0.2~0.4 molecule/nm^2. According to a molecular modeling study, the minimum energy conformation of GRGDSPC (Figure 4-1) has dimensions of about 2x1 nm^2. Assuming equidistant attachment sites this would correspond to an average separation of 2.2 nm of GRGDSPC on surface GM6.

Table 4-5   *Surface concentrations and surface coverages of amino group on surface A, of maleimide group on surfaces TiAM6, TiAM3, and TiMC, of RGD group on surfaces RM6, RM3, RMC, GM6, GM3, and GMC.*

Surface	Radiolabeling Reagents	Radioactivity (nCi/cm^2±S.D.)	Surface Concentration[a] (nmol/cm^2±S.D.)	Surface Coverage[a] (group/nm^2±S.D.)	Calculated Surface Coverage[b] (group/nm^2)
A	[^{14}C]-FA	53.3±5.4	1.0±0.2	6.0±1.2	
TiAM6	[^{35}S]-Cys	8.2±1.0	0.05~0.77	0.4~4.6	2.2±0.5
TiAM3	[^{35}S]-Cys	6.3±0.8	0.04~0.71	0.2~4.3	1.7±0.5
TiAMC	[^{35}S]-Cys	5.6±0.7	0.03~0.72	0.2~4.3	1.4±0.4
RM6	[^{14}C]-PG	2.81±0.43	0.052±0.008	0.31±0.05	0.3±0.1
RM3	[^{14}C]-PG	2.17±0.37	0.040±0.007	0.24±0.04	0.3±0.1
RMC	[^{14}C]-PG	1.84±0.27	0.034±0.005	0.20±0.03	0.2±0.1
GM6	[^{14}C]-PG	3.27±0.48	0.061±0.009	0.37±0.05	0.4±0.1
GM3	[^{14}C]-PG	2.45±0.40	0.045±0.007	0.27±0.04	0.3±0.1
GMC	[^{14}C]-PG	2.33±0.32	0.043±0.006	0.26±0.04	0.3±0.1

[a] To calculate the surface concentration and coverage from the radioactivity, we assume the following molar ratios: [FA]/[NH$_2$]= 1, [Cysteine]/[Maleimide] = R$_{X \to Y}$ in Table 4-4 respectively, [PG]/[RGD] = 2 (see text in Section 4.3.5.3). The specific radioactivity of [^{14}C]-FA is 54.0 nCi/nmol, of [^{35}S]-Cys is between 20-150 nCi/nmol, and of [^{14}C]-PG is 27.0 nCi/nmol.

[b] The values are calculated by a combination of the NH$_2$ surface coverage on **A** and the reaction yields from Table 4-4. The errors correspond to calculated values.

4.3.6 Optimization of conjugation reactions

4.3.6.1 Surface A to surface M

The linkers serve two purposes: (1) to covalently bind two distinct chemical entities that otherwise would remain unreactive toward each other; (2) to provide a physical spacer allowing for greater accessibility and/or orientational freedom of the attached biomolecules.
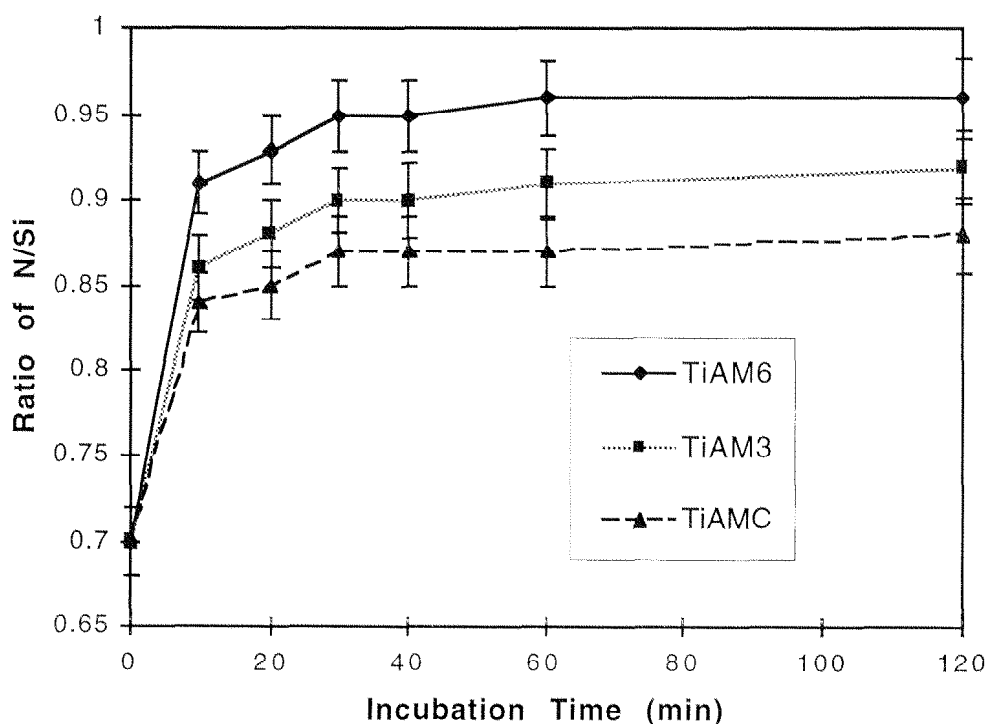

Figure 4-11 *The relationship between the atomic ratios N/Si (XPS) on the maleimide-modified surfaces and the incubation time.*

The succinimidyl ester reacts preferentially with amino groups, eliminating N-hydrosuccinimide as the leaving group. The reaction in aqueous solution is complete within 10 to 20 min at pH 6 to 9.[108] The competing reaction is the hydrolysis of the succinimidyl ester. The reaction was carried out in different solvents, e.g., aqueous buffer, N,N-dimethyl-formamide (DMF), dimethyl sulfoxide (DMSO), and acetonitrile. The highest yield was achieved in CH_3CN, while aqueous buffer is least suitable due to the low solubility of the crosslinkers and the hydrolysis of both the succinimidyl ester and the maleimide.

The effect of crosslinker concentration in the range of 1.0 mM to 10.0 mM was checked by XPS; no obvious differences were observed with a molar ratio of 2 crosslinkers to 1 primary amine. Thus, a 5.0 mM solution was used as the standard. All the experiments were carried out at 20 °C under ambient atmosphere. The main variable is the reaction time, which is an

important parameter, controlling both the extent of reaction and the surface uniformity. Figure 4-11 shows the relationship of the atomic ratio N/Si (XPS) with the incubation time. The reaction is very fast within the first 10 min, reaching its maximum after approximately 30 min.

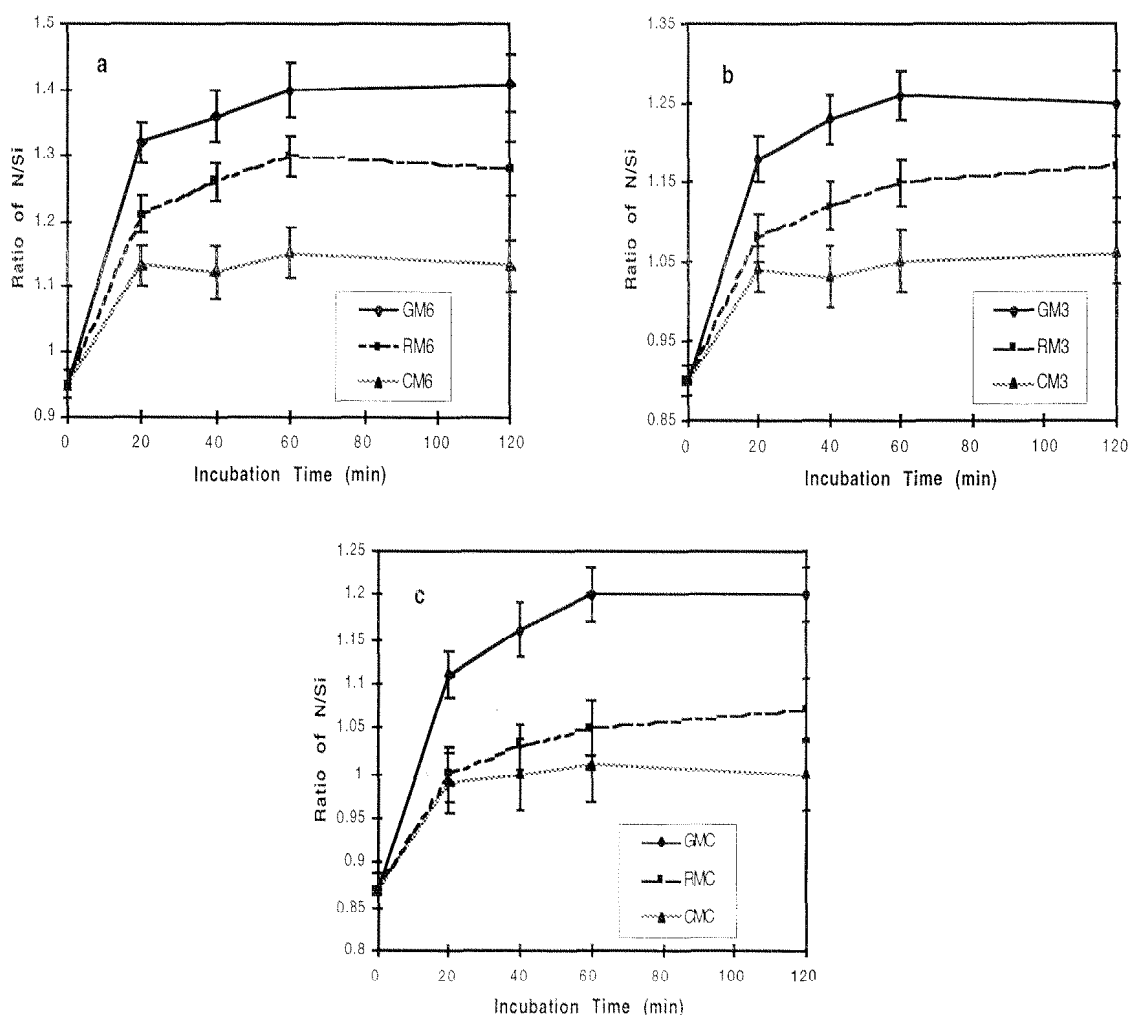## 4.3.6.2 Surface M to surface P

Figure 4-12   The dependence of the atomic ratios N/Si (XPS) of the peptide- or L-cysteine modified surfaces on the incubation time.

Maleimides are quite specific to the thiol group, especially at pH<7, where other nucleophiles are protonated. In acidic and near-neutral solutions, the reaction rate with simple thiols is about 1000-fold faster than with the corresponding simple amines.[109] The other major competing reaction is the hydrolysis of maleimide to maleamic acid. However, this reaction is much slower than the thiolether formation in near-neutral solutions. At pH 7, it is estimated that the half-life reaction time between millimolar concentrations of mercaptan and maleimide is of the order of one second.[109] The resulting thioether bond is very stable and cannot be

cleaved under physiological conditions. The peptide modification was carried out in aqueous solution. Samples treated in different concentrations and incubation times were evaluated by XPS. The effect of varying the peptide concentration in the range of 0.1 mM to 5 mM was not significant. Figure 4-12 shows the effect of incubation time on the atomic ratio N/Si (XPS). A sharp increase in the peptide surface concentration takes place in the first 20 min, followed by a slow increase. A reaction time of 1 h was chosen for the standard protocol. Although N/Si slowly increases with longer incubation time, this could be due to hydrolysis of siloxane films.

4.3.6.3 Degradation in water
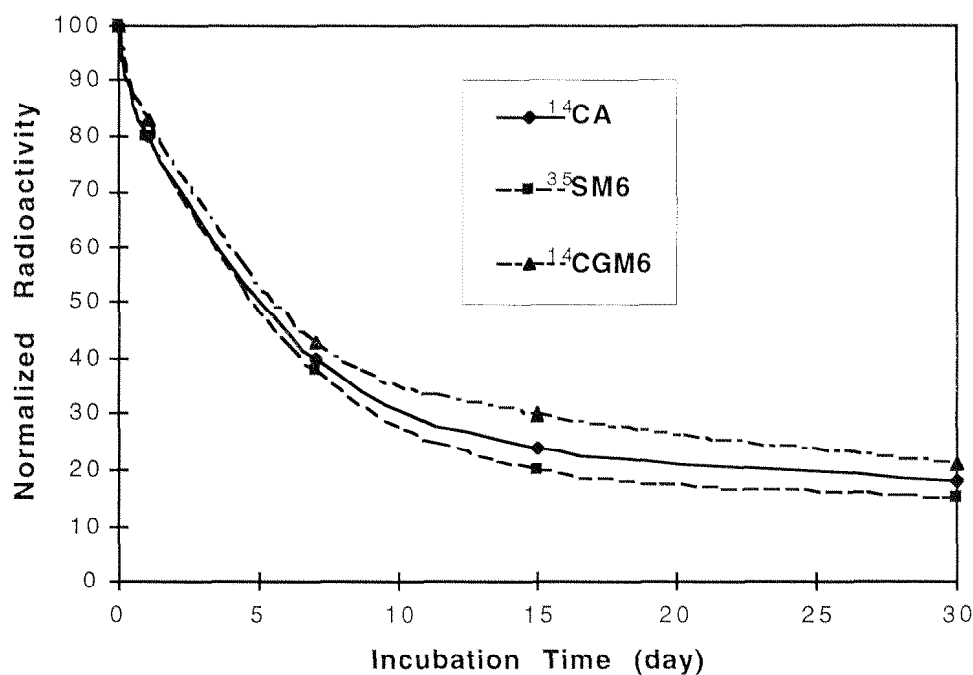
Figure 4-13   The degradation of ^{14}CA, $^{35}SM6$, and $^{14}CGM6$ in water measured through the loss of radioactivity. The data are normalized to the initial value.

A problem related to the application of immobilized biomolecules via silanization techniques is the bioactivity loss due to hydrolysis of the siloxane films. Degradation was followed by measuring the radioactivity loss of the radiolabeled samples immersed in water (Figure 4-13). Comparing degradation kinetics of the different surfaces, ^{14}CA, $^{35}SM6$, and $^{14}CGM6$, the main origin for the loss of peptide functionality appears to be the hydrolysis of siloxane films. A loss of about 50% occurs in the first week, followed by a gradual loss over several months.

4.3.7 Infrared reflection absorption spectroscopy measurements

Infrared reflection absorption spectroscopy (IRAS) has been thoroughly described.[54] It relies on reflecting an infrared beam at near-grazing incidence from the mirror-like metallic surface on which the thin film of interest has been deposited. Since the surface roughness of the modified samples is much smaller ($R_a \approx 1.7$ nm from AFM data) than the wavelength of the IR radiation, the electric field vector of the incident and reflected beams in our IRAS studies is expected to be along the normal of the surface plane. Hence, only the surface normal component of the dipole moment change can interact with the IR standing wave electric field at the surface, since the field vector and dipole moment derivative vector must be parallel. Thus, information on the orientation of the IRAS-active functional groups can be obtained.
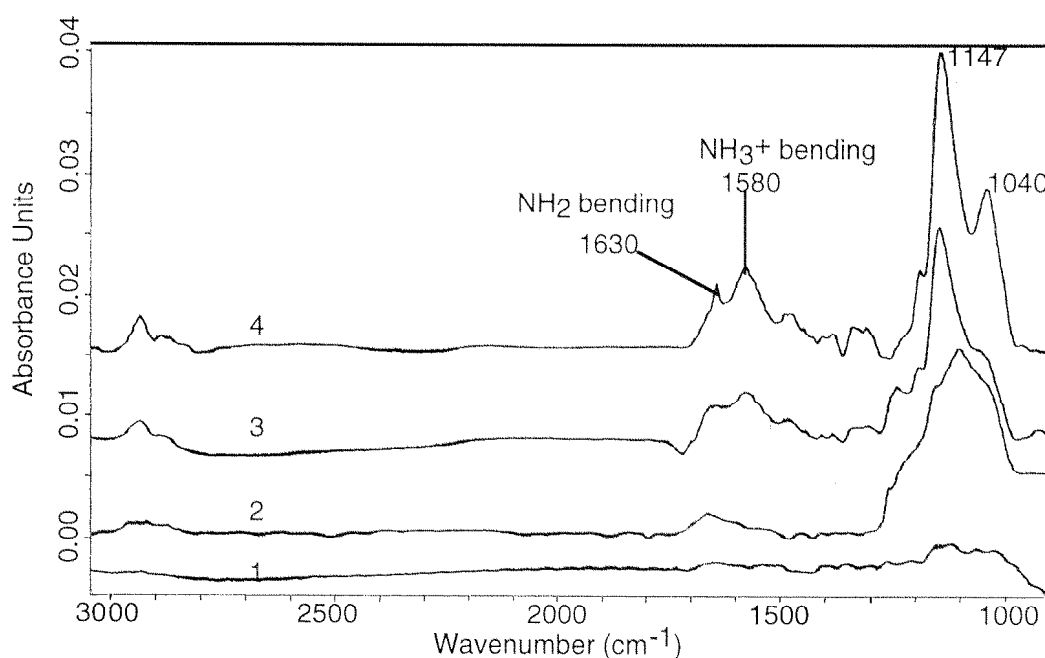

Figure 4-14   *Evolution of IRAS spectra of APS films on Ti surfaces with increasing the film thickness: Spectrum 1, 1~2 nm; spectra 2 and 3, 3~4 nm; spectrum 4, 5~6 nm.*

Different infrared techniques have been applied to study the APS structure on silica[27] and metal surfaces.[101] Generally, the broad strong bands occurring around 1150 cm^{-1} and 1040 cm^{-1} are due to the Si-O-Si and Si-O-C stretching modes, respectively. Absorption bands around 1600 cm^{-1} are caused by amine groups. Figure 4-14 shows the change of bands with increasing the APS film thickness. When the thickness is below ~2 nm, only the Si-O-Si and Si-O-C stretching bands between 1300 and 1000 cm^{-1} are visible. With increasing film thickness, the broad band in this region split into two sharp peaks, 1147 cm^{-1} of Si-O-Si asymmetric stretching and 1040 cm^{-1} of Si-O-C asymmetric stretching modes. The bending

bands of free amines and prontonated amines appear at 1630 and 1580 cm^{-1} respectively for thick APS films.
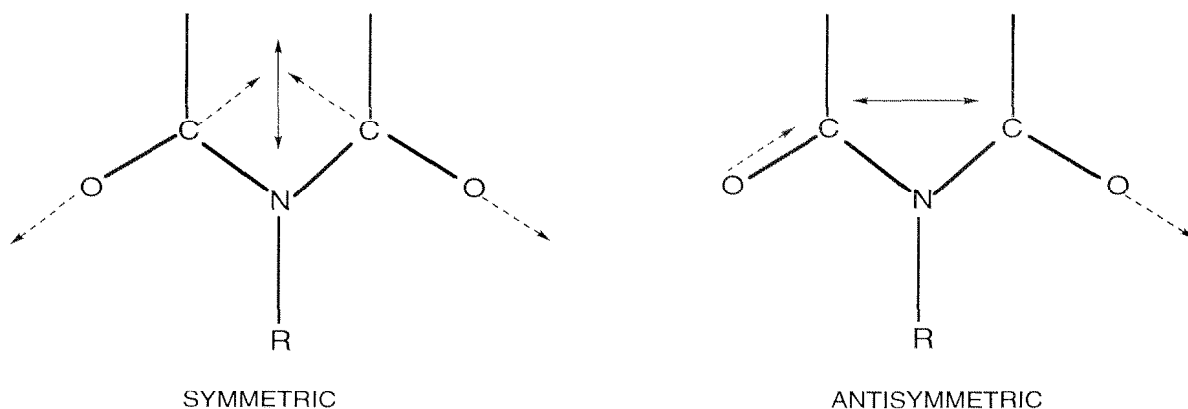

SYMMETRIC ANTISYMMETRIC

Figure 4-15 Symmetric and antisymmetric stretching vibrations of the imide moiety. Both-end-arrow lines represent the directions of the transition dipole moments.

The cyclic imide carbonyl groups in the crystalline state or in liquid solution exhibit at least two bands in the 1700-1800 cm^{-1} region.[110] One weak band is located between 1800 and 1740 cm^{-1} (symmetric stretch) and a more intense band between 1740 and 1700 cm^{-1} (antisymmetric stretch). The separation of the two bands is due to vibrational coupling of the carbonyls, leading to symmetric and antisymmetric stretching modes (Figure 4-15). Various explanations have been offered[110] for the symmetric and antisymmetric carbonyl stretch being assigned at the higher and lower frequency respectively. These explanations include mechanical coupling, hydrogen bonding, and electronic effects. The antisymmetric vibration of the O=C-N-C=O group alternatively stabilizes the two resonance structures with a positive coupling constant lowering the frequency of the antisymmetric vibration.

The imide absorption bands on maleimide-modified surfaces are shown in Figure 4-16. The antisymmetric vibration bands for TiAM3, TiAM4, and TiAMC surfaces are at 1711, 1709, and 1710 cm^{-1} respectively, while the symmetric one above 1740 cm^{-1} is barely detected, similar to the intensity distribution of polycrystalline maleimide derivatives with random orientation. However, on the TiAM6 surface, in addition to the antisymmetric vibration of the maleimidyl group at 1707 cm^{-1}, there are three further peaks at 1745 (strong), 1782 (weak), and 1818 (weak) cm^{-1}. As studied in the following chapter, 1745 and 1818 cm^{-1} are the asymmetric and symmetric succinimide stretching bands respectively, while 1782 cm^{-1} is due to the ester carbonyl stretch. That is to say, the reason for these differences is the presence of a succinimidyl ester byproduct on the surface. TiAM8 and TiAM11 always have the antisymmetric stretching bands at 1704 and 1709 cm^{-1} respectively, but the ester vibration bands appear occasionally as shoulder at ~1742 cm^{-1}.
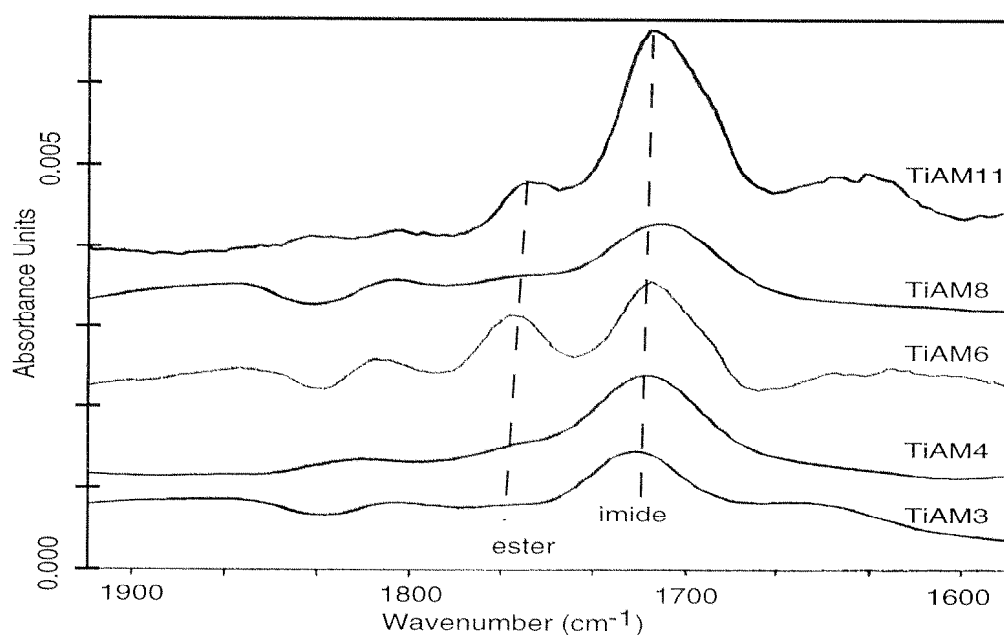
Figure 4-16   *IRAS spectra of TiAM3, TiAM4, TiAM6, TiAM8 and TiAM11 in the region of 1600-1900 cm^{-1}after subtraction of A. The asymmetric stretching band (~1710 cm^{-1}) of imide appear on all surfaces; the succinimidyl ester stretching bands, however, appear only on TiAM6 and TiAM11 surfaces.*

After the peptide attachment step, part of the maleimide is converted to succinimide as deduced from the XPS and radiolabeling measurements. Figure 4-16 shows the IRAS spectra of GM6 and TiAM6 in the region 1400~1800 cm^{-1}. The partial conversion can also be deduced from the appearance of the bands at 1707 and 1745 cm^{-1}, the imide and ester carbonyl group stretching bands. An obvious character on GM6 is the enhanced amide groups. Additional information can be gained in the amide vibration regions: amide I at around 1660 cm^{-1} and amide II at around 1540 cm^{-1} are the characteristic absorption bands for peptides and proteins. Although an amide group is already present on TiAM6 before coupling the peptides, the strong increase in intensity at 1665 cm^{-1} (amide I) and at 1536 cm^{-1} (amide II) on surface GM6 reflects the increased number of amide functionalities.
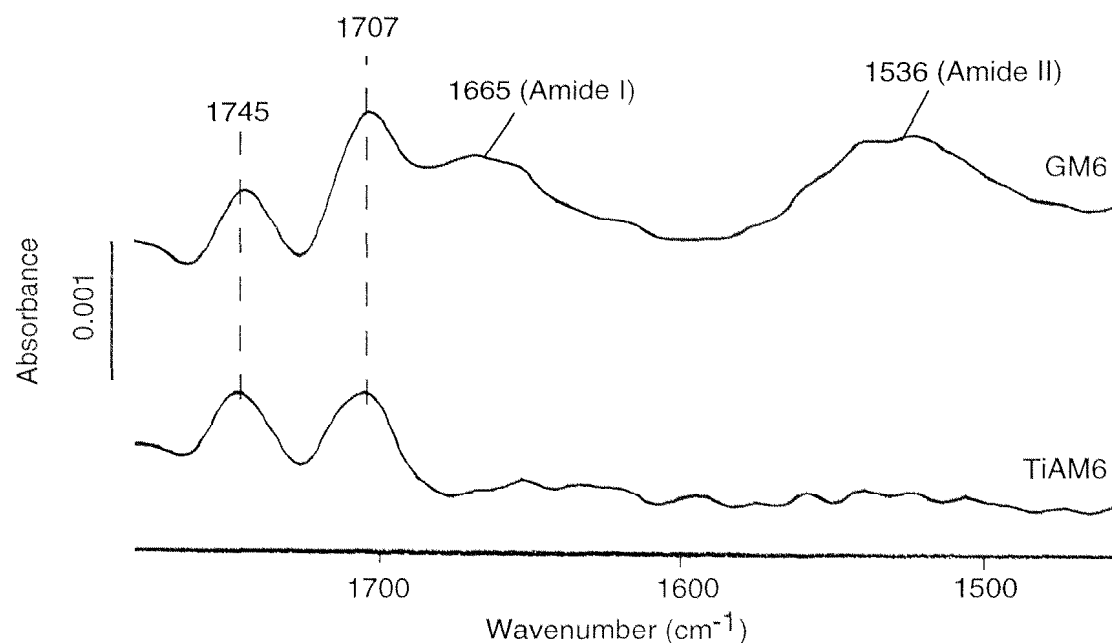
Figure 4-17   IRAS spectra of TiAM6 and GM6. The obvious amide I and II peaks on the GM6 surface confirm the covalently bound peptide GRGDSPC.

4.3.8 Time-of-flight secondary ion mass spectroscopy measurements

ToF-SIMS is particularly appropriate to study ultrathin organic films by virtue of its high surface sensitivity, its capability to detect all elements and isotopes, and because it provides molecular structural information on organic materials. The ToF-SIMS technique allows detailed fingerprinting of ultrathin organic films because of its much higher mass resolution and mass range. The former aspect enables a more accurate peak identification, and the latter is very useful for the detection of crosslinking and condensation reactions.

APS- and maleimide-modified surfaces

The APS films on oxide surfaces contain partial polymer net structures of $(Si-O)_n$ and partial monomer structures. The positive fragments are listed in Table 4-6. An interpretation of the spectra leads to the following conclusions:

- Higher yields of Si- and Si-O-containing ions are observed, such as those at +28, +62, and +102 amu.

- Many fragments contain nitrogen and they appear at +59, +72, +91, +102, +105, and +113 amu.

- The intensity of Ti at +48 amu decreases with the increase of APS film thickness.

Table 4-6   Fragments of thin APS films on Ti surfaces (positive).

m/z	Composition	Error (ppm)	Rel. intensity (%)
+27	$C_2H_3^+$	+13	24.94
+28	Si^+	+4	7.22
+29	$C_2H_5^+$	-23	22.96
+39	$C_3H_3^+$	-3	17.67
+41	$C_3H_5^+$	-6	51.95
+43	$C_3H_7^+$	-33	31.30
+48	Ti^+	+35	100
+55	$C_4H_7^+$	-41	32.89
+57	$C_4H_9^+$	-64	11.53
+59	$C_2H_5NO^+$	-68	3.71
+62	SiO_2^+	+43	5.16
+67	$C_5H_7^+$	-52	11.86
+72	$C_3H_6NO^+$	-56	3.93
+91	$CH_7N_4O^+$	+38	3.15
+102	$C_2H_4NSiO_2^+$	+64	0.81
+105	$CHN_2O_4^+$	+89	1.03
+113	$C_3HN_2O_3^+$	+87	1.30

The ToF-SIMS spectra of maleimide-modified surfaces give the evidence for maleimidyl group (m/z) at -96 amu, although TiO_3^- is also present at -96 amu. The two peaks at -96 amu are due to the maleimide fragment ($C_4H_2NO_2^-$) and TiO_3^-. The high CNO^- (m/z: 42) counts, not detected on APS films, also indicate the existence of the maleimide group.

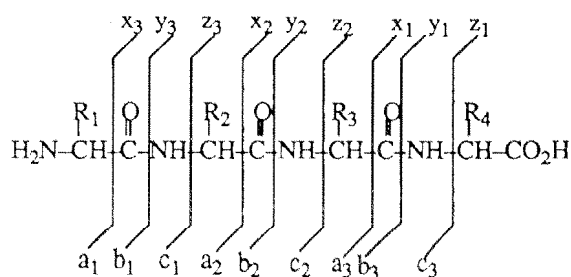*Table 4-7*   *Secondary ion fragments of TiAM3 (negative spectrum).*

m/z	Composition	Error (ppm)	Rel. intensity (%)
-16	O^-	+313	100
-26	CN^-	+33	25.94
-32	O_2^-	+60	0.75
-38	$C_3H_2^-$	-11	0.79
-40	C_2O^-	+4	0.41
-40	$C_2H_2N^-$	+81	0.47
-41	C_2OH^-	+45	2.13
-42	CNO^-	+49	15.80
-43	$C_2H_3O^-$	+60	0.93
-45	CHO_2^-	-35	3.07
-60	SiO_2^-	+20	0.72
-61	$SiOH_2^-$	+1	0.73
-80	$TiONH_2^-$	+41	1.56
-96	TiO_3^-	+197	0.34
-96	$C_4H_2NO_2^-$	+7	0.37
-97	TiO_3H^-	+148	0.89
-137	$HSi_2O_4NH_2^-$	+220	0.15

Peptide-modified surfaces

To assign the peptide fragments, we adopt the basic nomenclature for mass spectral peptide sequence ions proposed by Roepstorff and Fohlma.[111] There are six main types of cleavage of the amide backbone (a, b, c, x, y, z) of a linear peptide ion (Table 4-8), each of which may or may not be accompanied by hydrogen rearrangement, and each of these cleavages can give rise to a series of peaks whose adjacent members differ in mass by that of an amino acid residue. In addition, there are three sidechain fragmentations (d, v, w) and three nonspecific sequence-type fragmentations.

Table 4-8   *Common types of fragment ions arising from linear peptides.*

$$\begin{array}{cccccccccc}
& x_3 & y_3 & z_3 & x_2 & y_2 & z_2 & x_1 & y_1 & z_1 \\
\end{array}$$

$$\begin{matrix}
& R_1 & O & & R_2 & O & & R_3 & O & & R_4 \\
H_2N{-}CH{-}C{-}NH{-}CH{-}C{-}NH{-}CH{-}C{-}NH{-}CH{-}CO_2H
\end{matrix}$$

$$\begin{array}{ccccccccc}
a_1 & b_1 & c_1 & a_2 & b_2 & c_2 & a_3 & b_3 & c_3
\end{array}$$

Name	Type of cleavage	Terminal contained	Assumed structure
a_n	Backbone	N	$H\,(NHCHRCO)_{n-1}\,\overset{+}{N}H{=}CHR$
b_n	Backbone	N	$H\,(NHCHRCO)_{n-1}\,NH{-}CHR{-}\overset{+}{C}{\equiv}O$
$c_n{+}2$	Backbone	N	$[H\,(NHCHRCO)_n\,NH_2]H^+$
x_n	Backbone	C	$\overset{+}{O}{\equiv}C\,(NHCHRCO)_n\,OH$
$y_n{+}2$	Backbone	C	$[H\,(NHCHRCO)_n\,OH]\,H^+$
$z_n{+}1$	Backbone	C	$[CHR{-}CO\,(NHCHRCO)_{n-1}\,OH]\,H^+$
d_n	Sidechain	N	$[H\,(NHCHRCO)_{n-1}\,NH{-}CH{=}CHR']H^+$
v_n	Sidechain	C	$[HN{=}CH{-}CO\,(NHCHRCO)_{n-1}\,OH]\,H^+$
w_n	Sidechain	C	$[R'CH{=}CH{-}CO\,(NHCHRCO)_{n-1}\,OH]\,H^+$
Internal acyl	Backbone	Neither	$H\,(NHCHRCO)_{n-1}\,NH{-}CHR{-}C{\equiv}O^+$
Internal immonium	Backbone	Neither	$H\,(NHCHRCO)_{n-1}{-}\overset{+}{N}H{=}CHR$
Amino acid immonium	Backbone	N(a1), C or neither	$H_2\overset{+}{N}{=}CHR$

Note: R and R' represent a sidechain and the β-substitutent of a sidechain, respectively.

In our case, the possible fragments from the RGDC-modified Ti surface (RM6) can be cleaved as in Figure 4-18. The fragments of RGDC can be assigned in Table 4-9 according to Figure 4-18.
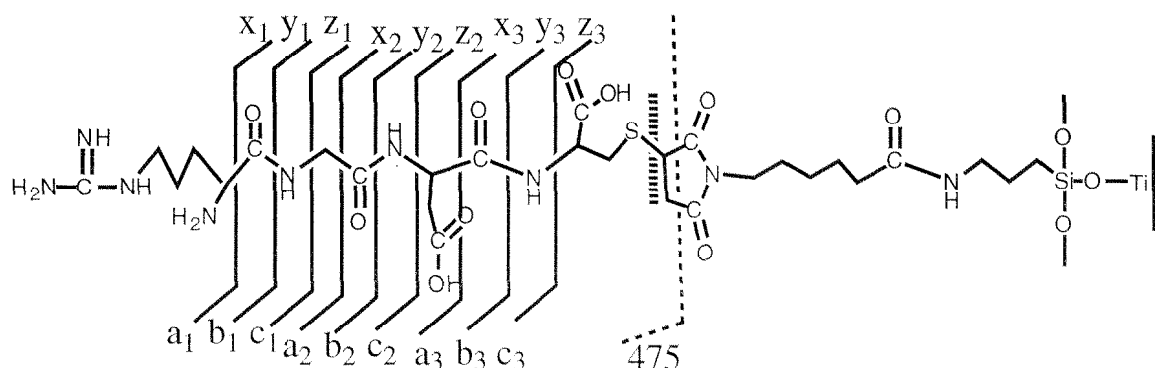
Figure 4-18   Cleavage of the grafted RGDC on Ti surfaces (surface RM6) according to Table 4-8.

Table 4-9   Fragment assignments of the positive ToF-SIMS spectrum of RM6.

m/z	Fragments	m/z	Fragments
+475	$RGDC-1+CHCH_2$	+253	a_3-3-COOH
+461	RGDC-1+CH	+242	a_3-CH_2COOH / or d_3
+447	RGDC-2	+241	a_3-1-CH_2COOH / or d_3-1
+429	$RGDC-2-H_2O$	+239	a_3-3-CH_2COOH / or d_3-3
+417	RGDC-SH	+221	z_2+1
+413	$RGDC-2H_2O$	+219	y_2+2-H_2O
+401	$RGDC-S-NH_2$	+211	c_2-1-NH_3
+326	c_3-H_2O	+155	c_1+1-H_2O
+313	b_3-NH_3	+149	x_1+1
+300	a_3-1	+147	x_1-1
+299	a_3-2	+141	b_2+3-NH_3
+281	a_3-2-H_2O		

The fragment analysis leads to the following conclusions:

- The thioether bond between RGDC and maleimide is confirmed by the fragments at +461 and +475 amu which contain the C-S-C group (Figure 4-18).

- The molecular weight of RGDC is 449. However a fragment at +447 amu is observed instead of the molecular ion mass. This may be due to the hydrogen rearrangement and loss.

- Most of the fragments are a types and include some b, c, x, y, and z types. Many fragments have hydrogen loss and neutral loss of NH_3 or H_2O.
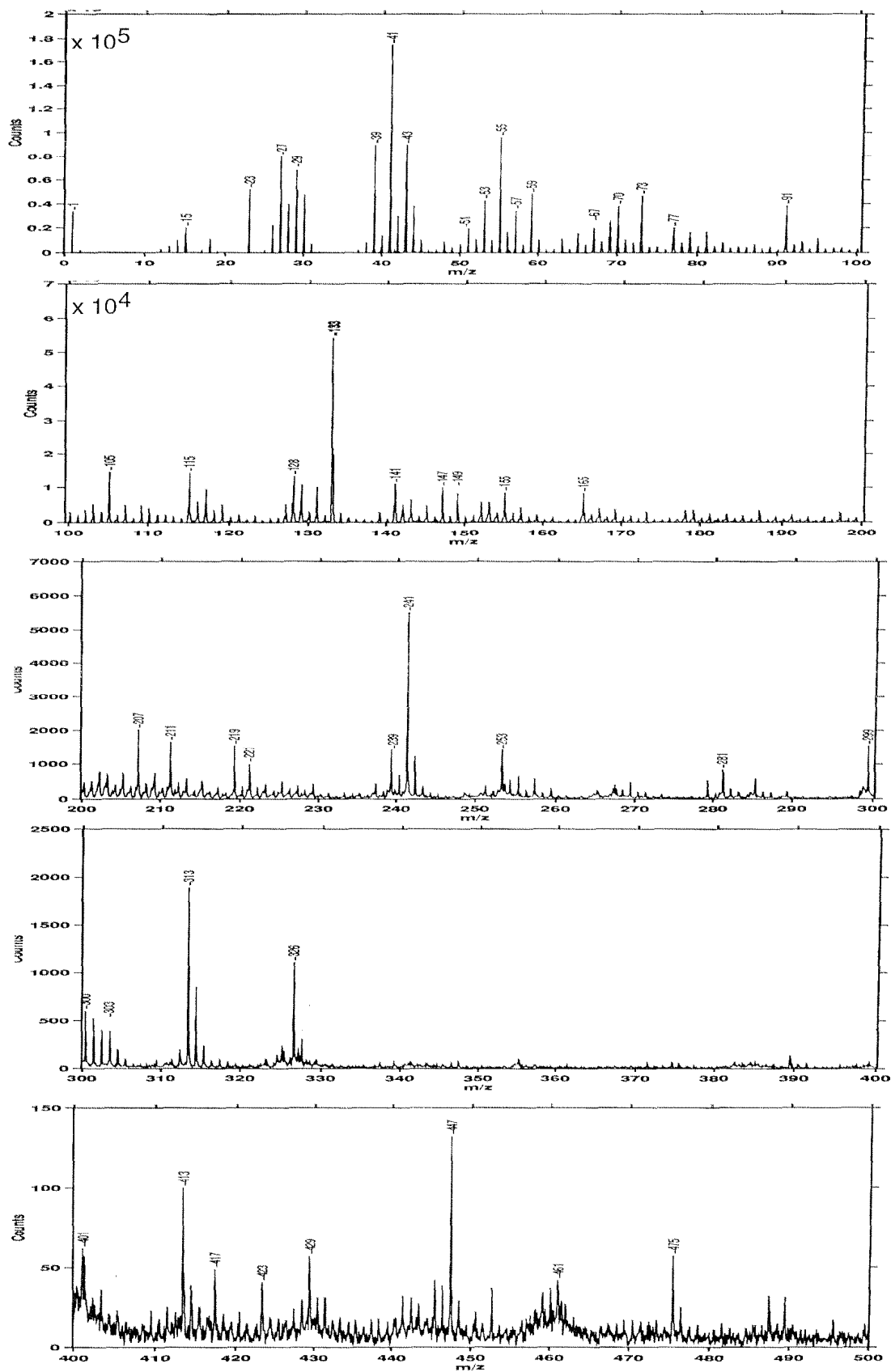
Figure 4-19   The positive ToF-SIMS spectrum of RM6.

The molecular ion mass of GRGDSPC (690.7) was not detected on GM6. The meaningful fragments are shown in Figure 4-20 and listed in Table 4-10. The significant difference from RGDC is the strong fragment at +243 amu which comes from the GRG sequence.

Table 4-10 Some ToF-SIMS fragment assignments for the major peaks in the positive spectrum of GM6.

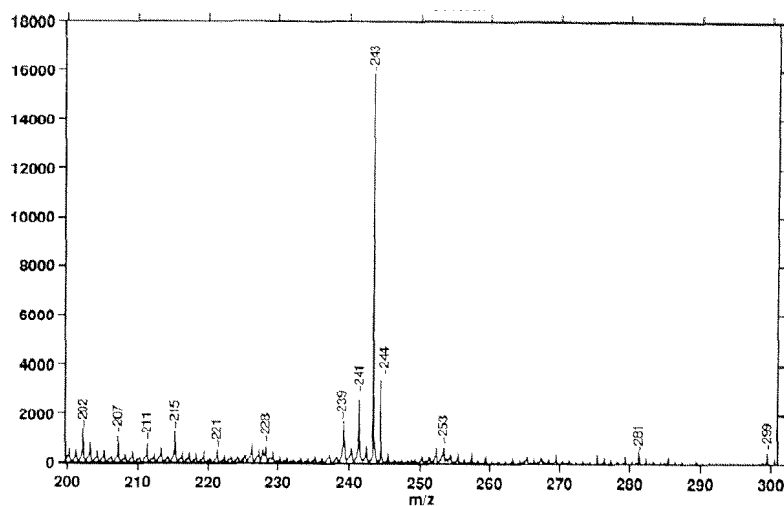| m/z	Fragments	m/z	Fragments
+341	a_4+1-H_2O	+252	b_3-1-H_2O
+327	?	+244	a_3+1
+325	?	+243	a_3
+314	a_4-CO_2	+241	a_3-2
+313	a_4-1-CO_2	+239	a_3-4
+303	y_3-1	+228	c_2-1
+302	y_3-2	+221	?
+301	y_3-3	+215	b_2+1
+299	y_3-5	+211	c_2-H_2O
+281	?	+207	?
+253	b_3-H_2O	+202	z_2

Figure 4-20 ToF-SIMS spectra of GM6 in the region of 200 to 300 amu.

4.3.9 Cell culture tests

This work was performed in cooperation with Prof. Dr. E. Wintermantel's group (chair of biocompatible materials science and engineering, ETHZ), particularly with Ms. Viola Schlosser and Dr. Arend Bruinink.

The objective of the work is to study the effect of RGD-containing-peptide-modified Ti surfaces on the proliferation and differentiation of bone cells. Another aim is to compare the performance of cells of the osteoblastic cell line MC3T3-E1 with those of adult primary rat bone marrow cells (RBM). The MC3T3 cell line is taken since it is one of the most commonly used cell lines in studies related to load-bearing implants and bone diseases. RBM are used here since most bone replacement materials are implanted in an adult bone and therefore are in direct contact with bone marrow. Characterization of the effect on both types of cell cultures enables us: (a) to compare our data with existing literature based on both types of cultures and (b) to define a platform on which data of osteoblastic cell lines and those of primary cell cultures can be compared. The latter platform will help to clarify those processes taking place at bone implant surfaces that discriminate optimal osteogenic from moderate osteogenic implant surfaces.

Bone tissue formation depends on the generation of adequate cellular signals that reduce the degree of encapsulation by fibroblasts and dedifferentiated bone cells and shift the balance between bone formation and resorption towards bone formation. The cell type responsible for bone resorption is the osteoclast and for bone formation is the osteoblast cell. The osteoclast activity can be characterized by determining Tartrate Resistant Acidic Phosphatase (TRAP), and the osteoblast function (differentiation activity) can be characterized by assaying Alkaline Phosphatase (ALP) activity.

4.3.9.1 Materials and methods

Cells

Two kinds of cells, an embryonic mouse calvarial osteoblast-like cell line (MC3T3-E1) and primary rat bone marrow cells (RBM) were used for cell-culture testing.

Cloned osteoblast-like MC3T3-E1 cells derived from new born mouse calvaria were maintained in α-Minimum Essential Medium (α-MEM, Gibco, Basel, Switzerland) containing 10% heat-inactivated fetal calf serum (FCS) at 5% CO_2/95% air. MC3T3-E1 cells were subcultured until passage numbers of 25-30 in PSN(antibiotics cocktail)-free culture medium (α-MEM). Cells were harvested by trypsinization (Trypsin-EDTA solution, Gibco, Basel,

Switzerland), counted by using a Coulter Counter (Coulter® Z1, Coulter Electronics Ltd., Luton, Beds., USA), and cooled in ice until use.

The RBM cells were freshly isolated from femoral and tibial bone of adult male Wistar rats. Tibiae and femora after removal of the periosteum were dissected longitudinally and bone marrow was collected using a scalpel. The bone marrow was resuspended in phosphate buffered saline (PBS, pH 7.4), supplemented with 10% antibiotics (PSN antibiotic mixture, Gibco, Basel, Switzerland, consisting of 5 mg/ml penicillin, 5 mg/ml streptomycin, 1 mg/ml Neomycin). This cell suspension was filtered through a 200 µm mesh nylon filter to remove bone fragments and coagula. After centrifugation of 60 g at 4° C for 10 minutes, the cell pellet was resuspended in culture medium (α-MEM), supplemented with 10% heat inactivated fetal calf serum and 1% PSN.

Cell Cultivation

The bare Ti coatings (diameter: 15 mm) were used as controls. The biofunctionalized titanium samples, **A**, CM6, RM6, and GM6 were used for cell culture tests. They were immersed with 400 µl 70% ethanol per well in a 24-well plate. One milliliter containing 500'000 RBM or 40'000 MC3T3-E1 cells were added to each sample. Medium was exchanged at day 2 and 5 (MC3T3-E1) and at day 5 and 11 (RBM) after seeding. Cultures were kept at 37°C, in a humidified 5% CO_2 atmosphere. After 7 (MC3T3-E1) and 14 (RBM) days *in vitro* cultivation, the cells were analyzed morphologically by SEM and biochemically (ALP activity, DNA content, total protein content). Morphological effects were determined by scanning electron microscopic analysis. Basal cell functions were estimated by measuring culture well protein content (Pierce BCA assay) and mitochondrial activity (MTT-dehydrogenase activity).[112] Cell proliferation was estimated by measuring cell culture DNA content (Sigma Hoechst assay). Degree of differentiation was assessed by determining ALP activity.[113]

4.3.9.2 Cell compatibility of biofunctionalized surfaces

MC3T3-E1 cell culture results

Surfaces **Ti**, **A** (with 1.0 nmol/cm^2 NH$_2$ groups), RM6 (with 0.05 nmol/cm^2 RGD), and GM6 (with 0.06 nmol/cm^2 RGD) were tested with MC3T3-E1 cells *in vitro*. Three independent group samples were tested. Three parameters, DNA, ALP/DNA, and Protein/DNA, are used for cell assays. Each cell has a definite quantity of DNA; therefore the DNA value represents the total number of cells. ALP/DNA is a parameter for evaluation of the cell differentiation. The ratio Protein/DNA represents the cell size. Figure 4-21 shows the cell culture results after 7 days incubation. Compared to the reference sample **Ti**, the cell number (DNA) on the modified surfaces (**A**, RM6, and GM6) decreases, the cell size (Protein/DNA)

increases, and the cell differentiation (ALP/DNA) significantly increases. However, APS modified surfaces with exposed amino groups seem to be the best surface for cells. Although cells are affected by some specific peptide sequences like RGD, they are also sensitive to physicochemical properties of the substratum surface such as surface charge, surface energy, and surface morphology. APS-modified surfaces have densely distributed amino groups with positive charges. The positive charges are believed to be the main factor for regulating the cell behavior on **A**.
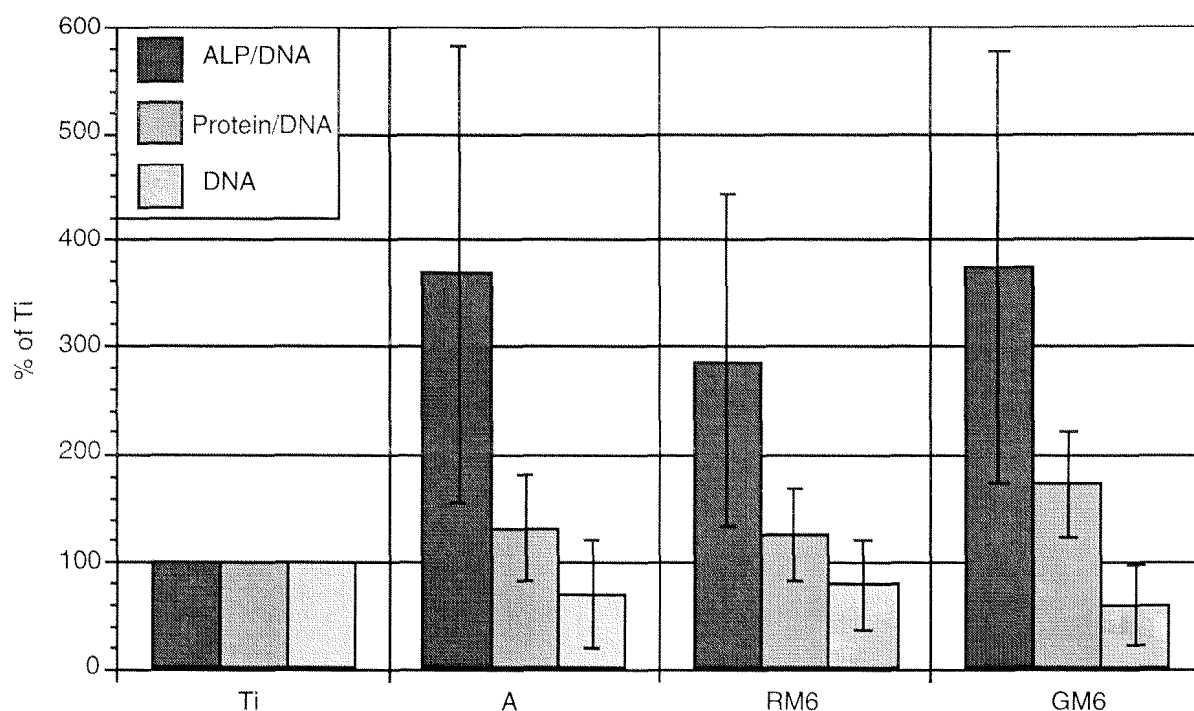

Figure 4-21   MC3T3-E1 cells cultivated in vitro for 7 days. Compared to the reference sample Ti, the cell number (DNA) of modified surfaces (A, RM6, and GM6) decreases, the cell size (Protein/DNA) increases, and the cell differentiation (ALP/DNA) significantly increases. Standard Errors of the Mean are represented as error bars.

Figure 4-22 shows the cell morphologies on **Ti, A, RM6,** and GM6 after 7 days incubation. On the reference sample **Ti**, cells are smaller (~80x30 μm^2) and densely packed. They have three-dimensional structures rather than two-dimensional structures, and are arranged longitudinally. These indicate the relatively higher proliferation. On the aminosilanized surface **A**, the cells are significantly bigger (the biggest one in the graph is 300x500 μm^2) and flatter, and their shapes are irregularly round. There are more gaps among the cells. The cell morphologies on GM6 are similar to **A**; however, there are less holes in one cell (or in other words, the individual cell organizes itself perfectly). On RM6, the cell density is higher than on **A** and GM6, but lower than on **Ti**. The cell growth direction is in a semicircle rather than like a linear line. As demonstrated in Section 4.3.5, the surface coverages of RGDC and

GRGDSPC are 0.3 and 0.4 molecules/nm^2. Considering the average cell size on GM6 300x500 μm^2, then one cell can cover 6×10^{10} GRGDSPC groups. This value should be enough for regulating the cell activities.
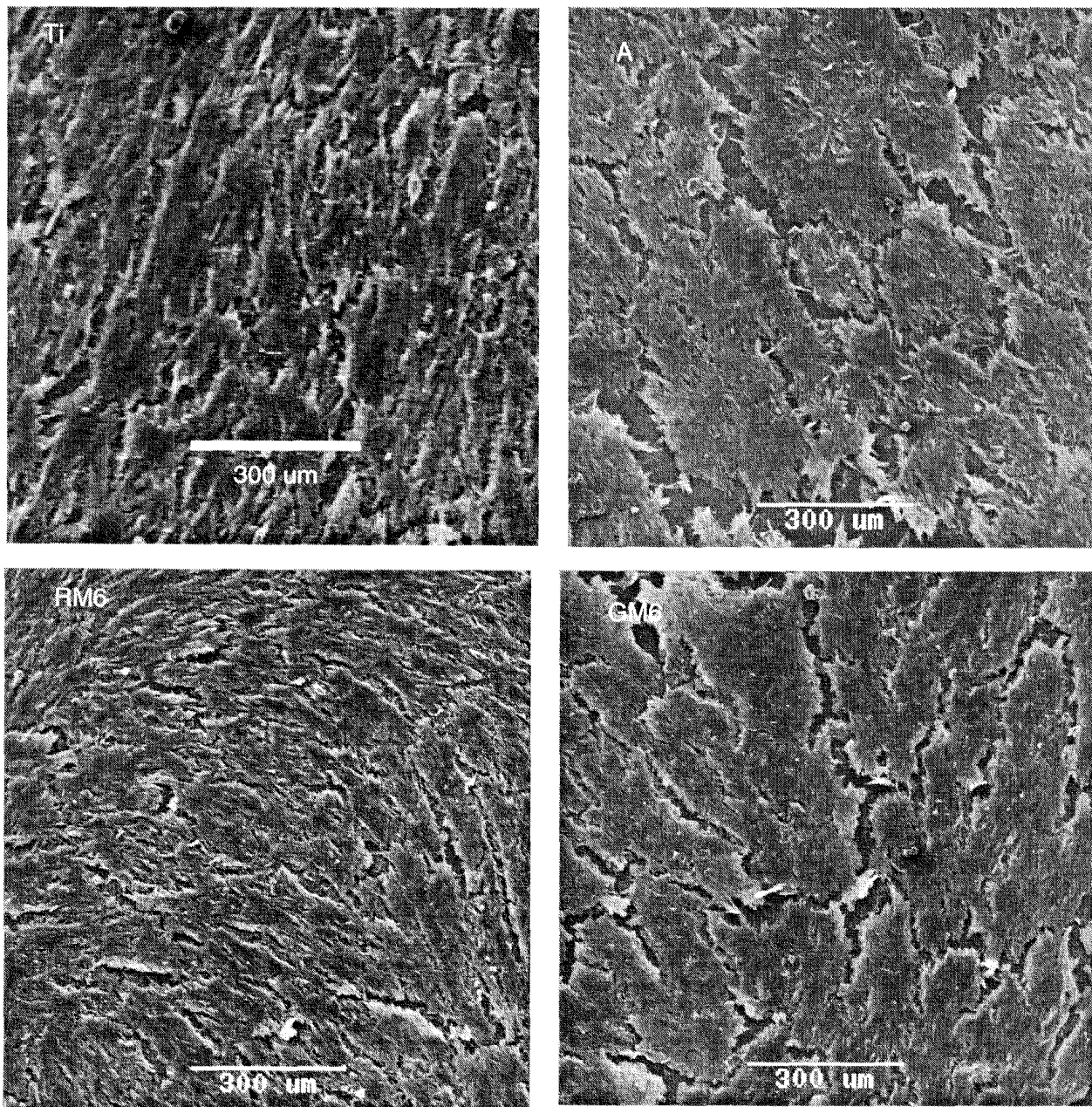

Figure 4-22   *MC3T3-E1 cell morphologies on surfaces **Ti**, **A**, RM6, and GM6 imaged by Scanning Electron Microscopy (SEM). It is obvious that the cells are smaller on **Ti** and form three dimensional structures, and they are much larger and form monolayers on **A**, RM6, and GM6. The cell boundaries and connections are quite different on each of the four samples.*

Preliminary RBM cell culture results

For the RBM cell culture, surfaces **Ti**, **A**, CM6, RM6 (0.05 nmol/cm^2), RM6(l) (0.01 nmol/cm^2), GM6 (0.06 nmol/cm^2), and GM6(l) (0.01 nmol/cm^2) were tested (Figure 4-23). Besides the two parameters ALP/DNA and Protein/DNA, a new parameter TRAP/DNA is used to evaluate the osteoclast activity (or the resorption of the bone remodeling). Unfortunately, the RGD-modified surfaces (whether RM6 or GM6) induced a significant decrease in cell differentiation (ALP/DNA and TRAP/DNA) and nearly had no effect on cell proliferation (Protein/DNA), compared to the reference sample **Ti**. Furthermore, no big difference of the cell activities was observed between the higher and lower surface coverages of RM6 and GM6. On the contrary, the aminosilanized surface **A** showed positive effect on cell differentiation and proliferation, and the cysteine-modified surface CM6 nearly had no effect on the cell behavior. This research is still in progress.

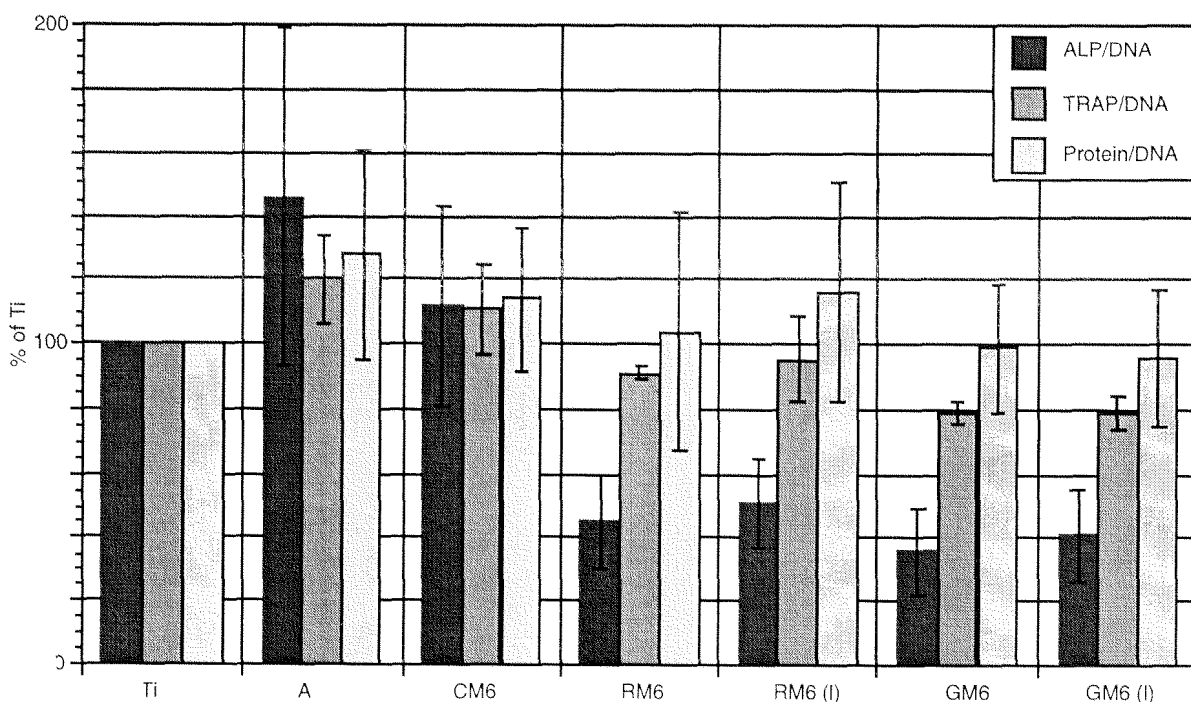*Figure 4-23*   *Rat bone marrow cells cultivated for 14 days. Compared to the reference sample **Ti**, surface **A** shows the increase of cell differentiation and size, but RM6 and GM6 (whether higher or lower density) show the significant decrease of cell differentiation. RM6(l) and GM6(l) represent the lower surface coverages of RM6 and GM6. Standard Errors of the Mean are represented as error bars.*

4.4 Summary

In summary, a three-step reaction procedure was employed to attach RGD-containing peptides onto a titanium surface. First, water-vapor-plasma-pretreated titanium surfaces were silanized with (3-aminopropyl)triethoxysilane in dry toluene, resulting in a multilayer film of poly(3-aminopropyl)siloxane. Secondly, the free primary amino groups were linked to one of the three heterocrosslinkers: N-succinimidyl-6-maleimidylhexanoate, N-succinimidyl-3-maleimidylpropionate, and N-succinimidyl trans-4-(maleimidylmethyl)cyclohexane-1-carboxylate. Finally, onto the resulting terminal-maleimide surface, two model, cell-adhesive peptides, H-Gly-Arg-Gly-Asp-Ser-Pro-Cys-OH (GRGDSPC) and H-Arg-Gly-Asp-Cys-OH (RGDC), were immobilized through covalent addition of the cysteine thiol (-SH) group. X-ray photoelectron spectroscopy (XPS), infrared reflection absorption spectroscopy (IRAS), and radiolabeling techniques were applied to characterize the surfaces. The main results are as follows: (1) Silanization on Ti surfaces is shown to be the key step in terms of reproducibility in the subsequent modification steps. Samples produced in one batch with a surface coverage of 6 amino groups per nm^2 were used for further surface reactions. (2) The maleimidyl group introduced in the second-step reaction has been characterized using XPS (binding energy of C 1s at 289.0 eV), IRAS (band around 1707 cm^{-1}), and radiolabeling techniques with [^{35}S]-cysteine. (3) The atomic ratio N/Si determined by XPS is used to estimate the reaction yields and to follow the reaction kinetics. The reaction yields are estimated to be about 30% for the conversion step of aminosiloxane to maleimide and about 18% from maleimide to peptide. Optimal incubation times are 30 min for the former reaction and 1 h for the latter. (4) The grafted peptides, RGDC and GRGDSPC, have been qualitatively and quantitatively characterized with XPS, IRAS, ToF-SIMS, and [^{14}C]-phenylglyoxal radiolabeling techniques. The amide bands from IRAS and the specific cleaved ToF-SIMS fragments from RGDC and GRGDSPC definitely confirm the covalent attachment of these peptides. The surface coverage is estimated to be 0.2~0.4 peptide molecules per nm^2. (5) The preliminary cell culture results show positive effects for both the silanized as well as the peptide (RGD) modified titanium surfaces in osteoblastic cell line MC3T3-E1 culture tests, but negative effects for RGD-modified titanium surfaces in rat bone marrow cell culture tests.

5. Surface reactions of succinimidyl esters with amino-terminated SAMs on gold surfaces

5.1 Introduction

Two different synthesis routes are often chosen, in order to graft biomolecules onto substrate surfaces:

a) one-step self-assembling process: synthesis, isolation, and characterization of the final functional molecule, followed by self-assembly of the molecule on solid substrates.

b) multi-step reaction: activation of the inert substrate by self-assembling a less complex precursor-molecule with terminal functional groups such as NH_2, COOH, and OH, followed by a stepwise grafting reaction to bind the biologically active molecule onto the pre-assembled substrate surface by covalent binding.

Both methods have their advantages and disadvantages and are worthwhile to be evaluated and compared in Table 5-1.

To summarize: Using method a) may take longer time and cost more to synthesize and purify the goal molecule, but the surface modification is better controllable and better defined compared to method b). Method b) has the advantage of higher flexibility regarding the choice of biomolecules.

Surface OH, COOH, and NH_2 are very useful groups for chemical transformations. Monolayers with terminal COOH functionality react with alkanoic acids[114] and decylamine to form bilayer H-bonding-stabilized structures, which lack long-term stability due to the strong electrostatic repulsion in the newly formed charged interface. The carboxylate group can be transformed to the corresponding acid chlorides by using $SOCl_2$.[115] Further reactions with amines and alcohol yield bilayer structures with amide and ester linkages, respectively. Reacting the acid chloride with a terminal thiol provides the corresponding thioester. SAMs of OH-terminated alkanethiols have been used in many surface modification reactions. They were reacted with octadecyltrichlorosilane (OTS) to yield a well-ordered bilayer,[116] with $POCl_3$,[117] with glutaric anhydride,[118] and with chlorosulfonic acid.[119]

Table 5-1   Summary of advantages and disadvantages of one-step and multi-step modification methods.

a) One-step assembling process	b) Multi-step reaction
Advantages	
-well characterized molecule with known properties -easy and reproducible preparation of the functionalized surfaces -surface coverage easily adjustable -well characterized surfaces	-reagents in each step commercially available or easy to prepare -a variety of crosslinking groups (e.g. thiol-, amino-, and photo-reactive crosslinkers) available to graft different biomolecules -controlled reactions feasible on the surface but often impossible in solution (one tailed reactive group is blocked by the surface) -purification by rinsing -small volumes of diluted solutions adequate; therefore lower costs in the case of expensive molecules
Disadvantages	
-laborious synthesis and isolation -higher costs in case of expensive molecules -only specific substrates -restricted availability of target biomolecules	-surface coverage difficult to adjust -side reactions may produce unwanted functionalities - explanation of observations often difficult -surface reactions are generally less well understood

For covalent immobilization of proteins onto SAMs, the general procedure involves the formation of either a thioether or an amide. One method for amide bond formation utilizes the production or termination of SAMs with an N-succinimidyl ester.[120,121] Immobilization occurs by displacement of the succinimidyl ester group by lysine residues of the protein. Frey and Corn have shown that polylysine can be immobilized onto an 11-mercaptoundecanoic acid SAM by activation of the terminal carboxylate group with an N-hydroxysulfosuccinimidyl ester intermediate.[122] Successful formation of the ester intermediate relies on the accessibility of the terminal carboxylate groups; steric packing of these acid groups can limit the rate of formation of intermediates, with full conversion of accessible acid groups occurring only after several repeated reaction cycles.

SAMs of alkanethiols with terminal NH_2 were soaked in a solution of the N-carbonic anhydrides of L-alanine or L-phenylalanine to initiate polymerization, resulting in the growth of virtually defect-free α-helical poly-L-alanine and poly-L-phenylalanine films, with the desired thickness being attained by controlling the exposure time to the respective N-carbonic anhydride.[123,124] They have also been used to immobilize the fluorescence probes pyrene, pyrrolinone, and ferrocene.[125]

The above studies are supported by complementary surface analytical techniques, including static secondary ion mass spectrometry (SIMS), X-ray photoelectron spectroscopy (XPS), infrared reflection absorption spectroscopy (IRAS), and surface plasmon resonance (SPR).

5.2 Objective

The reaction of terminal NH_2 groups on SAMs with succinimidyl esters can be used to introduce a variety of functional crosslinking groups onto solid surfaces such as maleimidyl, iodoacetyl, succinimidyl ester, aryl azido, and benzophenone groups. With such groups, a variety of biomolecules can be immobilized on solid surfaces. However, the details of the reaction, e.g. regarding turn-over, by-product formation, etc. are often not well understood. In the previous chapter, we grafted the crosslinking group, maleimide, on aminosilanized Ti surfaces. There is still some controversy, however, as regards the interpretation of the IRAS spectra, specially for the maleimidylhexanoyl pendant surface. On the other hand, due to the poor reproducibility of siloxane film formation and the variable degree of polymerization, the IRAS spectra in the region 1650-1000 cm^{-1} show variations. This is a situation rather unsuited for a clear assignment and explanation of IR bands of the crosslinking groups. To clarify the IRAS spectral assignments and to study the reaction mechanism in detail, two model aminothiol (cystamine and 4-aminothiophenol) SAMs were self-assembled on Au surfaces. Different types of thiol-, amino-, and photo-reactive crosslinkers were attached to the two terminal NH_2 SAMs. Based on infrared reflection absorption spectroscopy (IRAS) and x-ray photoelectron spectroscopy (XPS) measurements, two types of reaction schemes have been observed: (1) modification through single group binding, (2) occurrence of side reactions and production of multiple-group-modified surfaces. A typical example for the latter case is the reaction of N-succin-imidyl-6-maleimidyl hexanoate (EMCS) with terminal-NH_2 groups, producing a mixture of both maleimidyl and succinimidyl ester groups on the surface. The conclusion is confirmed by the study of SAMs of pure N, N'-bis(maleimidylhexanoyl)cystamine (BMHC), synthesized separately. The functionalized surfaces with specific crosslinking groups can be used for further attachment of specific biomolecules.

5.3 Materials and experimental

5.3.1 Materials

N-Succinimidyl iodoacetate (SIA) and N-succinimidyl 4-benzoylbenzoate (SBB) were purchased from Molecular Probe (Netherlands). N-5-Azido-2-nitrobenzoyloxysuccinimide (ANS) and Di-(N-succinimidyl) suberate (DSS) were purchased from Pierce. All other molecules and crosslinkers were purchased from Fluka. The molecular structures, compound names, and abbreviations of all crosslinkers are shown in Appendix.

The different surfaces are defined as follows: AuC: Au+cystamine; AuB: Au+4-ATP; AuCM3, AuC+SMP; AuCM4, AuC+SMB; AuCM6: AuC+EMCS; AuCM8: AuC+SMO; AuCM11: AuC+SMU; AuCMC: AuC+SMCC; AuCMB: AuC+SMBZ; AuCMP: AuC+SMPB; AuCIA: AuC+SIA; AuCAZ: AuC+ANS; AuCBB: AuC+SBB; AuCSC: AuC+SC; AuCTP: AuC+DTSP; AuCS8: AuC+DSS; AuBM3: AuB+SMP; AuBM4: AuB+SMB; AuBM6: AuB+EMCS; AuBM8: AuB+SMO; AuBM11: AuB+SMU; AuBMC: AuB+SMCC; AuBMB: AuB+SMBZ; AuBMP: AuB+SMPB; AuBIA: AuB+SIA; AuBSC: AuB+SC; AuBTP: AuB+DTSP; AuBS8: AuB+DSS; MX (X = 3, 4, 6, 11, B, P): the functional group produced by the surface reaction of NH_2 with the correspondent precursor molecule (M3 = maleimidyl propionoyl group, M4 = maleimidyl butanoyl group, M6 = multiple groups of hexanoyl maleimide and succinimidyl ester, M8 = multiple groups of octanoyl maleimide and succinimidyl ester, M11 = multiple groups of undecanoyl maleimide and succinimidyl ester, MB = maleimidyl benzoyl group, MP = maleimidylphenyl butanoyl group).

5.3.2 Experimental

The substrates used for the experiments at room temperature consisted of 200-nm-thick, gold-sputtered Si(100) wafers with a 6-nm chromium interlayer as an adhesion promoter. The XPS analysis of the freshly evaporated Au (30 min stored in argon) shows about 20 at% of hydrocarbon contamination. Oxygen can also be detected in a range of 1 to 3 at% if the Au samples are stored for a long time (e.g. > 4 h).

The SAMs of 4-aminothiophenol (4-ATP) were prepared by immersing the polycrystalline gold substrates in a 2-mM solution of 4-ATP in ethanol for 3 h, then rinsing with ethanol 3 times. The SAMs of cystamine were prepared by immersing gold substrates in a 2 mM

solution of cystamine dihydrochloride in methanol or ethanol for 24 h, then rinsing with methanol, 1 mM NaOH aqueous solution, and water. The solubility of cystamine dihydrochloride in ethanol is very low. Therefore some solid powder sediments can be even seen in 2 mM solution of cystamine dihydrochloride in ethanol. However, this does not interfere with the SAM formation. No difference was found between the SAMs prepared in methanol or ethanol.

Standard procedure of the reaction of terminal amino groups with succinimidyl-bearing crosslinkers: The SAMs were immersed in 0.5 mM solution of individual crosslinker in acetonitrile for 30 min, with sonication for 1 min every 10 min. After reaction, the substrates were washed with acetonitrile at least 3 times.

5.4 SAMs of cystamine and 4-aminothiophenol
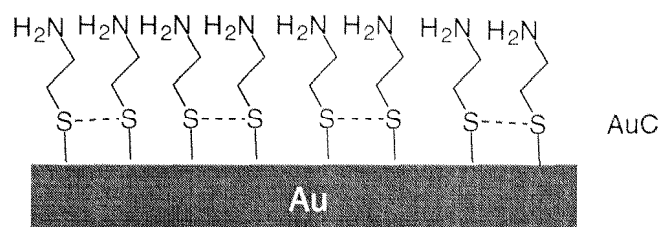
5.4.1 Cystamine SAMs (AuC)

H_2N H_2N H_2N H_2N H_2N H_2N H_2N H_2N

S----S S----S S----S S----S   AuC

Au

Figure 5-1   *Schematic structures of cystamine SAMs on Au surfaces (AuC).*

It has been reported that cystamine dihydrochloride forms a loosely packed SAM on Au substrates and the maximum surface coverage is about 35%.[126] This is due to the absence of Van der Waals interaction, which is necessary to produce a dense SAM. Our observation also confirms the submonolayer deposition. The IRAS spectrum of cystamine SAMs on Au surfaces does not show any distinguishable peaks in the region 700 ~ 2000 cm^{-1}. Its multilayers prepared without thorough washing, however, exhibit some obvious peaks in Figure 5-2. The stretching mode of amino group at ~3300 cm^{-1} is very broad and can not be clearly distinguished from the background. The CH_2 symmetric stretch is at 2855 cm^{-1}, and the asymmetric stretch at 2926 cm^{-1}. The peaks 2882 cm^{-1} and 2964 cm^{-1} are attributed to the stretching modes of contaminated methyl groups. The NH_2 deformation mode exhibits a medium peak at 1665 cm^{-1}. The wagging mode of methylene $CH_2(S)$ exhibits a sharp and narrow peak at 1257 cm^{-1}.
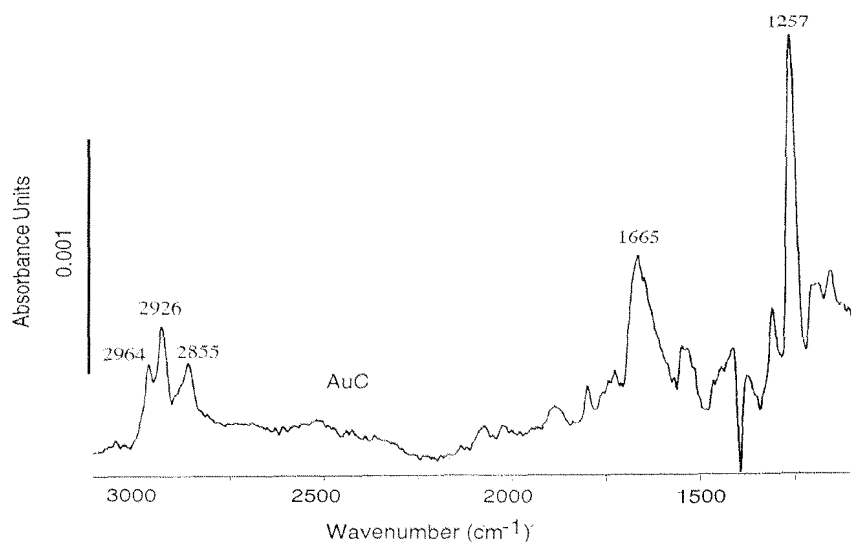
Figure 5-2   *The IRAS spectrum of cystamine ultrathin films on Au surfaces.*

Table 5-2   *XPS results for AuC: binding energies E_B, rel. peak areas   %*
(deconvolution), assignments, experimental and theoretical atomic
concentrations (%).

Element	E_B (eV)	Assignment	Atomic concentration (%)		
(orbital)	rel. peak area %		experimental		theoretical
C (1s)	285.1 (75)	C-H*, C-C	20	71	50
	287.4 (25)	C-N, C-SO$_3$			
N (1s)	399.8 (80~50)	NH$_2$	3	11	25
	401.5 (20~50)	NH$_3^+$, N-Au			
O (1s)	532.0	S-O, Au-O	2	7	—
S (2p$_{3/2}$)	162.3 (61)	thiolate	3	11	25
(2p$_{1/2}$)	163.6 (28)	thiolate			
(2p)	168.0 (11)	S-O			
Au (4f$_{7/2}$)	84.2 (57)	Au	72	—	—
(4f$_{5/2}$)	87.9 (43)	Au			
Σ	—	—	100	100	100

*C-H means contaminated hydrocarbons

Table 5-2 shows the XPS results of cystamine SAMs. The C 1s can be fitted into two peaks at 285.1 and 287.4 eV. The main peak at 285.1 eV is attributed to cystamine C-S carbons and contaminated hydrocarbons and the peak 287.4 eV attributable to part of C-N (cystamine) and oxidized sulfur species $(C-SO_3)$ carbons. The oxidized sulfur is also detected in the S 2p spectrum at 168.0 eV, in addition to a doublet at 162.3 and 163.6 eV from disulfide. Additional O 1s at 532.0 eV is attributed mainly to a possible surface gold oxide and oxidized sulfur species. The N 1s is fitted with two peaks at 399.8 and 401.5 eV, which are generally assigned to free NH_2 and protonated NH_3^+. Although 399.8 eV is the main peak, its changeable percentage, from 80 to 50 %, may be caused by complexation between N and Au, in addition to the protonated amines. The atomic ratio of N/S is close to the theoretical value of 1. However, the carbon content (compared to S and N) is much higher than theoretically expected because of the carbon contamination.
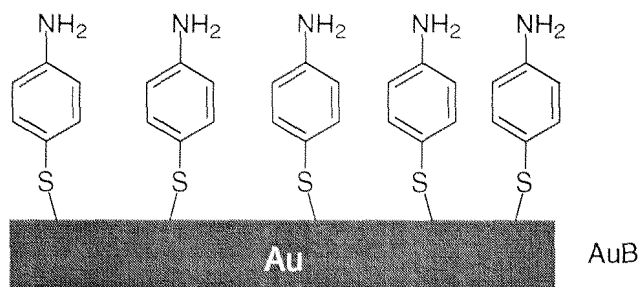
5.4.2 4-Aminothiophenol SAMs (AuB)

Figure 5-3   Schematic structures of 4-aminothiophenol SAMs on Au surfaces (AuB).

In contrast to the intense attention devoted to SAMs prepared from aliphatic thiols or disulfides, corresponding aromatic compounds have received relatively little interest. Pioneering work on the adsorption of pure aromatic thiols was done by Hubbard et al.[127,128] who studied the adsorption of thiophenol, benzyl mercaptan, 2,5-dihydroxythiophenol, 2,5-dihydroxy-4-methylbenzyl mercaptan, 4-mercaptopyridine, and various fluorinated thiophenols on platinum and silver. These studies have shown that adsorption takes place through the sulfur atom instead of the aromatic ring. Nevertheless, a variety of structural details are proposed. It is noted that for the simplest member of the arylthiol, thiophenol, the detailed structure has not been unambiguously determined. It has been suggested that thiophenol forms poorly defined monolayers. The formed monolayers did not, however, possess long-range order, except on Ag(111) surfaces. A well-ordered lattice structure was not found by high-impedance scanning tunneling microscopy for thiolphenol monolayer either.[129] In addition, aromatic moieties incorporated within a long aliphatic hydrocarbon tail do not interfere with the formation of an ordered SAM.[130] The aromatic molecules had

smaller tilt angles with respect to surface normal than alkanethiols. In all cases, interactions between the aromatic moieties play an important role.

Although SAMs prepared using thiophenol do not exhibit high order, 4-aminothiophenol (4-ATP) seems to form well-ordered monolayers on gold surfaces. Scanning tunneling microscopy (STM) studies suggest that it forms a $(\sqrt{3} \times \sqrt{3})R30^0$ monolayer on Au(111) surfaces, with the nearest and next nearest neighbor spacing of 4.9 ± 0.3 and 8.9 ± 0.5 Å, respectively.[131] Surface-enhanced raman and infrared spectroscopy studies indicate that 4-ATP has a near-vertical orientation with the principal axis of the molecule nearly normal to the surface.[136] 4-Aminothiophenol SAMs are also used to bind negatively charged solution-phase probe molecules when solution pH is low enough so that the surface-bound amino group is protonated.[133] The pKa value of 4-aminothiophenol on gold surface has been determined by differential capacitance measurements to be 6.9 ± 0.5 (at +0.2 V versus Ag/AgCl).[134] In mixed monolayers of thiophenol/4-ATP and octadecanethiol/4-ATP, two phase regions exist: 4-ATP domains separate from its partner-rich regions.[132,135] 4-ATP SAMs have been applied to produce densely packed polyaniline films with improved adhesion, optical and electrochemical properties. In particular, the charge transfer processes in the polyaniline film are greatly facilitated. Therefore, it has been used for "underpotential polymerization" of aniline on gold electrodes. Nanometer scale polyaniline patterns can be grown on mixed SAMs of 4-aminothiophenol and octadecanethiol because of the existence of phase-separated 4-ATP domains.[135]
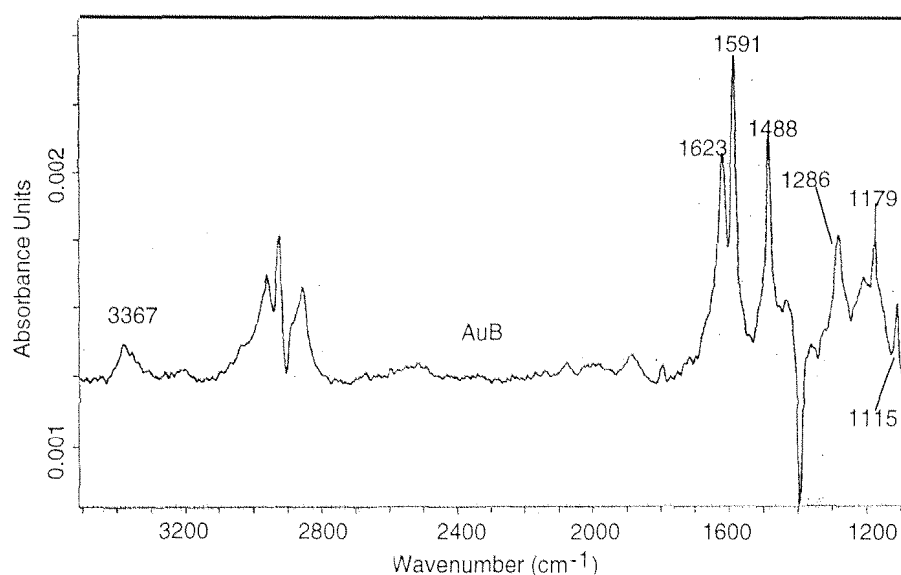

Figure 5-4   *The IRAS spectrum of AuB. Peak assignments; see text and Table 5-3.*

The vibrations characteristic of p-disubstituted benzenes are given by notions of the corresponding vibrations of benzene (refer to Figure 3-8) together with the symmetry

species under assumption of C_{2v} symmetry, where the axes are chosen such that the molecule is in the yz plane and z is the C_2 axis. The benzene ring vibrations are classified as a_1, a_2, b_1, and b_2 species. The a_1 and b_2 species are in-plane modes, and a_2 and b_1 species out-of-plane modes. All but a_2 are infrared active.

Table 5-3 IR band frequencies and assignments of 4-ATP in KBr and on Au .

Frequency (cm^{-1}) of 4-ATP		Mode assignment[1]
in KBr	on Au	
3335 s[2]	3367 w	NH$_2$ stretching
3036 s	3030 vw	CH stretching, 13 (a$_1$)
	3000~2800	CH stretching (hydrocarbon contaminants)
2564 m		SH stretching
1620 s	1623 s	NH$_2$ deformation
1595 vs	1591 vs	CC stretching, 8a (a$_1$)
1493 s	1488 s	CC stretching + CH bending, 19a (a$_1$)
1423 w		CC stretching + CH bending, 19b (b$_2$)
1284 s	1286 m	CH stretching, 3 (b$_2$)
1176 m	1179 w	CH bending, 9a (a$_1$)
1119 w	1115 w	CH bending, 18b (b$_2$)

[1]For ring vibrations, the corresponding vibrational modes of benzene and the symmetry species under C_{2v} symmetry are indicated. [2] Frequencies (in cm^{-1}) followed by relative intensities (vs, very strong; s, strong; m, medium; w, weak; vw, very weak; b, broad; sh, shoulder).

Three prominent absorption bands are observed in this spectrum at 1488, 1591, and 1623 cm^{-1} and are assigned to the benzene ring vibration bands (1488: CC stretching + CH bending, 19a; 1591: CC stretching, 8a) and the NH bending band (1623 cm^{-1}), respectively. The other bands are the stretching mode of NH$_2$ at 3367 cm^{-1}, the in-plane bending of CH at 1286 (3), 1179 (9a), and 1115 cm^{-1} (18b). The observed frequencies and relative band intensities are nearly identical to what has been observed for 4-ATP on Ag surfaces.[136] As noted by these workers for 4-ATP on Ag, all of the bands appearing in the IRAS spectrum are of a$_1$ symmetry; in particular, the b$_2$ ring mode that appears at ~1420 cm^{-1} in the bulk spectrum is entirely absent from the surface spectrum, indicating that the principal axis C$_2$ of adsorbed 4-ATP is oriented along the surface normal. However, as shown in Table 5-3, we assign the in-plane C-H bending bands 1286 to vibration mode 3

(b_2) and 1115 cm^{-1} to vibration mode 18b (b_2), different from the assignments to a_1 modes by the above authors. Since the transition dipole moment of a_1 modes is parallel to the C_2 axis and that of b_2 is perpendicular to it, we suggest that there is a small tilt angle between the C_2 axis and the surface normal.

Table 5-4   XPS results for 4-aminothiophenol SAMs on Au (AuB).

Element (orbital)	E_B (eV) rel. peak area %	Assignment	Atomic concentration (%)		theoretical
			experimental		theoretical
C (1s)	284.3 (65)	aryl C-C, C_{aryl}-S	31	81.6	75.0
	285.5 (25)	C_{aryl}-N, C-H*			
	287.0 (10)	C-SO$_3$			
N (1s)	399.5 (86)	NH$_2$	3	7.9	12.5
	401.0 (14)	NH$_3^+$			
O (1s)	532.0	S-O and Au-O	1	2.6	–
S (2p$_{3/2}$)	162.1 (60)	thiolate	3	7.9	12.5
(2p$_{1/2}$)	163.4 (30)	thiolate			
(2p)	168.2 (10)	SO$_3$			
Au (4f$_{7/2}$)	84.2 (57)	Au	62	–	–
(4f$_{5/2}$)	87.9 (43)	Au			
Σ	–	–	100	100	100

We carried out measurements with XPS on AuB. The results for elemental analysis are presented in Table 5-4. The C 1s spectra are proved to be the most informative for the chemical nature of the organic SAMs. The elemental ratio for N and S is close to the theoretical value, but the ratios C/N and C/S ($\cong$ 10) are higher than the theoretical value (6) due to hydrocarbon contamination. In addition, some oxygen was observed, attributable mainly to oxidized sulfur species and a possible gold oxide. The S 2p spectra showed, in addition to the doublet at 162.1 and 163.4 eV due to thiolate bound to gold, a small contribution (~10%) from oxygen-containing sulfur species, probably sulfonate, at 168.2 eV.[137] The higher oxidation states of sulfur have not usually been detected in SAMs formed from aliphatic sulfides or disulfides, but a recent study of an aromatic disulfide SAM revealed a substantial amount of sulfonate species on the surface.[138] The C 1s spectrum can be fitted using three peaks at 284.3, 285.5, and 287.0 eV, which are assigned to the aryl C-C and C_{aryl}-S, C_{aryl}-N and contaminated C-H*, and C_{aryl}-SO$_3$ carbons, respectively

(compare literature values 284.6 and 285.6 eV for aryl C-C or C_{aryl}-S and C_{aryl}-N, respectively).[137,139] Two nitrogen species were found in the N 1s spectra of 4-aminothiophenol SAMs. The major component at 399.5 eV can be attributed to neutral amino groups and the lower component at the higher binding energy (401.0 eV) to charged amino groups (~14% of the total nitrogen). In summary, XPS data confirm the formation of a 4-aminothiophenol SAM on gold.

5.5 Functional crosslinking groups attached to amino-terminated SAMs on gold surfaces

In the following text, we will discuss the results of the different functional crosslinking groups attached to NH$_2$-terminated Au surfaces:
1.   Amino-reactive crosslinking groups
2.   Photo-reactive crosslinking groups
3.   Thiol-reactive crosslinking groups

5.5.1 Amino-reactive crosslinking groups

The amino group is a strong nucleophile in peptides and proteins. Because of its abundance and omnipresence in peptides and proteins, it is the most important target for chemical modification, particularly in cases where cysteine residues are absent. Since the protonated species are not active, the rate increases with increasing pH as the free amine is formed. Due to the relatively high pKa of the ammonium ion, most of the reagents that react with the amino group will also react with other functionalities. However, many stable acylated products are formed only with the amino groups, providing the basis of selectivity. The most common reactions of amines are alkylation and acylation reactions. Here we only discuss the often used reagents, N-succinimidyl esters. They react preferentially with amino groups eliminating N-hydroxysuccinimide as the leaving group. The reaction is complete within 10 to 20 min at pH 6 to 9.

1. Surface reaction with bi-(N-succinimidyl)carbonate
Bi-(N-succinimidyl)carbonate (SC) has only a carbonyl group between two succinimidyl groups. The question is whether it forms a bridge of carbamide or not; in this case both succinimidyl esters are replaced by amino groups. In fact, the succinimidyl group is still detectable with IRAS and XPS. Therefore it is likely that some SC molecules only react with one free NH$_2$ group. The terminal succinimidyl ester can be used for immobilization of biomolecules with free amino groups.
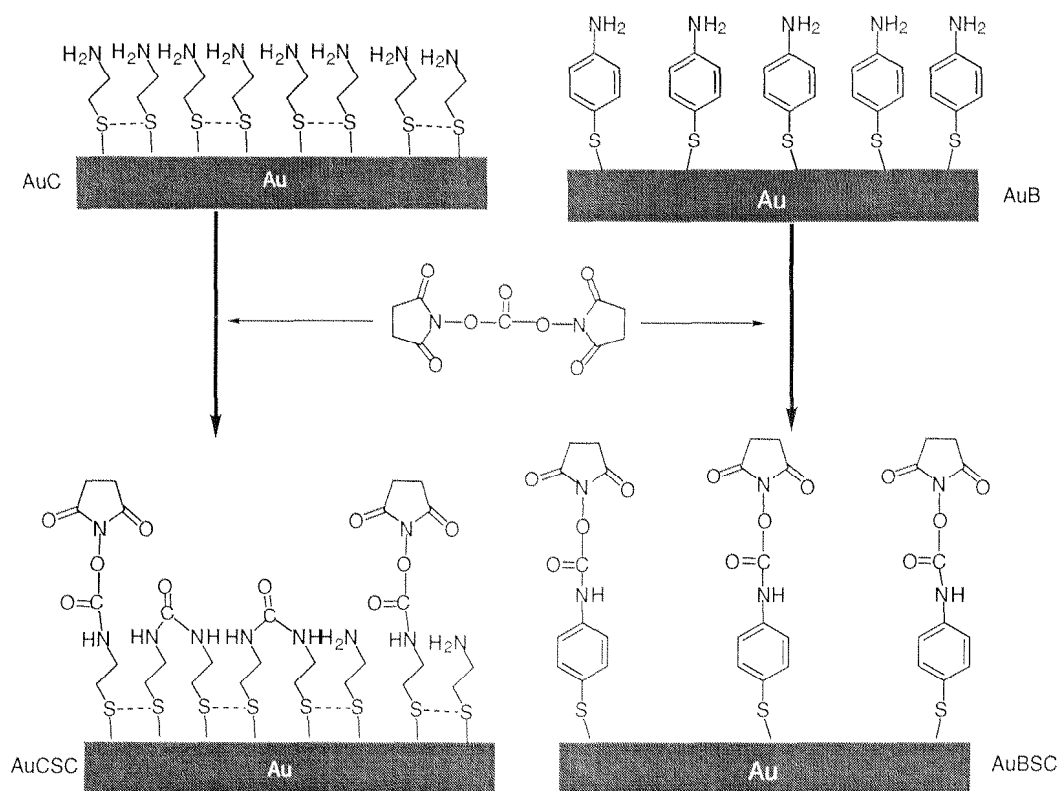
Figure 5-5   *Possible molecular structures of AuCSC and AuBSC.*

Figures 5-6 and 5-7 show the IRAS spectra of AuCSC and AuBSC respectively. On the AuCSC surface, the significant peaks are succinimidyl ester stretch at 1744 (strong) and 1791 cm^{-1}, amide I at 1670 cm^{-1} (strong and broad), and amide II at 1530 cm^{-1}. The strong amide I indicates formation of a bridge of carbamide. Otherwise, there will be no amide I peak because the mono-substituted group -NH-C(=O)-O- has a strong C=O stretch band at 1744 cm^{-1}.[140] Thus the product on surface AuCSC is a mixture of succinimidyl esters and carbamides (Figure 5-5). The formation of bridge is most likely thought as a two-step reaction: One amino group replaces the first succinimidyl group; then the second amino group attacks the carbonyl group and replaces the second succinimidyl group. However, the spectrum of AuBSC is different from AuCSC. The significant peaks are: 1745 and 1781 cm^{-1} attributable to succinimidyl ester, 1592 cm^{-1} to benzene (4-ATP) stretch, and a strong and sharp amide II at 1532 cm^{-1}. The obvious difference from AuCSC is the absence of amide I and the strong amide II. The strong amide II peak indicates that the orientation of N-C bond is nearly perpendicular to the surface plane. The absence of amide I indicates that the bridging structure of carbamide does not exist on the surface. Otherwise, the carbamide C=O group would be present on the surface and enhances the amide I intensity. The strong steric hindrance from the benzene group may be the reason of not forming such a bridge. It is suggested that only one product, succinimidyl ester, is present on the surface (Figure

5-5). The disappearance of NH_2 deformation at 1627 cm^{-1} indicates the nearly complete conversion efficiency.
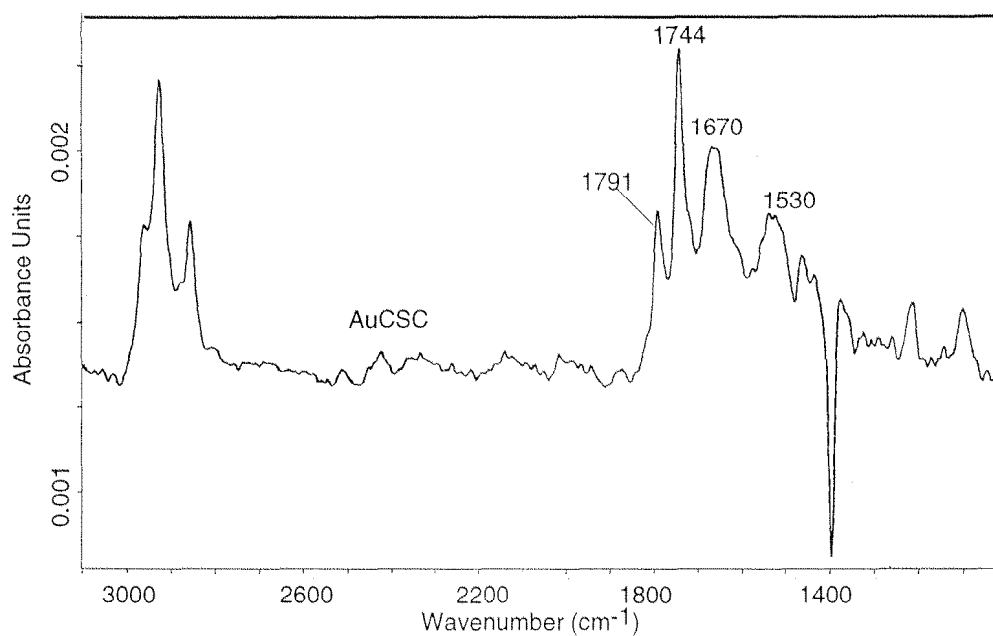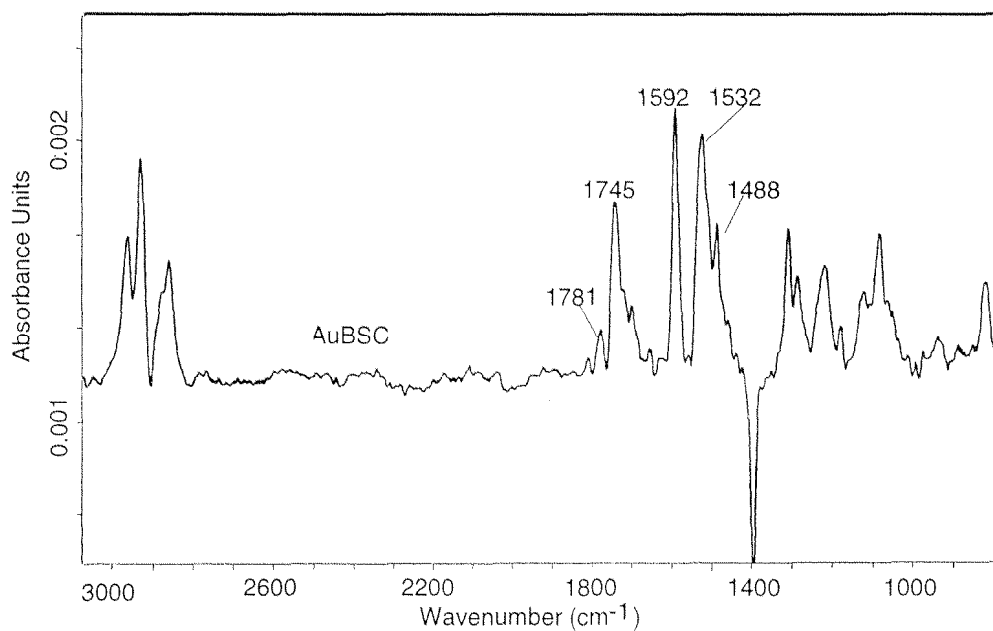

Figure 5-6   The IRAS spectrum of AuCSC.

Figure 5-7   The IRAS spectrum of AuBSC.

The XPS C 1s spectra are shown in Figure 5-8. On AuCSC or AuBSC, the newly introduced carbamidyl groups NC(=O)N, NC(=O)O and imidyl group C(=O)NC(=O) have C 1s around 289 eV. The C 1s peak on both surfaces can be deconvoluted into 3 peaks.

The only difference is that the alkyl C 1s on AuCSC occurs at ~285.0 eV, while the aromatic C 1s on AuBSC occurs at ~284.4 eV. The larger portion of C 1s at 285.1 eV on AuCSC and 284.4 eV on AuBSC may be attributed to hydrocarbon contaminants.
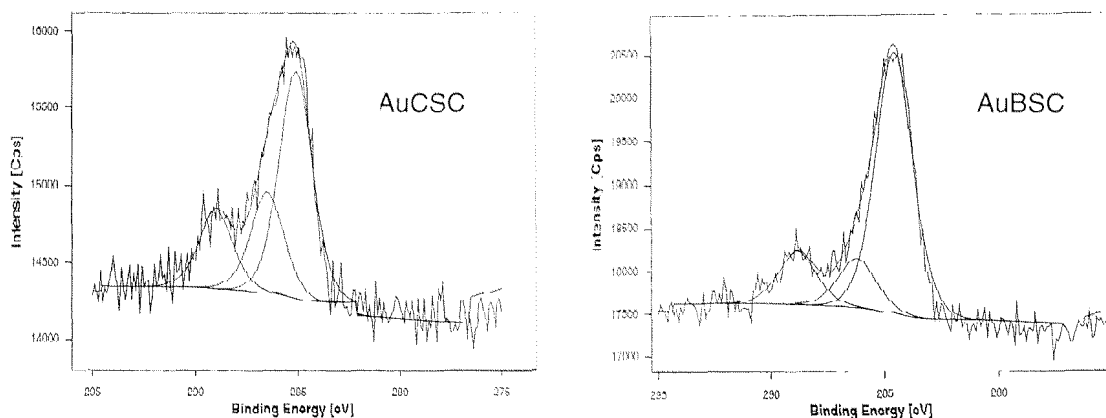

Figure 5-8   XPS results of C 1s deconvolution for AuCSC and AuBSC.

Table 5-5   Curve fitting results of C 1s for the spectra of Figure 5-8.

Surface	E_B of C 1s (eV) rel. peak area %	Assignment
AuCSC	285.1 (56)	C-S, C-H*
	286.5 (25)	C-N, C-C=O
	289.0 (19)	imide-, carbamido-C
AuBSC	284.4 (71)	aryl C, C-H*
	286.2 (14)	C-C=O
	289.0 (15)	imide-C, NC(=O)O

2. Surface reaction with dithiobis(N-succinimidyl propionate) (DTSP)

DTSP has a disulfide bond between two succinimidyl esters. The advantage is that the disulfide bond can be cleaved with thiol compounds. The reaction of DTSP with terminal NH_2 is similar to that of SC. The products can be a disulfide bridge and/or a terminal succinimidyl ester. The IRAS spectrum of AuCTP (Figure 5-10) shows only the broad amide I (1660 cm^{-1}) and amide II (1535 cm^{-1}) bands, indicating formation of the disulfide bridge, but no or a trace of succinimidyl esters on the surface (Figure 5-9). On AuBTP, the characteristic bands of succinimidyl ester at 1745, 1785, and 1820 cm^{-1} are clearly seen. The amide I and II bands can be occasionally detected. In this case, both products are

possible, but the dominant product is the terminal succinimidyl ester (Figure 5-9). These structures in Figure 5-9 are further confirmed by XPS measurements. AuBTP has an increase of S and O contents and the imide C 1s exists at 289.0 eV. AuCTP has an increase of S and O contents, but no imide C 1s is detected at 289.0 eV.
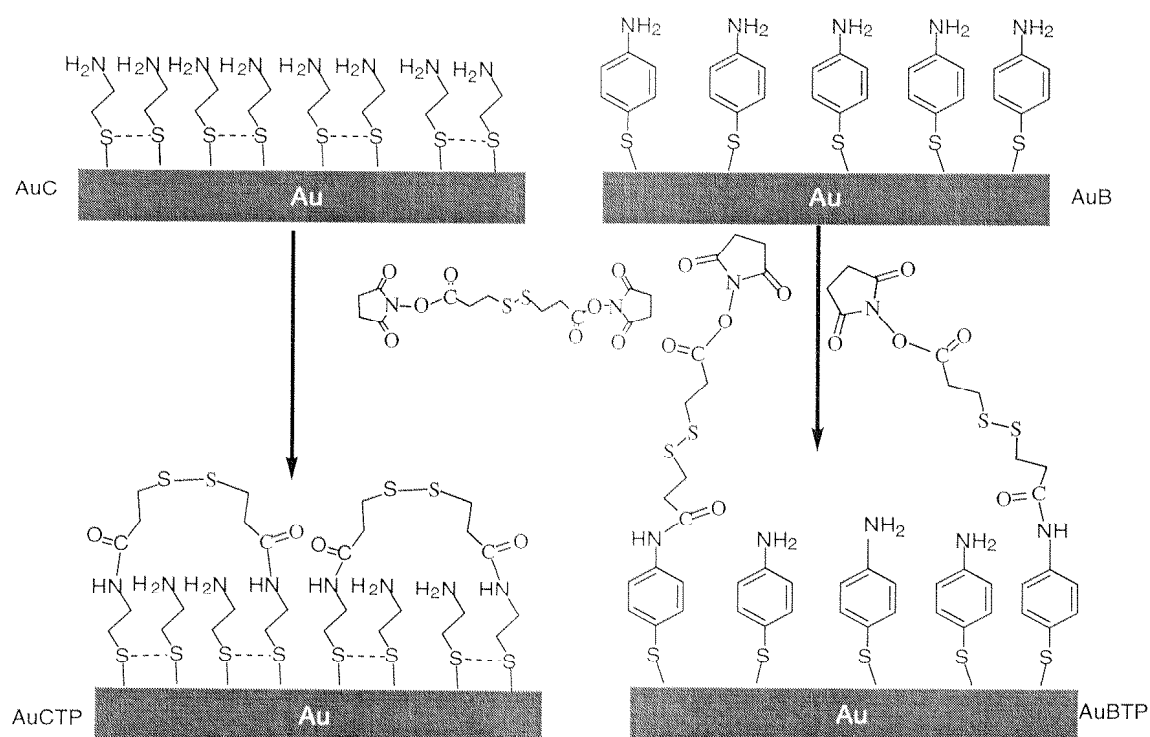

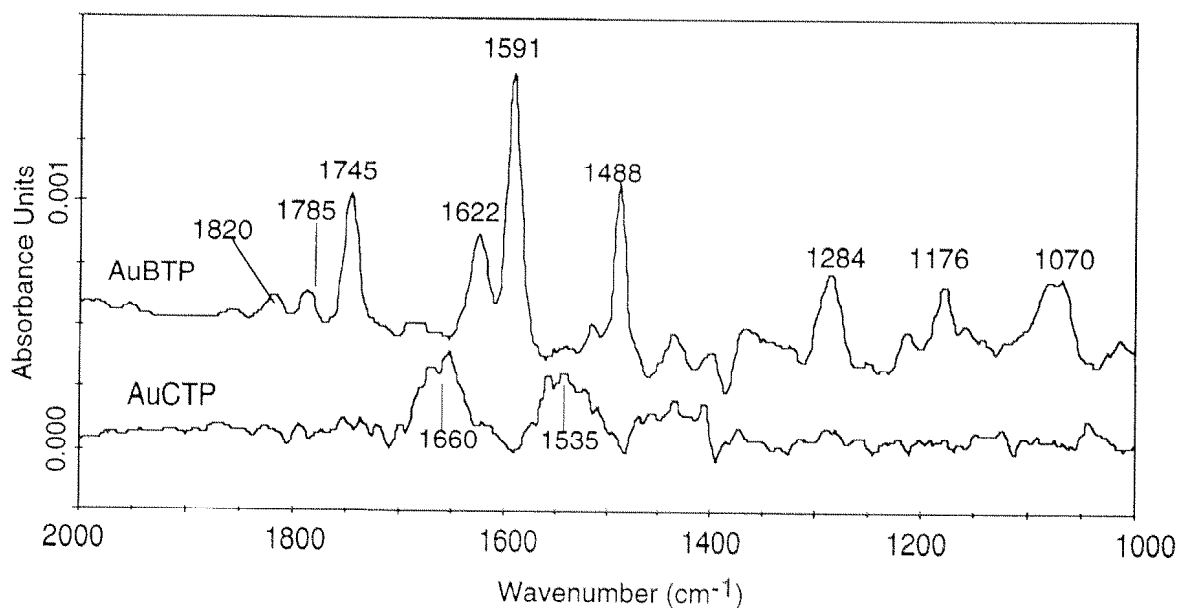*Figure 5-9   Possible molecular structures of AuCTP and AuBTP.*

Figure 5-10   IRAS spectra of AuCTP and AuBTP.

3. Surface reaction with di-(N-succinimidyl) suberate (DSS)

The reaction of DSS with both AuC and AuB forms bridging structures on the surface, which are confirmed by the appearance of amide bands in IRAS spectra and the increase of C and O contents from XPS measurements. Neither succinimidyl ester stretch bands nor imide C 1s signals were detected by IRAS and XPS respectively.
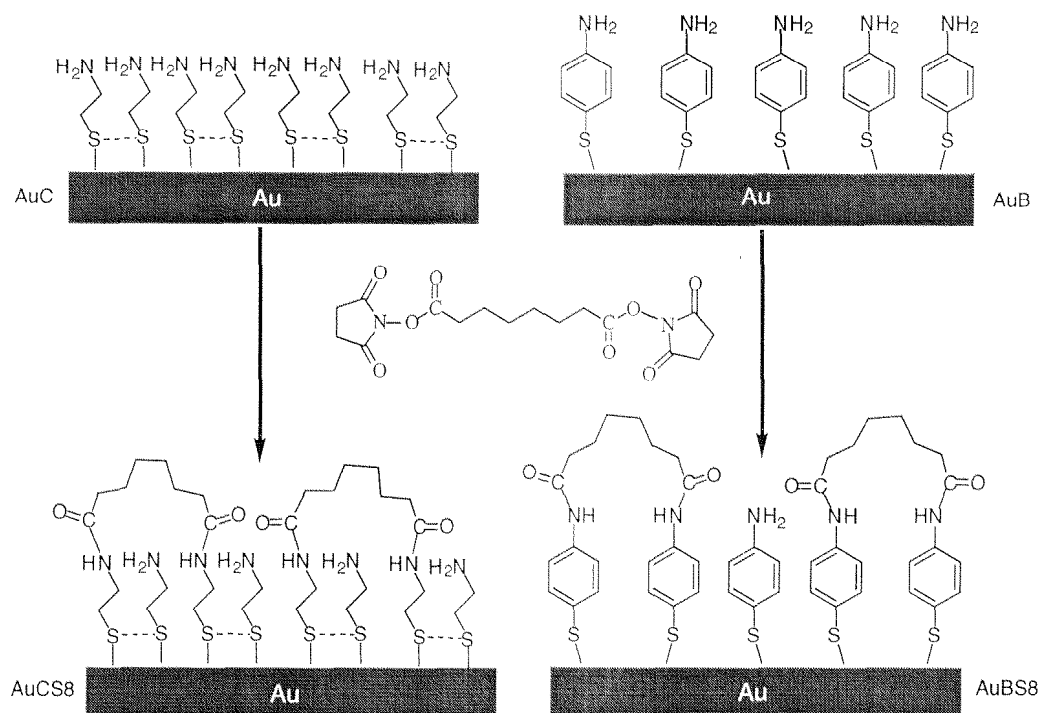

Figure 5-11   Possible molecular structures of AuCS8 and AuBS8.

5.5.2 Photo-reactive crosslinking groups

Photosensitive heterobifunctional crosslinkers represent a large portion of the heterobifunctional reagents. Because these functionalities are inert until they are photolyzed, these reagents are first linked to a protein or solid matrix in the dark through a group directed reaction. The photolabeled materials are then irradiated to activate the photosensitive group which reacts indiscriminatively with its environment.

The photosensitive labels are generally classified according to the active species they produce. Nitrenes are generated from azides whereas carbenes are derived from diazo compounds and benzophenones. Azido derivatives constitute the majority of the photoactivable cross-linking agents. Three types of azides, the aryl, alkyl and acyl azides, are often used. Among them, arylazides have been extensively used in photoactivable crosslinkers. Aryl azides have a low activation energy and can be photolyzed in the soft UV region. The presence of electron-withdrawing substitutes such as nitro- and hydroxyl

groups further increases the wavelength of absorption into the 300 - 400 nm region. The principal reactions for nitrenes are outlined in Figure 5-12. The arylnitrenes have a half-life reaction time in the order of 10^{-2} to 10^{-4} seconds[141] and, therefore, the cross-linking reaction is expected to be finished after a very short period of time.

$\lambda_{max} = 265\text{-}275nm$
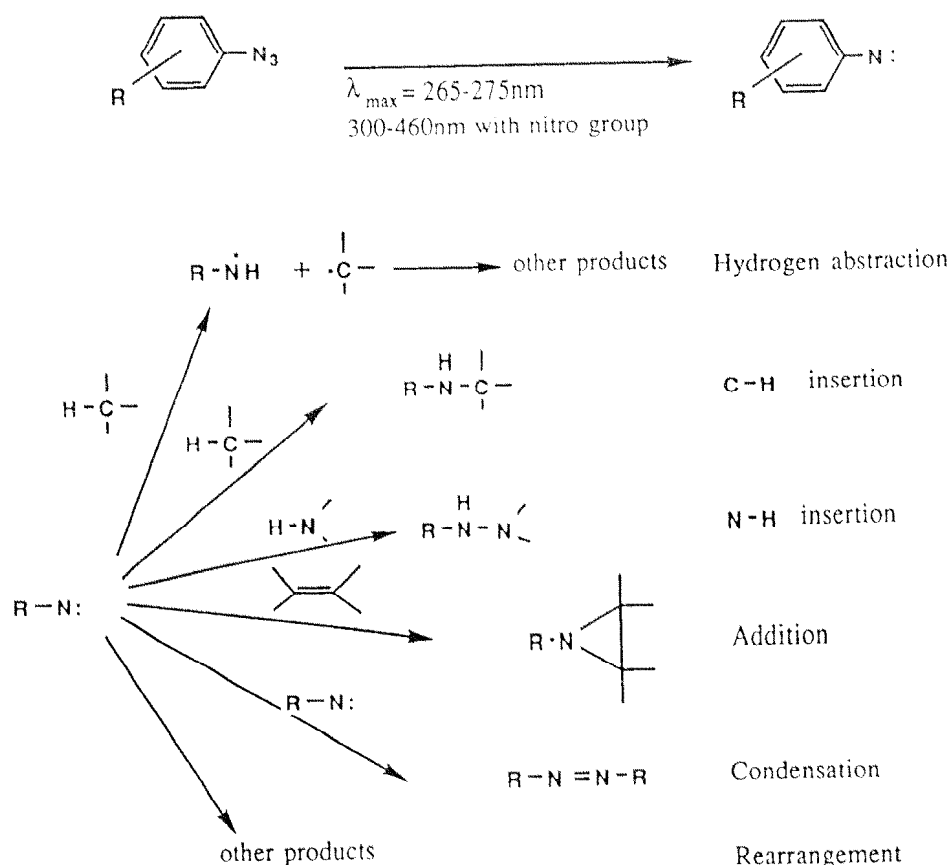
300-460nm with nitro group

Figure 5-12   Nitrene formation and the main reaction types of nitrenes.[57]

The benzophenone derivatives, as shown in Figure 5-13, can form covalent adducts on irradiation with nearby amino acid residues leading to crosslinking. Unlike the azides, which are irreversibly photolyzed in most cases, the excited triplet state of benzophenones may be inert to water and may revert back to the starting material if no photoreaction takes place. Since benzophenones can be re-excited, their cross-linking efficiency can in principle reach 100%.
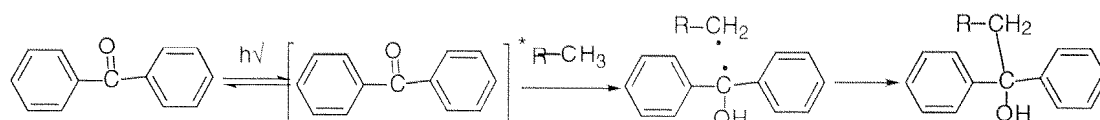

Figure 5-13   Reaction mechanism of the photocrosslinker-benzophenone.

Two typical model photocrosslinkers, N-5-azido-2-nitrobenzoyloxysuccinimide (ANS) and N-succinimidyl 4-benzoylbenzoate (SBB), are chosen for reaction with AuC and AuB. No reaction was found on AuB because of the bulky size of the two groups and the strong steric hindrance from the benzene group on AuB. Both azide and benzophenone groups can be covalently attached on AuC.
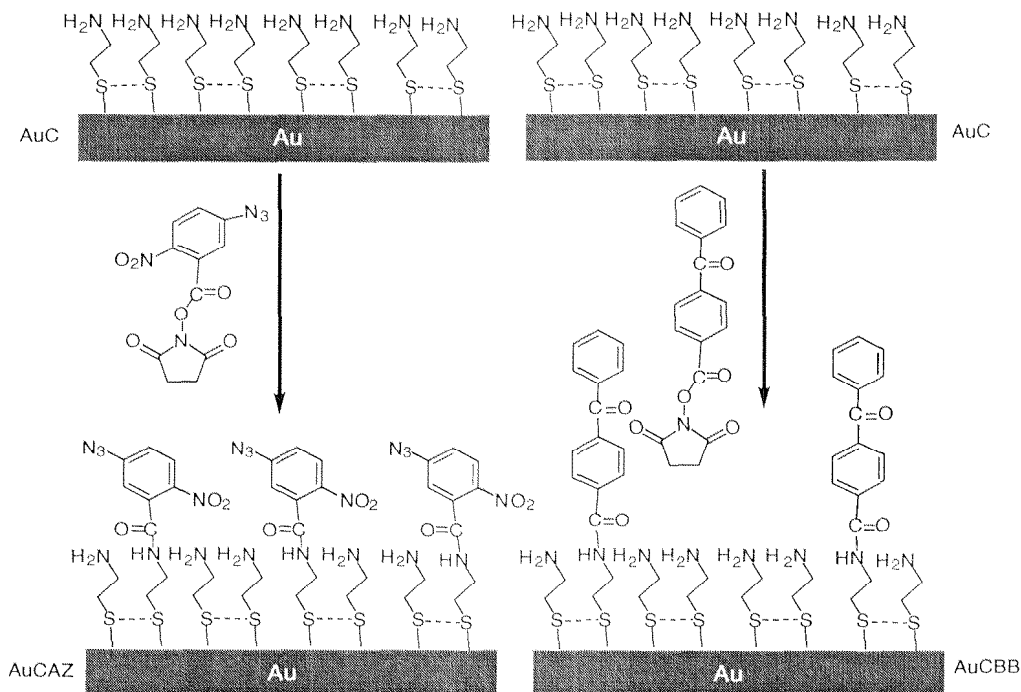

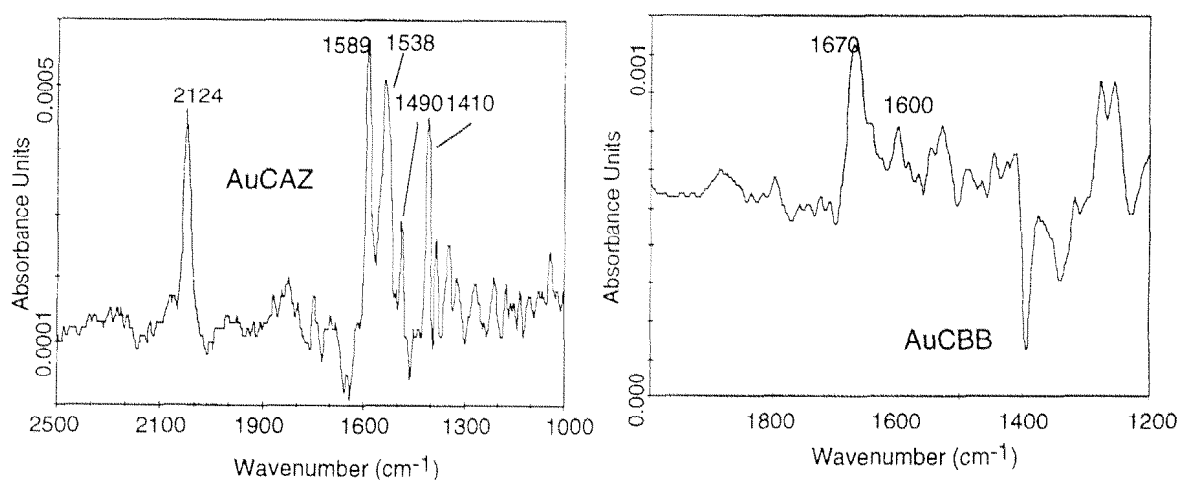*Figure 5-14   Formation of photo-reactive surfaces (AuCAZ and AuCBB).*

Figure 5-15   IRAS spectra of AuCAZ and AuCBB.

The IRAS spectra of AuCAZ and AuCBB are shown in Figure 5-15. For the azido group, the characteristic peak is the asymmetric stretch of (N_3) at 2124 cm^{-1}. The benzene ring vibrations exhibit two peaks at 1589 (s) and 1490 (w) cm^{-1}. The nitro group absorbs

strongly at 1538 and 1410 cm^{-1}. For the benzophenone group, a strong peak at 1670 cm^{-1} is due to the aromatic carbonyl group and/or amide I. Other peaks at 1600 and 1527 cm^{-1} correspond to the benzene ring stretch and amide II respectively.

XPS spectra of AuCAZ show very informative signals in the N 1s region. It can be fitted into 3 peaks: the main peak at 399.6 eV (60%) is attributed to NH, NH-CO, and N$\underline{N}$N, the second peak at 401.2 eV (20%) to N$\underline{N}$N, the third peak at 406 eV (20%) to NO$_2$. The azido group is sensitive to x-ray radiation. therefore after 1 h radiation, the peak intensity at 401.2 eV decreases significantly.
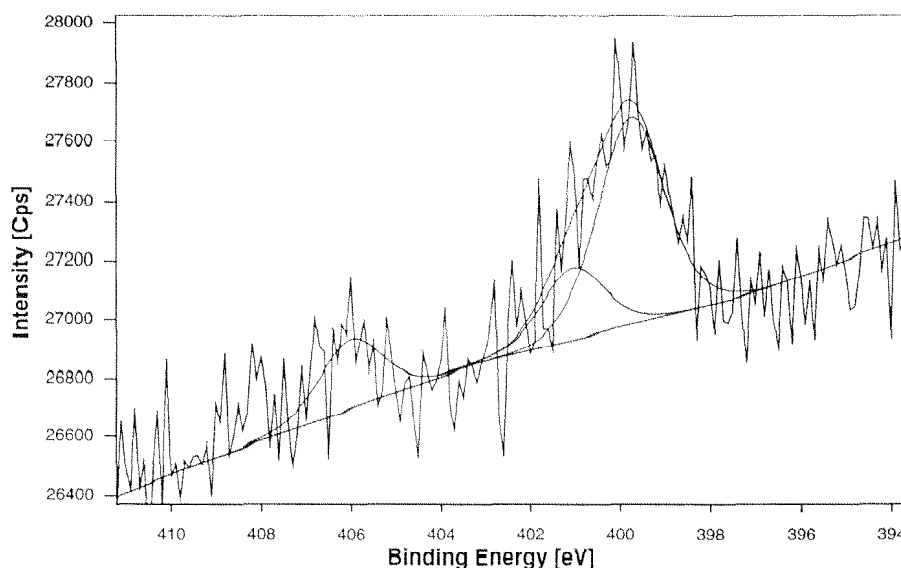

Figure 5-16   The detailed N 1s XPS spectrum of AuCAZ.

5.5.3 Thiol-reactive crosslinking groups

The thiol moiety, with the thiolate ion as the active species, is the most reactive functional group in a protein. With a pKa of about 8.6, the reactivity of the thiol is expected to increase with increasing pH, toward and above its pKa. There are many reagents that react faster with the thiol than any other groups. The thiol-reactive functional groups are primarily alkylating reagents, including α-iodoacetamides, maleimides, benzylic halides and bromomethylketones. We introduced α-iodoacetamide and a series of maleimides on gold surfaces through the reaction of amino groups with succinimidyl esters.

5.5.3.1 α-Iodoacetamide

Iodoacetamides readily react with all thiols, including those in peptides, proteins, and thiolated polynucleotides, to form thiolethers (Figure 5-17); they are somewhat more

reactive than bromoacetamides. The reaction involves nucleophilic attack of the thiolate ion resulting in a displacement of iodine. However, when a protein's cysteine residues are blocked or absent, iodoacetamides can sometimes react with methionine residues. They may also react with histidine or potentially tyrosine, but generally only if free thiols are absent. Although iodoacetamides can react with the free base form of amines, most aliphatic amines, except the α-amino group at a protein's N-terminus, are protonated and thus unreactive below pH 8. Iodoacetamides are intrinsically unstable in light, especially in solution; reactions should therefore be carried out under subdued light.
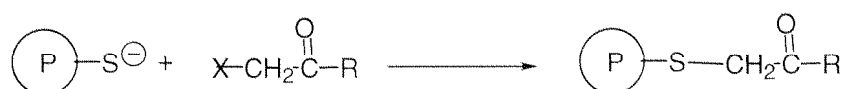

Figure 5-17   A schematic reaction equation of α-iodoacetamide with a protein bearing available thiol groups.

α-Iodoacetamide was attached on both AuC and AuB, forming surfaces AuCIA and AuBIA (Figure 5-18). The IRAS spectrum of AuCIA in Figure 5-19 shows three dominant peaks at 1721, 1676 (amide I), and 1531(amide II) cm^{-1}. The peak at 1721 cm^{-1} is unexpected and may be attributable to CHO since part of CH$_2$I can be oxidized to CHO under daylight. On AuBIA, insides the peaks from the background AuB (1591, 1486, and 1286), a strong amide II around 1521 cm^{-1} indicates the amide bond. Additional peaks at 1745 and 1780 cm^{-1} from succinimidyl esters point to the side-reaction of iodoacetyl groups with amino groups.
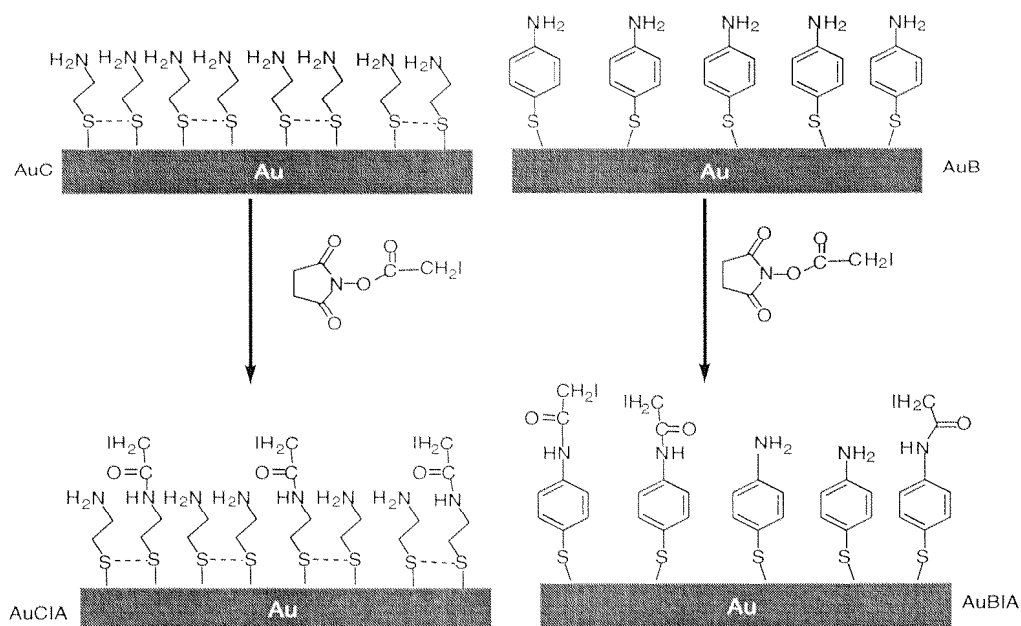
Figure 5-18   Formation of AuCIA and AuBIA with terminal α-iodoacetamide groups.
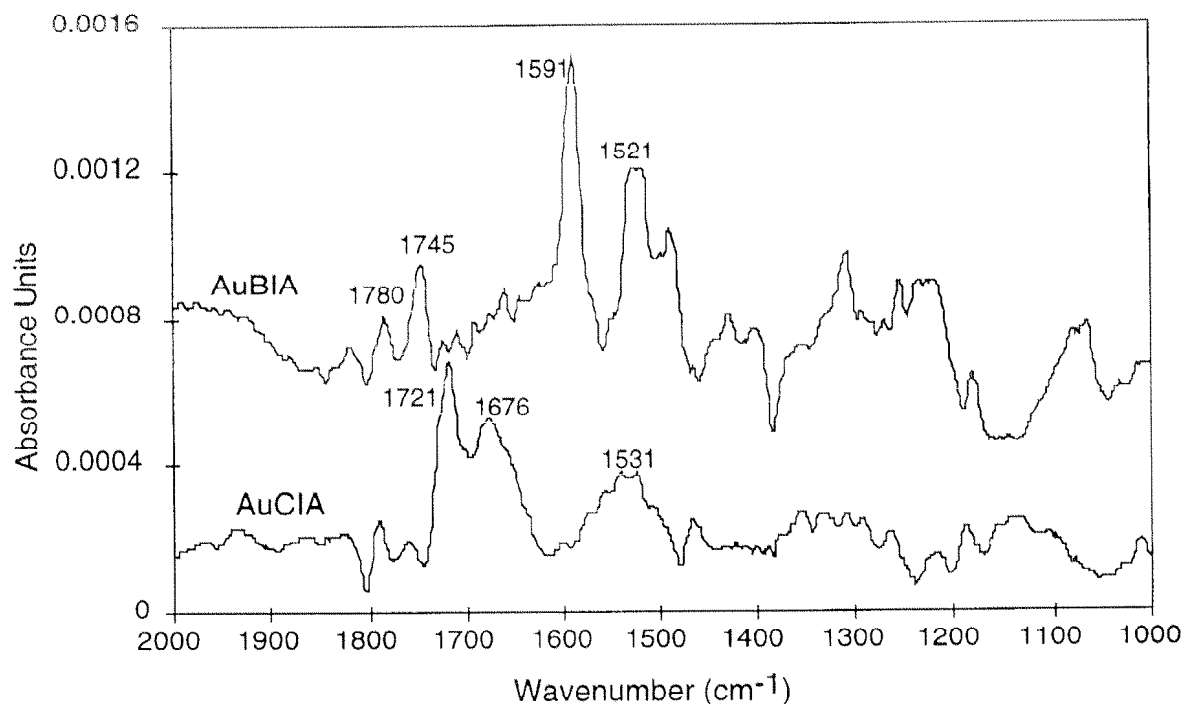
Figure 5-19   IRAS spectra of AuCIA and AuBIA in the region 1000 to 2000 cm^{-1}.

The survey XPS spectrum of AuCIA (Figure 5-20) show six elements: C, N, O, S, I, and Au, in which I $3d_{5/2}$ and I $3d_{3/2}$ are at 619.0 eV and 630.5 eV. The atomic concentrations shown in the inset indicate the high conversion efficiency from NH_2 to iodoacetamide because the atomic ratio I/N is 0.85, close to the theoretical value 1. AuBIA has a similar XPS spectrum and not shown here.

Figure 5-20   The XPS survey of AuCIA. I 3d doublet peaks are observable.

5.5.3.2 Maleimides

Maleimide is the crosslinking group primarily used and discussed in this thesis. The molecular structures of crosslinkers are shown in Appendix. We selected the analogous derivatives with different alkyl chains (3, 4, 6, 8, and 11 carbons) between the succinimidyl ester and maleimidyl groups. Additional three crosslinkers with cylcohexane and benzene groups between the two crosslinking groups were also studied.
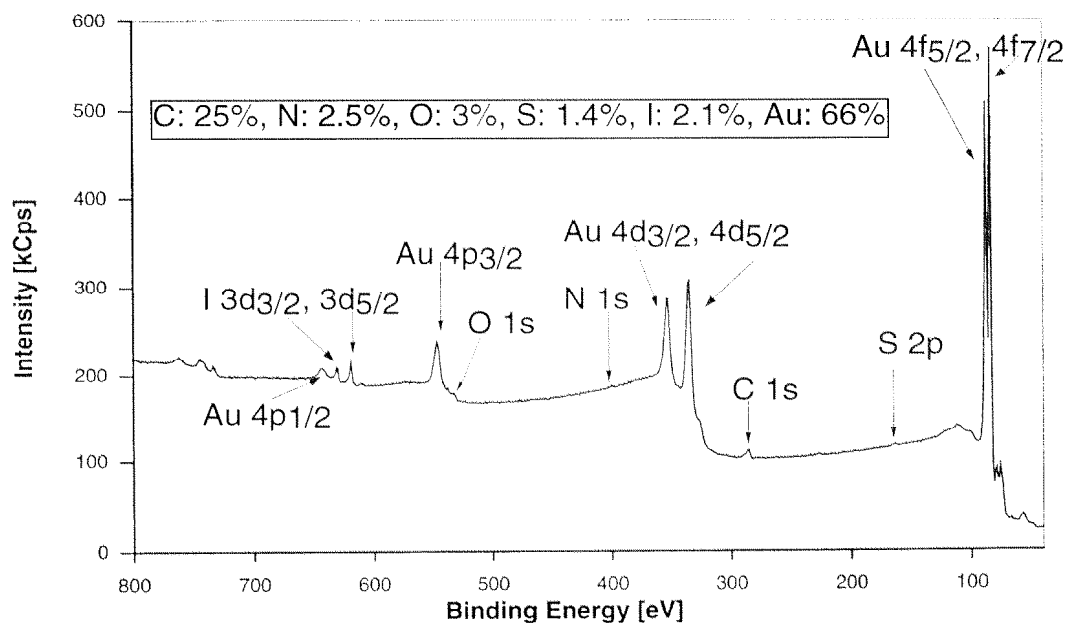
Before discussing the results, the basic IR spectra of maleimide-derivatives are introduced below. Maleimide has the following structural parameters:

Bond	Bond length (Å)	Bond angle	Angle value
C-N	1.38	∠CNC	110.0^0
C-C	1.48	∠NCC	106.8^0
C=C	1.303	∠HNC	125.0^0
C=O	1.22	∠NCO	124.0^0
C-H	1.1	∠CCH	125.0^0

Most of the authors apply the C_{2v} symmetry on maleimide-derivatives,[142] although other people use C_s instead of C_{2v} for the N-substituted maleimide. The 24 fundamentals will accordingly split up into the symmetry species: $9a_1+3a_2+4b_1+8b_2$. The a_1 and b_2 fundamentals represent in plane, and a_2 and b_1 out-of-plane modes. All the modes are Raman active, and all but a_2 are infrared active. There are 3 main IR-active groups: imidyl group (-CONCO-), =C-H, and C-N-C. The imidyl group generally shows more than 2 stretching vibration bands between 1700 and 1800 cm^{-1}. The intense peak at lower frequency is attributed to the asymmetric stretching mode, and the weak peak at higher frequency to the symmetric stretching mode. The maleimide =C-H exhibits the stretching band at ~3100 cm^{-1} and the out-of-plane bending band at ~830 cm^{-1}. The symmetric C-N-C stretching band around 1350-1440 cm^{-1} is suggested because very strong Raman lines appear for the imide-derivatives around the same region, where no phenyl and carbonyl modes are expected.[143] The stretching mode of a C-N group adjacent to a C=O group also appears around 1420-1300 cm^{-1}. The coupling between the different types of C-N stretching modes may split this mode into several medium-intensity bands in this region.

5.5.3.2.1 IRAS results

From the expected reaction products in Figure 5-21, one can assume that the unifying structural features are the presence of maleimide and amide groups. It is expected that all surfaces should have similar spectra. The IRAS spectra of the analogous surfaces AuCM3,

AuCM4, AuCM6, AuCM8, and AuCM11 are collected together in Figure 5-23. The spectra of the same functional groups grafted on AuB are shown in Figure 5-25. Three regions: 3500-2700 (C-H stretching), 1900-1500 (imide and amide bands), and 1500-1000 cm^{-1} are the most interesting areas to be discussed in detail.

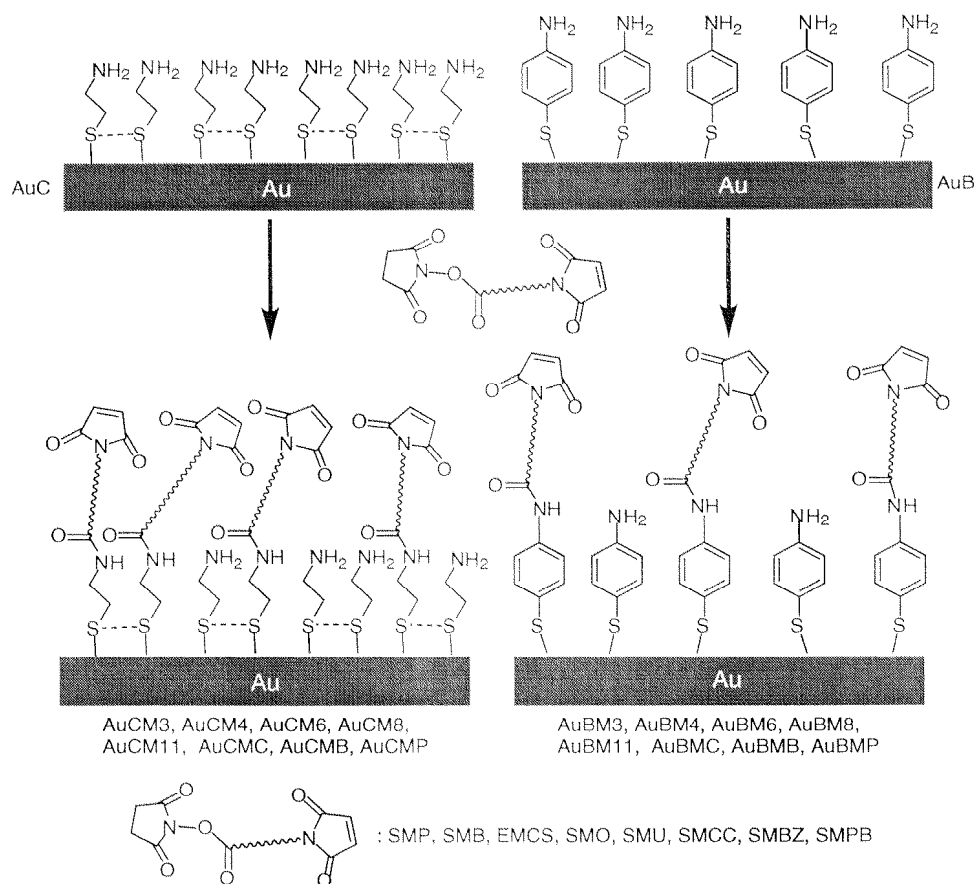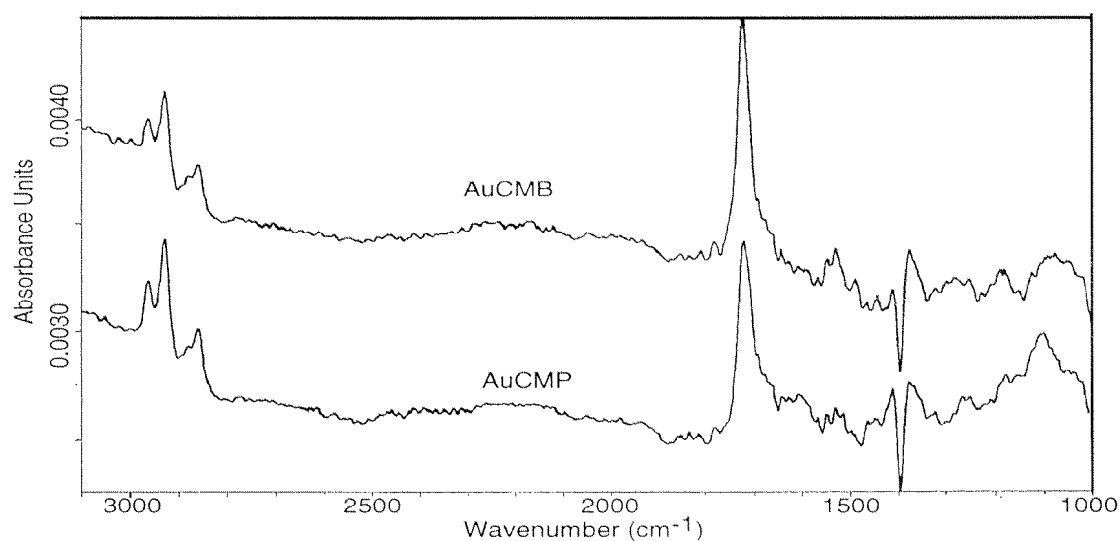*Figure 5-21*   *Expected maleimide-modified surfaces.*

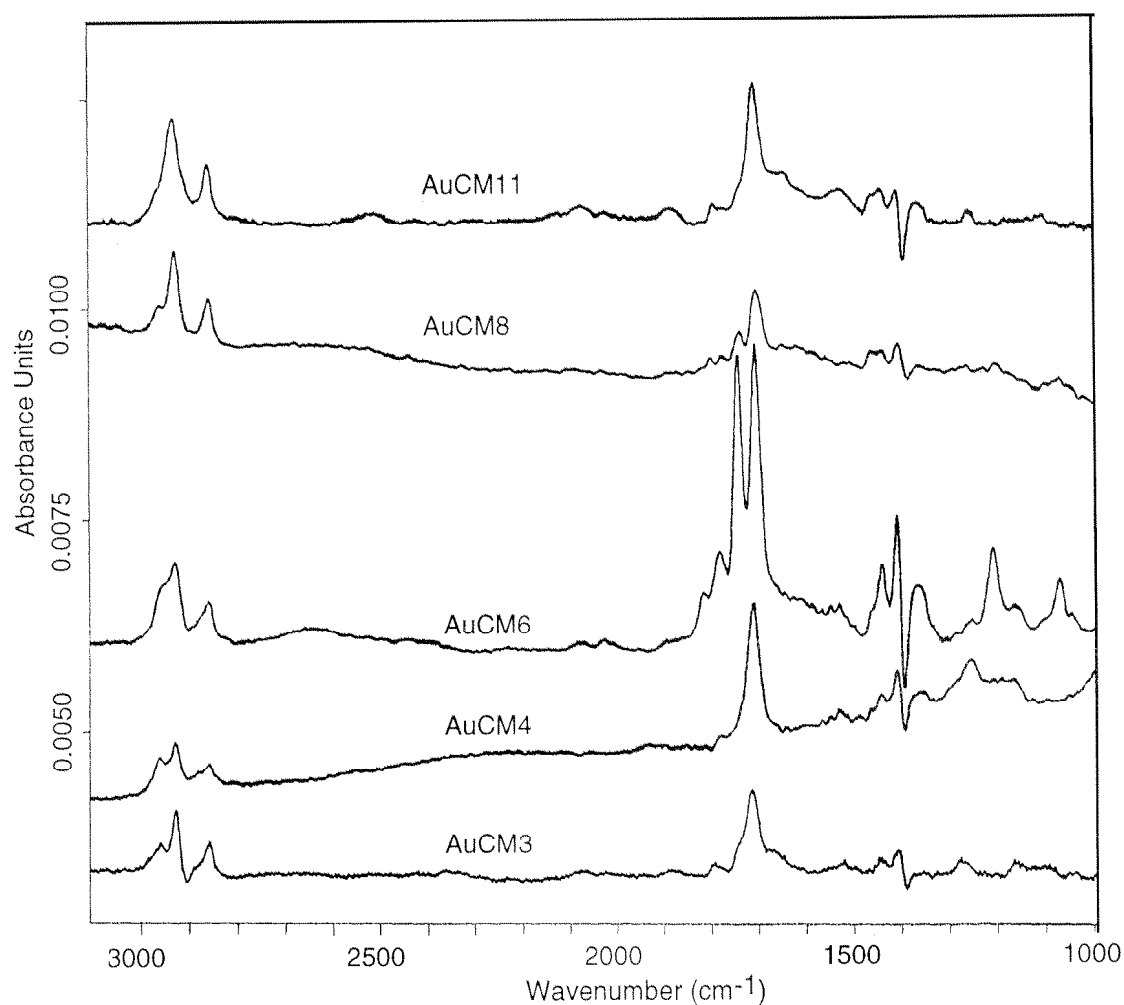*Figure 5-22*   *IRAS spectra of AuCMB and AuCMP.*

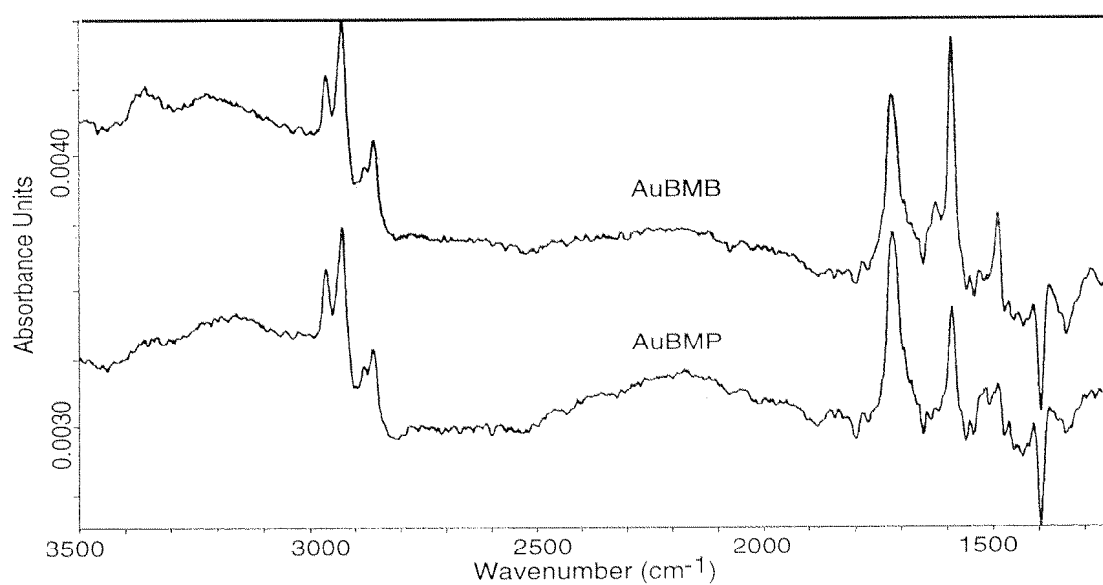*Figure 5-23   IRAS spectra of AuCM3, AuCM4, AuCM6, AuCM8, and AuCM11.*

Figure 5-24   IRAS spectra of AuBMB and AuBMP.
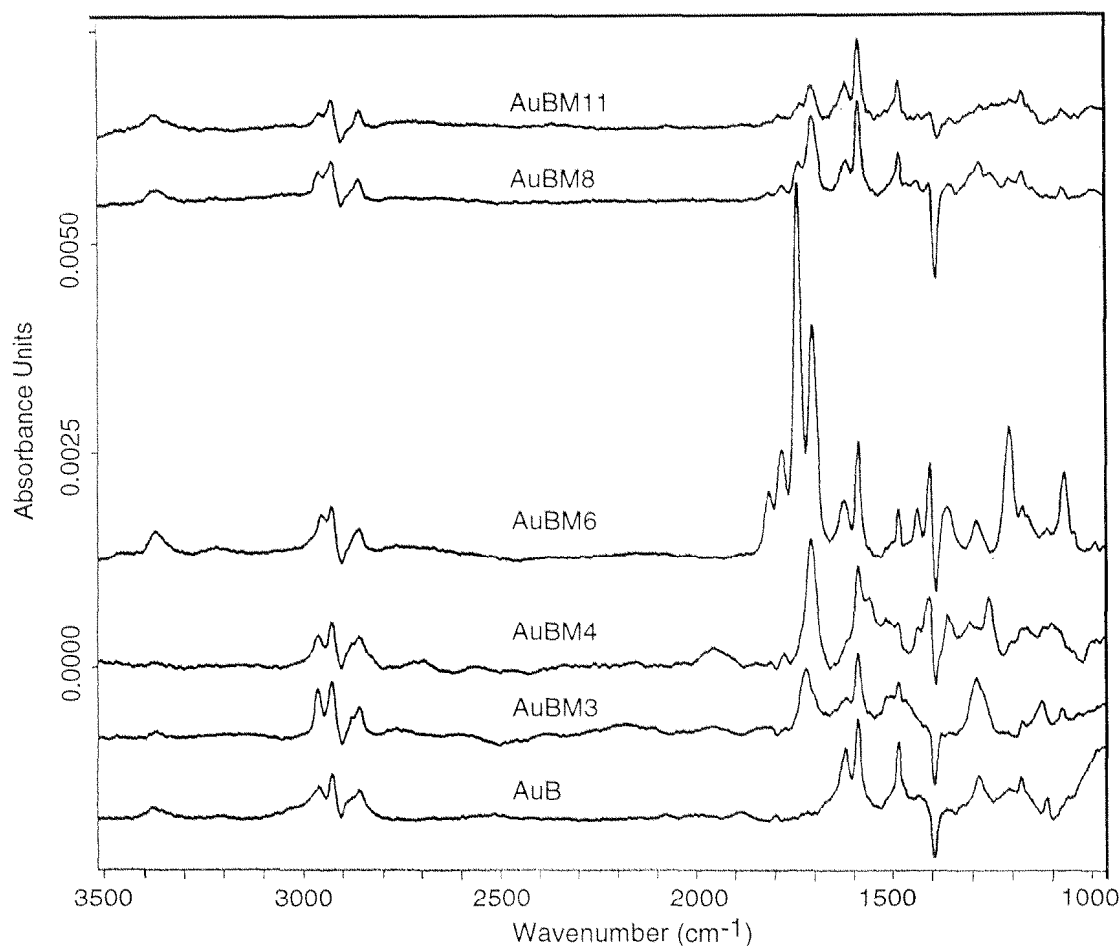
Figure 5-25 IRAS spectra of AuB, AuBM3, AuBM4, AuBM6, AuBM8, and AuBM11. Some peaks from 4-aminothiophenol (AuB) are observable on crosslinker-reacted surfaces.

1. C-H stretching vibrations

The C-H stretching vibrations can provide information about conformation and orientation of hydrocarbon chains. Studies of bulk and self-organized alkanethiols with different chain-lengths have shown that the asymmetric and symmetric CH_2 stretching bands are sensitive indicators for lateral interactions between long alkyl chains.[144] Their precise positions can be used to distinguish the all-trans (crystalline-like) and gauche (liquid-like) conformations of alkyl chains. It was suggested that the arrangement of hydrocarbon chains of the n-alkanethiol SAMs on Au and Ag with a chain-length between hexadecylthiol to docosylthiol is very similar to that in the bulk crystalline phase.

Table 5-6 lists the values from literature for the band positions of the symmetric and asymmetric CH_2 stretching vibrations of some alkylthiol SAMs on gold. It can be seen that the wavenumber decreases with increasing the hydrocarbon chain. By comparing band positions of bulk crystalline and liquid alkylthiols, it has been concluded that the

wavenumber correlates with the degree of order of the hydrocarbon chain: crystalline-like layers show absorption maxima between 2917 and 2920 cm^{-1} for the asymmetric and between 2849 and 2851 cm^{-1} for the symmetric CH_2 vibrations whereas very disordered layers show band positions up to 2928 cm^{-1} for the asymmetric and 2856 cm^{-1} for the symmetric CH_2 vibrations. Both the symmetric and the asymmetric CH_2 stretching vibrations thus show a similar trend, but in the case of the symmetric mode it is usually less pronounced.

Table 5-6   *IRAS band positions (cm^{-1}) of symmetric CH_2 and asymmetric CH_2 stretching modes of various alkylthiols from literature.*

HS(CH$_2$)$_n$CH$_3$	Type of sample	CH$_2$ asym stretch	CH$_2$ sym stretch	Ref.
n = 5	Self-assembled on gold	2921	2852	
n = 7		2921	2852	
n = 9		2920	2851	
n = 11		2919	2851	144
n = 15		2918	2850	
n = 17		2917	2850	
n = 21		2918	2850	
HS(CH$_2$)$_{22}$H	Crystalline in KBr	2918	2851	
HS(CH$_2$)$_7$CH$_3$	Liquid in a liquid prism cell	2924	2855	

The CH_2 symmetric and asymmetric stretch bands of the maleimide-modified surfaces are listed in Table 5-7. These values are in the region of liquid alkylthiols. Therefore we conclude that the alkyl chains of these ultrathin films are randomly ordered.

It is worth noting that careful attention must be paid to assigning and explaining the peaks in the C-H stretching regions because the peaks from the goal molecule often combine with those from the contaminants. If the reference Au sample is not fresh, negative peaks are often observed in this region. However, if the reference Au is fresh, stored not more than 30 min in argon after coating, C-H stretching peaks from the contaminants are often observable in this region.

Table 5-7   *IRAS band positions of CH₂ asymmetric and symmetric stretch for maleimide-modified Au surfaces*

Surface	CH₂ asym stretch	CH₂ sym stretch
AuCM3, AuBM3	2926, 2929	2855, 2859
AuCM4, AuBM4	2926, 2928	2858, 2858
AuCM6, AuBM6	2927, 2910	2859, 2861
AuCM8, AuBM8	2928, 2927	2858, 2858
AuCM11, AuBM11	2930, 2929	2858, 2858
AuCMC, AuBMC	2928, 2928	2858, 2858
AuCMB, AuBMB	2928, 2929	2859, 2858
AuCMP, AuBMP	2928, 2929	2859, 2859

2. C=O stretching vibrations

The heterobifunctional crosslinkers bearing succinimidyl ester and maleimidyl groups (SMP, SMB, EMCS, SMO, SMU, SMCC, SMBZ, and SMPB, see Appendix for molecular structures) have 4 peaks in the C=O stretch region (1700-1900 cm⁻¹) around 1710 (s), 1740 (s), 1780 (m), and 1820 (w) cm⁻¹. The peak 1710 cm⁻¹ is assigned to the asymmetric stretch of maleimide-C=O, 1740 cm⁻¹ to the asymmetric stretch of succinimide-C=O, 1780 cm⁻¹ to the ester group -(C=O)O-, and 1820 cm⁻¹ to the symmetric stretch of succinimide-C=O. The symmetric stretch band of maleimide is weak and may be hidden by the above 4 peaks with higher intensity. The expected structures after reaction with terminal amino groups are shown in Figure 5-21. The maleimidyl groups are immobilized on the surface but the succinimidyl ester groups are replaced by amide groups. From the suggested structures, the strong IR-active groups should be maleimide and amide. Therefore it is expected that:

• The maleimide stretching bands around 1710 cm⁻¹ will be observable but the succinimidyl ester stretching bands above 1740 cm⁻¹ will disappear.

• The amide I around 1660 cm⁻¹ and/or amide II around 1540 cm⁻¹ will be observable.

In fact, the experimental results in Figures 5-23 and 5-25 show some differences from the above suggestions. They are discussed below. (In order to avoid repetition, the functional groups attached on AuC or AuB surfaces exhibit the similar behavior in IRAS spectra and are discussed together, since the background spectra of AuC and AuB are different.)

Firstly, the band at ~1710 cm⁻¹ is observable for all maleimide-modified surfaces, pointing to the existence of maleimidyl groups. The wavenumber of this band decreases from maleimidyl propionoyl group (M3) at 1717 cm⁻¹ to maleimidyl octanoyl group (M8) at 1705 cm⁻¹, and then increases to 1710 cm⁻¹ for maleimidyl undecanoyl group (M11). This may be related to the interaction between the maleimide group and the amide group. The shorter alkyl chain stiffens the maleimide bond and thus increases the stretch band. The maleimidyl phenyl group (MB or MP) modified surfaces show this band around 1720 cm⁻¹ due to the direct connection of benzene to the imide group (Figures 5-22 and 5-24). Surfaces with M3, M4, MC, MB, and MP groups have only this band in the region 1700 ~ 1900 cm⁻¹, in agreement with the suggested structures in Figure 5-21. However, surfaces AuCM6, AuCM8, AuBM6, and AuBM8 show additional multiple bands in this region, similar to their precursors, EMCS and SMO, respectively. M11 pendant surfaces show polymorphism in this region. AuCM11 shows a single peak at 1710 cm⁻¹, while AuBM11 has two peaks at 1710 and 1736 cm⁻¹.

Table 5-8   *The C=O stretching vibration bands of maleimide-modified surfaces.*

Surface	Frequency (cm⁻¹)	Surface	Frequency (cm⁻¹)
AuCM3	1717	AuBM3	1716
AuCM4	1712	AuBM4	1710
AuCM6	1707, 1745, 1784, 1822	AuBM6	1706, 1745, 1786, 1821
AuCM8	1705, 1743, 1783, 1820	AuBM8	1707, 1745, 1783, 1821
AuCM11	1710	AuBM11	1710, 1736
AuCMC	1715	AuBMC	1714
AuCMB	1723	AuBMB	1719
AuCMP	1721	AuBMP	1721

Secondly, the weak intensities or disappearance of amide I around 1670 cm⁻¹ and/or amide II around 1530 cm⁻¹ for maleimide-modified surfaces are unexpected. Amide II bands are somewhat stronger than amide I. Sometimes a medium and broad band of amide II can be found on AuCM6 (Figure 5-26) and AuBM6. The SAMs bearing amide groups on Au surfaces have been reported to exhibit strong or medium peaks of amide I and/or amide II.[126] However, the amide bonds here were produced from the surface reaction, different from the self-assembling process. The orientations of amide groups can be quite different. We believe that the orientation of amide groups makes amide I and II bands weak or missing. Similarly, the very weak or even missing bands of the benzene ring stretching

modes at ~1590 and ~1488 cm^{-1} on AuCMB and AuCMP surfaces may also be attributed to the orientation of the benzene group (Figures 5-22 and 5-24).

The remaining important bands are the C-N and/or C-N-C stretching modes. M4, M6, and M8 pendant surfaces show two peaks at ~1410[145,146] and ~1370 cm^{-1} with medium intensities. They can be assigned to the C-N-C symmetric stretch and C-N stretch modes.
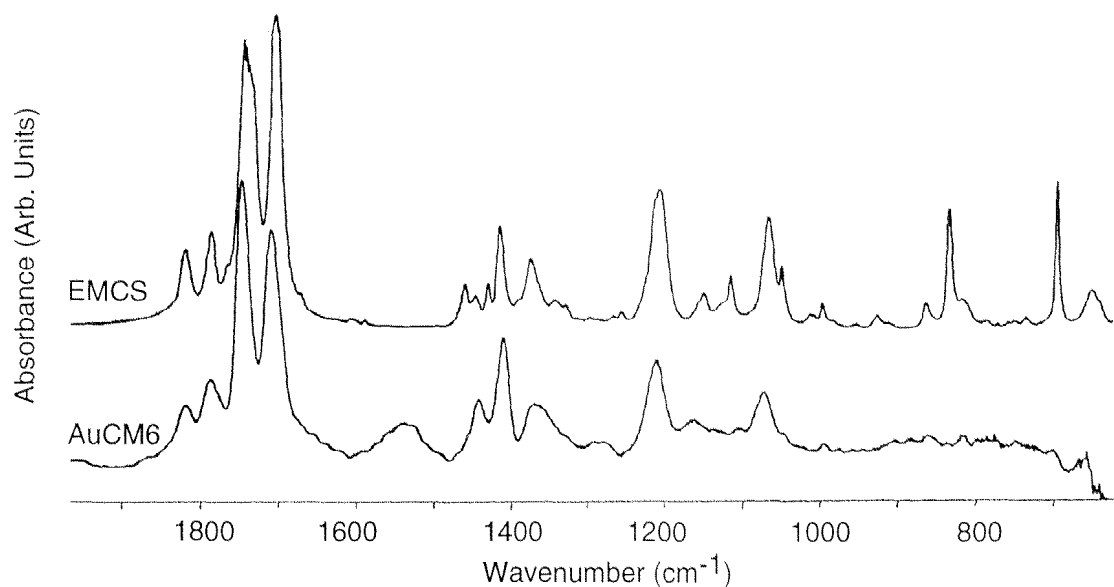

Figure 5-26   Comparison of the IR spectrum of EMCS in KBr (upper) and the IRAS
               spectrum of AuCM6.

Why do the spectra of M6, M8, and M11 pendant surfaces show multiple bands in the region 1700-1900 cm^{-1}, different from other derivatives? We compared the IRAS spectrum of the typical surface AuCM6 with the IR spectrum of its precursor EMCS (in KBr), and found that nearly every peak on AuCM6 has its correspondent one in EMCS (KBr) (Figure 5-26 and Table 5-9). In the region 1700-1900 cm^{-1}, all four peaks at 1707, 1745, 1784, and 1821 cm^{-1} on AuCM6 match those peaks in EMCS (KBr). Even in the lower frequency region, 1442 (CH$_2$ bending), 1410 (symmetric maleimide C-N-C stretching), 1370 (C-N stretching), 1210 (asymmetric succinimide C-N-C stretching), and 1071 (ester C-O-N stretching) cm^{-1} also have their correspondent peaks in EMCS. Does it just mean a physical adsorption of EMCS on amino-terminated surface? Although we can not exclude this assumption absolutely, the following evidences support the chemical reaction but not the physical adsorption. These arguments are: The decrease or disappearance of the NH$_2$ deformation band at 1623 cm^{-1} on AuB-based surfaces points to the chemical conversion of NH$_2$ to other amine types, either secondary or tertiary amines; the amide II band on AuCM6 (Figure 5-26) definitely confirms the formation of peptide bond; the incubation of samples

in organic solvents over 24 h does not remove the succinimidyl ester group; the other competitive chemical reaction, like with acetyl anhydride for acetylation of amino groups, does not remove the succinimidyl ester group.

Table 5-9   Frequencies (cm^{-1}) and assignments for EMCS in KBr pellets and AuCM6.

Frequency (cm^{-1})		Assignment*
EMCS in KBr	AuCM6	
3504 w		2 x 1741
3092 m		mal CH stretching
2946 s		asym CH_2 stretching
2871 m		sym CH_2 stretching
1817 m	1821 w	sym suc C=O stretching
1784 m	1784 m	ester C=O stretching
1741 s	1745 s	asym suc C=O stretching
1701 s	1707 s	asym mal C=O stretching
	1540 w, b	amide II
1445 w	1442 w	CH_2 deformation
1413 m	1410 m	sym mal C-N-C stretching
1372 m	1370 w	mal C-N stretching
1205 s	1210 m	asym suc C-N-C stretching
1065 s	1071 w	ester C-O-N stretching
863 m		suc CH_2 rocking
833 m		mal CH bending
695 m		mal ring deformation
650 m		suc ring deformation

*Abbreviations: mal, maleimide; suc, succinimide; sym, symmetric; asym, asymmetric; other abbreviations in Table 5-3.

Another possibility is the formation of by-products from side-reactions. It is well known that the main organic reaction in bulk states is accompanied by many side reactions. The surface organic reaction should have a similar behavior. The possible reactive sites for EMCS are the succinimidyl ester and the double bond of the maleimidyl group. As pointed out before, the reaction of amino groups with maleimides becomes significant only when the pH is larger than 7.0. However, here the reaction is carried out in organic solution, the

reaction mechanism could be more complicated. For EMCS and SMO, maybe the molecular structures approaching the surface have strong interactions with the surface and thus promote the side reaction. In this case, both reactions occur, and the resulted bonds are -C(=O)—NH- and -CH—NH-. The peptide bond has been definitely confirmed by the amide II band from IRAS spectra; there is no direct evidence, however, to prove the bond -CH—NH-. The indirect evidences can be obtained from the yielded products. Three products can be anticipated: maleimidyl-pendant, succinimidyl ester-pendant, and bridging structures. The succinimidyl ester is definitely confirmed by the ester stretching bands at 1745, 1784, and 1821 cm^{-1}. The existence of maleimide is definitely confirmed by combination of IRAS, XPS, and NEXAFS measurements: the maleimide IR band at 1707 cm^{-1}, the imide-C in XPS (C 1s at 289.0 eV), and the double bond C=C from NEXAFS measurements (Figure 5-27). The angle-dependent NEXAFS measurements (Figure 5-27) also indicate that all groups are randomly arranged. Although the bridging structure can not be excluded definitely, we suggest that the steric hindrance blocks the formation of such a bridge with a very high tension. Thus, even if it exists, it will be a small portion on the surface. As described above, the surface reactions of amino groups with EMCS and SMO produce a mixture of both maleimidyl and succinimidyl ester groups (Figure 5-28). The molar ratios of maleimide to succinimidyl ester can be estimated to 1 and 4 for M6 and M8 pendant surfaces, respectively, according to the intensity ratios of the peaks at 1707 and 1745 cm^{-1}.
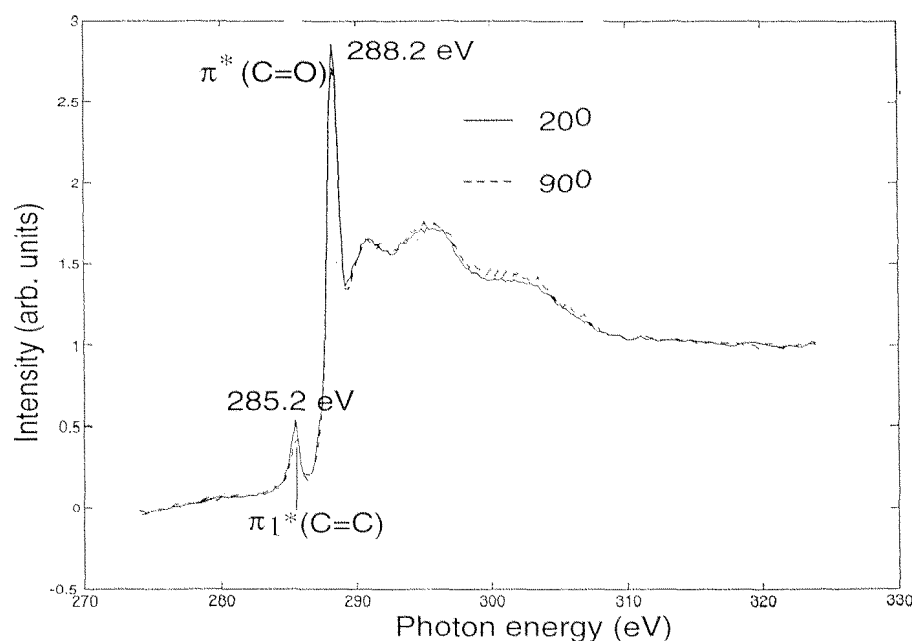

Figure 5-27   NEXAFS spectra of AuCM6 at the C 1s edge recorded for two angles of incidence. The overlapping of two lines between grazing (20^0) and normal (90^0) angles indicates the random orientation of maleimidyl groups.

Additional reactions were carried out to examine the side reaction. The reaction of amino-terminated SAMs with molecules bearing the single succinimidyl ester group such as N-succinimidyl hexadecanoate (SH) occurs easily under the mild reaction conditions. In the case of maleimidyl molecules such as N-ethyl maleimide, no reaction occurs at room temperature, but reactions do occur at a higher temperature (above 50 ^{0}C). The side-reaction of terminal NH$_2$ with maleimide is also observed on M3 and M4 pendant surfaces if the reaction temperature is raised to 50 ^{0}C. Figure 5-29 shows the IRAS spectra of M3 and M4 pendant surfaces produced at 50 ^{0}C. The shoulder peak around 1740 cm^{-1} is clearly observable. This hints that the relative rate of side reaction relates not only to the molecular structure (e.g. EMCS) but also to the reaction temperature.
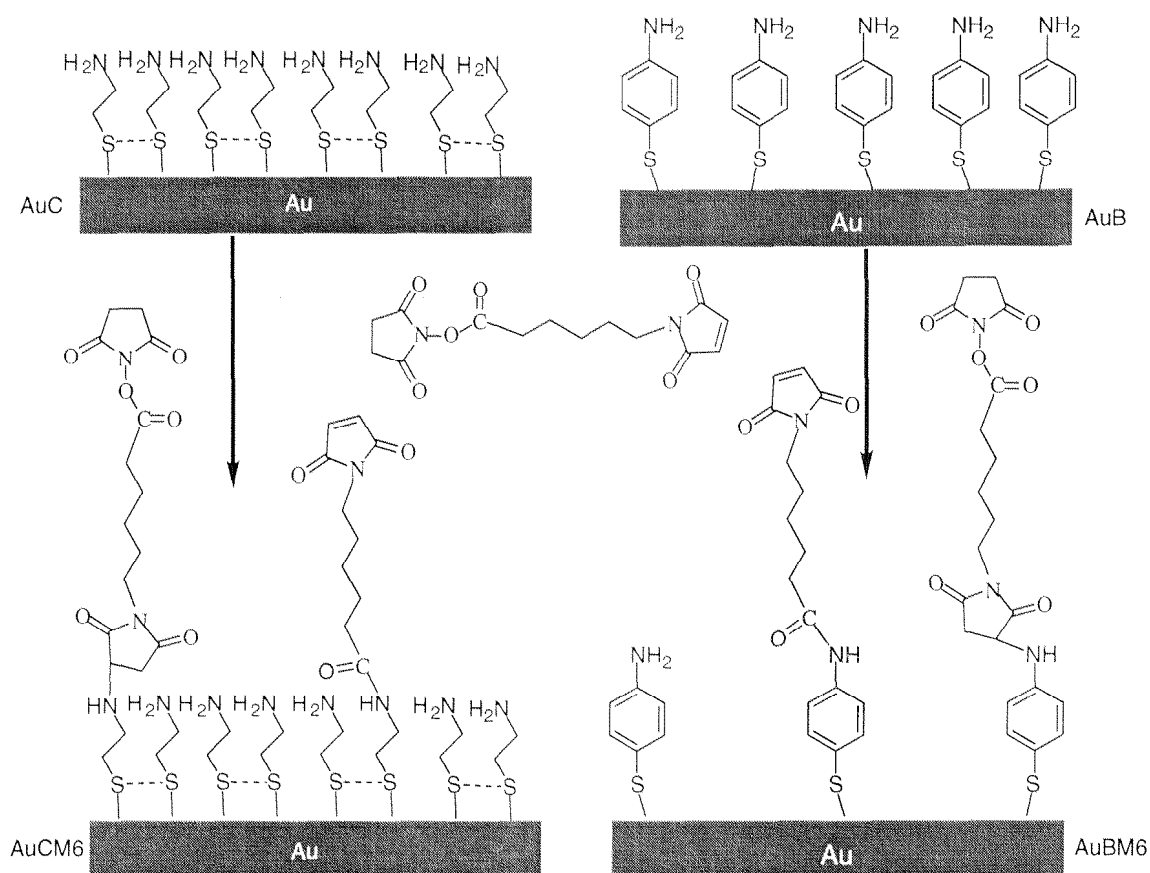

Figure 5-28   Side reactions on AuCM6 and AuBM6: Both succinimidyl ester and maleimidyl groups react with terminal NH$_2$ groups.
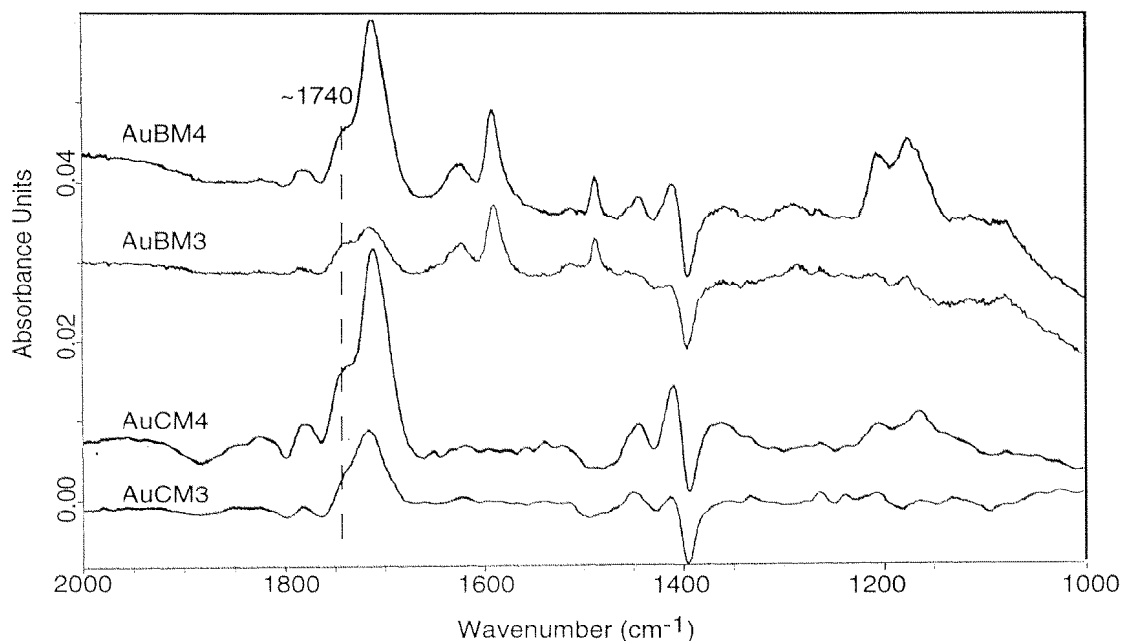
Figure 5-29   IRAS spectra of AuCM3, AuCM4, AuBM3, and AuBM4 show peaks around 1740 cm^{-1}, the evidence for the existence of succinimidyl ester. These surfaces were produced at 50 ^{0}C.

5.5.3.2.2 Reaction yields

The reaction yield can be calculated from IRAS spectra. Specially for 4-ATP, the unchanged benzene ring stretching peak at 1591 cm^{-1} is an internal reference. The decrease or disappearance of the NH$_2$ deformation peak at 1623 cm^{-1} can be used to calculate the reaction yield. The absorbance ratios for the two bands on AuB are from Beer's law:

$$A_1/A_2 = a_1bc/a_2bc = a_1/a_2$$

where A$_1$ is the absorbance of NH$_2$ at 1623 cm^{-1} (peak 1), A$_2$ the absorbance of benzene at 1591 cm^{-1} (peak 2), a$_1$ and a$_2$ the absorptivities of peaks 1 and 2 respectively, b the monolayer thickness, and c the surface concentration of 4-ATP.

After the reaction with crosslinkers, some or all amino groups are transformed to amide groups. This causes the intensity of the NH$_2$ deformation at 1623 cm^{-1} to decrease or disappear. It is reasonable to assume that the reaction has no large effect on the benzene ring structure and that no aminothiol SAMs are released during the reaction. Therefore, the absorptivities a$_1$ and a$_2$, and the benzene concentration c' of the SAM are the same as that before the reaction (we use c' instead of c because the individual sample does not have the identical surface concentration).

$$A_1'/A_2' = a_1bc_1/a_2bc' = a_1c_1/a_2c' = (A_1/A_2)(c_1/c')$$

where A_1' and A_2' are the absorbances of peaks 1 and 2 after reaction, c_1 the surface concentration of NH_2, and c' the surface concentration of benzene.

$$\text{Reaction yield} = (c'-c_1)/c' = 1 - (A_1'/A_2')\cdot(A_2/A_1)$$

where A_1/A_2 and A_1'/A_2' can be easily determined from the IRAS spectra.

The above formula can only be applied to AuB-based surfaces and are not suitable for the calculation of AuC-based reactions. We estimate the reaction yields of AuC-based reactions by using the formula in Section 4.3.4. deduced from the XPS measurements. The atomic ratio (N/S or others) of each AuC-based surface is employed to calculate the reaction yield.

Table 5-10   *Reaction yields of AuB-based reactions calculated from IRAS spectra and those of AuC-based surface reactions deduced from XPS measurements.*

Reaction	Yield (%)	Reaction	Yield (%)
AuB → AuBM3	40 ~ 70	AuC → AuCM3	50 ~ 80 (via N/S)
AuB → AuBM4	40 ~ 80	AuC → AuCM4	50 ~ 90 (via N/S)
AuB → AuBM6	50 ~ 90	AuC → AuCM6	60 ~ 100 (via N/S)
AuB → AuBM8	30 ~ 45	AuC → AuCM8	30 ~ 60 (via N/S)
AuB → AuBM11	20 ~ 40	AuC → AuCM11	30 ~ 50 (via N/S)
AuB → AuBMB	40 ~ 80	AuC → AuCMB	50 ~ 80 (via N/S)
AuB → AuBMP	40 ~ 80	AuC → AuCMP	50 ~ 80 (via N/S)
AuB → AuBSC	60 ~ 90	AuC → AuCSC	60 ~ 90 (via N/S)
AuB → AuBTP	30 ~ 50	AuC → AuCTP	40 ~ 60 (via N/S)
AuB → AuBS8	40 ~ 60	AuC → AuCS8	40 ~ 60 (via C=O/N)
AuB → AuBIA	40 ~ 70	AuC → AuCIA	50 ~ 90 (via I/N)

The reaction yields of AuB- and AuC-based surfaces are listed in Table 5-10. They are in a range of values, similar to the chemical reaction in solution. Although the complete conversion can be achieved through extending the reaction time and/or via other stringent conditions such as stronger sonication and/or higher temperature, the molecular loss from the surface also gets greater, and thus the surface coverage becomes smaller.

5.5.3.2.3 XPS characterization

Five elements are detectable on these maleimide-modified surfaces: C, N, O, S, and Au. The average atomic concentrations of each surface are indicated in Figures 5-30 and 5-31,

respectively. AuCM6 has the highest C content and the lowest Au content on AuC-based surfaces in Figure 5-30. The same tendency is shown in Figure 5-31 for AuBM6 on AuB-based surfaces. These point to the highest surface coverages of M6 pendant species among maleimide-modified surfaces.
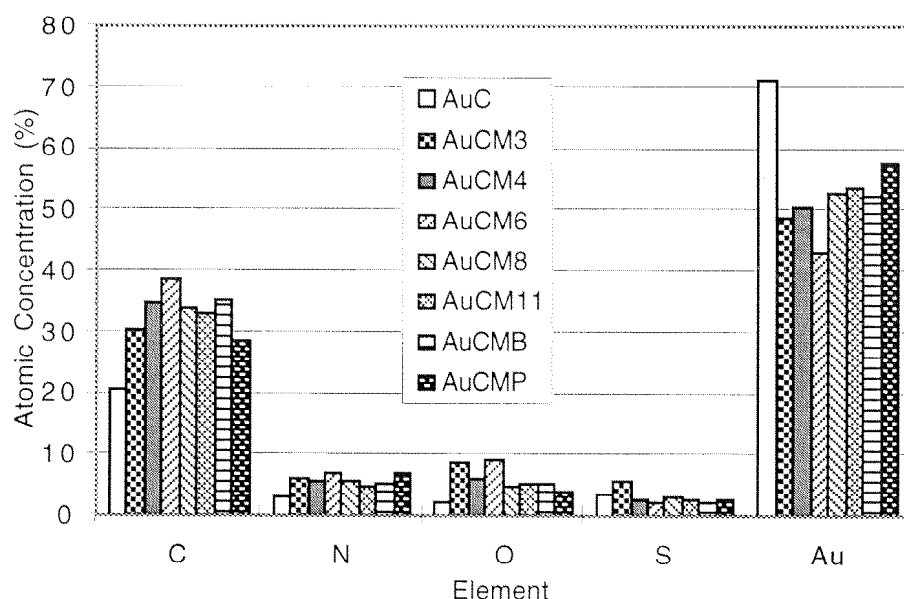

Figure 5-30   The mean values of atomic concentrations of AuC-based surfaces calculated from XPS measurements of three samples for each surface.
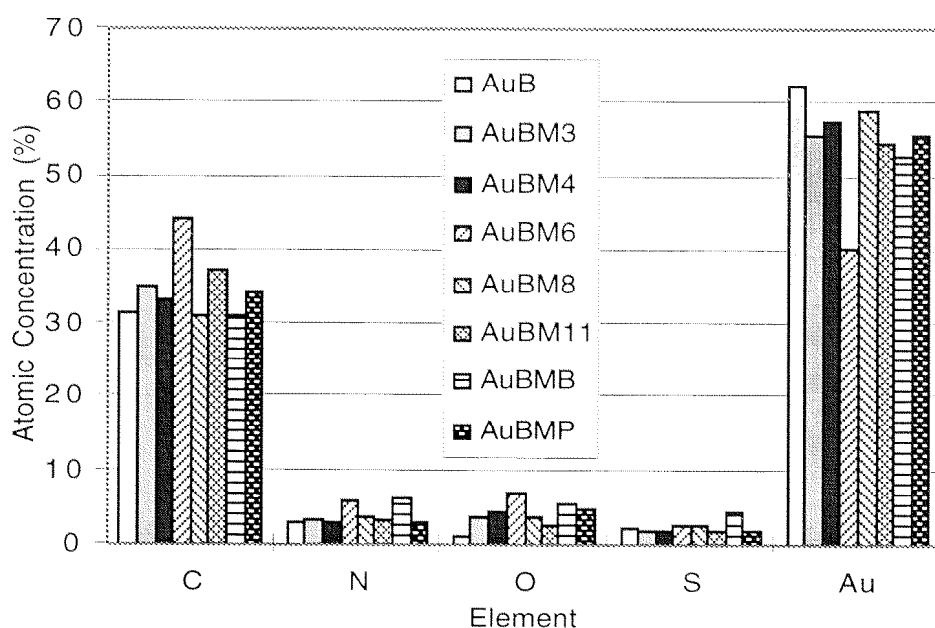

Figure 5-31   The mean values of atomic concentrations of AuB-based surfaces calculated from XPS measurements of three samples for each surface.

The chemical shifts indicate the oxidation states of the elements. Before giving the fitting results, the chemical shifts of C 1s, O 1s, and N 1s are described below.

C 1s binding energies

1. Alkyl carbon bound to itself and/or hydrogen only, no mater what hybridization, gives C 1s = 285.0 eV (often used as a binding energy reference).
2. Aryl carbon bound to itself and/or hydrogen only gives C 1s = 284.5 eV.
3. Oxygen and nitrogen induce shifts to higher binding energy by 1.5 eV per C-O (or C-N) bond.
4. Carbonyl carbon (C=O in aldehyde, ketone, and amide) gives C 1s = 288.0 eV.
5. Imide carbon gives C 1s = 289.0 eV.

Table 5-11   Summary of some C 1s binding energies.

Group	E_B of C 1s
aryl-C	~ 284.5 eV
alkyl-C	~ 285.0 eV
C-O, C-N	~286.5 eV
C=O	~ 288.0 eV
imide-C	~ 289.0 eV

The deconvolution results of C 1s spectra are based on the carbon oxidation states in Table 5-11. On AuC-based surfaces, the carbon oxidation state can be deconvoluted into 4 peaks except the aryl-C. On AuB-based surfaces, C 1s can be deconvoluted to 5 peaks. The exceptions are AuBMB and AuBMP fitted with only 4 peaks without the alkyl C 1s. It is worth noting that the variable reaction yields make the reproducible evaluation difficult.

O 1s binding energies

O 1s from most organic functionalities fall within a narrow range of ~2 eV around 533.0 eV. The extremes are seen in carboxyl and carbonate groups in which the singly bound oxygen has the higher binding energy. In our case, the carbonyl O 1s from amide and imide is around 533.0 eV.

N 1s binding energies

Many common organic nitrogen functionalities give N 1s binding energies in the narrow region 399 - 401 eV. These include -CN, $-NH_2$, amide $-CONH_2$ and imide-N. Quarternization, as in $-NH_3^+$, only increases the binding energy by ~1.5 eV above that of the free amine.

The binding energies of S and Au are similar to those on AuC and AuB and not discussed again.

Among the 5 detectable elements, C, N, O, S, and Au, the most informative peak is C 1s. The other 4 elements do not show significant features from AuC (or AuB) and the lower contents of N, O, and S enable the deconvolution uncertain. Thus the deconvolution results of N, O, and S are omitted. The fitting results of C 1s on the maleimide-modified surfaces are shown in Figures 5-32 and 5-33 and listed in Table 5-12. On AuC-based surfaces, AuCM3 and AuCM4 have similar C 1s shapes and the fitting results are also similar. AuCM6 showing the best resolution of C 1s at 289.0 eV indicates the highest coverage of imide groups on the surface. With increasing the carbon chains to AuCM8 and AuCM11, the hydrocarbon contents increase. On the two phenyl maleimide-modified surfaces, AuCMB and AuCMP, the aromatic C 1s at 284.5 eV merges together with hydrocarbons at 285.0 eV. On AuB-based surfaces, an additional peak of aromatic C 1s at 284.5 eV is isolated. They show the similar deconvolution trends to AuC-based surfaces.
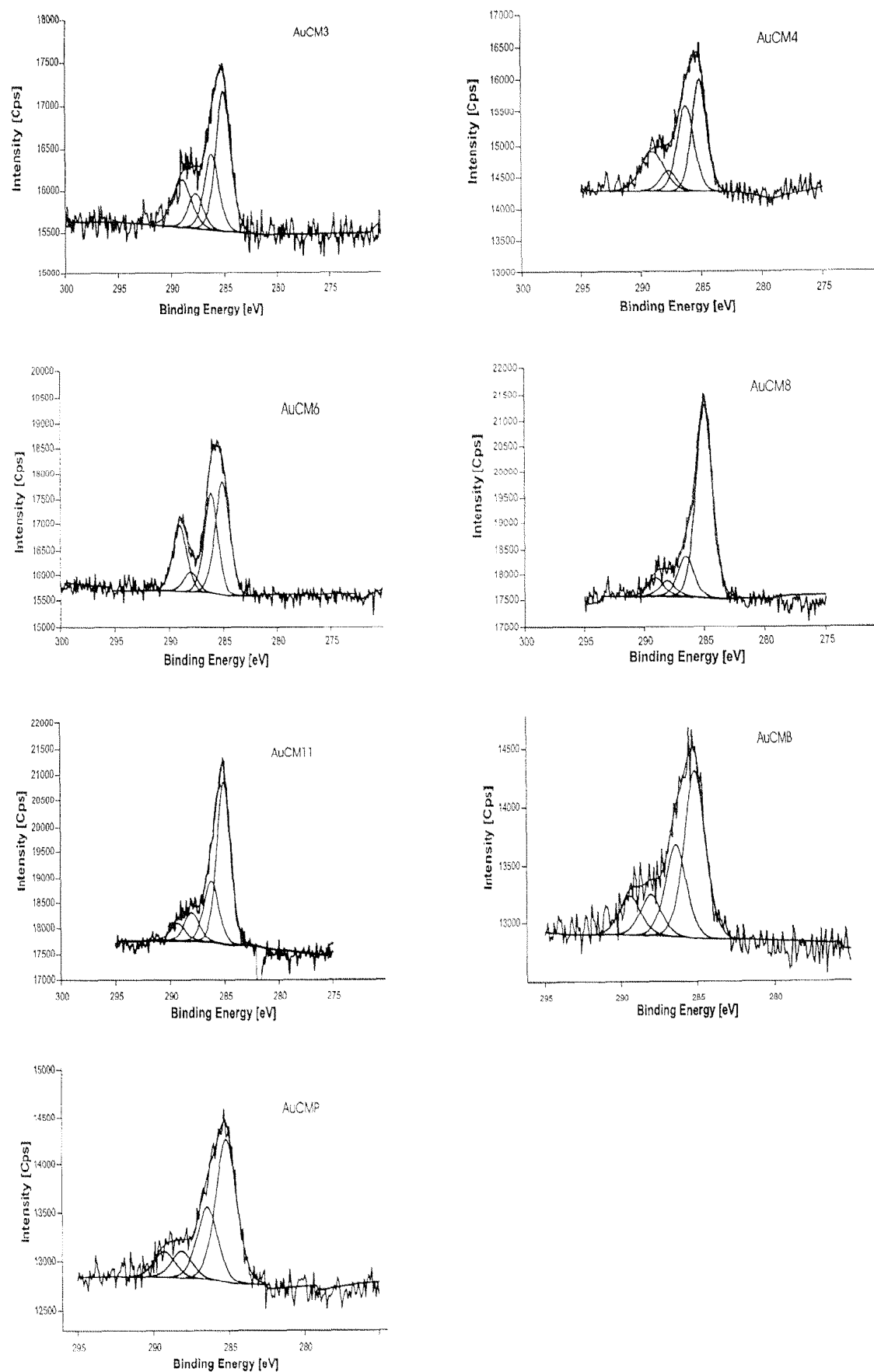
Figure 5-32   *Deconvolutions of XPS C 1s spectra on AuC-based, maleimide-modified surfaces.*
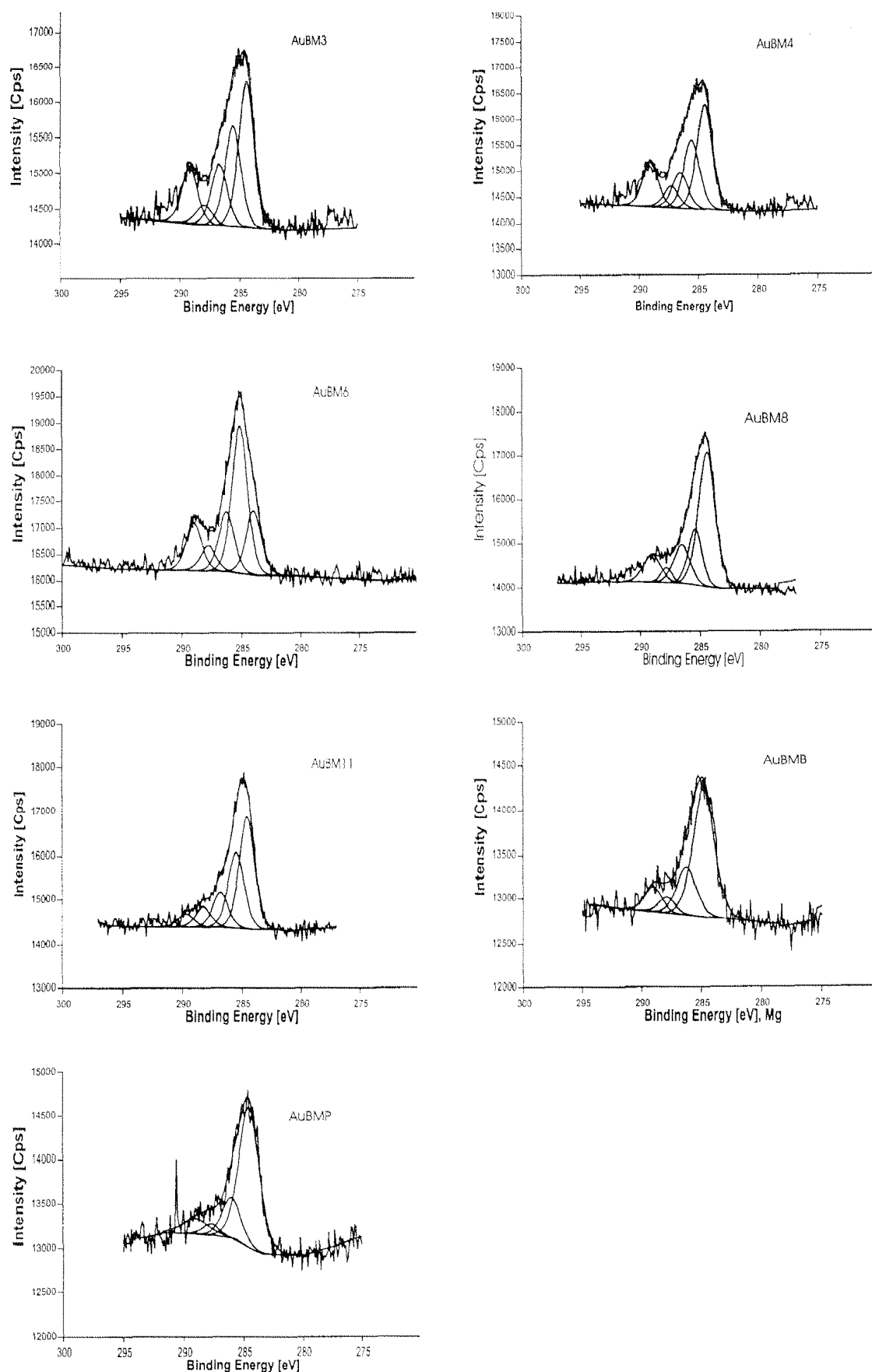
Figure 5-33   Deconvolutions of XPS C 1s spectra on AuB-based, maleimide-modified surfaces.

Table 5-12   *The deconvolution results of C 1s of Figures 5-32 and 5-33.*

Surface	C 1s region E_B(eV), %	Surface	C 1s region E_B(eV), %
AuCM3	285.1 (45) 286.2 (24) 287.7 (11) 289.0 (20)	AuBM3	284.6 (43) 285.5 (30) 286.8 (13) 288.2 (8) 289.4 (6)
AuCM4	285.1 (38) 286.2 (32) 287.7 (9) 289.0 (21)	AuBM4	284.4 (38) 285.5 (25) 286.5 (13) 287.2 (8) 289.0 (16)
AuCM6	285.1 (40) 286.2 (32) 288.0 (7) 289.0 (21)	AuBM6	284.0 (19) 285.1 (43) 286.3 (17) 287.8 (7) 289.0 (14)
AuCM8	285.0 (67) 286.3 (19) 287.8 (6) 289.0 (8)	AuBM8	284.4 (52) 285.4 (18) 286.5 (15) 287.8 (4) 289.0 (11)
AuCM11	285.1 (62) 286.3 (17) 287.8 (9) 289.0 (12)	AuBM11	284.6 (43) 285.5 (30) 286.8 (13) 287.8 (8) 289.4 (6)
AuCMB	285.1 (50) 286.4 (27) 288.0 (12) 289.3 (12)	AuBMB	284.5 (67) 286.0 (18) 287.7 (5) 289.0 (10)
AuCMP	285.2 (55) 286.4 (27) 288.1 (9) 289.3 (9)	AuBMP	284.8 (64) 286.2 (20) 287.9 (6) 289.0 (10)

5.5.3.2.4 Film thickness and contact angle measurements

The film thickness was measured with ellipsometry. Normally, if the film is homogenous and densely packed, the film thickness will increase with increasing the alkyl chain. The measurements, however, showed that AuCM6 and AuBM6, not AuCM11 and AuBM11, had the thickest films on AuC- and AuB-based surfaces respectively. This is in accordance with XPS and IRAS measurements, pointing to the largest surface coverages on M6 pendant surfaces.

The advancing contact angles on these surfaces are around 50^0.

Table 5-13   *The film thickness and contact angle on some maleimide modified Au surfaces.*

| Surface	Thickness ± 7 (Å)	Contact angle $\pm 4^0$
AuC	7	45^0
AuCM3	23	56^0
AuCM4	26	57^0
AuCM6	35	60^0
AuCM8	22	59^0
AuCM11	21	51^0
AuB	10	50^0
AuBM3	23	58^0
AuBM4	26	57^0
AuBM6	36	58^0
AuBM8	27	54^0
AuBM11	25	53^0

5.6 Self-assembled monolayers of N,N'-bis(maleimidylhexanoyl) cystamine (AuBMHC)

In Section 5.5.3.2, we discussed the possible surface structures of AuCM6 and AuBM6 mainly based on comparing their IRAS spectra with the IR spectrum of their precursor molecule EMCS in KBr. We suggested a mixture of maleimide and succinimidyl ester groups on the surface due to the side reaction of NH_2 with maleimide. However, other

factors such as molecular orientation can also influence the IRAS spectrum. In order to prove our suggestion, two compounds, N,N'-bis(maleimidylhexanoyl)cystamine (BMHC) and N-(maleimidylhexanoyl)aniline (MHA) were synthesized and purified. BMHC is the product expected on AuCM6 and can be self-assembled on Au (briefly as AuBMHC). Studies of the IR spectrum of BMHC in KBr and the IRAS spectrum of its SAMs on Au surfaces give the details of the peak assignments and the orientation of maleimidyl groups. Comparison of the IRAS spectra between AuCM6 and AuBMHC provides more evidence for the mixed species on AuCM6. The orientation of maleimide on AuBMHC is estimated by using a method developed by K. Iida.[81] MHA is just a model compound synthesized for comparison of the maleimide C=O stretching bands with AuBM6.

5.6.1 Synthesis of N-(maleimidylhexanoyl)aniline (MHA) and N,N'-bis(maleimidylhexanoyl)cystamine (BMHC)

1. N-(Maleimidylhexanoyl)aniline (MHA)
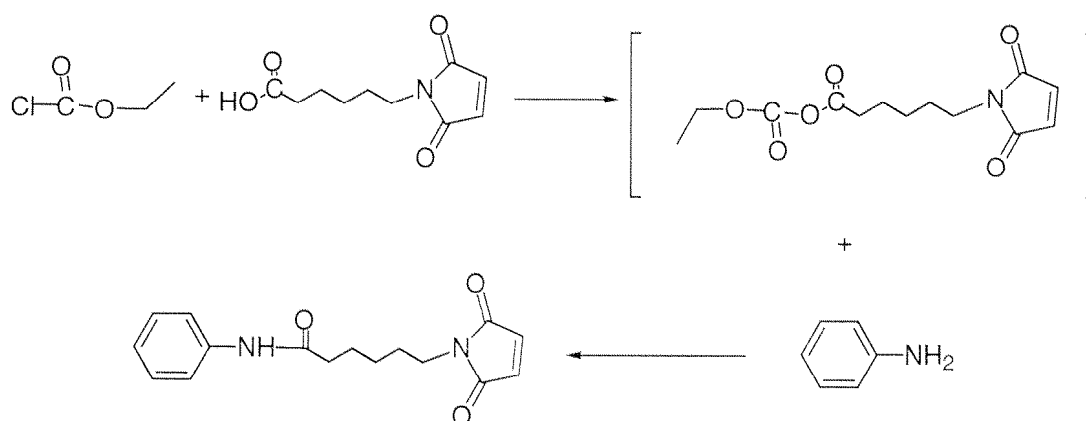
MHA is a new compound synthesized according to a method used by Collioud et al.,[147] 6-Maleimidylhexanoic acid (0.21 g, 1 mmol) was dissolved in 10 ml of DMF and cooled to -10 °C under nitrogen. Triethylamine (168 µl, 1.2 mmol) was added to the stirred solution followed by dropwise addition of ethyl chloroformate (113.4 µl, 1.2 mmol) in 1 ml of DMF. The reaction mixture was stirred for 15 min and the aniline (103.4 µl, 1.1 mmol) in 1 ml DMF was slowly added. After 20 min stirring, the solution was allowed to warm to ambient temperature and was stirred for 1.5 h. The reaction mixture was poured into 20 ml of 1 M NaCl on ice under vigorous stirring. The solid product was collected by filtering and washed with enough water. After drying, a white solid of 0.1 g was obtained.

NMR (CDCl$_3$) δ 7.55 (d, 2 H, ArH), 7.38 (t, 2 H, ArH), 7.19 (s, 1 H, NHC=O), 7.16 (t, 1 H, ArH), 3.52 (t, 2 H, CH$_2$N), 2.37 (t, 2 H, CH$_2$C=O), 1.72 (m, 4 H, CH$_2$, CH$_2$), 1.38 (m, 2 H, CH$_2$)
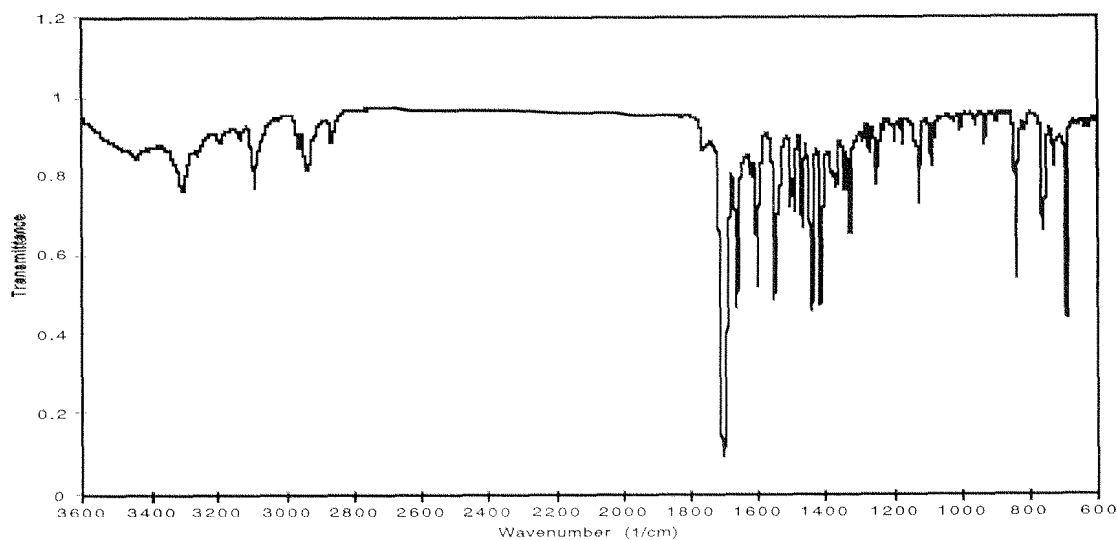
Figure 5-34   The IR spectrum of MHA in KBr pellets.

Table 5-14   Frequencies (cm⁻¹) and assignments of MHA in KBr pellets (Abbreviations in Tables 5-3 and 5-9).

Frequency (cm⁻¹)	Assignment	Frequency (cm⁻¹)	Assignment
3442 w	1704+1740	1601 s	aryl CC stretching
3310 m	asym amide NH stretching	1551 s	amide II
3306 s	sym amide NH stretching	1441 s	CH_2 bending
3261 w	amide I + aryl CC (1601)	1415 s	sym C-N-C stretching
3094 s	mal CH stretching	1370 w	C-N stretching
3070 w	aryl CH stretching	1328 m	aryl CC stretching
2937 s	asym CH_2 stretching	1251 m	amide III
2866 m	sym CH_2 stretching	1125 m	asym C-N-C stretching
1770 w	sym mal C=O stretching	840 s	mal CH bending
1704 vs	asym mal C=O stretching	762 m	aryl CC bending
1664 s	amide I	693 s	mal CC bending
1620 w	NH deformation		

Infrared spectra and assignments of MHA are shown in Figure 5-34 and Table 5-14. The maleimide group exhibits only one strong peak at 1710 cm⁻¹ and weak shoulders above this frequency, quite different from AuBM6. The assignments are based on comparing similar compounds and are not discussed in detail.

2. N, N'-Bis(maleimidylhexanoyl)cystamine (BMHC)
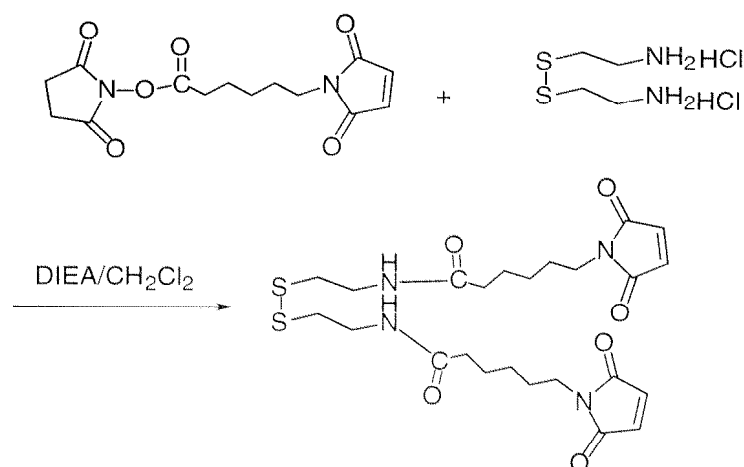
BMHC is a new compound synthesized according to a method used by Doughty et al.[148] A solution of EMCS (62 mg, 0.2 mmol) in 1 ml CH_2Cl_2 was added dropwise to a stirred suspension of cystamine dihydrochloride (23.0 mg, 0.1 mmol) and diisopropylethylamine (72 μl, 0.42 mmol) in CH_2Cl_2 (2 ml) under nitrogen. After allowing the reaction mixture to stir for 16 h, the precipitated solid was removed by filtration, and the solvent of the filtrate was removed under reduced pressure to give a viscous oil. The crude residue was purified by flash chromatography (silica gel, 2.5 x 30 cm, EtOH:Ethyl acetate = 1 :9) to afford a white solid (25 mg).

NMR (CDCl$_3$) δ 6.70 (s, 4 H, mal H), 6.42 (t, CONH), 3.52 (m, 8 H, CH_2NH, CH_2N), 2.82 (t, 4 H, CH_2S), 2.21 (t, 4 H, $CH_2C=O$), 1.63 (m, 8 H, CH_2, CH_2), 1.32 (m, 4 H, CH_2).
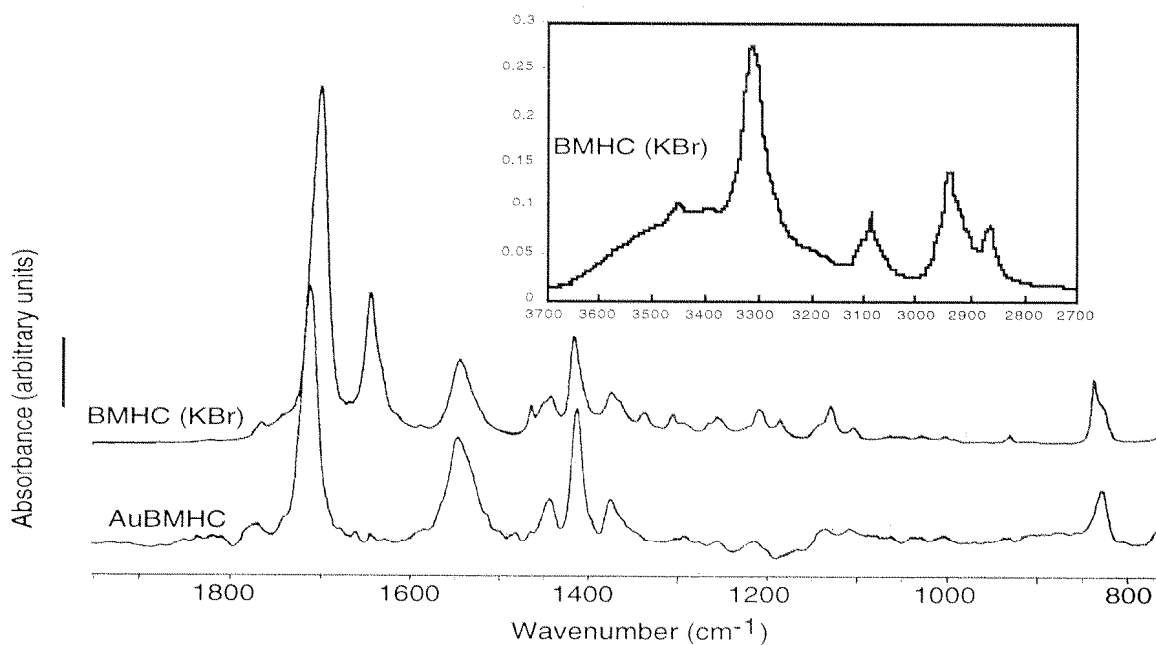

Figure 5-35   IR spectra of BMHC in KBr pellets and its SAMs on Au.

5.6.2 Infrared spectra of BMHC in KBr and in SAMs

Table 5-15   *Frequencies and assignments of IR bands for BMHC in KBr pellets and of IRAS bands for AuBMHC (Abbreviations in Tables 5-3 and 5-9).*

Frequency (cm^{-1})		Assignment
BMHC in KBr	on Au	
3450 b		1700 + 1745
3310 vs		amide NH stretching
3093 m		mal CH stretching
2940 s		asym CH$_2$ stretching
2866 m		sym CH$_2$ stretching
1767 vw	1774 vw	sym imide C=O stretching
1700 vs	1712 s	asym imide C=O stretching
1646 s		amide I
1546 s	1543 m, b	amide II
1443 w	1443 w	CH$_2$ bending
1418 m	1412 m	sym C-N-C stretching
1375 w	1377 w	C-N stretching
1337 w		CH$_2$ bending
1307 w		CH$_2$ bending
1254 w		amide III
1210 w	1217 vw	asym C-N-C stretching
1186 w		
1129 w		
838 m	830 w	mal CH bending
698 m		mal CC deformation

5.6.2.1 Peak assignments for the bulk (KBr) spectrum of BMHC

3500-2700 cm^{-1} region: The bulk spectra of BMHC (Figure 5-35 and Table 5-15) show a broad band at 3470 cm^{-1} attributable to the overtone of imide C=O stretching mode (1700 +1767); a weak, sharp peak at 3450 and a strong one at 3310 cm^{-1} are attributable to the amide N-H asymmetric and symmetric (amide A) stretching vibrations; three weaker bands are around 3100 cm^{-1} (3104, 3088, 3070), in which 3104 cm^{-1} can be assigned to the amide

B caused by the Fermi resonance-enhanced overtone of the amide II band at 1546 cm^{-1}, and 3088 and 3070 cm^{-1} to the asymmetric and symmetric vibrations of maleimidyl =C-H stretching mode; the peaks at 2939 (strong) and 2866 (medium) cm^{-1} are attributed to the asymmetric and symmetric stretching vibrations of methylene groups. Both of these methylene stretches are in close agreement with the reported values for a more liquid-like state, rather than the expected ideal crystalline-like state.

1800-1500 cm^{-1} region: The imide group -C(=O)N(O=)C- exhibits a strong asymmetric stretching band at 1700 cm^{-1} and a weak but broad shoulder around 1770 cm^{-1} attributable to the symmetric stretching mode. The amide carbonyl (C=O) functionality usually exists in a trans configuration with the N-H group, with the C=O stretching band (amide I) appearing very strongly at 1646 cm^{-1} and amide II at 1546 cm^{-1}. The different torsional motions involved in the amide II band for such a trans configuration are also believed to be responsible for the amide III band (1254 cm^{-1}), although it is usually much weaker compared to the amide I and II bands.

1500-1000 cm^{-1} region: It is difficult to exactly assign every peak in the fingerprinting regions. However, based on the references, we tentatively assign the peak at 1443 cm^{-1} (weak) to CH$_2$ deformation band, 1418 cm^{-1} (medium) to C-N-C symmetric stretching band, 1375 cm^{-1} (weak) to C-N stretching band, 1254 cm^{-1} to amide III, and 1210 cm^{-1} (weak) to the C-N-C asymmetric stretching band. Here the assignments are uncertain but reasonable.

1000-600 cm^{-1} region: The maleimide alkenyl C-H out-of plane bending mode of species b$_1$ is observed at 838 cm^{-1}. The strong infrared band 698 cm^{-1} is connected with a ring deformation mode of species b$_2$. This vibration seems characteristic for five-membered heterocyclic ring systems.[149]

5.6.2.2 Peak assignments for the SAMs of BMHC on Au surfaces

The peak frequency shift observed in the imide band (1712 vs 1700) to higher values suggests that the interchain interactions, e.g., the Van der Waals interaction within the bulk KBr and the monolayer on gold, are different. The amide II band around 1540 cm^{-1}, which was reported by Tam-Chang et al.[150] to indicate the presence of hydrogen bonding, correlates well with the experimental value obtained in this study (1543 cm^{-1}). It is possible to assign the other absorption frequencies from the surface spectra that seem to correlate well with the characteristic peaks observed in the bulk spectra. The 1443 cm^{-1} is assigned to the CH$_2$ deformation, 1412 cm^{-1} to the C-N-C symmetric stretch, 1377 cm^{-1} to the C-N

stretch, 1260 cm^{-1} to the amide III, and 830 cm^{-1} to the maleimide C-H bend. The possibility of making these unique peak assignments implies that the maleimide moiety is not lying parallel or standing perpendicular to the gold substrate surface. The exact orientation of the maleimide group will be discussed later on in detail.

We observed the absence of the amide I band in AuBMHC, similar to that observed by Lenk et al.[151] and Clegg et al..[152] A conclusion can be deduced from the surface selection rule that both the N-H and C=O bonds within the monolayers are possibly parallel to the surface plane. This is different from some other reports, in which both amide I and II are visible. Two possible reasons may be responsible for the discrepancies: one is the alkyl chain length of the monolayer system; the other is the position of the amide functionality. Generally, when there are longer alkyl chains and the amide functionalities locate close to the gold surface, the monolayers should have favored orientations in which the alkyl chain axis is nearly perpendicular to the surface plane. In this case the amide group is in trans-form and the amide I band is often absent.

5.6.3 Estimation of maleimide orientation

A method was suggested by Kazuo Iida, et. al.[81] to estimate the orientation of molecules in ultrathin films. This method is easier than other methods when used in the orthogonal systems, i.e. there are 3 transition dipole moments perpendicular to each other. The principle is as follows.

The IR absorption intensity I_i of the ith vibration mode is proportional to the mean square of inner product of the transition moment μ and field component E of IR light.

$$I_i \propto \left\langle \left| \mu_i \times E \right|^2 \right\rangle$$

Ratios of peak intensities, I_i, I_j, and I_k, due to the molecular orientation with transition moments perpendicular to each other are described by the following equation:

$$I_i : I_j : I_k = \mu_i^2 E^2 < \cos^2 \theta_i > : \mu_j^2 E^2 < \cos^2 \theta_j > : \mu_k^2 E^2 < \cos^2 \theta_k >$$

where θ is the angle between μ and E. Since $\cos\theta$ is the direction cosine in the rectangular coordinates,

$$<\cos^2\theta_i> + <\cos^2\theta_j> + <\cos^2\theta_k> = 1$$

For organic molecules in the unoriented bulk state such as in KBr pellets,

$$<\cos^2\theta_i> = <\cos^2\theta_j> = <\cos^2\theta_k> = 1/3$$

Thus, ratios of peak intensities, $I_i^{KBr}, I_j^{KBr}, I_k^{KBr}$ are expressed as follows:

$$I_i^{KBr} : I_j^{KBr} : I_k^{KBr} = \mu_i^2 : \mu_j^2 : \mu_k^2$$

This equation means that the ratios of the peak intensities in the spectrum of KBr pellets correspond to the ratios of the square of the transition dipole moments. Since there is only a perpendicular field component at the surface in IRAS spectroscopy, only molecules with a finite transition moment component perpendicular to the substrate are observable. Ratios of peak intensities, $I_i^{IRAS}, I_j^{IRAS}, I_k^{IRAS}$ in IRAS spectrum are given by

$$I_i^{IRAS} : I_j^{IRAS} : I_k^{IRAS} = I_i^{KBr} <\cos^2\theta_i> : I_j^{KBr} <\cos^2\theta_j> : I_k^{KBr} <\cos^2\theta_k>$$

Therefore, $<\cos^2\theta_i>$, $<\cos^2\theta_j>$, and $<\cos^2\theta_k>$ can be determined as follows:

$$<\cos^2\theta_i> = \frac{I_i^{IRAS} I_j^{KBr} I_k^{KBr}}{I_i^{IRAS} I_j^{KBr} I_k^{KBr} + I_i^{KBr} I_j^{IRAS} I_k^{KBr} + I_i^{KBr} I_j^{KBr} I_k^{IRAS}}$$

$$<\cos^2\theta_j> = \frac{I_i^{KBr} I_j^{IRAS} I_k^{KBr}}{I_i^{IRAS} I_j^{KBr} I_k^{KBr} + I_i^{KBr} I_j^{IRAS} I_k^{KBr} + I_i^{KBr} I_j^{KBr} I_k^{IRAS}}$$

$$<\cos^2\theta_k> = \frac{I_i^{KBr} I_j^{KBr} I_k^{IRAS}}{I_i^{IRAS} I_j^{KBr} I_k^{KBr} + I_i^{KBr} I_j^{IRAS} I_k^{KBr} + I_i^{KBr} I_j^{KBr} I_k^{IRAS}}$$

Based on these equations, the molecular orientation of organic compounds on metallic substrate can be quantitatively evaluated from the IRAS spectrum and the transmission spectrum of the same molecule in the unoriented bulk state such as in KBr pellets. The three transition dipole moments are not necessarily perpendicular to each other, but, if so, $<\cos^2\theta>$ should be represented by means of a more complicated expression. Fortunately,

rigid molecules may usually have three vibration modes with transition dipole moments perpendicular to each other.
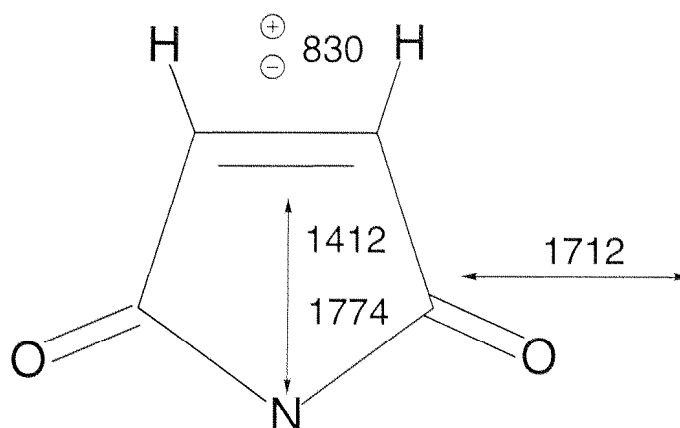
Figure 5-36   *The directions of transition dipole moments of maleimide on AuBMHC. The imide asymmetric stretch band of 1712 cm^{-1} is in the ring plane and parallel to the C=C double bond; the imide and C-N-C symmetric stretch bands (1774, 1412 cm^{-1}) are in the ring plane and perpendicular to the C=C double bond; the maleimide C-H out-of-plane bending band of 830 cm^{-1} is perpendicular to the ring plane.*

Here we apply this theory to our model molecule. As pointed out in the IR assignment tables, the rigid maleimide group has enough vibrational modes with transition dipole moments perpendicular to each other (Figure 5-36).

The directions of the transition dipole moments of maleimide C=O symmetric stretching at 1774 cm^{-1} and of C-N-C symmetric stretching at 1412 cm^{-1} are perpendicular to the C=C double bond. The direction of the transition dipole moment of C=O asymmetric stretching at 1712 cm^{-1} is parallel to the C=C double bond. The direction of the transition dipole moment of the maleimide C-H out-of-plane bending at 830 cm^{-1} is perpendicular to the malcimide ring plane. Two groups of vibration modes can be used to calculate the orientation of maleimide. One consists of 1774, 1712, and 830 cm^{-1}, and the other consists of 1414, 1712, and 830 cm^{-1}. However, both IR intensities of C=O symmetric stretching at 1774 cm^{-1} in KBr and on Au surfaces are too low to be precisely determined. As the peak intensity at 1412 cm^{-1} is much stronger, it is satisfied for calculation. Therefore, the second group is used to evaluate the orientation of the maleimidyl group.

Two problems must be noted when using this evaluation method. One is the sample thickness. We described that there is only a perpendicular field component in IRAS measurements. This is valid only if the film thickness is sufficiently small as compared with the IR wavelength. Even the shortest wavelength of peak used in above estimation, 5.8 μm,

corresponding to 1712 cm^{-1}, is much larger than the SAM thickness, ~2 nm. The other problem is how the peak intensity is evaluated. The peak intensity is evaluated from peak height in this thesis. For the accuracy of the orientation analysis, the evaluation of the peak intensity from peak area may be, if anything, reasonable, but is inconvenient.
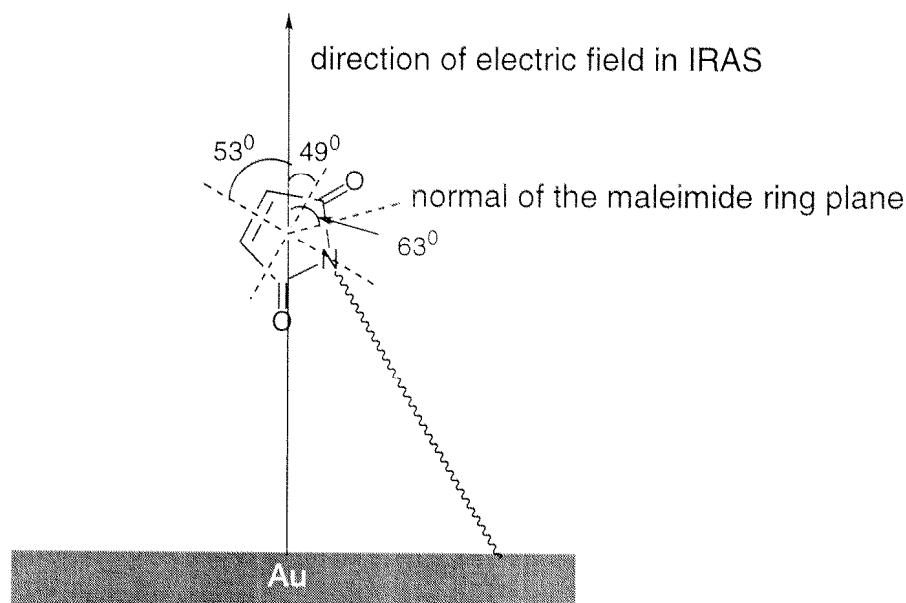

Figure 5-37   Schematic orientation of the maleimide ring of AuBMHC relative to the Au surface plane normal.

Table 5-16   Orientation of the maleimide group on AuBMHC estimated from IR spectra.

$<\cos^2\theta_{1712}>$	$<\cos^2\theta_{1412}>$	$<\cos^2\theta_{830}>$
0.42	0.37	0.21
θ_{1712}	θ_{1412}	θ_{830}
49	53	63

The calculated results are shown in Table 5-16 and Figure 5-37. The angle between the maleimide ring plane and the Au plane normal is 27^0, i.e., the ring is nearly standing on the gold surface. Simple calculations show that the outermost atom is oxygen from one carbonyl group. This structure is not beneficial for further reactions with proteins bearing thiol groups because the double bond C=C can not be easily reached due to the hindrance by the oxygen. This may be one of the reasons for that a 100% conversion efficiency can not be achieved when coupling proteins and peptides with this type of structures.

5.6.4 Comparison of AuBMHC and AuCM6

The differences of their IRAS spectra between AuBMHC and AuCM6 (Figure 5-38) are:

1) The amide II (1543 cm^{-1}) is a sharp and strong peak on AuBMHC, however a weak and broad peak on AuCM6.

2) The asymmetric stretching vibration peak of maleimide on AuBMHC is at 1712 cm^{-1}, however it is at 1707 cm^{-1} on AuCM6, possibly due to the hydrogen bond formation between the amide groups on AuBMHC or between the maleimide carbonyl group and the unreacted amino group on AuCM6, or a single maleimidyl arm on AuCM6 but double maleimidyl arms on AuBMHC regarding the disulfide bond which may not be broken although the broken one is generally accepted, or the oriented packing way of maleimidyl groups, or the different microenvironments around maleimidyl groups such as the neighboring groups of succinimidyl esters on AuCM6. The higher frequencies 1745, 1782, and 1821 cm^{-1} on AuCM6 from succinimidyl ester do not appear on AuBMHC.

3) The maleimide C-H out-of-plane bending peak at 830 cm^{-1} appears on AuBMHC, but not on AuCM6, possibly attributable to the orientation of maleimidyl group.

4) The frequencies, 1210 and 1071 cm^{-1} on AuCM6, related to succinimidyl ester CNC and C(=O)-O-N vibrations do not appear on AuBMHC.

In summary, all peaks except 830 cm^{-1} on AuBMHC can be found on AuCM6. On the other hand, the peaks from the succinimidyl ester group on AuCM6 do not appear on AuBMHC. These strongly support the presence of a mixture of maleimidyl and succinimidyl ester groups on AuCM6.
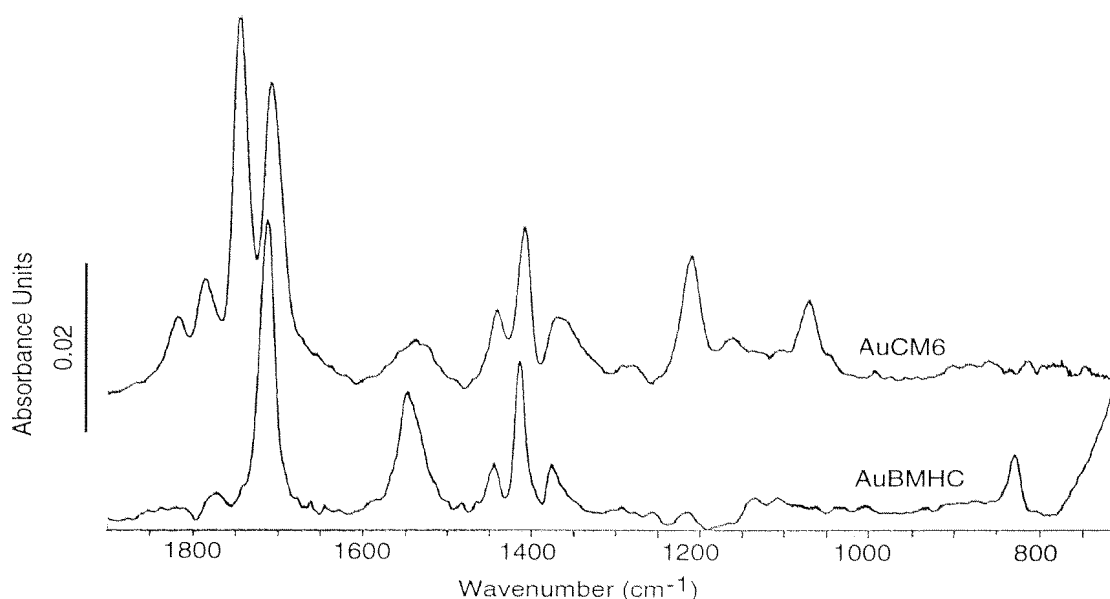

Figure 5-38   IRAS spectra of AuCM6 and AuBMHC.

The XPS results of AuBMHC are shown in Table 5-17. The atomic concentrations from experiments are very close to those of theoretical values. The ratio of imide-C to amide-C is 1.8, close to the ideal value 2. The XPS results of AuCM6 have been shown in Figures 5-30, 5-32, and Table 5-12. The atomic concentrations and binding energies of all elements are similar to AuBMHC. However the content of imide-C (C 1s at ~289 eV) on AuCM6 is larger than that on AuBMHC, and amide-C (C 1s at ~288 eV) is less than that on AuBMHC. This also indicates the existence of succinimidyl ester on AuCM6.

Table 5-17   XPS results of AuBMHC.

Element (orbital)	E_B (eV) rel. peak area	Assignment	Atomic concentration		
			experimental		theoretical
C (1s)	285.0, (42)	CH, CC, CS			
	286.0, (30)	CN, $\underline{C}$-C=O	38	70	67
	287.7, (10)	amide-C			
	289.0, (18)	imide-C			
N (1s)	399.8, (50)	amide-N	5	9	11
	400.7, (50)	imide-N			
O (1s)	532.0, (50)	C=O	9	17	17
S ($2p_{3/2}$)	162.0, (70)	S	2	4	5
($2p_{1/2}$)	163.4, (30)	S			
Au ($4f_{7/2}$)	84.2, (57)	Au	46	–	–
($4f_{5/2}$)	87.9, (43)	Au			
Σ	–	–	100	100	100

5.7 Summary

In this chapter, we described the surface reactions of succinimidyl ester groups with two aminothiol SAMs (AuC and AuB) on Au surfaces. The main studies are as follows: (1) The cystamine and 4-aminothiophenol SAMs on Au were characterized with IRAS and XPS respectively. Cystamine forms a loosely packed submonolayer, while 4-aminothiophenol forms a dense and oriented monolayer. (2) The surface reactions of AuC and AuB with the homobifunctional crosslinkers bearing bi—succinimidyl esters form a bridge, or a terminal succinimidyl ester group, or both on the surface. (3) Two model photocrosslinking groups,

N-5-azido-2-nitrobenzoyl and benzophenone, were grafted on AuC, but not on AuB because of the bulky size of the two groups and the strong steric hindrance from the benzene group of AuB. (4) The thiol-reactive crosslinking groups, α-iodoacetamide and maleimide, were grafted on both AuC and AuB surfaces. (5) A series of heterobifunctional crosslinkers with different alkyl chains between maleimide and succinimidyl ester were studied and compared. The following conclusions can be deduced: At room temperature, the reactions with SMP, SMB, SMCC, SMBZ and SMPB produce the functionalized surfaces with predominant maleimide-pendant groups which are specific for grafting thiol-bearing proteins; the reactions with EMCS and SMO, however, produce surfaces with both maleimide- and succinimidyl ester-pendant groups which are nonspecific for grafting proteins; the reaction with EMCS has the highest conversion efficiency; the reaction yields of AuB-based products are calculated from the intensity ratios of the NH_2 deformation band (1623 cm^{-1}) to the benzene ring stretching band (1591 cm^{-1}). (6) In order to understand the specific reaction of EMCS with amino-terminated SAMs, the target molecule, N,N'-bis(6-maleimidylhexanoyl)cystamine (BMHC), was synthesized and self-assembled on Au surfaces. By comparing the IR spectra of AuCM6 with its precursor EMCS, and the IRAS and XPS results of AuCM6 with those of AuBMHC, we conclude that both maleimidyl and succinimidyl ester groups are grafted on AuCM6 due to the side reaction of maleimidyl groups with amino groups. (6) The orientation of maleimide on AuBMHC is estimated from its IR spectra in KBr and on Au according to a method developed by K. Iida, but maleimide on AuCM6 is believed to be randomly oriented according to NEXAFS measurements.

6. Grafting poly(ethylene glycol) to amino-terminated surfaces

6.1 Introduction

Poly(ethylene glycol) (PEG) coatings are well known for their protein resistance.[153] They enhance the wettability of surfaces, cover and hide surface charge groups, and significantly reduce the nonspecific adsorption of proteins and cells. PEG coatings may be used in biomaterials, chromatography, electrophoresis, biosensors, and other applications. In this work, two kinds of PEG compounds have been covalently bound to titanium and gold surfaces via reaction of succinimidyl esters with primary amino groups respectively: O-[2-(N-succinimidyloxycarbonyl)-ethyl]-O'-methylpolyethylene glycol 5000 (MW 5000, methoxy-PEG-SPA) (Fluka) and Di-N-hydroxysuccinimidyl ester poly(ethylene glycol)-propionic acid (MW 3400, SPA-PEG-SPA) (Shearwater Polymers Europe). Figure 6-1 shows the grafting reaction of methoxy-PEG with surfaces AuC and AuB. The methoxy-PEG should have a freely mobile PEG chain and the methoxyl group should be located at the outermost layer.
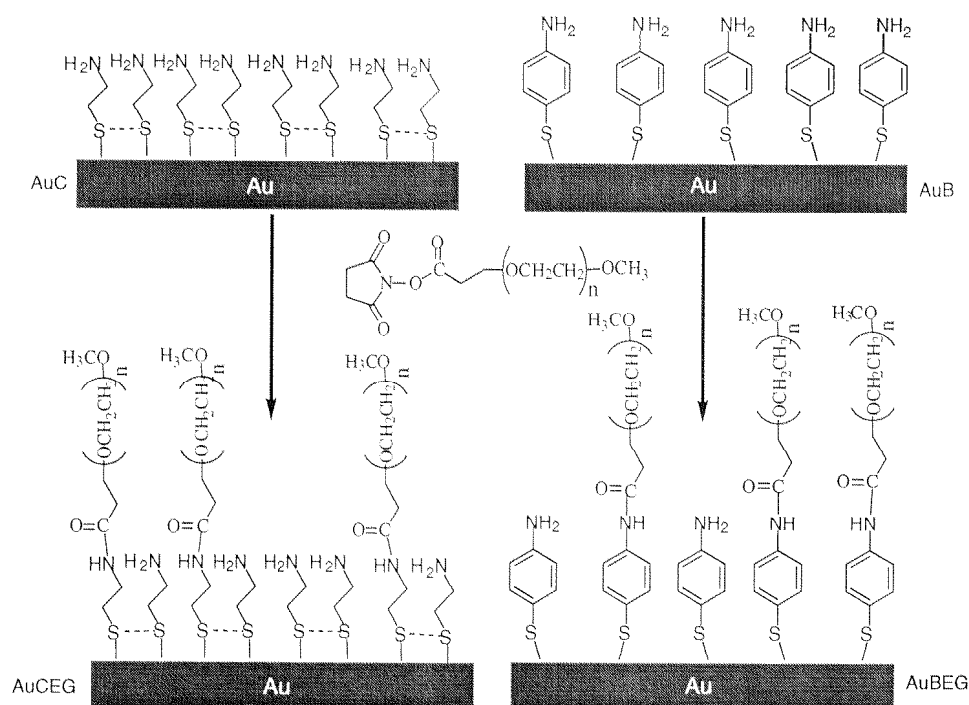

Figure 6-1   *Formation of the methoxy-PEG on NH₂-terminated SAMs. The abbreviations are AuCEG for the left and AuBEG for the right.*

As discussed in Chapter 5, the reaction of NH_2-terminated surfaces with succinimidyl esters at both ends of a homobifunctional crosslinker (in the present case SPA-PEG-SPA) may result in two products. One is the bridging form, the other is the mono-succinimidyl ester pendant product. With the long poly(ethylene glycol) chain between the two succinimidyl esters, SPA-PEG-SPA is expected to easily form bridging structures (Figure 6-2). The mono-succinimidyl ester pendant structures can be excluded from both XPS and IRAS measurements.
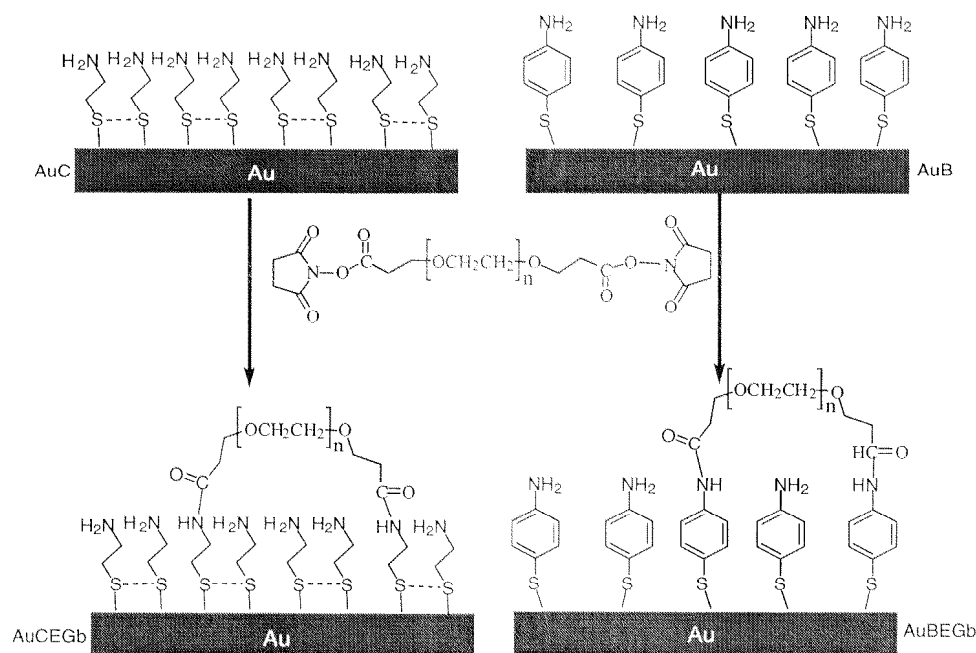

Figure 6-2   Formation   of   the   bridging   PEG   on NH_2-terminated   SAMs.   The abbreviations are AuCEGb for the left and AuBEGb for the right.

6.2 Experimental

All surface modification experiments were carried out according to the standard procedure described in Chapters 4 and 5. The contact angles of all PEG modified surfaces are in the range of 38 to 48 degrees.

Optical waveguide lightmode spectroscopy measurements
The protein resistance of PEG coatings has been evaluated in this thesis using optical waveguide lightmode spectroscopy (OWLS,).[154] The waveguides were first coated with a 10 nm TiO_2 film, then silanized in toluene with APTES, and finally grafted with PEG. The

parallel experiments were run on coated titanium metal samples and characterized with XPS and IRAS. The results are similar to PEG-grafted Au surfaces and are omitted.

The measuring principle of OWLS is shown in Figure 6-3. The laser beam enters from below through the transparent supporting glass and is then incoupled into the waveguiding layer by the diffraction grating. Any adsorption on the surface in contact with a gaseous or liquid phase results in a phase shift of the guided modes and can be measured by varying the angle α at which the laser beam hits the grating. From the phase shift, quantitative data regarding the time-dependent amount of adsorbed species and hence the adsorption kinetics can be deduced.

In a typical experiment, buffer is first pumped through the flow-through cell to establish a baseline. Then the input is switched to the test solution (e.g. proteins dissolved in the same buffer) and the formation of the adlayer on the surface is monitored. Assuming the adlayer of proteins is homogeneous, the mass of the proteins in the adlayer can be calculated as follows:

$$m = d_A \frac{n_A - n_C}{dn / dc}$$

where d_A is the mean thickness of the adlayer, n_A and n_C are the refractive index of the adlayer and the cover media respectively, dn/dc is a coefficient depending on the molecules and has a quasi universal value of 0.182 for most proteins.
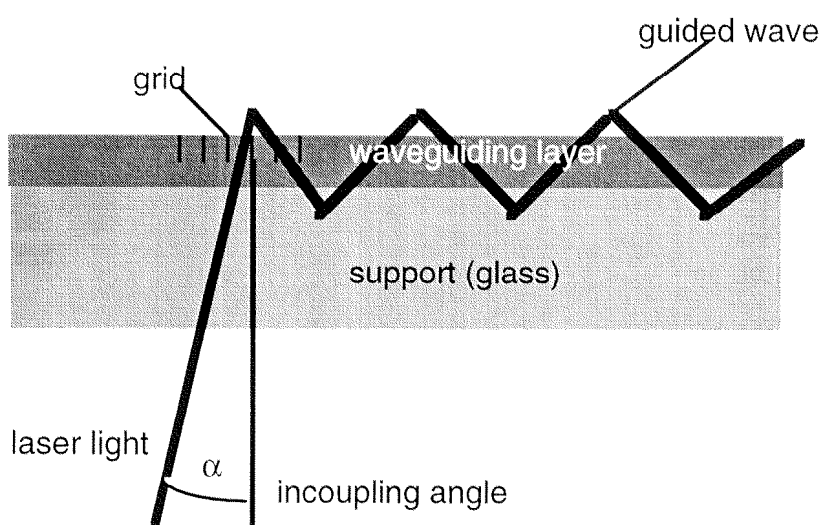

Figure 6-3   Schematic drawing of OWLS measurements.

The experimental procedure is described according to Figure 6-7. After 5 h incubation of a PEG-modified chip in a 10 mM HEPES buffer (pH 7.4), the waveguide chip was installed in a IOS-1 instrument (ASI, Zürich, Switzerland). Measurements were started using a 10 mM HEPES (pH 7.4) buffer for baseline control, then switched to Serum N (human) (Roche) for protein adsorption, and finally switched to HEPES buffer again for evaluation of tightly bound proteins.

6.3 Results

6.3.1 Infrared spectroscopy measurements

Since AuC has no IRAS peaks that interfere with the subsequent grafted surface layer, the IRAS spectra of AuCEG and AuCEGb are chosen and discussed in details. The other PEG-grafted surfaces on AuB and on aminosilanized Ti have similar characteristics and are therefore omitted in the discussion.
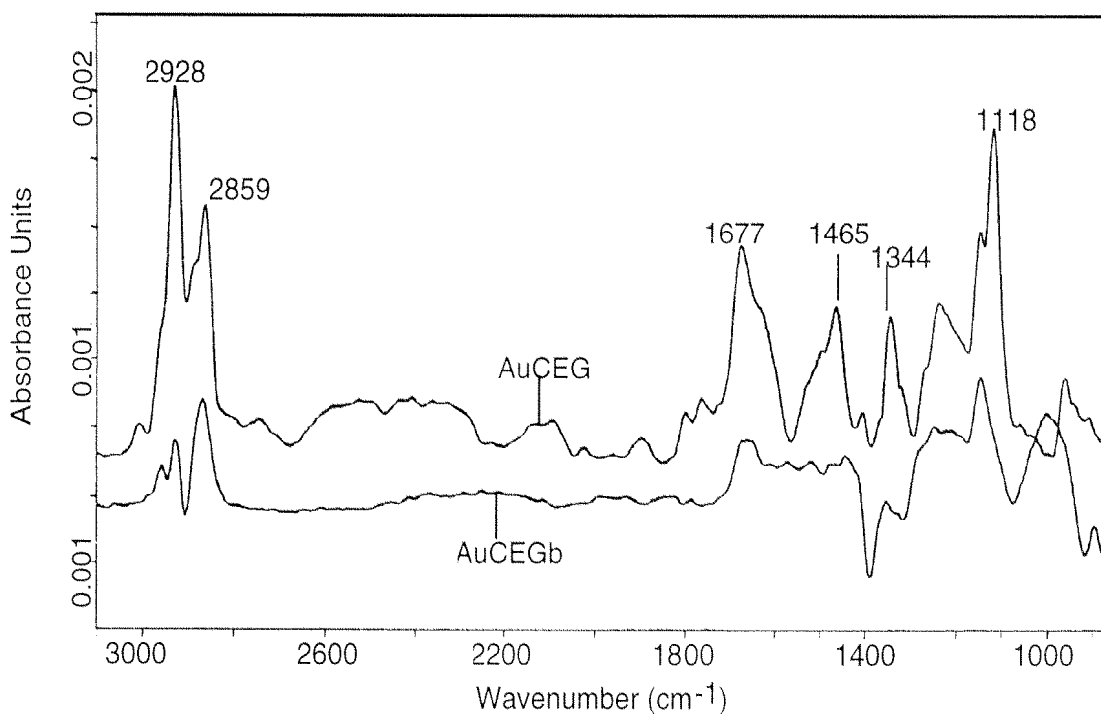

Figure 6-4   IRAS spectra of AuCEG and AuCEGb.

Table 6-1   *IR spectral mode assignments for bulk PEG and for PEG grafted on Au surfaces.*

Mode assignment	PEG, crys.	PEG, amor.	AuCEG	AuCEGb
PEG CH_2 asym stretching	2950	ca. 2930 sh	2965 sh	2958 w
alkyl CH_2 asym stretching			2928 s	2926 w
PEG CH_2 sym stretching	2890 s	2865 b		
	2885 s			
	2865 sh		2867 sh	2868 sh
alkyl CH_2 sym stretching			2859 s	2859 s
amide I			1677 s	1675 m
amide II			1535 w	1536 w
PEG CH_2 bending	1470 m	1460 m	1465 s	
	1460 m			
PEG CH_2 wagging	1345 s	1352 m	1344 m	
PEG CH_2 wagging		1325 w		
PEG CH_2 twisting	1283 m	1296 m		
PEG CH_2 twisting	1244 m	1249 m	1242 w	
C-O, C-C stretching	1149 s	1140 sh	1150 m	1147 s
	1119 s		1118 s	
	1102 vs	1107 s		
	1062 m	1038 m		
PEG CH_2 rocking	963 s	945 m	963 w	

For the discussion of the vibrational spectra of the PEG-terminated surfaces, we will refer to the band assignments of unfunctionalized poly(ethylene glycol). The IRAS spectra of AuCEG and AuCEGb are shown in Figure 6-4. The bands at 2859 and 2926 cm^{-1} are ascribed to the symmetric and asymmetric CH_2-stretching bands of the methylene units, respectively. The methylene stretching frequencies are representative for a liquid with gauche and trans conformations in the alkyl compounds. The CH_2-stretching vibrations of the PEG molecular entities are expected to give a broad band at ca. 2890 cm^{-1} and a shoulder at 2930 cm^{-1}, but these features are masked by the sharper alkane CH_2-stretching bands.

The amide bond formed during the reaction is confirmed by the strong bands around 1677 (amide I) and 1535 cm^{-1} (amide II). The C-O-C stretching vibration band on AuCEG is very strong at 1118 cm^{-1}, but weak on AuCEGb because most of C-O-C chains are parallel to the Au surface (Figure 6-2). The PEG CH_2 bending, wagging, and twisting bands at

1465, 1344, and 1242 cm^{-1} are present on AuCEG, however absent on AuCEGb, mainly attributable to the surface selection rule. The band 963 cm^{-1} is associated with the ether CH$_2$-rocking mode.

6.3.2 X-ray photoelectron spectroscopy (XPS) measurements

Five elements were detected on the surfaces AuCEG, AuCEGb, AuBEG, and AuBEGb: C, N, O, S, and Au. Their atomic concentrations are shown in Figure 6-5. Compared to the starting surfaces AuC and AuB discussed in Section 5.5, the PEG-modified surfaces have more oxygen contents (5 to 10 %). Considering the theoretical atomic ratio O/C (=0.5) of PEG, the higher carbon contents (~30%) indicate the incomplete conversion of amino groups. The binding energies of N 1s, O 1s, S 2p, and Au 4f are similar to those on AuC and AuB surfaces and not discussed.
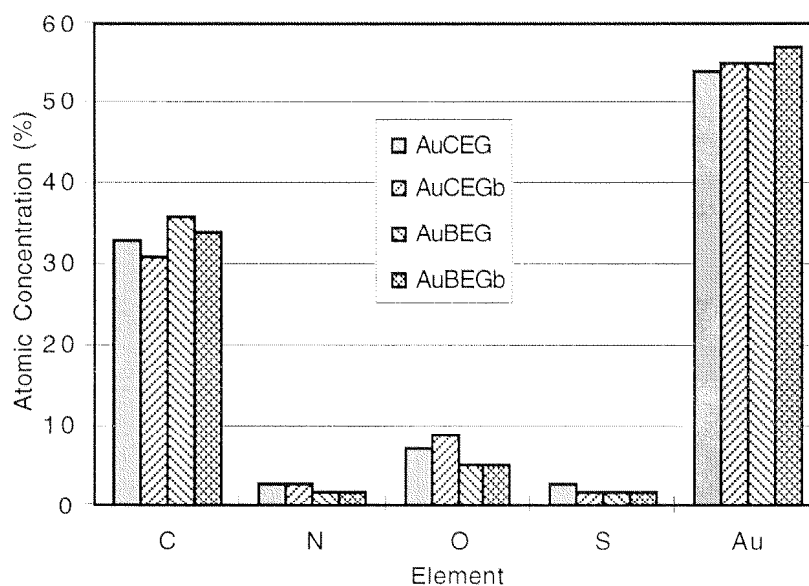

Figure 6-5   *The mean values of atomic concentrations of PEG-grafted Au surfaces from XPS measurements of three samples for each surface.*

The most informative peak is still C 1s because the alkyl, aryl, and ether carbons can be distinguished by their binding energies at ~285.0, ~284.5, and ~286.5 eV, respectively (Figure 6-6). C 1s can be fitted to the alkyl (aryl), polyether, and amide fractions. The deconvolution results of C 1s are shown in Table 6-2. The ratios of ether carbon to alkyl (aryl) carbon are close to 1. From these ratios, it is easy to deduce that the conversion efficiency of NH$_2$ to amide is quite low because one polymer molecule contains ~100 ethylene groups. If the conversion is complete, the ratios would be in the range of ten to hundred. One oligomer of methoxy-PEG-SPA (MW 5,000) contains ~110 ethylene groups, therefore the conversion efficiencies for AuCEG and AuBEG are estimated to be

~1% and ~4%, respectively. One oligomer of SPA-PEG-SPA (MW 3,400) contains ~77 ethylene groups, corresponding to the conversion efficiencies of ~2% and ~7% for AuCEGb and AuBEGb, respectively. Since the molecular weight of the PEG polymer is several thousand times larger than that of cystamine, the geometric size must also be correspondingly larger. Thus, the estimated conversion efficiencies are plausible if the PEG chain is not linear. From the above estimations, we can speculate that the methoxy-PEG chain forms a stack of rope on AuCEG and AuBEG surfaces with exposed methoxyl groups. For the bridging PEG, it is reasonable to conclude that most PEG chains are parallel to the surface.
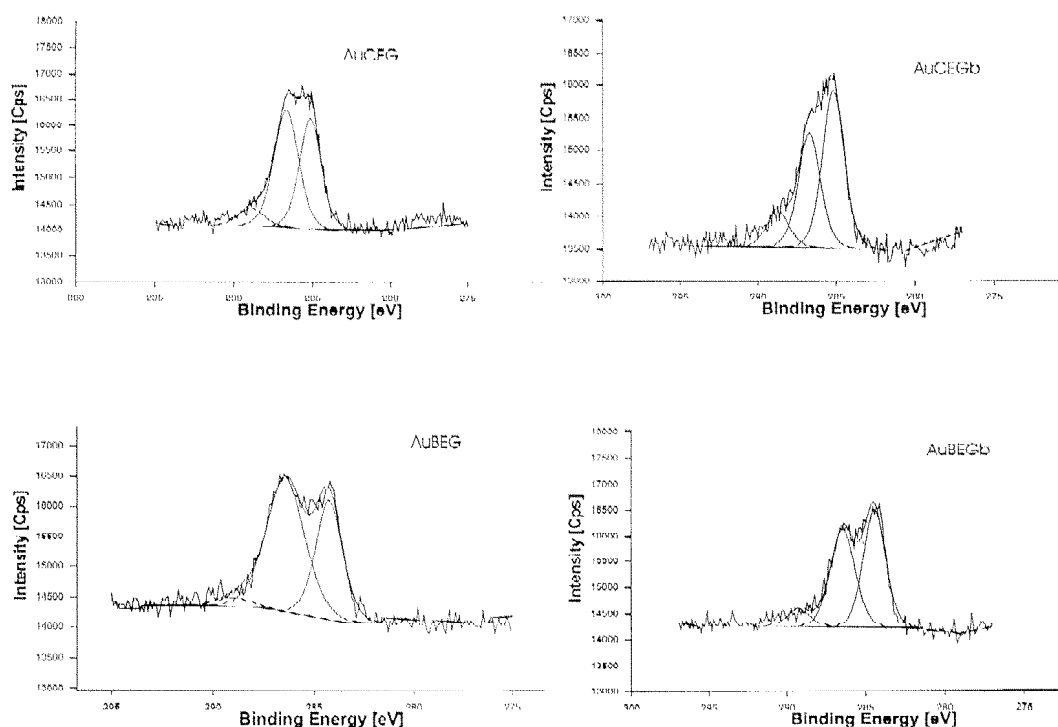

Figure 6-6   XPS C 1s spectra of methoxy-PEGs (AuCEG and AuBEG) and bridging PEGs (AuCEGb and AuBEGb) grafted on Au surfaces.

Table 6-2   Deconvolution results of C 1s of Figure 6-6.

Surface	E_B (eV), %, assignment	Surface	E_B (eV), %, assignment
AuCEG	285.2, (42), alkyl-C	AuBEG	284.2, (40), aryl-C
	286.7, (50), ether-C		286.4, (56), ether-C
	288.5, (8), amide-C		288.7, (4), amide-C
AuCEGb	285.2, (50), alkyl-C	AuBEGb	284.4, (48), aryl-C
	286.7, (38), ether-C		286.4, (44), ether-C
	288.5, (12), amide-C		288.7, (8), amide-C

6.3.3 Protein resistance evaluation

As discussed on AuC surfaces, the methoxy-PEG and bridging PEG can be grafted on APS modified waveguide surfaces (TiO_2). The protein adsorption on TiO_2, APS, methoxy-PEG, and bridging PEG modified surfaces are compared in Figure 6-7. The tightly bound protein mass can be calculated from the height between the last plateau after buffer rinsing and the baseline. The serum adsorption region is difficult for evaluation because the serum solution has changeable refractive index.
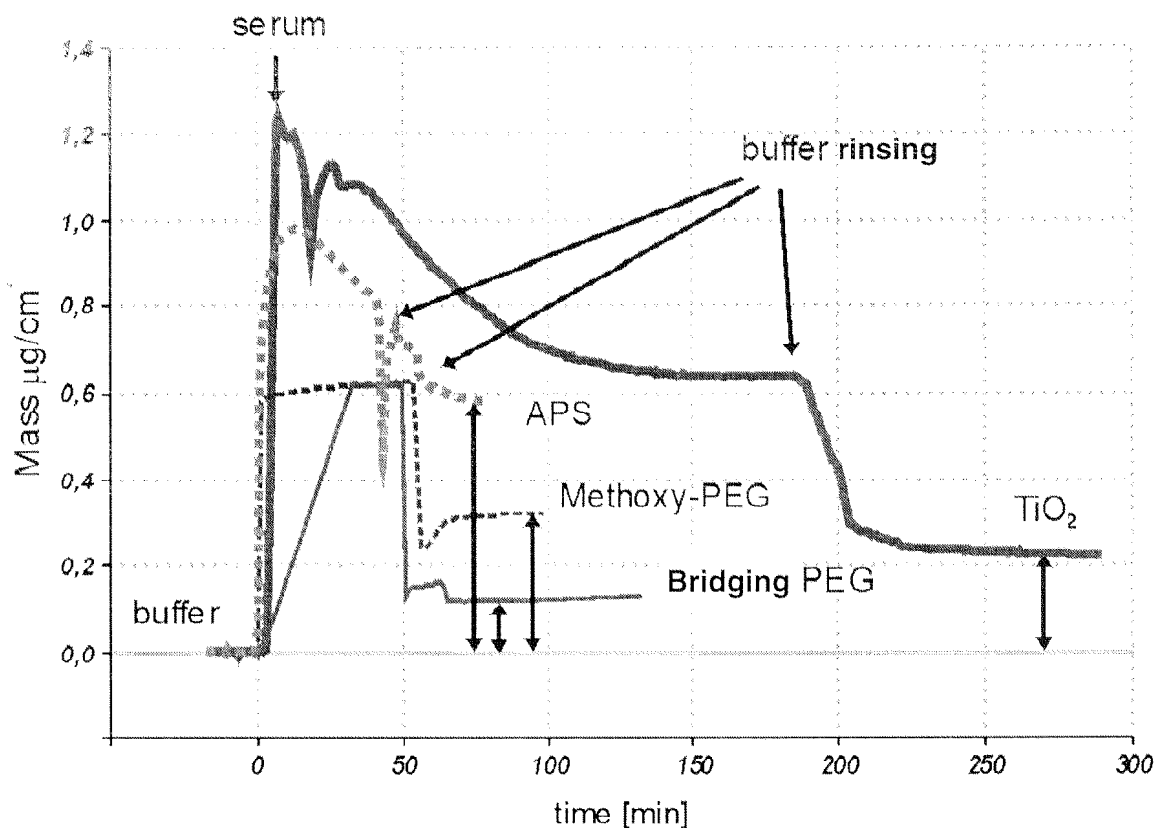

Figure 6-7   *Serum adsorption versus time measured by OWLS on TiO_2, APS, methoxy-PEG, and bridging-PEG coated waveguides followed by rinsing in buffer. The mass of tightly bound proteins are indicated with double-headed arrows. All operations were performed with a serum flow rate of 1.5 μl s^{-1}.*

Table 6-3   *The calculated mass of proteins irreversibly adsorbed on modified waveguide chips from OWLS measurements.*

Surface	Mass of proteins
TiO_2	$0.2 \ \mu g/cm^2$
APS film	$0.58 \ \mu g/cm^2$
Methoxy-PEG	$0.32 \ \mu g/cm^2$
Bridging PEG	$0.12 \ \mu g/cm^2$

The reference surface, TiO_2, has a protein adsorption mass of $0.2 \ \mu g/cm^2$ after buffer washing. As discussed in Section 2.1, the surface of TiO_2 contains weakly negatively charged hydroxyl groups at pH 7.4, which initially tend to repel molecules (most noncollageneous proteins possess a negative charge), and the interfacial free energy between clean surfaces and protein-containing media is relatively low. However, clean TiO_2 surfaces are extremely hydrophilic and possess a high surface energy. Therefore, there is a driving force for protein deposition to take place on clean surfaces and subsequently lower the energy of the surface. APS has the highest adsorption mass of $0.58 \ \mu g/cm^2$, which is mainly attributable to its positive surface charges. Although the surface energy of APS is lower than that of the TiO_2 surface, there is a high interfacial free energy between the APS surface and the protein-containing medium. The APS surface will attempt to lower its interfacial free energy with the medium by allowing molecules to adsorb to it. Methoxy-PEG does not show any protein resistance and the adsorption mass is $0.32 \ \mu g/cm^2$, higher than on TiO_2, but lower than on the APS modified surface. This may be caused by the partial coverage of amino groups. The bridging PEG has the lowest protein adsorption of $0.12 \ \mu g/cm^2$. As generally accepted, the protein resistance of PEG is due to the steric repulsion effect, where the polymer prevents the adsorption of proteins from reaching the substrate surface. The balance among three forces: steric repulsion, Van der Waals attraction, and hydrophobic interaction between proteins in solution and the PEG surface influence the protein adsorption. One of the reasons that PEG surfaces do not adsorb protein is because of the unique way that PEG molecules bind water. Hydrogen bonding between water and PEG oxygen molecules is thought to form a protective hydration shell around PEG molecules. On the bridging PEG grafted surface, water is tightly bound to each ethylene glycol repeat unit ($-CH_2CH_2-O-$). Since the polymer chain of PEG is parallel to the surface, the bound water is just on the outermost layer and has the largest steric repulsion among these surfaces. Also, PEG's neutrality, chain mobility, and associated excluded volume effects are responsible for steric stabilization of a surface and

subsequent prevention of protein adsorption. When any type of molecule attempts to adsorb to a PEG-rich area, the energetic result is a negative entropic contribution due to the confinement of the PEG chain. The overall relevance to the system is that the adsorption event is improbable.

6.4 Summary and outlook

In this chapter, two types of PEG were grafted to amino-terminated surfaces, methoxy-PEG in a "standing-up" configuration and bridging-PEG in a "lying-down" configuration. They were characterized with IRAS and XPS. The covalent bonding through the -C(=O)-NH- bond is confirmed by the amide I band in IRAS spectra. The so-called "standing-up" or "lying-down" configuration of the PEG chain can be deduced from the appearance or disappearance of the C-O-C stretching band at 1118 cm^{-1}. The XPS measurements showed the evidence of the ether carbon (C 1s at ~286.5 eV), and the turn-over can be deduced from XPS data in the range 1 ~ 10 %. The protein resistance of PEG-coatings was evaluated with the optical waveguide lightmode spectroscopy (OWLS), and only the bridging PEG exhibited a good protein resistance.

Future work on grafting peptides or proteins can be done by using the heterobifunctional crosslinkers bearing succinimidyl ester and maleimide (or other amino-resistant crosslinking groups) with the PEG chain between them. In such a case, the PEG chain is a flexible spacer in which the chain length can be in variable ranges from several to several thousand ethylene glycol groups. The PEG chain is also as a resistant background to protein adsorption, cell and bacteria adhesion. PEG-tethered proteins may exhibit enhanced activity due to reduced protein-surface interaction, greater molecular freedom, and shielding from local surface charge and pH effects. They may be used in chromatography, electrophoresis, biosensors, and other applications.

7. Summary and outlook

The reaction of amino-terminated ultrathin organic films with succinimidyl esters can be used to introduce a variety of functional crosslinking groups onto solid surfaces such as maleimidyl, iodoacetyl, succinimidyl ester, aryl azido, and benzophenone groups. With such groups, the immobilization of many kinds of biomolecules on solid surfaces is feasible, and thus it provides potential techniques for applications in biosensors, bioreactors, chromatographic supports, and biomaterials. The advantages of this method are:

1. Mild reaction conditions
2. A variety of possibilities to graft different functional crosslinking groups on solid surfaces and thus enabling the immobilization of biomolecules feasible
3. Higher surface coverages of bound biomolecules compared to other available methods
4. No polymerization problems which are very common for other crosslinkers such as diglutaraldehyde

The main work done in this thesis can be divided into three parts:
1. Covalent attachment of RGD-containing peptides to titanium (oxide) surfaces for biocompatibility improvement
2. Investigation of the surface reactions of succinimidyl esters with aminothiol SAMs on Au surfaces
3. Immobilization of poly(ethylene glycol) on amino-terminated surfaces for protein-resistance studies

In more details, a three-step reaction procedure was applied to introduce RGD-containing peptides to the titanium surface. Water-vapor-plasma-pretreated titanium surfaces were first silanized with (3-aminopropyl)triethoxysilane, resulting in a multilayer film of poly(3-aminopropyl)siloxane. In a second reaction step, the free primary amino groups were linked to the maleimidyl groups via amide bonds. Onto the resulting terminal maleimide surface, two model, cell-adhesive peptides, H-Gly-Arg-Gly-Asp-Ser-Pro-Cys-OH (GRGDSPC) and H-Arg-Gly-Asp-Cys-OH (RGDC) were immobilized through covalent addition of the cysteine thiol (-SH) group. X-ray photoelectron spectroscopy (XPS), infrared reflection absorption spectroscopy (IRAS), time-of-flight secondary ion mass spectroscopy (ToF-SIMS), ellipsometry, and radiolabeling techniques were applied to characterize the surfaces. From independent quantitative analyses, an approximate coverage of 0.2~0.4 peptides per nm^2 was calculated. The RGD-modified samples were

tested with the osteoblastic cell line MC3T3-E1 and the rat bone marrow cells *in vitro*. Preliminary cell culture results show positive effects for osteoblastic cell line MC3T3-E1 but negative effects for rat bone marrow cells in cell adhesion, differentiation and integration. For further studies to improve the biocompatibiliy of titanium surfaces, the future work should be done in:

1. Use of other specific proteins or peptides such as bone sialoproteins for specific interactions with bone cells

2. Use of cyclic RGD-containing peptides for controlling their configuration and conformation on the surface

3. Building up the standard biological protocol to assess the function of RGD-coated surfaces

4. Use of the OWLS technique to investigate the kinetic mechanism of cell adhesion and spreading

As presented in this thesis, the surface reaction of succinimidyl esters with amino-terminated surfaces is the key step of this method. Although this type of crosslinking reactions have been thoroughly studied in solution, the surface reactions are just at the beginning stage and are not yet well understood regarding the turn-over, steric hindrance, and side reactions. Some rules used in the bulk chemistry may be not suitable or need modifications when applied to the surface chemistry. During grafting maleimidyl groups onto aminosilanized Ti surfaces, we found some controversy regarding the interpretation of the IRAS spectra, especially for the maleimidylhexanoyl pendant surface. In order to clarify the IRAS spectral assignments and to study the detail of this reaction, two model aminothiol (cystamine and 4-aminothiophenol) SAMs on Au surfaces were used as the amino-terminated surface instead of the aminosilanized titanium surface. Different types of crosslinking groups such as thiol-, amino-, and photo-reactive groups were attached to the two terminal amino SAMs. Based on IRAS and XPS measurements, two types of reaction schemes have been observed: (1) modification through single group binding, (2) occurrence of side reactions and production of multiple-group-modified surfaces. A typical example for the latter case is the reaction of N-succinimidyl-6-maleimidyl hexanoate (EMCS) with terminal amino groups, producing a mixture of both maleimidyl and succinimidyl ester groups on the surface. The conclusion is further confirmed by the study of SAMs of pure N, N'-bis(maleimidylhexanoyl)cystamine (BMHC), synthesized separately. The functionalized surfaces with crosslinking groups can be used for specific or non-specific attachment of biomolecules.

From the above investigations, it is obvious that the main surface organo-biochemical reaction is often accompanied by some side reactions, similar to the bulk reactions in solution or in solid states, specially when there are several reactive sites. Unlike in the

bulk reaction, however, where the pure product can be separated and definitely identified by many analysis methods such as NMR, elemental analysis, and X-ray single crystal diffraction, the molecular structure of the surface product can only be deduced from the surface sensitive techniques such as IRAS, XPS, ToF-SIMS, NEXAFS, and AFM. These methods only provide partial information of the molecular structure. Therefore, the surface molecular structure deduced from the above mentioned techniques is very reasonable but not absolutely definite.

Although we deduced some surface molecular structures, there are still many questions to be answered in the future:

1. What is the general relationship between the bulk chemistry and the surface chemistry? How to apply or modify the rules of the bulk chemistry to the surface chemistry?

2. Why is the reaction of succinimidyl esters with amino groups in organic media is easier on the surface than in the bulk?

3. Why is the surface reaction of amino groups with EMCS obviously different from its analogs? (The 3-D structures of the heterobifunctional crosslinkers and the reaction mechanisms must be built up to answer this question).

Finally, two types of poly(ethylene glycol) (PEG) were grafted to amino-terminated surfaces, methoxy-PEG in a "standing-up" configuration and bridging-PEG in a "lying-down" configuration. The protein resistance of PEG-coatings was evaluated with the optical waveguide lightmode spectroscopy (OWLS), and only the bridging PEG exhibited a good protein resistance. Future work on grafting peptides and proteins should be done by using the heterobifunctional crosslinkers bearing succinimidyl ester and maleimide (or other amino-resistant crosslinking groups) with the PEG chain between them. In such a case, the PEG chain is as a flexible spacer whose chain length can be in variable ranges from several to thousand ethylene glycol groups. The PEG chain is also as a background resistant to protein adsorption, cell and bacteria adhesion. PEG-tethered proteins may exhibit enhanced activity due to reduced protein-surface interaction, greater molecular freedom, and shielding from local surface charge and pH effects. They may be used in chromatographies, electrophoreses, biosensors, and other applications.

8. References

1.	Hong, H. G.; Bohn, P. W.; Sliger, S. G. *Analytical Chemistry* **1993**, *65*, 1635.

2.	Hong, H. G.; Jiang, M.; Sliger, S. G.; Bohn, P. W. *Langmuir* **1994**, *10*, 153.

3.	Bhatia, S. K.; Teixeira, J. L.; Anderson, M.; Shriver-Lake, L. C.; Calvert, J. M.; Georger, J. H.; Hickman, J. J.; Dulcey, C. S.; Schoen, P. E.; Ligler, F. S. *Analytical Biochemistry* **1993**, *208*, 197.

4.	de Gennes, P. G. *Ann. Chim.* **1987**, *77*, 389.

5.	Andrade, J. D.; Hlady, V. *Adv. Polymer Sci.* **1986**, *79*, 1.

6.	Wang, R. L. C.; Kreuzer, H. J.; Grunze, M. *J. Phys. Chem. B* **1997**, *101*, 9767.

7.	Gold, J. M.; Schmidt, M.; Steinemann, S. G. *Helvetica Physica Acta* **1989**, *62*, 246.

8.	Geckeler, K. E.; Rupp, F.; Geis-Gerstorfer, J. *Advanced Materials* **1997**, *9*, 513.

9.	Pröbster, L.; Krämer, A.; Wall, G. Z. *Zahnärztl. Implantol.* **1991**, *7*, 84.

10.	Ektessabi, A. M. *Nuclear Instr. Methods Phys. Res. B* **1995**, *99*, 610.

11.	Kim, C. S.; Ducheyne, P. *Biomaterials* **1991**, *12*, 461.

12.	Ducheyne, P.; Van Raemdonck, W.; Heughebaert, J. C.; Heughebaert, M. *Biomaterials* **1986**, *7*, 97.

13.	Ducheyne, P.; Radin, S.; Heughebaert, M.; Heughebaert, J. C. *Biomaterials* **1990**, *11*, 244.

14.	Lacefield, W. R., *Bioceramics: Material Characteristics versus In Vivo Behavior*, Ducheyne, P.; Lemons, J.E., Ed; Ann. N.Y. Acad. Sci., **1988**; Vol. 523, p 72.

15.	Tang, L.; Tsai, C.; Gerberich, W. W.; Kruckeberg, L.; Kania, D. R. *Biomaterials* **1995**, *16*, 483.

16.	Hilton, M. R.; Salmeron, G. A.; Somorjai, G. A. *Thin Solid Films* **1988**, *167*, L31.

17.	Williams, A. M.; Buchanan, R. A. *Mater. Sci. Eng.* **1985**, *69*, 237.

18.	Muraleedharan, T. M.; Meletis, E. I. *Thin Solid Films* **1992**, *221*, 104.

19.	Petrov, I.; Hultman, L.; Helmersson, J. E.; Greene, J. E. *Thin Solid Films* **1989**, *169*, 299.

20.	Krämer, A.; Weber, H.; Geis-Gerstorfer, J. Z. *Zahnärztl. Implantol.* **1989**, *5*, 283.

21.	Wisbey, A.; Gregson, P. J.; Peter, L. M.; Tuke, M. *Biomaterials* **1991**, *12*, 470.

22.	Browne, M.; Gregson, P. J. *Biomaterials* **1994**, *15*, 894.

23. Wälivara, B.; Aronsson, B.-O.; Rodahl, M.; Lausmaa, J.; Tengvall, P. *Biomaterials* **1994**, *15*, 827.

24. Ban, S.; Maruno, S.; Hasegawa, J. *Jpn. J. Appl. Phys.* **1991**, *30*, L1333.

25. Caiazza, S.; Taruscio, D.; Ciaralli, F.; Crateri, P.; Chistolini, P.; Bedini, R.; Colangeno, S.; Pintucci, S. *Biomaterials* **1991**, *12*, 474.

26. Sukenik, C. N.; Balachander, N.; Culp, L. A.; Lewandowska, K.; Merritt, K. *Journal of Biomedical Materials Research* **1990**, *24*, 1307.

27. Vandenberg, E. T.; Bertilsson, L.; Liedberg, B.; Uvdal, K.; Erlandsson, R.; Elwing, H.; Lundström, I. *Journal of Colloid and Interface Science* **1991**, *147*, 103.

28. McGovern, M. E.; Kallury, K. M. R.; Thompson, M. *Langmuir* **1994**, *10*, 3607.

29. Chiang, C. H.; Koenig, J. L. *Journal of Colloids and Interface Science* **1981**, *83*, 361.

30. Okusa, H.; Kurihara, K.; Kunitake, T. *Langmuir* **1994**, *10*, 3577.

31. Hook, D. J.; Vargo, T. G.; Gardella, J. A. Jr.; Litwiler, K. S.; Bright, F. V. *Langmuir* **1991**, *7*, 142.

32. Tada, H. *Langmuir* **1996**, *12*, 966.

33. Tripp, C. P.; Hair, M. L. *Langmuir* **1995**, *11*, 149.

34. Wasserman, S. R.; Tao, Y.-T.; Whitesides, J. M. *Langmuir* **1989**, *5*, 1074.

35. Banga, R.; Yarwood, J.; Morgan, A. M.; Evans, B.; Kells, J. *Langmuir* **1995**, *11*, 4393.

36. Schwartz, D. K.; Steinberg, S.; Israelachvili, J.; Zasadzinski, Z. A. N. *Phys. Rev. Lett.* **1992**, *69*, 3354.

37. Bierbaum, K.; Kinzler, M. Wöll, Ch.; Grunze, M.; Hähner, G.; Heid, S.; Effenberger, F. *Langmuir* **1995**, *11*, 512.

38. Lee, Y. W.; Reed-Mundell, J.; Sukenik, C. N.; Zull, J. E. *Langmuir* **1993**, *9*, 3009.

39. Balachander, N.; Sukenic, C. N. *Langmuir* **1990**, *6*, 1621.

40. Lynn, M. *Inorganic Support Intermediates*; in *Immobilized Enzymes, Antigens, Antibodies, and Peptides* Weetall, H. H., Ed.; Marcel Dekker: New York, **1975**.

41. Kennedy, J. F.; Cabral, J. M. S. *Immobilized Enzymes* in *Solid Phase Biochemistry Aspects* Scouten, W.H.; Ed., **1983**.

42. Bain, C. D.; Whitesides, G. M. *Adv. Mater.* **1989**, *1*, 506.

43. Dubois, L. H.; Nuzzo, R. G. *Ann. Phys. Chem.* **1992**, *43*, 437.

44. Sellers, H.; Ulman, A.; Shnidman, Y.; Eilers, J. E. *J. Am. Chem. Soc.* **1993**, *115*, 9389.

45. King, D. E. *J. Vac. Sci. Technol.* **1995**, *13*, 1247.

46. Camillone III, N.; Leung, T. Y. B.; Scoles, G. *SPIE, OE/LASE Proc.* **1994**, 2125.

47. Bain, C. D.; Troughton, E. B.; Tao, Y.-T.; Evall, J.; Whitesides, G. M.; Nuzzo, R. G. *J. Am. Chem. Soc.* **1989**, *111*, 321.

48. Biebuyck, H. A.; Bain, C. D.; Whitesides, G. M. *Langmuir* **1994**, *10*, 1825.

49. Hickman, J. J.; Ofer, D.; Zou, C.; Wrighton, M. S.; Laibinis, P. E.; Whitesides, G. M. *J. Am. Chem. Soc.* **1991**, *113*, 1128.

50. Collard, D. M.; Fox, M. A. *Lanmuir* **1991**, *7*, 1192.

51. Groat, K. A.; Creager, S. E. *Langmuir* **1993**, *9*, 3668.

52. Schlenoff, J. B.; Li, M.; Ly, H. *J. Am. Chem. Soc.* **1995**, *117*, 12528.

53. Nuzzo, R. G.; Dubois, L. H.; Allara, D. L. *J. Am. Chem. Soc.* **1990**, *112*, 558.

54. Allara, D. L.; Nuzzo, R. G. *Langmuir* **1985**, *1*, 52.

55. Alber, T. *Annu. Rev. Biochem.* **1989**, *58*, 765.

56. Falb, R. D. *Covalent linkage. I. Enzyme Immobilization by Covalent Linkage on Insolubilized Support* Plenum publishing: New York, **1977**; Vol. 1.

57. Wong, S. S. *Chemistry of Protein Conjugation and Cross-linking*, CRC Press: USA, **1991**.

58. Pierschbacher, M. D.; Ruoslahti, E. *Nature* **1984**, *309*, 30.

59. Ruoslahti, E.; Pierschbacher, M. D. *Science* **1987**, *238*, 491.

60. Pierschbacher, M. D.; Ruoslahti, E. *Proc. Natl. Acad. Sci. USA* **1984**, *81*, 5985.

61. Ruoslahti, E. ; *Cell Biology of Extracellular Matrix* Plenum Press: New York, **1991**, chap. 10.

62. Craig, W. S.; Cheng, S.; Mullen, D. G.; Blevitt, J.; Pierschbacher, M. D. *Biopolymers (Peptide Science)* **1995**, *37*, 157.

63. Massia, S. P.; Hubbell, J. A. *Analytical Biochemistry* **1990**, *187*, 292.

64. Massia, S. P.; Hubbell, J. A. *The Journal of Cell Culture* **1991**, *114*, 1089.

65. Massia, S. P.; Hubbell, J. A. *Journal of Biomedical Materials Research* **1991**, *25*, 223.

66. Glass, J. R.; Dickerson, K. T.; Stecker, K.; Polarek, J. W. *Biomaterials* **1996**, *17*, 1101.

67. Dee, K. C.; Rueger, D. C.; Andersen, T. T.; Bizios, R. *Biomaterials* **1996**, *17*, 209.

68. Roberts, C.; Chen, C. S.; Mrksich, M.; Martichonok, V.; Ingber, D. E.; Whitesides, G. M. *J. Am. Chem. Soc.* **1998**, *120*, 6548.

69. Drumeller, P. D.; Elbert, D. L.; Hubbell, J. A. *Biotechno. Bioeng.* **1994**, *43*, 772.

70. Pierschbacher, M. D.; Polarek, J. W.; Craig, W. S.; Tschopp, J. F.; Sipes, N. J.; Harper, J. R. *J. Cell. Biochem.* **1994**, *56*, 150.

71. Reinholt, F. P.; Haltenly, K.; Oldberg, Å.; Heinegård, D. *Proc. Natl. Acad. Sci. USA* **1990**, *87*, 4473.

72. Fisher, J. E.; Caulfield, M. P.; Sato, M.; Quartuccio, H. A.; Gould, R. J., *Endocrinology* **1993**, *132*, 1411.

73. Evans, S.; Pritchard, R. G.; Thomas, J. M. *J. Electron Spectrosc. Relat. Phenom.* **1978**, *14*, 341.

74. Eischen, R. P.; Plisken, W. A.; Sims, M. L. *J. Chem. Phys.* **1954**, *22*, 1786.

75. Pritchard, J.; Sims, M. L., *Trans Farady Soc.* **1970**, *66*, 427.

76. Bradshaw, A. M.; Pritchard, J.; Sims, M. L. *J. Chem. Soc. Chem. Commun.* **1968**, 1519.

77. Greenler, R. G. *J. Chem. Phys.* **1966**, *44*, 310.

78. Parikh, A. N.; Allara, D. L. *J. Chem. Phys.* **1992**, *96*, 927.

79. Debe, M. K. *Applications of Surface Science* **1982**(3), *14*, 1.

80. Debe, M. K. *J. Vac. Sci. Technol.* **1982**, *21*, 74.

81. Iida, K.; Imamura, Y.; Liao, C.; Nakamura, S.; Sawa, G. *Polymer Journal* **1996**, *28*, 352.

82. Varsanyi, G. *Vibrational Spectra of Benzene Derivatives* ACADEMIC PRESS, INC., **1969**.

83. Binnig, G.; Gerber, C.; Quate, C. F. *Phys. Rev. Lett.* **1986**, *56*, 930.

84. Fodor, S. P. A.; Read, L.; Pirrung, M. C.; Stryer, L.; Lu, A. T.; Solas, D. *Science* **1991**, *251*, 767.

85. Nawrocki, J.; Dunlap, J.; Carr, P. W.; Blackwell, J. A. *Biotechnol. Prog.* **1994**, *10*, 561.

86. Doherty, P. J.; Williams, D. F. *Biomaterial-Tissue Interfaces: Advances in Biomaterials* Elsevier, **1992**, Vol. 10.

87. Brown, S. A.; Lemons, J. E. *Medical Application of Titanium and its Alloys: The Material and Biological Issues* ASTM, **1996**.

88. Brandly, B. K.; Schaar, R. L. *Anal. Biochem.* **1988**, *172*, 270.

89. Puleo, D. A. *Journal of Biomedical Materials Research* **1995**, *29*, 951.

90. Puleo, D. A. *Biomaterials* **1996**, *17*, 217.

91. Dee, K. C.; Andersen, T. T.; Bizios, R. *Tissue Engineering* **1995**, *1*, 135.

92. Bhatia, S. K.; Shriver-Lake, L. C.; Prior, K. J.; Georger, J. H.; Calvert, J. M.; Bredehorst, R.; Ligler, F. S. *Analytical Biochemistry* **1989**, *178*, 408.

93. Heyse, S.; Vogel, H.; Sanger, M.; Sigrist, H. *Protein Science* **1995**, *4*, 2532.

94. Chrisey, L. A.; Lee, G. U.; O'Ferrall, C. E. *Nucleic Acids Research* **1996**, *24*, 3031.

95. Chrisey, L. A.; O'Ferrall, C. E.; Spargo, B. J.; Dulcey, C. S.; Calvert, J. M. *Nucleic Acids Research* **1996**, *24*, 3040.

96. Matsuzawa, M.; Umemura, K.; Beyer, D.; Sugioka, K.; Knoll, W. *Thin Solid Films* **1997**, *305*, 74.

97. Kurrat, R.; Textor, M.; Ramsden, J. J.; Böni, P.; Spencer, N. D. *Rev. Sci. Instrumen.* **1997**, *68*, 2172.

98. Sittig, C.; Wieland, M.; Textor, M.; Vallotton, P.-H.; Spencer, N. D. *J. Mater. Sci. Mater. Med.* **1999**, *10*, 35.

99. Plueddemann, E. P. *Silane Coupling Agent* Plenum Press, New York, **1991**.

100. Haller, I. *J. Am. Chem. Soc.* **1978**, *100*, 8050.

101. Ondrus, D. J.; Boerio, F. J. *Journal of Colloid and Interface Science* **1988**, *124*, 349.

102. Yates, D. E.; James, R. O.; Healy, T. W. *J. Chem. Soc., Faraday Trans.* **1980**, *76*, 1.

103. Kallury, K. M. R.; Macdonald, P. M.; Thompson, M. *Langmuir* **1994**, *10*, 492.

104. Beamson, G.; Briggs, D. *High Resolution XPS of Organic Polymers* John Wiley & Sons Ltd., **1992**.

105. Jentoft, N.; Dearborn, D. G. *The Journal of Biological Chemistry* **1979**, *254*, 4359.

106. Yankeelov, J. A., Jr. *Methods Enzymol.* **1972**, *25*, 566.

107. Liao, T. H.; Ho, H. C.; Abe, A. *Biochim. Biophys. Acta* **1991**, *1079*, 335.

108. Lindsay, D. G. *FEBS Lett.* **1972**, *21*, 105.

109. Glaser, A. N.; *The Proteins*, Neurath, H.; Hill, R. L., Ed.; Academic Press: New York, **1976**.

110. Mckittrick, P. T.; Katon, J. E. *Applied Spectroscopy* **1990**, *44*, 812.

111. Roepstorff, P.; Fohlman, J. *Biomed. Mass. Spectrom.* **1984**, *11*, 601.

112. Bruinink, A.; in *The Brain in Bits and Pieces*, Zbinden, G. Ed., Zollikon, **1992**, p 23.

113. Minkin, C. *Tissue Int.* **1982**, *34*, 285.

114. Sun, L.; Kepley, J.; Crooks, R. M. *Langmuir* **1992**, *8*, 2102.

115. Duevel, R. V.; Corn, R. M. *Anal. Chem.* **1992**, *64*, 337.

116. Ulman, A.; Tillman, N. *Langmuir* **1989**, *5*, 1418.

117. Bent, S. F.; Schilling, M. L.; Wilson, W. L.; Katz, H. E.; Harris, A. L. *Chem. Mater.* **1994**, *6*, 122.

118. Keller, H.; Schrepp, W.; Fuchs, H. *Thin Solid Films* **1992**, *210/211*, 799.

119. Bertilson, L.; Liedberg, B. *Langmuir* **1993**, *9*, 141.

120. Wagner, P.; Zaugg, F.; Kernen, P.; Hegner, M.; Semenza, G. *J. Vac. Sci. Technol. B* **1996**, *14*, 1466.

121. Wagner, P.; Hegner, M.; Kernen, P.; Zaugg, F.; Semenza, G. *Biophys. J.* **1996**, *70*, 2052.

122. Frey, B. L.; Corn, R. M. *Anal. Chem.* **1996**, *68*, 3137.

123. Whitesell, J. K.; Chang, H. K.; Whitesell, C. S. *Angew. Chem., Int. Ed. Engl.* **1994**, *33*, 871.

124. Whitesell, J. K.; Chang, H. K. *Science* **1993**, *261*, 73.

125. Fox, M. A.; Whitesell, J. K.; McKerrow, A. J. *Langmuir* **1998**, *14*, 816.

126. Arias, F.; Godínez, L. A.; Wilson, S. R.; Kaifer, A. E.; Echegoyen, L. *J. Am. Chem. Soc.* **1996**, *118*, 6086.

127. Shannon, C.; Frank, D. G.; Hubbard, A. T. *Annu. Rev. Phys. Chem.* **1991**, *42*, 393.

128. Hubbard, A. T. *Chem. Rev.* **1988**, *88*, 633.

129. Dhirani, A.; Zehner, R. W.; Hsung, R. P.; Guyot-Sionnest, P.; Sita, L. R. *J. Am. Chem. Soc.* **1996**, *118*, 3319.

130. Chang, S.-C.; Chao, I.; Tao, Y.-T. *J. Am. Chem. Soc.* **1994**, *116*, 6792.

131. Kim, Y.-T.; McCarley, R. L.; Bard, A. J. *J. Phys. Chem.* **1992**, *96*, 7416.

132. Hayes, W. A.; Shannon, C. *Langmuir* **1996**, *12*, 3688.

133. Sun, L.; Johnson, B.; Wade, T.; Crooks, R. M. *J. Phys. Chem.* **1990**, *94*, 8869.

134. Bryant, M. A.; Crooks, R. M. *Langmuir* **1993**, *9*, 385.

135. Hayes, W. A.; Kim, H.; Yue, X.; Perry, S. S.; Shannon, C. *Langmuir* **1997**, *13*, 2511.

136. Osawa, M.; Matsuda, N.; Yoshii, K.; Uchida, I. *J. Phys. Chem.* **1994**, *98*, 12702.

137. Johnson, S. R.; Evans, S. D.; Mahon, S. W.; Ulman, A. *Langmuir* **1997**, *13*, 51.

138. Bandyopadhyay, K.; Sastry, M.; Paul, V.; Vijayamohanan, K. *Langmuir* **1997**, *13*, 866.

139. Young, J. T.; Boerio, F. J.; Zhang, Z.; Beck, T. L. *Langmuir* **1996**, *12*, 1219.

140. Saito, Y.; Machida, K.; Uno, T. *Spectroschim. Acta, Part A* **1975**, *31A*, 1237.

141. DeGraff, B. A.; Gillespie, D. W.; Sundberg, R. J. *J. Am. Chem. Soc.* **1974**, *96*, 7491.

142. Mazat, E. *Acta Cryst.* **1972**, *B28*, 415.

143. Ishida, H.; Wellinghoff, S. T.; Baer, E.; Koenig, J. L. *Macromolecules* **1980**, *13*, 826.

144. Porter, M. D.; Bright, T. B.; Allara, D. L.; Chidsey, C. E. D. *J. Am. Chem. Soc.* **1987**, *109*, 3559.

145. Parker, S. F.; Mason, S. M.; Williams, K. P. J. *Spectrochimica Acta* **1990**, *46A*, 315.

146. Parker, S. F. *Spectrochimica Acta Part A* **1995**, *51*, 2067.

147. Collioud, A.; Clémence, J.-F.; Sänger, M.; Sigrist, H. *Bioconjugate Chem.* **1993**, *4*, 528.

148. Doughty, M. B.; Chaurasia, C. S.; Li, K. *J. Med. Chem.* **1993**, *36*, 272.

149. Woldbaek, T.; Klaboe, P.; Nielsen, C. J. *J. Mol. Struct.* **1975**, *27*, 283.

150. Tam-Chang, S.-W.; Biebuyck, H. A.; Whitesides, G. M.; Jeon, N.; Nozzo, R. A. *Langmuir* **1995**, *11*, 4371.

151. Lenk, T. J.; Hallmark, V. M.; Hoffmann, C. L.; Rabolt, J. F.; Castner, D. G.; Erdelen, C.; Ringsdorf, H. *Langmuir* **1994**, *10*, 4610.

152. Clegg, R. S.; Hutchison, J. E. *Langmuir* **1996**, *12*, 5239.

153. Harris, J. M., Ed., *Poly(Ethylene Glycol) Chemistry: Biotechnical and Biomedical Applications*, Plenum Press: New York, **1992**.

154. Ramsden, J. J. *J. Statist. Phys.* **1993**, *73*, 853.

155. Benninghoven, A. *Angew. Chem. Int. Ed. Engl.* **1994**, *33*, 1023.

156. Brundle, C. R.; Hopster, H.; Swalen, J. D. *J. Chem. Phys.* **1979**, *70*, 5190.

157. Bain, D. B.; Whitesides, G. M. *J. Phys. Chem.* **1989**, *93*, 1670.

158. Hähner, G.; Kinzler, M.; Thummer, C.; Woll, C.; Grunze, M. *J. Vac. Sci. Technol. A* **1992**, *10*, 2758.

159. Hähner, G.; Woll, C.; Buck, M.; Grunze, M. *Langmuir* **1993**, *9*, 1955.

160. Fisher, D.; Marti, A.; Hähner, G. *J. Vac. Sci. Technol. A* **1997**, *15*, 2173.

161. Briggs, D.; Seah, M. P. *Practical Surface Analysis*, 2nd edition, Volume 1, *Auger and X-ray Photoelectron Spectroscopy* John Wiley & Sons, **1990**, p 201.

9. Appendix

Crosslinker structures, names, and abbreviations

- **Heterobifunctional crosslinkers**
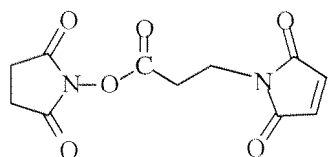
N-Succinimidyl-3-maleimidylpropionate (SMP)
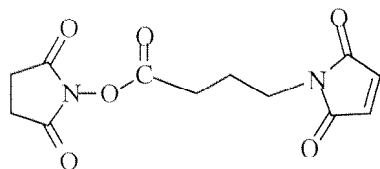
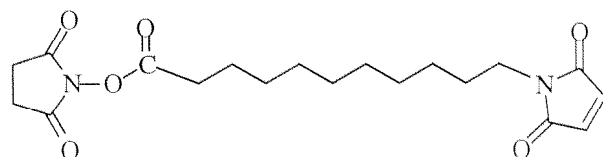N-Succinimidyl-4-maleimidylbutyrate (SMB)
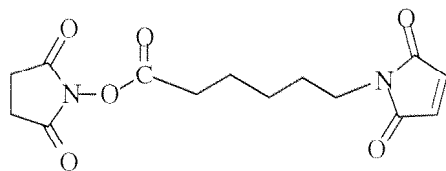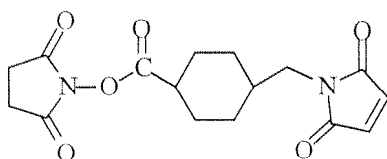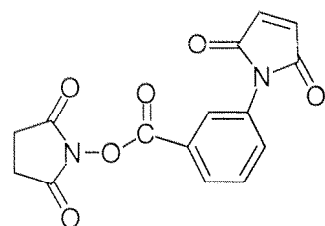

N-Succinimidyl-6-maleimidylhexanoate (EMCS)
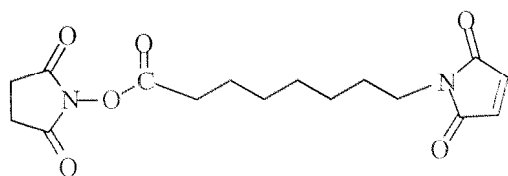
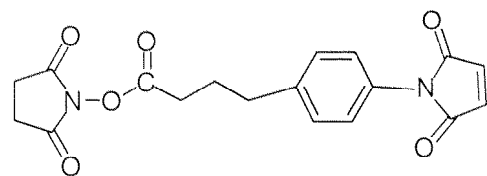N-Succinimidyl-8-maleimidyloctanoate (SMO)
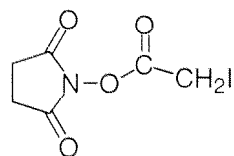

N-Succinimidyl-11-maleimidylundecanoate (SMU)

N-Succinimidyl trans-4-(maleimidylmethyl) cyclohexane-1-carboxylate (SMCC)
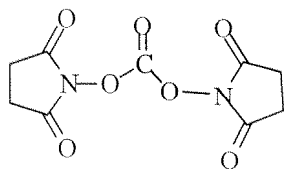

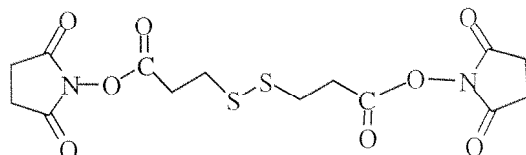N-Succinimidyl-3-maleimidylbenzoate (SMBZ)

N-Succinimidyl-4-(4-maleimidylphenyl)-butyrate (SMPB)
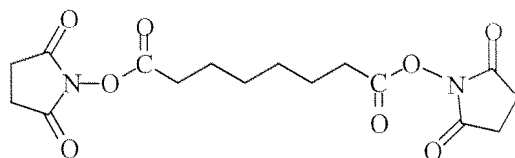

N-Succinimidyl iodoacetate (SIA)

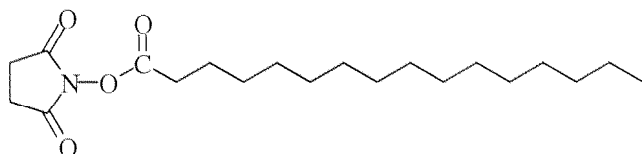- **Homobifunctional crosslinkers**

Di-(N-succinimidyl) carbonate (SC)

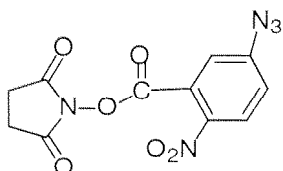Dithiobis(N-succinimidyl propionate) (DTSP)
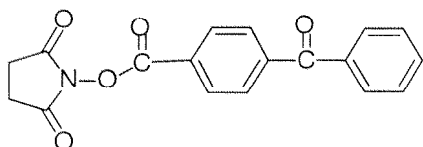

Di-(N-succinimidyl) suberate (DSS)

N-Succinimidyl hexadecanoate (SH)
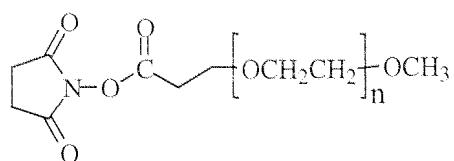
- **Photocrosslinkers**

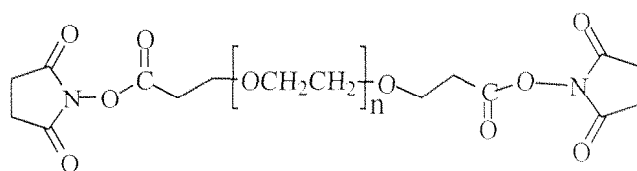N-5-Azido-2-nitrobenzoyloxysuccinimide (ANS)

N-Succinimidyl-4-benzoylbenzoate (SBB)

- **PEG with succinimidyl esters**

Mono-methyl-polyethylene glycol 5000 propionoic acid-N-succinimidylester
(Methoxy-PEG-SPA) MW 5000

SPA-PEG-SPA, MW 3400

Curriculum Vitae

Date of Birth: Dec. 07, 1963

Nationality: Chinese

1970 - 1979:   Primary school in Tianmen County, Hubei Province, China

1979 - 1981:   High school in Jingzhou, Hubei Province, China

1981 - 1985:   Undergraduate student at the Department of Chemistry, Fudan University, Shanghai, China; B.Sc. in 1985

1985 - 1988:   Graduate student major in organic chemistry at the Department of Chemistry, Fudan University, Shanghai, China; M.Sc. in 1988

1988 - 1994:   Lecturer at the Department of Biomedical Engineering, Southeast University, Nanjing, China

1994 - 1995:   Studying biomedical technology at Neu-Technikum Buchs, Switzerland

1996 - 1999:   PhD student guided by Prof. Dr. N.D. Spencer and Dr. M. Textor at the Laboratory for Surface Science and Technology, Department of Materials, Swiss Federal Institute of Technology Zürich

Publications

Journals

1. Covalent attachment of cell-adhesive, (Arg-Gly-Asp)-containing peptides to titanium surfaces S.J. Xiao, M. Textor, N.D. Spencer, H. Sigrist *Langmuir 14*, 5507-16, **1998**
2. Immobilization of the cell-adhesive peptide Ary-Gly-Asp-Cys (RGDC) on titanium surfaces by covalent chemical attachment S.J. Xiao, M. Textor, N.D. Spencer, M. Wieland, B. Keller, H. Sigrist *J. Mater.: Mater. Med. 8* 867-872 **1997**

Pending papers

3. Surface reactions of amino-terminated self-assembled films with heterobifunctional crosslinkers bearing succinimidyl ester and maleimide for grafting biomolecules
4. Surface reactions of amino-terminated self-assembled films with homobifunctional crosslinkers of succinimidyl esters
5. The bone-like cell interactions with surface-coupled (Arg-Gly-Asp)-containing peptides on titanium surfaces

Presentations

1. Immobilization of RGD-containing peptides on titanium surfaces 13th European Conference on Biomaterials, S.J. Xiao, H. Sigrist, M. Textor, N.D. Spencer, Goeteborg September **1997** Proceedings p.114
2. Surface reactions of succinimidyl esters with amino-tailed ultrathin organic films for grafting biomolecules Shou-Jun Xiao, Werkstoff-Kolloquium WS 98/99, Department of Materials, ETH Zürich, Nov. 21, **1998**

Posters

1. Immobilization of the cell adhesive peptides containing RGD-sequences on titanium surfaces, S.J. Xiao, M. Wieland, H. Sigrist, M. Textor, B.A. Keller, N.D. Spencer Biosurf Zürich Sept. 25-26, **1997**, Proceedings, P16
2. Surface reactions of succinimidyl esters with amino-terminated SAMs for grafting biomolecules S. J. Xiao, S. Brunner, M. Textor, N.D. Spencer, Biosurf II, Lausanne, Oct. 1-2, **1998**, B22
3. Functionalization of titanium surfaces: Covalent attachment of cell-adhesive biomolecules, S.J. Xiao, M. Textor, H. Sigrist, V. Schenk, A. Bruinink, E. Wintermantel, N.D. Spencer, XIth Aachen Colloquium on Biomaterials RWTH Aachen, Germany, Feb. 12-13, **1998**, Poster 16

Publications

Journals

1. Covalent attachment of cell-adhesive, (Arg-Gly-Asp)-containing peptides to titanium surfaces S.J. Xiao, M. Textor, N.D. Spencer, H. Sigrist *Langmuir 14*, 5507-16, **1998**
2. Immobilization of the cell-adhesive peptide Ary-Gly-Asp-Cys (RGDC) on titanium surfaces by covalent chemical attachment S.J. Xiao, M. Textor, N.D. Spencer, M. Wieland, B. Keller, H. Sigrist *J. Mater.: Mater. Med. 8* 867-872 **1997**

Pending papers

3. Surface reactions of amino-terminated self-assembled films with heterobifunctional crosslinkers bearing succinimidyl ester and maleimide for grafting biomolecules
4. Surface reactions of amino-terminated self-assembled films with homobifunctional crosslinkers of succinimidyl esters
5. The bone-like cell interactions with surface-coupled (Arg-Gly-Asp)-containing peptides on titanium surfaces

Presentations

1. Immobilization of RGD-containing peptides on titanium surfaces 13th European Conference on Biomaterials, S.J. Xiao, H. Sigrist, M. Textor, N.D. Spencer, Goeteborg September **1997** Proceedings p.114
2. Surface reactions of succinimidyl esters with amino-tailed ultrathin organic films for grafting biomolecules Shou-Jun Xiao, Werkstoff-Kolloquium WS 98/99, Department of Materials, ETH Zürich, Nov. 21, **1998**

Posters

1. Immobilization of the cell adhesive peptides containing RGD-sequences on titanium surfaces, S.J. Xiao, M. Wieland, H. Sigrist, M. Textor, B.A. Keller, N.D. Spencer Biosurf Zürich Sept. 25-26, **1997**, Proceedings, P16
2. Surface reactions of succinimidyl esters with amino-terminated SAMs for grafting biomolecules S. J. Xiao, S. Brunner, M. Textor, N.D. Spencer, Biosurf II, Lausanne, Oct. 1-2, **1998**, B22
3. Functionalization of titanium surfaces: Covalent attachment of cell-adhesive biomolecules, S.J. Xiao, M. Textor, H. Sigrist, V. Schenk, A. Bruinink, E. Wintermantel, N.D. Spencer, XIth Aachen Colloquium on Biomaterials RWTH Aachen, Germany, Feb. 12-13, **1998**, Poster 16